12-2017

Exploratory Hydrothermal Synthesis and Crystal Growth of Refractory Rare-Earth Oxides with Tetravalent and Pentavalent Metal Oxide Building Blocks

Kyle Raymond Fulle
Clemson University

EXPLORATORY HYDROTHERMAL SYNTHESIS AND CRYSTAL GROWTH OF REFRACTORY RARE-EARTH OXIDES WITH TETRAVALENT AND PENTAVALENT METAL OXIDE BUILDING BLOCKS

A Dissertation
Presented to
the Graduate School of
Clemson University

In Partial Fulfillment
of the Requirements for the Degree
Doctor of Philosophy
Chemistry

---

by
Kyle Raymond Fulle
December 2017

Accepted by:
Dr. Joseph W. Kolis, Committee Chair
Dr. Shiou-Jyh Hwu
Dr. William T. Pennington
Dr. Joseph S. Thrasher

ABSTRACT

The crystal growth of large, defect-free and optically transparent materials has been an active area of research for over two centuries. A multitude of crystal growth techniques have been employed during this time, each submitting advantages and disadvantages to the solid-state community. As the heart of solid-state lasers, communication devices and semiconductors, synthetically grown crystals for optical and magnetic applications hold the key for future innovation and design. There are large classes of materials that display recumbent characteristics that inhibit their manipulation by most current solid-state techniques on the market. These refractory oxides display extreme melting ranges (> 2000 °C) which inhibit solubility in the melt-based solid-state techniques typically engineered in crystal growth laboratories. Herein, this dissertation employs the high-temperature and high-pressure technique to drive the solubility of select refractory oxides into solution several hundred degrees prior to their melting points being attained.

The investigation of pentavalent and tetravalent oxides (Nb_2O_5, Ta_2O_5, TiO_2, GeO_2, and SiO_2) with rare-earth oxides (La-Lu, Sc) under hydrothermal conditions has led to the discovery of several new compounds previously unattainable by conventional solid-state growth techniques. These included, but are not limited to, $RENbO_4$ (RE = La-Lu), $La_5Ti_4O_{15}(OH)$, $Lu_5Ti_2O_{11}(OH)$, and $Ba_2Lu_2Si_4O_{12}F_2$ single crystals. The discovery of new classes of materials will lead to further investigations of optical properties. Furthermore, the ability to solubilize metal oxides, hundreds of degrees below their

melting point, is leading to high-quality, defect-free, bulk single-crystal growth of new and existing materials. As the solution chemistry of metal oxides continues to be investigated and explored under hydrothermal conditions, new optical and magnetic materials continue to emerge and display desirable traits in applied sciences.

DEDICATION

I dedicate this work to my mom Lavonne Fulle, without whom, I would not be where I am today. Thank you for working multiple jobs so that I could go to school and attain a good education. You are loved beyond measure, and there is no way I could ever repay all that you have done for me. Thank you for also teaching me this life lesson from Philippians 3:7-8: “But whatever were gains to me I now consider loss for the sake of Christ. What is more, I consider everything a loss because of the surpassing work of knowing Christ Jesus my Lord, for whose sake I have lost all things. I consider them garbage, that I may gain Christ and be found in Him, not having a righteousness of my own that comes from the law, but that which is through faith in Christ- the righteousness that comes from God on the basis of faith.”

ACKNOWLEDGEMENTS

I would like to extend my deepest gratitude to my advisor, Dr. Joseph Kolis for his inspiration and guidance on these projects. I would also like to thank Dr. Hwu, Dr. Pennington, and Dr. Thrasher for serving as members of my committee. Additionally, I would be lost without the constant advice and guidance of Dr. Colin McMillen and Dr. Duminda Sanjeewa. I would also like to thank current and past Kolis group members Dr. Martin Kimani, Dr. Cherie Moore, Dr. Sara Comer, Dr. Brad Stadelman, Rylan Terry, and Daniel Vinton for their support of projects and work in the lab throughout the years.

Last but certainly not least, I would like to thank my friends and family for their love and support throughout this journey. I am grateful to my beautiful and incredibly intelligent wife Raicheal, my parents Robert and Lavonne Fulle, and my younger brothers Ethan and Hunter Fulle for endless love they continue to show me.

TABLE OF CONTENTS

LIST OF TABLES

List of Tables (Continued)

List of Tables (Continued)

Table Page

LIST OF FIGURES

List of Figures (Continued)

Figure Page

List of Figures (Continued)

Figure Page

List of Figures (Continued)

Figure Page

List of Figures (Continued)

Figure Page

List of Figures (Continued)

Figure Page

List of Figures (Continued)

Figure Page

List of Figures (Continued)

Figure Page

List of Figures (Continued)

Figure Page

CHAPTER ONE

INTRODUCTION

Perspective on Crystal Growth

Crystal growers need a wide skill set from understanding the underlying physics of electronic transitions of materials, crystal engineering to grow large single crystals absent of defect, and a deep understanding of material and electrical limitations in solid-state techniques, just to list a few. While the field of crystal growth encompasses several disciplines, chemistry and the chemist aspire to achieve essentially three key components. First, propose a new or existing material that could be beneficial for study over several disciplines. Secondly, design and implement new strategies and techniques for crystal growth of selected materials. Third, perform extensive research and studies to elucidate the crystal structure, phase transitions, powder composition, electronic transitions, etc., of the desired material. While these three components are deeply entangled and not always step-wise, the basis for the scientific method proposed is consistent for most crystal growers.

While crystal growth is an extraordinary and meaningful skill, it is primarily an avenue to greater atomic level understanding revealing new and different ionic connectivities, electronic transitions, and possibly magnetic susceptibility. To a crystal grower, the pursuit of new compounds will undoubtedly lead to a deeper understanding on the atomic level that can be compared to current and existing research. Production of a new transition metal germanate, for example, will lead to the study of the crystal lattice

of said material. Inquiry into the crystal lattice will reveal the crystal structure and connectivities in the crystal lattice. The researcher will be able to distinguish the coordination environment and connectivities of the transition metal, germanate ion and oxygen ions within the lattice. Transition metal studies will reveal the oxidation state, electronic and molecular geometries, in addition, overall long-range periodicity of the crystal lattice will be revealed. The researcher will in turn learn the site symmetry and allowed or forbidden electronic transitions of the metal center. While this is an ambiguous example, its aim is to reveal that crystal growth, at its core, is the beginning of a cascade to further research and development. The possibility for discovery of new or even existing materials provides the researcher with the drive and motivation needed for the countless hours of forthcoming research. However, even the most well devised schemes and blue prints contain unforeseen road-blocks and detours. It is the challenge and journey of a crystal grower to utilize intuition, experience, and current and existing research as a road map to new discovery. The Chapters to follow are a description of the design, implementation, and study of new materials to better understand their function as a greater part of solid-state science.

Fundamental Crystal Growth Materials

The impact of crystal growth on current technology and culture is nothing short of astounding. To better understand the proposed research, a brief historical view of the impact of crystal growth on technological advancements will be discussed. When discussing fundamental solid-state materials, the importance of quartz, and primarily α-quartz (SiO_2) cannot go untouched. It is unclear whether the supply and demand drove

the technological advancements of α-quartz or vice-versa, but it is clear that they are deeply intertwined. During WWII, the availability of naturally available quartz was low due to the high demand for SONAR and radio applications. This piezoelectric material finds abundance in Brazil.[1] During WWII, U.S. efforts to divert high quantities of α-quartz to the states resulted in shortages for German utilization. German U-boat activities in specific Atlantic locations created difficulty for U.S. imports into the country. Because of blockades from both countries, the research and development of synthetic α-quartz found a technological jumpstart.[2] A greater discussion will continue in the Hydrothermal Crystal Growth section.

The 1950s and 60s are arguably the greatest times for technological advancements of the solid-state laser. Charles Townes, Arthur Schawlow, and Gordon Gould were key researchers in this idea of "light amplification by stimulated emission".[3] While the earliest lasers were microwave radiation, a quick progression to visible and infrared lasers was realized with the ruby laser, namely the 694 nm emission of Cr: Al_2O_3.[4] The current drive for higher powered (megawatt) lasers and the technology therein, is a direct result of this early work. The current technology employed in this research has been greatly influenced by the demand for further progression in this field.

Early advancements in solid-state lasers led to investigation of materials that display characteristics such as improved thermal lensing, increased quantum yield, and reduced parasitic oscillation of radiation. More recently, the investigation of the crystal growth of lutetium oxide (Lu_2O_3) and rare-earth doped analogues has led to high quality hydrothermal crystal growth of a promising material with high thermal conductivity.[5]

Er^{3+}: Lu_2O_3 is of special interest as a 1.5 um eye safe laser for the automotive industry. These few examples demonstrate how technological breakthroughs and the demand for new materials have aggressively motivated and driven the area of crystal growth.

Current Solid-State Scintillators and Industry Demands

Before proposing new materials as suitable candidates for solid-state scintillators, a brief look at current industry standards and popular candidates will be examined. First, a brief discussion of scintillator efficiency will be addressed.

Inorganic scintillators play a key role in radiation detection over several scientific, medical, and military fields. At the essence of scintillator technology is a need to convert incoming X-rays or gamma rays into quantifiable intensities. Three general qualifications of scintiallators are fast response times (10-100 ns), high light yield (> 20,000 photons per absorbed particle), and high density for efficient quantum yields. In general, the number of photons emitted by a scintillator can be described by Equation 1.1.

$$N_{ph} = (SQ)E/\beta E_{gap} \qquad (1.1)$$

(N_{ph}) represents the number of emitted photons when a quantifiable amount of energy (E) is absorbed, (E_{gap}) represent the HOMO/LUMO gap of the valence and conduction bands, (β) is the energy required to produce an electron-hole pair, (S) is the efficiency of the electron-hole transport, and (Q) represents the quantum efficiency.[6] From this equation, a few observations can be made. First, highly efficient scintillators will maximize the quantum efficiency (Q) while minimizing the band gap (E_{gap}). Additionally, the electron-hole energy will be minimized while transport efficiency is maximized. It is important to

note that quantum efficiency (*S*) is the least predictable term. Its value is heavily factored by crystal growth technique, impurities and lattice strain.[6] With these observations in mind, an examination of more common inorganic scintillators and their crystal growth challenges is examined.

One example of a family of commonly sought inorganic scintillators is the rare-earth orthovanadates, $REVO_4$ (RE = La^{3+}, Gd^{3+}, Lu^{3+}, Y^{3+}). These optically inactive rare-earth lanthanides make excellent hosts for doping optically active rare-earth ions such as Ce^{3+}, Nd^{3+}, Er^{3+}, and Yb^{3+} into the crystal lattice. Nd^{3+}: YVO_4 has been shown to be a capable Q-switching laser with a frequency of 500 kHz and power capacity of 108 W.[7] The tetragonal unit cell and high absorption cross-section coupled with high birefringence ($\Delta n = 0.220$ at 1 μm) makes this rare-earth vanadate a competitive material for microlasing compared to traditional hosts, such as yttrium aluminum garnet (YAG) $Y_3Al_5O_{12}$.[8-9] However, with increased optical and thermal properties does come significant physical drawbacks. Most notably, a weak *c*-plane leads to physical striations that compromise the integrity of the material at elevated pumping temperatures.[10]

A related rare containing scintillator can be considered when examining the rare-earth oxy-orthosilicates RE_2SiO_5 (RE= Lu^{3+}, Sc^{3+} and Y^{3+}). The orthosilicate is an attractive candidate for luminescence owing partly to smaller quantum defect, which results in decreased thermal loading of the laser.[11] In particular, Yb^{3+}:Y_2SiO_5 has been shown to contain a simpler $^2F_{7/2}$ and $^2F_{5/2}$ lasing manifold compared to cubic YAG leading to reduced quenching, longer lifetime and higher Yb^{3+} doping concentration ability. The presence of two non-equivalent RE^{3+} sites in a less than cubic space group setting leads to

increased crystal field strength in a quasi-three-level-laser.[12] However, while Y_2SiO_5 and its analogues present an attractive material for scintillation, the crystal growth of the material is more complex. Traditional crystal growth techniques such as the Czochralski pulling method tend to contain crystals with physical defects such as metal inclusions from high-temperature crucibles and incongruent melting of starting materials.[13] Even for well-known materials like the rare-earth oxy-orthosilicate, a closed-system route to high quality crystal growth is desirable to avoid crystal lattice defects that deter even the most robust lasing systems. The inspiration for hydrothermally grown rare-earth silicates is discussed in more detail in Chapter 3.

A lesser known but equally important scintillator is found in the eulytine mineral-type bismuth germanate oxide $Bi_4Ge_3O_{12}$. While the mineral eulytine ($Bi_4Si_3O_{12}$) was discovered in 1827 by Breithaupt, research and investigation into the uses of $Bi_4Ge_3O_{12}$ as a scintillator were not investigated until 1975 by Nestor and Huang.[14] $Bi_4Ge_3O_{12}$ crystallizes in non-centrosymmetric space group *I4-3d* with GeO_4 tetrahedra and a distorted BiO_6 octahedron.[15] $Bi_4Ge_3O_{12}$ is an intrinsic scintillator and has been investigated as a high-energy gamma radiation detector with limits up to 50 MeV. $Bi_4Ge_3O_{12}$ has also been shown to rival NaI(Ti) in terms of full energy efficiencies while suffering in energy resolution at peak power. The bismuth germanate oxide is extensively used in high-energy physics and positron tomography; however, like many melt and Czochralski pulled materials, it suffers from incongruent melting, complex phase diagram distribution, incorporation of metal contaminants, and a heterogeneous mixture of metal oxides that give rise to drastically different metal oxide vapor pressures in traditional

solid-state techniques.[16] Clearly, a simpler, closed-system solid-state technique is needed to grow single crystals of $Bi_4Ge_3O_{12}$ in hopes of diminished thermal strain, reduced or eliminated metal contaminates from high-temperature crucibles, and higher quality single crystal growth. The investigation of trivalent metal germanates is also of interest as bismuth germanate oxide is largely accepted as an industry standard. This material inspired much of the rare-earth germanate chemistry described in Chapter 4.

For many years the industry standards for inorganic scintillators were dominated primarily by relatively simple compounds such as NaI, CaF_2, Gd_2SiO_5, $Bi_4Ge_3O_{12}$, and BaF_2, just to list a few.[17] The main area of concern is that while these materials display excellent properties for energy resolution, stopping power, or timing resolution, none display excellent properties of all three at the same time.[18] While NaI(Tl) has amazing energy resolution, it suffers in stopping power and time resolution. One could say that the limiting factor for the next generation scintillator is the ability to solubilize metal oxides in such a way that allows for high quality single crystals with limited thermal strain and metal contamination from the solid-state technique used to synthesize the crystals. While powder scintillators for beta or gamma-ray interactions have been investigated, they suffer because only light from the outer layer has the capability to fluoresce and reach the photo detector.[19-20] To understand the limits of current industry standards for inorganic scintillators, a brief review of solid-state techniques used to grow single crystals of these in addition to highlighting their pros and cons will prove beneficial to the reader.

Conventional Solid-State Techniques

The umbrella of single crystal growth is a wide and complex array of techniques and instrumentation used to attain a similar goal. A brief examination of conventional solid-state techniques will highlight the advantages and disadvantages of each technique. When discussing single crystal growth, one must first address what are surely the most commonly used techniques in melt-based crystal growth. Czochralski, flux and top-seeded solution growth are the most common melt-based techniques. A brief discussion of each of these techniques will highlight a brief history and the limits of each technique.

Czochralski (CZ) melt pulling was first developed in 1916 by Jan Czochralski by a serendipitous discovery involving an ink pen and a molten tin crucible.[21] The essence of the CZ pulling method involved a high-temperature crucible, a target single crystal mounted to a rotating arm above the heated crucible melt, and a target phase melt composition within the crucible. The high-temperature crucible, usually iridium or tantalum, is heated so that the melt composition is above the highest melting point range of the charge material.[22] The seed crystal is then lowered into the molten material and slowly raised and rotated. The rate of rotation and pulling varies from system to system and is governed by many variables such as melt composition, target crystal size, thermal buoyancy, melt convections, and cost effectiveness. It is a typical industrial standard to rotate both the crucible as well as the crystal to gain greater systematic control over crystal-melt interface shape, suppress impurities, and control the temperature profile over the melt gradient.[23] Over years of research, the crystal size of CZ grown materials has

greatly increased and has surpassed 400 mm diameter boules with 150-200 kg melts used as feedstock. Indeed, CZ grown crystals have become a cornerstone for industrial crystal targets.

It is important to note however, that CZ pulling does suffer from drawbacks. The large thermal gradient, typically several hundred degrees, between the melt and crystal interface can cause surface striations, cracking, oxygen defects, and metal oxidation state reduction by thermally favored reducing atmospheres.[24] High-temperature crucibles can cause metal contamination at high-temperatures, a highly unfavorable incorporation when considering the susceptibility of the quantum efficiency (*S*) to metal contaminations, as discussed earlier. However, even with these challenges, CZ pulling is an industry standard in the single crystal growth of vital systems like YAG, $YLiF_4$, $LiNbO_3$, $LiTaO_3$, and β-BaB_2O_4.[25-29]

Attractive alternatives to the Czochralski method are flux growth or molten solvent crystal growth. Unlike the Czochralski method, flux melts use a molten solvent, typically a low melting molybdate or alkali fluoride/chloride.[30] This molten solvent instigates solubility of the desired feedstock components, usually a stoichiometric mixture of metal oxides or salts of the desired crystal phase. Crystal growth occurs in a high-temperature, inert metal crucible. One of the appealing lures of the flux technique is the ability to dissolve heterogeneous mixtures of compounds with drastically different melting ranges. Unlike the Czochralski method, flux growth incorporates metal oxides and salts that typically are incongruently melting.[31] The proper choice of a molten solvent drives solubility of incongruently melting components, typically at temperatures lower

than those of the pure initial starting materials. The nature of the flux solvent allows simple separation of the solvent from the desired crystals once the reaction has reached completion. Typically, the flux solvent can be removed by washing the product with water or sulfuric acid. Characteristically, flux growth occurs at significantly lower temperatures compared to the CZ method. This allows crucibles to be used for longer durations without the need to replace or repair them . This improves the cost efficiency of the technique, in addition to increasing the longevity of furnaces used for heating. Of course, molten flux growth is not without its own shortcomings.[32] Typically, incorporation of the molten flux into the crystals is a significant problem. The low melting range of the molten flux equates to a mobile electrolytic component able to incorporate into the crystal at nearly all phases of the growth sequence. Additionally, high-temperature crucibles can become soluble in molten fluxes equating to metal contamination of crystal growth at elevated temperatures.[33]

The crystal growth of the superconductor $REBa_2Cu_3O_{7-\gamma}$ (RE = Y, Pr) is a prime example of inclusion in flux growth. In these experiments, a $BaCuO_2$-CuO mixture is combined in a high-temperature crucible: ThO_2, Au, Pt, Y_2O_3, Al_2O_3, ZrO_2, SnO_2 or MgO. Solubility of these crucibles creates melt impurities, which in turn, create impurities in the crystals or melts. Specifically, examining the crystal growth of $YBa_2Cu_3O_{7-\gamma}$ (YBCO) with a ZrO_2 crucible leads to two important conclusions. First, ZrO_2 mobility is initially a result of the crucible becoming corrosive with the aid of molten fluxes. Zr^{+4} ions crystallographically cannot incorporate in the YBCO lattice, but they can incorporate with Ba^{2+} ions within the flux to precipitate $BaZrO_3$ crystals.

Secondly, while $BaZrO_3$ does not inheritably contaminate crystal growth, the presence of $BaZrO_3$ changes the physical stoichiometry of Ba^{2+} in solution, altering the composition of the YBCO crystals produced.[34] This specific example examines a typical complication of high-temperature solid-state synthesis which is incorporation or contamination by flux solvents or reaction crucibles. While the single crystal growth of YBCO or its analogues was not investigated in this research, its examination is intended to highlight a desire in current solid-state sciences for alternative methods of crystal growth to avoid inherent problems.

The top seeded solution growth crystal growth method is a unique hybrid of CZ and flux growth. Essentially, the lower temperature solution flux is combined with the pulling technique of the CZ method. This allows for crystals to be grown at much lower temperatures and avoids the spontaneous nucleation that plagues simple flux growth. Additionally, lower reaction temperatures aid in cost effectiveness of expensive high-temperature metal crucibles. However, while this technique attains the advantages of both the CZ and flux growth methods, it also suffers from both of their drawbacks. Crystal growth is hindered by metal contaminations from crucibles, thermal strain from large thermal gradients between the melt and seed interface, and flux inclusion, especially if a molten solvent is needed to aid in solubility of feedstock.[35]

Conventional solid-state techniques are a broad area of chemistry, and surely all could not be represented within this limited scope. The aim in this brief review is to equip the reader to look methodically at solid-state and aqueous techniques for the advantages and disadvantages of modern techniques. Herein, a detailed discussion of the

hydrothermal technique will elucidate the technology that allowed this current research to be achieved.

Hydrothermal Crystal Growth

The hydrothermal method is a unique aqueous method of crystal growth, that at its core, aims to reproduce subterranean processes in a laboratory setting. Hydrothermal chemists and geochemists reproduce similar conditions that give rise to natural minerals found in all corners of the world.

The origins of the hydrothermal technique can be traced to mineralogists in the late 19th century as the first pressurized vessels were being engineered. Scientists like Morey, Niggli and Spezia paved the way for many of the fundamental techniques still used today.[36] While modern hydrothermal techniques find origins in European countries during the late 19th century, one could argue the most significant advances came by Robert Laudise during his career at Bell Laboratories beginning in 1956.[37] Besides creating one of the largest commercial hydrothermal productions of α-quartz, he also paved the way for synthetic crystals of $AlPO_4$, ZnO and $KTiO(PO_4)$, among many others. The technological advances at Bell Laboratories cultivated many of the thought processes and designs one uses to design chemical reactions for exploratory growth and directed synthesis of targeted single crystals today.[38-40]

The staple of hydrothermal crystal growth is surely the high-temperature and high-pressure vessels, or autoclaves, designed for laboratory or industrial use. Essentially, a high-pressure and high-temperature autoclave provides a closed system in which heat,

aqueous solutions and metal salts or oxides react under high-pressure. The hydrothermal autoclave is a reaction vessel of various shape and design that is made typically of high-temperature alloys to withstand the immense conditions of temperature and pressure they undergo. To avoid autoclave corrosion and crystal growth contamination by the dozens of metals represented in the alloys of modern hydrothermal autoclaves, a secondary enclosure, either that of a fixed or floating liner is used within the autoclave. The terms fixed and floating refer to an inert metal or metals that are fixed to the inner walls of the autoclave or allowed to freely float in water while the reaction proceeds. In modern hydrothermal reactions, gold, silver, and platinum are commonly used as liners as their inert physical characteristics allow a variety of mineralizers and feedstocks to be applied and investigated. Hydrothermal mineralizers are typically alkali or alkaline earth salts of various concentrations used to increase the solubility of metal oxides or salts of a desired target crystal. Mineralizers play a key role in catalyzing solubility in much the same way as molten flux does in flux growth. In modern growth, basic mineralizers are comprised of hydroxides (OH^-), fluorides (F^-), carbonates (CO_3^{2-}), chlorides (Cl^-) and mixtures therein. Acidic mineralizers can also be used in low temperature PTFE and Inconel autoclaves employing metal liners such as gold and platinum. Most commonly, nitrates (NO_3^-), sulfates (SO_4^{2-}) and acid chlorides (Cl^-) are used to aid solubility of component feedstocks in these systems.[41]

The aid of mineralizers allows solubility of even the most intractable metal oxides, usually several hundred degrees below their melting point. Much like molten fluxes, a hydrothermal mineralizer can serve in a catalytic fashion; however, many times

the presence of alkali or alkaline earth salts leads to inclusion into the crystal growth that occurs. For example, recently reactions involving alkali fluorides and rare-earth oxides and fluorides revealed an opportunity to study the crystal structure of several new ternary alkali rare-earth fluorides. Synthetic routes to ARE_2F_7 and ARE_3F_{10} (A = K, Rb, Cs), (RE = Y, Sm, Gd, Lu) revealed complex phase transitions dependent on the ratio of alkali/rare-earth ionic radii in with various mineralizers. In these systems, the mineralizer becomes an incorporated component of the overall final crystalline product.[42] Therefore, simply referring to hydrothermal mineralizers as catalytic spectator ions, in general, is not an accurate representation of the whole technique. It must be studied on a case-by-case basis to note effects on single and multi-component oxide systems. In the crystal growth of the sesquioxide lutetium oxide, Lu_2O_3, the hydrothermal crystal growth is most efficiently executed under > 15 *M* KOH solutions, essentially supersaturated solutions that become supercritical fluids at high-temperature hydrothermal conditions (> 350 °C). In this situation, the mineralizer is truly a spectator ion that catalyze the solubility of lutetium oxide several hundred degrees before the melting point is reached. The closed system design of the hydrothermal technique coupled with inert metal liners and ampoules allows not only greater solubility of recalcitrant oxides, but also improved crystal growth rates and limited contamination of metals.[43]

To attain a full perspective on the hydrothermal technique, a brief explanation of the drawbacks will be beneficial to the reader. While melt and flux growth techniques are widely studied and documented, the hydrothermal growth technique has a restricted audience and research niche for several reasons. The most likely candidate is the initial

startup cost and experience needed for crystal growth. Hydrothermal autoclaves, inert precious metal liners, high-pressure parts and equipment create a costly initial investment for researchers and industry. Coupled with the years of knowledge needed to understand solubility profiles for various metal oxides and the need for consistent engineering and machining collaborations, it becomes clearer why the hydrothermal technique has found a limited foothold, even today. However, as the subsequent Chapters will reveal, the hydrothermal method is a valid solid-state technique for synthesis of a variety of refractory oxides.

Allowing the Past to Mold the Future

Above the Norlin Library at the University of Colorado is a quote that reads, " Who knows his own generation remains always a child." It is true that we cannot know where we are going without knowing where we have been. The technological advances over the last 30 years have manufactured a generation that is more connected than ever. Within the context of science and research, the ability to attain published data is the easiest it is ever been. With that in mind, the following Chapters were molded and shaped from various research attained from decades of previous work. A brief examination of past success will reveal the motivation for the research herein.

Undeniably, current hydrothermal equipment and technology was sculpted by the pioneers of the field, such as Morey, Niggli, and Laudise. However, current research is consistently directed by market and industry demands. An examination of the crystal

growth of lutetia (Lu_2O_3) will give insight and direction into the next decade of research and development.

The hydrothermal crystal growth of the refractory oxide lutetium oxide, Lu_2O_3, has provided a single crystal host with desirable lasing potential. Lutetium oxide presents a difficult challenge to conventional solid-state crystal growth. The melting point of lutetium oxide exceeds 2400 °C and is therefore impervious to traditional solid-state techniques. High-temperature crucibles employed in flux and melt growth simply won't withstand treatment at these elevated temperatures. Additionally, high-temperature crucibles such as rhenium and tungsten are known to undergo deposition during reactions. The potential for Lu_2O_3 to become a high-density, high-power laser host is encouraging, especially considering Lu^{3+} is a good lattice match for active lasing ions such as Yb^{3+} and Er^{3+} for 1 μm and 1.5 μm lasing. Recently, the hydrothermal growth of lutetium oxide was investigated.[43] The ability to grow crystals on a 5 mm scale was shown to be possible with high-pressure and high-temperature treatment of lutetium oxide powder with high concentrations (> 10 *M*) solutions of potassium hydroxide. Interestingly, this growth can occur at or below 700 °C within a high-temperature autoclave. The ability to solubilize lutetium oxide 1300 °C before its melting point is worth noting and vital to high quality crystal growth. The hydrothermal growth of Lu_2O_3 inspired many of the investigations of rare-earth oxides outlined throughout this Dissertation.

In this Dissertation, the high-temperature and high-pressure crystal growth technique was used in tandem with soluble building blocks (SiO_2, GeO_2, TiO_2, Nb_2O_5), to

grow single crystals of refractory oxides and examine their structural and optical properties. By incorporating soluble building block with refractory oxides in solution, a route to increase the solubility of refractory oxides was accomplished. The subsequent Chapters outline the various projects that were completed in pursuit of the next generation of scintillators.

References

(1) Iwasaki, F.; Iwasaki, H. Historical Review of Quartz Crystal Growth. *J. Cryst. Growth* **2002**, *237-239*, 820-827.

(2) Brown, C. S.; Kell, R. C.; Thomas, T. L.; Wooster, N.; Wooster, W. A. The Growth and Properties of Large Single Crystal of Synthetic Quartz. *Min. Mag.* **1952**, *29*, 858-874.

(3) Schawlow, A. L.; Townes, C. H. Infrared and Optical Masers. *Phys. Rev.* **1958**, *112*, 1940-1949.

(4) Verneuil, A. Artificial Production of Rubies by Fusion. *Ann. Chim.* **1904**, *3*, 20-48.

(5) McMillen, C.; Thompson, D.; Tritt, T.; Kolis, J. Hydrothermal Single-Crystal Growth of Lu_2O_3 and Lanthanide-Doped Lu_2O_3. *Cryst. Growth Des.* **2011**, *11*, 4386-4391.

(6) Eijk, C. W. E. van.; Inorganic-Scintillator Development. *Nucl. Instr. Meth. A.* **2001**, *460*, 1-14.

(7) Yan, X.; Liu, Q.; Fu, X.; Wang, Y.; Huang, L.; Wang, D.; Gong, M. A. 108 W, 500 kHz Q-switching Nd:YVO_4 Laser with the MOPA Configuration. *Opt. Express* **2008**, *16*, 3356-3361.

(8) Fields, R. A.; Birnbaum, M.; Fincher, C. L. Highly Efficient Nd:YVO_4 Diode-Laser End-Pumped Laser. *Appl. Phys. Lett.* **1987**, *51*, 1885-1886.

(9) Lomheim, T. S.; DeShazer, L. G. Optical-Absorption Intensities of Trivalent Neodymiun in the Uniaxial Crystal Yttrium Orthovanadate. *J. Appl. Phys.* **1978**, *49*, 5517-5522.

(10) Palilla, F. C.; Levine, A. K.; Rinkevics, M. Rare Earth Activated Phosphors Based on Yttrium Orthovanadate and Related Compounds. *J. Electrochem. Soc.* **1965**, *112*, 776-779.

(11) Campos, S.; Denoyer, A.; Jandl, S.; Vianna, B.; Vivien, D.; Loiseau, P.; Ferrand, B. Spectroscopic Studies of Yb^{3+}- Doped Rare Earth Orthosilicate Crystals. *J. Phys. Condens. Matter.* **2004**, *16*, 4579-4590.

(12) Cooke, D. W.; McClellan, K. J.; Bennett, B. L.; Roper, J. M.; Whittaker, M. T.; Muenchausen, R. E.; Sze, R. C. Crystal Growth and Optical Characterization of Cerium-Doped $Lu_{1.8}Y_{0.2}SiO_5$. *J. Appl. Phys.* **2000**, *88*, 7360-7362.

(13) Iwaki, T.; Kobayashi, N. Residual Stresses of Czochroalski-Grown Crystal. *J. Appl. Mech.* **1981**, *48*, 866-870.

(14) Nestor, O. H.; Huang, C. Y. Bismuth Germanate: A High-Z Gamma-ray and Charged Particle Detector. *IEEE Trans. Nucl. Sci.* **1975**, *22*, 68-71.

(15) Gevay, G. Growth and Characterization of $Bi_4Ge_3O_{12}$ Single Crystals. *Prog. Cryst. Growth Charact.* **1987**, *15*, 145-186.

(16) Karabulut, Y.; Canimoglu, A.; Ekdal, E.; Ayvacikli, M.; Can, N.; Karali, T. Thermoluminscence Studies of Nd Doped $Bi_4Ge_3O_{12}$ Crystals Irradiated by UV and Beta Sources. *Appl. Radiat. Isot.* **2016**, *113*, 18-21.

(17) Derenzo, S. E.; Moses, W. W.; Cahoon, J. L.; Perera, R. C. C. Prospects For New Inorganic Scintillators. *IEEE Trans. Nucl Sci.* **1990**, *37*, 203-208.

(18) Hofstadter, R. Twenty Five Years of Scintillation Counting. *IEEE Trans. Nucl. Sci.* **1975**, *22*, 13-25.

(19) Lecoq, P.; Korzhik, M. New Inorganic Scintillation Materials Development for Medical Imaging. *IEEE Trans. Nucl. Sci.* **2002**, *49*, 1651-1654.

(20) Derenzo, S. E.; Weber, M. J. Bourret-Courchesne, E.; Mlintenbery, M. K. The Quest for the Ideal Inorganic Scintillator. *Nucl. Instrum. Meth. A.* **2003**, *505*, 111-117.

(21) Tomaszewski, P. E. Jan Czochralski-Father of the Czochralski Method. *J. Cryst. Growth.* **2002**, *236*, 1-4.

(22) Muiznieks, A.; Krauze, A.; Nacke, B. Convection Phenomena in Large Melts Including Magnetic Fields. *J. Cryst. Growth* **2007,** *303*, 211-220.

(23) Yang, F.; Pan, S. K.; Ding, D. Z.; Ren, G. H. Problems in the Growth of Ce^{3+}-doped $Li_6Gd(BO_3)_3$ Crystals by Czochralski Method. *Cryst. Res. Technol.* **2009**, *44*, 141-145.

(24) Vegad, M.; Bhatt, N. M. Review of Some Aspects of Single Crystal Growth Using Czochralski Crystal Growth Technique. *Procedia Tech.* **2014**, *14*, 438-446.

(25) Linares, R. C. Growth of Garnet Laser Crystals. *Solid State. Comm.* **1964**, *2*, 229-231.

(26) Bensalah, A.; Guyot, Y.; Ito, M.; Brenier, A.; Sato, H.; Fukuda, T.; Boulon, G. Growth of Yb^{3+}-Doped $YLiF_4$ Laser Crystal by the Czochralski Method. Attempt of Yb^{3+} Enery Level Assignment and Estimation of the Laser Potentiality. *Opt. Mater.* **2004**, *26*, 375-383.

(27) Ming, N-B.; Hong, J-F.; Feng, D. The Growth Striations and Ferroelectric Domain Structures in Czochralski-grown $LiNbO_3$ Single Crystals. *J. Mater. Sci.* **1982**, *17*, 1663-1670.

(28) Furukawa, Y.; Kitamura, K.; Suzuki, E.; Niwa, K. Stoichiometric $LiTaO_3$ Single Crystal Growth by Double Crucible Czochralski Method Using Automatic Powder Supply System. *J. Cryst. Growth.* **1999**, *197*, 889-895.

(29) Kouta, H.; Kuwano, Y. β-BaB_2O_4 Single Crystal Growth by Czochralski Method. *J. Cryst. Growth.* **1991**, *114*, 676-682.

(30) Schieber, M. Growth of Oxide Crystals by the Flux Method. *J. Am. Ceram. Soc.* **1964**, *47*, 537-538.

(31) Damen, J. P. M.; Robertson, J. M. Induced Non-periodic Growth Striations in Flux-Grown magnetic Oxide Single Crystals. *J. Cryst. Growth.* **1972**, *16*, 50-53.

(32) Burgaris, D. E.; zur Loye, H.-C. Materials Discovery by Flux Crystal Growth: Quaternary and Higher Order Oxides. *Angew, Chem. Int. Ed.* **2012**, *51*, 3780-3811.

(33) Chase, A. B.; Osmer, J. A. Localized Cooling in Flux Crystal Growth. *J. Am. Ceram. Soc.* **1967**, *50*, 325-328.

(34) Erb, A.; Walker, E.; Flukiger, R. BaZrO3: The Solution for the Crucible Corrosion Problem During the Single Crystal Growth of high-T_c superconductors $REBa_2Cu_3O_{7-\gamma}$: RE = Y,Pr. *Physica C.* **1995**, *245*, 245-251.

(35) Scheel, H. J. Historical Aspects of Crystal Growth Technology. *J. Cryst. Growth.* **2000**, *211*, 1-4.

(36) Byrappa, K.; Yoshimura, M. Handbook of Hydrothermal Technology. William Andrew Publishing: Norwich, NY, **2001**.

(37) Ballman, A. A.; Laudise, R. A. Hydrothermal Growth, in the Art and Science of Growing Crystals; J. J. Gilman., Wiley: New York, **1963**.

(38) Kolb, E. D.; Grenier, J.-C.; Laudise, R. A. Solubility and Growth of $AlPO_4$ in a Hydrothermal Solvernt: HCl. *J. Cryst. Growth* **1981**, *51*, 178-182.

(39) Laudise, R. A.; Ballman, A. A. Hydrothermal Synthesis of Zinc Oxide and Zinc Sulide. *J. Phys. Chem.* **1960**, *64*, 688-691.

(40) Laudise, R. A.; Cava, R. J.; Caporaso, A. J. Phase Relations, Solubility and Growth of Potassium Titanyl Phosphate, KTP. *J. Cryst. Growth.* **1986**, *74*, 275-280.

(41) McMillen, C. D.; Kolis, J. W. Bulk Single Crystal Growth from Hydrothermal Solutions. *Philos. Mag.* **2012**, *92*, 2686-2711.

(42) McMillen, C. D.; Comer, S.; Fulle, K.; Sanjeewa, L. D.; Kolis, J. W. Crystal Chemistry of Hydrothermally Grown Ternary Alkali Rare Earth Fluorides. *Acta Cryst. B.* **2015,** *71*, 768-776.

(43) McMillen, C. D.; Thompson, D.; Tritt, T.; Kolis, J. W. Hydrothermal Single-Crystal Growth of Lu_2O_3 and Lanthanide-Doped Lu_2O_3. *Cryst. Growth. Des.* **2011**, *11*, 4386-4391.

CHAPTER TWO

EXPERIMENTAL METHODS

Introduction

The ability to synthesize new and existing materials with interesting optical and magnetic properties continues to be an active area of research. Many known materials in use today suffer from negative effects due to the solid-state technique employed in synthesis. For example, materials grown from melt-based flux growth can demonstrate incorporation of metal contaminates from the fluxing material or the solid-state crucible into the crystal growth. Additionally, oxygen defects, thermal strain and incongruent melting can occur at or near the melting point of metal oxides. Essentially, this is the same list that plagues most, if not all, solid-state crystal growth techniques.

Herein, the experimental conditions for the high-temperature and high-pressure hydrothermal crystal growth are described. This technique allowed for the solubility of many refractory metal oxides to be increased in solvothermal mineralizers while lowering the reaction temperature several hundred degrees below the metal point of the binary oxides. This Chapter describes the hydrothermal technique of growing new materials and the supporting techniques used to characterize their physical and optical properties.

Synthetic Methods

Solid-State Techniques

To prepare feedstock for hydrothermal growth, materials were treated through initial solid-state reactions. Stoichiometric amounts of powdered sample were ground and

mixed using an agate mortar and pestle. These powders were added to an open platinum crucible with a ceramic cover. Heating profiles varied depending on the material being investigated, but they were typically treated for 1-3 days at 800-1200 °C in a Lindberg Blue box furnace (BF51866A-1). This allowed for a homogenous powder feedstock synthesis which was subsequently treated under hydrothermal conditions or examined by powder X-ray diffraction (PXRD) to determine phase stability.

Hydrothermal Crystal Growth

The essential technique employed throughout the subsequent Chapters was the high-temperature and high-pressure crystal growth technique. High-temperature Tuttle autoclaves constructed of Inconel 718 material served as the reaction vessels.[1] These reaction vessels contain a 27-mL internal volume. High-pressure adaptors, fittings, valves and analog pressure heads were supplied by High Pressure Parts (HPP). To heat the body of the autoclaves, 2" ceramic band heaters (N-76580) were supplied by Omega Heater company. Typically, two ceramic band heaters were affixed to the body of the autoclave to establish a thermal gradient for spontaneous nucleation or transport growth reactions. Omega 7600 thermal controllers with K-type thermocouples were utilized to drive and regulate the thermal regime of the band heaters. To isolate and insulate the autoclaves during the growth process, individual growth zones were established with concrete blocks. Vermiculate and/or zirconium blankets were used to insulate the autoclave bodies. To protect the nickel based autoclave from reacting with the feedstock and

hydrothermal mineralizers, and vice versa, fine silver (99.9%) ampoules were commissioned in each growth run, see **Figure 2.1**

Figure 2.1: Tuttle cold seal Inconel 718 autoclave featuring cap and head assembly. Fine silver ampoules are shown in front with 1/4" and 3/8" diameters.

Two different sized ampoules were utilized, namely 1/4" x 3" and 3/8" x 3" silver tubes.

To encapsulate and seal the feedstock and mineralizer within a silver ampoule, a CEA model TOP-165HF inert gas welder was utilized with a tungsten electrode under flowing argon to weld-seal one end of the ampoule. To the open end of the ampoule, the feedstock and mineralizer were added in a predetermined ratio and amount. For reported reactions, 0.2 g of total feedstock was added in conjunction with 0.4 mL of select mineralizer in 1/4" ampoules. For 3/8" tubing, 0.4 g of feedstock and 0.8 mL of mineralizer were added. The exact ratios and molar concentrations of mineralizer are described in each of the following Chapters. This combination ensured that both an ideal solubility was reached within the reaction and that the reactor could be readily welded. Once the reaction feedstock and mineralizer was loaded, the silver ampoule was crimped closed with needle-nose pliers and weld-sealed. In each autoclave, typically, 4-6 ampoules were loaded for reaction durations of 1-3 weeks depending on the material under investigation. Deionized (D.I.) water was employed to provide a counter-pressure in the autoclave and prevent the silver ampoules from bursting upon heating. The internal volume of the autoclave was filled to 75-90% full after addition of the ampoules. A head assembly consisting of a 316 SS plunger, cap, high-pressure valve and fittings was added and tightened to seal the autoclave for heating, **Figure 2.1**.

Characterization Techniques

Single Crystal X-ray Diffraction

To characterize new and existing hydrothermally synthesized crystals, single crystal X-ray diffraction (SCXRD) was employed to derive the crystal structures and to determine subsequent sample characterization. Single crystal structure characterization was directed using either a Bruker D8 Venture single crystal diffractometer with an Incoatec Mo Kα microfocus source and connected Photon 100 CMOS detector, or a Rigaku AFC8 single crystal diffractometer with a Mo Kα sealed glass tube source and connected Mercury CCD detector. Data was recorded at room temperature using phi and omega scans, and successively processed and scaled using the Apex3 (SAINT and SADABS) or CrystalClear (d*TREK and REQAB) software programs.[2] Space group determinations were unequivically made based on the absence of systematic HKL reflections. The structures were solved by direct methods and refined to convergence by full-matrix least squares on F^2 using the SHELXTL software program.[3] All atoms were refined anisotropically, except for hydrogen atoms. In the case of twinned crystals, PLATON or cell_now was used to determine the twin law and twin contribution.[4,5] Diamond software was used to construct 3-D representations along different crystallographic directions.[6]

Powder X-ray Diffraction

The powder X-ray diffraction data (PXRD) was collected using a Rigaku Ultima IV diffractometer equipped with Cu Kα radiation (λ = 1.5406 Å) at ambient temperature.

Data was collected in the range of 4-70° in 2θ with a scan speed of 0.20-1.5 degrees per minute with a step size of 0.02°. The phase stability and purity of hydrothermally grown powder or single crystals were investigated using PXRD. PDXL software was used to collect and process collected data.[7] The experimentally collected powder patterns were graphed and overlaid to calculated the powder patterns of hydrothermally grown single crystal via PCW crystallographic software. Origin 8 software was used to plot and overlay the experimental and calculated powder patterns of new and existing phases to realize the presence of minor products in the reactions.

Infrared Spectroscopy

Infrared spectroscopy (IR) was utilized to identify functional groups in hydrothermally grown crystals such as hydroxide, OH^-, H_2O, or lack thereof. The functional groups were identified via comparing their characteristic vibrational modes in the IR spectra with literature values. IR spectroscopy was used to support the single crystal and PXRD assignments made on hydrothermally grown single crystals. IR spectra were collected on a Manga 550 IR spectrometer under flowing nitrogen (N_2) using OMNIC software for processing the UV-vis/ IR spectrums from 400-4000 cm^{-1}.[8] Samples were prepared via grinding powders or single crystals in a mortar and pestle. A KBr pellet was used as the background for each new data collection. A small amount of hydrothermal powder (4-10 mg) was mixed with KBr powder (0.2 g) and pressed into a optically transparent pellet using a hydraulic pellet press in the lab. KBr was dried in a furnace at 100 °C for 2 hours to eliminate any moisture in the blank before use.

X-ray Luminescence Spectroscopy

An initial X-ray luminescence study of $EuNbO_4$ was conducted as part of a site symmetry investigation during the RE-Nb study. The $EuNbO_4$ sample (20 mg in a 1 dram glass vial) was placed on the stage of an inverted fluorescence microscope (DMI 5000, Leica Microsystems, Germany) and subsequently excited with a mini Ag X-ray tube (Amptek Inc. MA, USA). The X-ray source was operated at 40 kV and 99 μA. Luminescence emission was collected with a 10x microscope objective and sent to a spectrometer (DNS 300, Delta Nu, Laramie, WY) containing a cooled CCD camera (iDus-20BV, Andor, South Windsor, CT). Collection of light was enhanced using a cylindrical lens between the microscope and spectrometer. The sample was exposed for 3.0-5.0 s during the experiment.

Photoluminescence (PL)Spectroscopy

In a study of Tb^{3+} excitation and emission profiles, a photoluminescence measurement was made using a SYLGARD ® 184 Silicone Elastomer base (0.20 g) and was thoroughly mixed with a SYLGARD ® 184 Silicone Elastomer curing agent (0.02 g) in a glass vial for 5 minutes. The hydrothermal crystalline powder sample of $Tb_{13}(GeO_4)_6O_7(OH)$ (0.04 g) was incorporated into the mixture and air bubbles were removed through utilization of a vacuum chamber. The mixture was then put on a glass cover slip to make a layer of the powdered sample incorporated ona PDMS film. Subsequently, the sample was cured in an oven at 100 °C for 15 minutes. The prepared

sample was placed inside a cuvette at a 45-degree angle to the incident beam and fluorescence excitation and emission were measured. A QuantaMaster 800 High Speed Spectrofluorometer (PTI) equipped with an 814 (PTI) photomultiplier detection system was used to carry out the PL measurements.

Raman Single Crystal Scattering Spectroscopy

Single crystal Raman measurements were conducted using an Olympus IX71 inverted microscope with a 20x objective lens coupled to a TRIAX 552 spectrometer equipped with a thermoelectrically cooled CCD detector (Andor Technology, Model DU420A-BV) operating at -60 °C. An argon ion laser (Innova 100, Coherent) was employed to excite the Raman signal with 514.5 nm light in a 180° backscattering geometry. A PR-550 broadband polarization rotator (Newport Corp.) was utilized to rotate the polarization of the incident laser source. All data were processed and figures prepared with Spectra-Solve for Windows (Las Tek Pty. Ltd.) and Origin 8 software. Data were collected with a laser output power of 100 to 200 mW with a 2-minute integration time.

Thermal Analysis

Thermogravimetric analysis (TGA) and differential scanning calorimetry (DSC) provide an avenue for crystal growers to examine the thermal phase stability of single crystals and/or powders. This is an essential tool since materials for optical uses experience tremendous thermal strain when being excited by a diode or laser source. Additionally, TGA and DSC are excellent supporting characterization for materials that

may, or may not, contain water or hydroxide groups. Evaporative loss of these groups can be measured as weight loss and plotted as a function of temperature. A TA Instrument SDT Q600 (V20.9 Build 20) with concurrent DSC/TGA ability were utilized with TA Universal Analysis software program for data collection and analysis. Powdered samples were prepared via thorough grinding and placed in alumina crucibles, typically 10-25 mg per sample. A twin crucible was used as a standard and both the blank and sample were heated at a rate of 5 °C/ minute to 800 °C. The samples were held at 800 °C for 30 minutes while the furnace reached equilibrium. Observed weight loss was collected and compared to theoretical weight loss based on the molecular weight of the structure. Origin 8 software was utilized to plot the resulting data.

Electron Microscopy (Energy Dispersive X-ray Spectroscopy)

Elemental analysis is a key factor in deriving the correct molecular formula, especially in new materials with exotic structural features. EDX was used to support the assignment and stoichiometry of new and existing structures. It is especially useful when deciding between elements that display similar electron density in SCXRD, such as Cs^{+} and Ba^{2+}, and confirming or eliminating the presence of fluoride, F^{-}, within the crystal structure. EDX was collected via a Hitachi TM-3000 tabletop microscope equipped with a SwiftED 3000 detector. Powder and single crystal samples were prepared and placed on a carbon disk containing carbon tape to provide the necessary adhesion. A working distance of 10 mm was used during data collection with an accelerating voltage of 20 kV in charge during the reduction mode. Semi-quantitative data was then compared to the stoichiometry assigned during single crystal refinement.

References

(1) Tuttle, O. F. Two pressure vessels for silicate-water studies. *Geol. Soc. Am. Bull.* **1949**, *60* (10), 1727–1729.

(2) Apex3; Bruker AXS Inc.: Madison, WI, **2015**.

(3) Sheldrick, G. M. Crystal structure refinement with SHELXL. *Acta Crystallogr., Sect. C: Struct. Chem.* **2015**, *71* (1), 3–8.

(4) Sheldrick, G. M. *Cell_Now and TWINABS*; University of Göttingen, Germany, 2008.

(5) Spek, A. L. Structure validation in chemical crystallography. *Acta Crystallogr., Sect. D: Biol. Crystallogr.* **2009**, *65* (2), 148–155.

(6) Brandenburg, K.; Berndt, M. *Cryst. Impact GbR Bonn Ger.* **1999**.

(7) *PDXL*, *The Rigaku Journal* **2010**, *26*, 23–27.

(8) *OMNIC*, Version 6.1a, Thermo Nicolet Corporation, **2001**.

CHAPTER THREE

HIGH-TEMPERATURE, HIGH-PRESSURE HYDROTHERMAL GROWTH OF RARE-EARTH AND TETRAVLENT METAL SILICATES

Introduction

The lanthanide ions of the rare-earth oxides RE_2O_3 (RE = La – Lu) display interesting optical and magnetic properties, in tandem with varying coordination environments across the f-block.[1] For example, Nd^{3+} is well-known to generate 532 nm emission from frequency doubling of 1064 nm lasing from a Nd: YAG laser and NLO material KTP.[2] Additionally, Yb^{3+} has an attractive manifold that is utilized in 970 nm diode-pumped Yb:YAG lasers.[3] The low-lying f-orbitals in conjunction with predictable absorption and emission profiles make the lanthanide ions attractive in fields of applied science.

To synthesize the next generation of scintillators, optical hosts, fluorescence and magnetic materials, the ability to solubilize these refractory rare-earth oxides must be achieved. The rare-earth oxides display melting points > 2000 °C which limit their access from most traditional solid-state techniques. Additionally, the extremely high-temperatures required to experience chemical reactivity introduces a wide array of oxygen defects, metal contamination from high-temperature crucibles, low-quality crystal growth and inhomogeneous growth. The challenge becomes to solubilize these refractory oxides at much lower temperatures to mitigate substantial thermal strain, which has

negative effects on the as-grown material. Additionally, a technique is required that can produce high-quality bulk crystals with little to no contamination from the reaction vessel.

The second challenge in the synthesis and characterization of new materials is introducing chemical foundations, or building blocks that can be incorporated into the crystal growth. Crystal building blocks generally need to have three distinct characteristics to be useful to a chemist or materials scientist. First, a good building block should have a high degree of chemical flexibility. In general, this includes having multiple stable oxidative states, varying coordination environments, or varying connectivity with other building blocks. Second, these building blocks should contain a limited crystallographic radius to be highly adaptive into multiple structural phases. Lastly, reasonable chemical reactivity or solubility is necessary for new phases to be realized. This is not a new concept or idea, and, it is the basis of many of the known rare-earth silicates as illustrated by Felsche.[4]

The intent of this Chapter is to describe a coupling of the high-temperature and high-pressure hydrothermal methods in pursuit of new silicates. Silica, SiO_2, under hydrothermal conditions, is well known and is the basis for the crystal growth of quartz.[5] However, silica is also an attractive building block for the synthesis of new refractory materials for a number of reasons. While SiO_2 has a predictable tetrahedral tetravalent coordination environment, it also contains a small crystallographic radius (0.4 Å), making it an ideal building block. Additionally, due to the covalent character of SiO_2 and its ability to act as Lewis acid in solution, it can adapt several chain and ring structural (ex.

Si_4O_{13} and Si_4O_{12}) units. While the rare-earth and tetravalent oxides all display high melting points, SiO_2 displays a high solubility even at low hydrothermal temperatures (220 °C). Coupling the hydrothermal technique with a highly predictable crystallographic building block(s) has allowed a number of new and interesting materials to be characterized for the first time. While several known compounds have also been synthesized, their reactivity in hydrothermal fluids has allowed for bulk growth to occur and structural assignments to be made.

In the first study, a thorough examination into the hydrothermal chemistry of the BaO-RE_2O_3-SiO_2 ternary system was developed. This work is adapted from the original work "Fulle, K.; Sanjeewa, L. D.; McMillen, C. W.; Kolis, J. W. Crystal Chemistry of the Discrete Tetrasilicate Units with Rare Earth Dimers: $Ba_2RE_2Si_4O_{12}F_2$ (RE = Er-Lu) and $Ba_2RE_2Si_4O_{13}$ (RE = Pr-Sm) *Acta Cryst. B.* **2017**, *73*, 907-915, in agreement with copyright permission from IUCr journals. A copy of the copyright permission is listed in the Appendix.[6]

Some crystal chemistry of barium rare-earth silicates is known, including; $Ba_2RE_8(SiO_4)_6O_2$, $BaRE_6(Si_2O_7)_2(Si_3O_{10})$, $BaRE_4(Si_2O_7)(Si_3O_{10})$, and $Ba_2RE_2Si_4O_{13}$[7–10] but it is quite limited overall. While there is a diverse structural variety, the limits and the role of the rare-earth ions are not clearly developed. Additionally, the use of optically active Ln^{3+}: $Ba_2RE_2Si_4O_{13}$ highlights the use of these materials as optical phosphors and the understanding of the structural nuances of the different rare-earth host sites.[11–15] A full study was employed to study the role of the rare-earth ions and the solubility of rare-earth

oxides in mixed OH^-/F^- mineralizers. In this case a 6 M KF/ 1 M KOH solution provided ideal conditions for spontaneous nucleation to occur.

Experimental Methods for Barium Rare-Earth Silicates

Single crystals in this study were synthesized by a high-temperature, high-pressure hydrothermal synthetic method. Reactions consisted of component metal oxides that were mixed in welded silver ampoules also containing an aqueous mineralizer, 6 *M* KF/1 *M* KOH. Reaction ampoules were welded shut, loaded into a Tuttle cold seal autoclave and heated to 650 °C for 5-10 d. The autoclave was subsequently cooled and the contents were filtered and washed with deionized water. Specific synthetic details of the rare-earth silicate families are described below, and a reaction summary is included in **Table 3.1**.

As a representative of the general class of barium rare-earth silicates, $Ba_2Lu_2Si_4O_{12}F_2$ will be used to describe the synthetic details of this family. Colorless polyhedra of $Ba_2Lu_2Si_4O_{12}F_2$ were synthesized using a mixture of BaO (65 mg, 0.42 mmol; Alfa Aesar, 99.0%), Lu_2O_3 (0.84 g, 0.21 mmol; HEFA Rare Earth, 99.99%) and SiO_2 (51 mg, 0.85 mmol; Alfa Aesar, 99.99%) in a 2:1:4 molar ratio. The reaction was heated for 7 d at 650 °C, generating 160 MPa (23 kpsi) pressure. Crystals containing the other rare-earth ions (La-Yb) were grown in a similar fashion using the appropriate oxide components as starting materials in a similar 2:1:4 molar ratio. In the cases of the moderate to heavier lanthanide elements (Sm-Lu), the rare-earth tetrasilicate phase ($Ba_2RE_2Si_4O_{13}$ or $Ba_2RE_2Si_4O_{12}F_2$) was present as a phase pure product, with only a trace of minor products, with the only exception being the $Ba_2Yb_2Si_4O_{12}F_2$ system, which crystallized only as a minor product alongside $BaYb_2Si_3O_{10}$.[7] Sample growth of $Ba_2Ho_2Si_4O_{13}$ is show in **Figure 3.7**. In the cases of the lighter lanthanide elements (RE =

La-Nd), $Ba_2RE_2Si_4O_{13}$ was synthesized in low yield (~5%) with the majority product appearing as $KRE_9(SiO_4)_6O_2$ apatite phases, as determined by PXRD.[16] In all cases, the products were isolated as high quality polyhedra in sizes ranging from 0.25-1.5 mm. For the $Ba_2RE_2Si_4O_{12}F_2$ compounds, the presence of fluoride in the crystals was verified semi-quantitatively using EDX (see Chapter 2 for details). In all cases the EDX analysis for heavy ions was satisfactory in terms of the elemental ratios, **Figures 3.4, 3.9, and 3.12**.

Table 3.1: Product distribution for the hydrothermal crystal growth of barium rare-earth silicates: BaO + RE_2O_3 + SiO_2+ 6 *M* KF/1 *M* KOH at 650 °C for 7 days. Table reused with permission from IUCr (http://journals.iucr.org/10.1107/S2052520617009544).

RE^{+3}	Products
La^{3+}	$Ba_2La_2Si_4O_{13}$ (*P*-1) + $KLa_9(SiO_4)_6O_2$
Ce^{3+}	$Ba_2Ce_2Si_4O_{13}$ (*P*-1) + $KCe_9(SiO_4)_6O_2$
Pr^{3+}	$Ba_2Pr_2Si_4O_{13}$ (*P*-1) + $KPr_9(SiO_4)_6O_2$
Nd^{3+}	NdF_3 +BaF_2 + $KNd_9(SiO_4)_6O_2$
Sm^{3+}	$Ba_2Sm_2Si_4O_{13}$ (*C*2/*c*)
Eu^{3+}	$Ba_2Eu_2Si_4O_{13}$ (*C*2/*c*)
Gd^{3+}	$Ba_2Gd_2Si_4O_{13}$ (*C*2/*c*)
Tb^{3+}	$Ba_2Tb_2Si_4O_{13}$ (*C*2/*c*)
Dy^{3+}	$Ba_2Dy_2Si_4O_{13}$ (*C*2/*c*)
Ho^{3+}	$Ba_2Ho_2Si_4O_{13}$ (*C*2/*c*)
Er^{3+}	$Ba_2Er_2Si_4O_{12}F_2$ (*P*-1)
Tm^{3+}	$Ba_2Tm_2Si_4O_{12}F_2$ (*P*-1)
Yb^{3+}	$Ba_2Yb_2Si_4O_{12}F_2$ (*P*-1) + $BaYb_2Si_3O_{10}$
Lu^{3+}	$Ba_2Lu_2Si_4O_{12}F_2$ (*P*-1)

Crystal Structure of $Ba_2RE_2Si_4O_{12}F_2$(RE=Er^{3+}-Lu^{3+})

A series of new barium rare-earth silicate oxy-fluoride crystals, $Ba_2RE_2Si_4O_{12}F_2$ (RE = Er^{3+}-Lu^{3+}) has been synthesized under hydrothermal conditions. Crystallographic data for this new series of compounds are listed below in **Tables 3.2** and **3.3**. The new structural type, $Ba_2RE_2Si_4O_{12}F_2$, crystallizes in space group *P*-1 and possesses a two-dimensional rare-earth silicate fluoride structure with Ba^{2+} ions residing between layers (**Figure 3.1a, Figure 3.2**). The rare-earth ions display a six-coordinate environment, creating distorted REO_5F octahedra. These octahedra form a dimer in which a $RE_2O_8F_2$ configuration is realized, **Figure 3.2b**. Within the structure, a $[Si_4O_{12}]$ unit provides the necessary building block for crystallization to occur. This $[Si_4O_{12}]$ units represents a tetrameric arrangement that displays inversion symmetry. Several cyclosilicate arrangements of $[Si_4O_{12}]$ can be found within the literature. These include, but are not limited to: $Ba_2Cu_2Si_4O_{12}$, $K_2(NbO)_2Si_4O_{12}$, $M_6Cl_{10}Si_4O_{12}$ (M = Sm^{3+}, Gd^{3+}-Dy^{3+}) and Cs_2USiO_6.[17–20] The $[Si_4O_{12}]$ arrangement can exhibit a wide range of bridging Si–O–Si angles, sometimes approaching 180°. The $[Si_4O_{12}]$ groups in the present structures exhibit Si–O–Si angles ranging from 133.6(4)° to 143.6(4)°, and most closely resemble those in $Sr_4Si_4O_{12}$ with respect to the inversion symmetry and bridging angles of the $[Si_4O_{12}]$ group.[21]

Table 3.2: Crystallographic data of $Ba_2RE_2Si_4O_{12}F_2$ determined by single crystal X-ray diffraction. Table reused with permission from IUCr (http://journals.iucr.org/10.1107/S2052520617009544).

empirical formula	**$Ba_2Er_2Si_4O_{12}F_2$**	**$Ba_2Tm_2Si_4O_{12}F_2$**	**$Ba_2Yb_2Si_4O_{12}F_2$**	**$Ba_2Lu_2Si_4O_{12}F_2$**
formula weight (g/mol)	951.56	954.90	963.12	966.98
temperature (K)	293	293	293	293
crystal size (mm)	0.15 x 0.14 x 0.12	0.13 x 0.12 x 0.09	0.11 x 0.06 x 0.06	0.15 x 0.14 x 0.13
crystal system	triclinic	triclinic	triclinic	triclinic
space group	*P*-1	*P*-1	*P*-1	*P*-1
Unit cell parameters				
a, Å	5.476(4)	5.4609(4)	5.4461(3)	5.451(3)
b, Å	7.166(6)	7.1258(5)	7.1212(3)	7.1227(18)
c, Å	8.958(8)	8.9379(7)	8.9128(4)	8.8937(18)
α, °	108.138(18)	107.809(2)	107.7984(14)	107.73(3)
β, °	102.03(2)	101.987(2)	101.8656(14)	101.81(4)
γ, °	92.742(19)	92.866(2)	92.9455(14)	93.01(3)
volume ($Å^3$)	324.3(4)	321.50(4)	319.66(3)	319.5(2)
Z, calcd density ($\mu g/m^3$)	1, 4.873	1, 4.932	1, 5.003	1, 5.026
absorption coefficient (mm^{-1})	19.254	20.166	21.033	21.860
F(000)	418	420	422	424
Tmax, Tmin	1.0000, 0.4687	1.0000, 0.8387	1.0000, 0.8387	1.0000, 0.2726
Θ range for data	2.46-26.71	2.46-33.22	2.46-26.49	3.03-25.24
reflections collected	2675	8263	8268	2710
data/restraints/parameters	1168/0/101	2236/0/101	1316/0/101	1148/0/101
goodness-of-fit on F^2	1.145	1.141	1.138	1.066
R_1, wR_2 ($I \geq 2\sigma(I)$)	0.0352, 0.0933	0.0224, 0.0623	0.0141, 0.0574	0.0359, 0.0983
R_1, wR_2 (all data)	0.0362, 0.0944	0.0368, 0.0625	0.0143, 0.0575	0.0368, 0.0990

Table 3.3: Selected interatomic distances (Å) and angles (°) of the $Ba_2RE_2Si_4O_{12}F_2$ series.

Table reused with permission from IUCr

(http://journals.iucr.org/10.1107/S2052520617009544).

	$Ba_2Er_2Si_4O_{12}F_2$	**$Ba_2Tm_2Si_4O_{12}F_2$**	**$Ba_2Yb_2Si_4O_{12}F_2$**	**$Ba_2Lu_2Si_4O_{12}F_2$**
RE(1)O_5F				
RE(1)−O(2)	2.268(7)	2.267(3)	2.255(3)	2.250(6)
RE(1)−O(2)	2.280(7)	2.267(3)	2.260(3)	2.258(6)
RE(1)−O(4)	2.264(7)	2.250(3)	2.236(3)	2.232(6)
RE(1)−O(5)	2.236(7)	2.222(3)	2.216(3)	2.213(6)
RE(1)−O(6)	2.244(7)	2.219(3)	2.208(3)	2.206(6)
RE(1)−F(1)	2.181(6)	2.175(3)	2.160(3)	2.137(6)
Si(1)O_4				
Si(1)−O(1)	1.634(6)	1.630(3)	1.633(3)	1.631(6)
Si(1)−O(2)	1.629(7)	1.625(3)	1.623(3)	1.627(6)
Si(1)−O(3)	1.650(7)	1.642(3)	1.644(3)	1.648(7)
Si(1)−O(4)	1.594(7)	1.595(3)	1.596(3)	1.588(7)
Si(2)O_4				
Si(2)−O(1)	1.626(7)	1.633(3)	1.625(3)	1.626(6)
Si(2)−O(3)	1.643(7)	1.644(3)	1.644(3)	1.648(7)
Si(2)−O(5)	1.609(7)	1.609(3)	1.610(3)	1.612(6)
Si(2)−O(6)	1.606(7)	1.608(3)	1.605(3)	1.611(7)
<RE−O>	2.258(7)	2.245(3)	2.235(3)	2.232(6)
<Si−O>	1.624(7)	1.623(3)	1.622(3)	1.624(7)
Si(1) −O(3) −Si(2)	135.4(4)	134.4(2)	134.3(2)	133.6(4)
Si(1) −O(1) −Si(2)	143.6(4)	142.9(2)	142.6(1)	142.5(4)

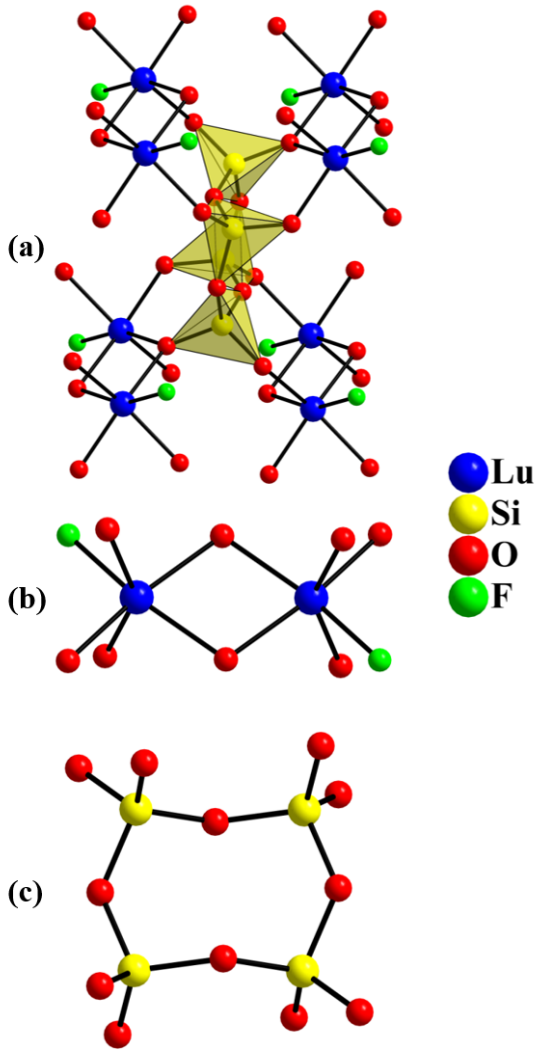

Figure 3.1: Connectivity between the $Lu_2O_7F_2$ dimers and Si_4O_{12}-rings in $Ba_2Lu_2Si_4O_{12}F_2$. (a) Each Si_4O_{12} unit connects to four $Lu_2O_7F_2$ dimers to form Lu–O–Si slabs along the *ac*-plane. *(*b) $Lu_2O_7F_2$ dimer. (c) Si_4O_{12}-rings formed from $Si(1)O_4$ and $Si(2)O_4$ tetrahedra units via corner sharing. Figure reused with permission from IUCr (http://journals.iucr.org/10.1107/S2052520617009544).

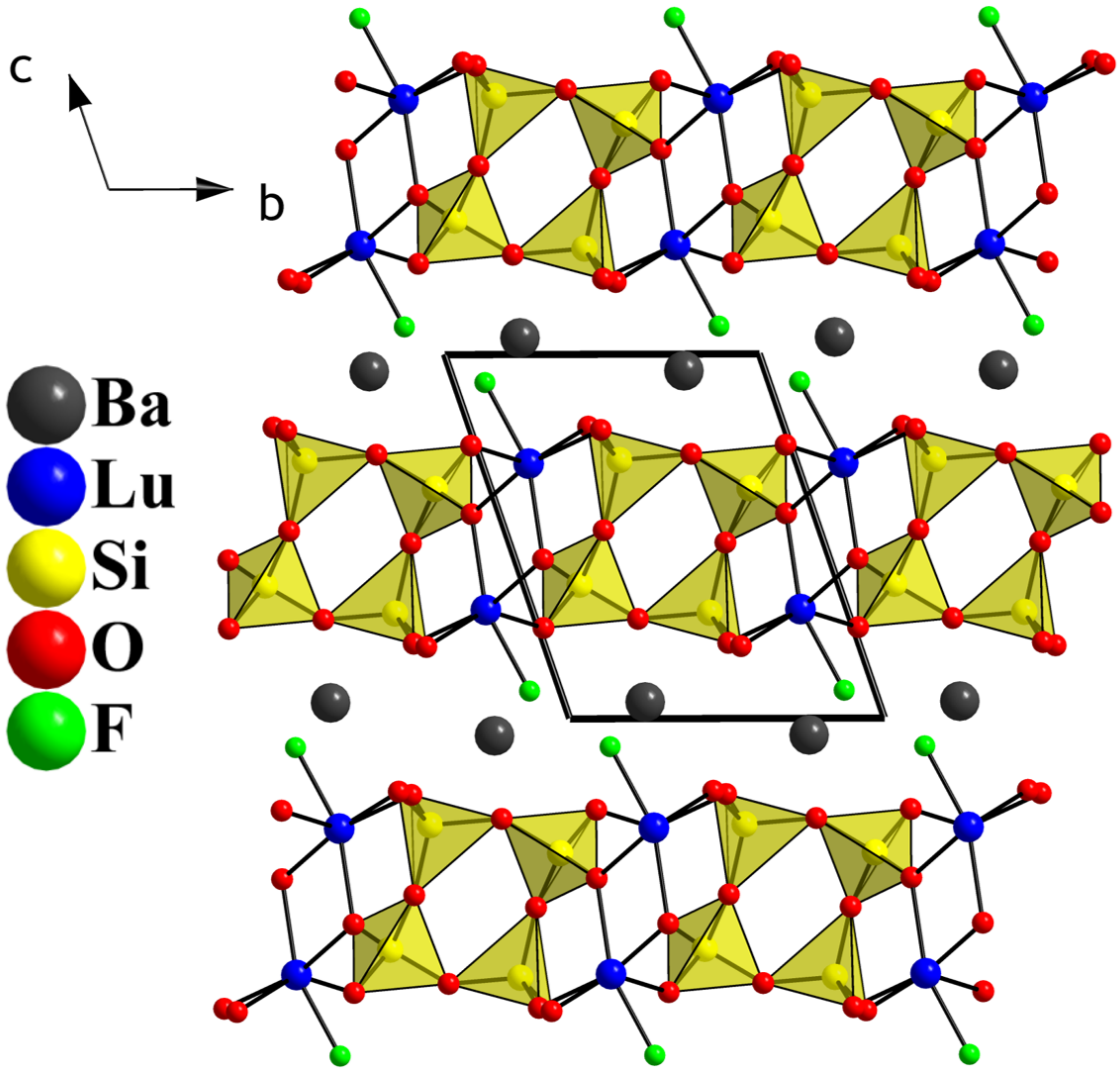

Figure 3.2: Layered $Ba_2Lu_2Si_4O_{12}F_2$ structure showing the connectivity between $Lu_2O_7F_2$ dimers and Si_4O_{12}-rings. Figure reused with permission from IUCr (http://journals.iucr.org/10.1107/S2052520617009544).

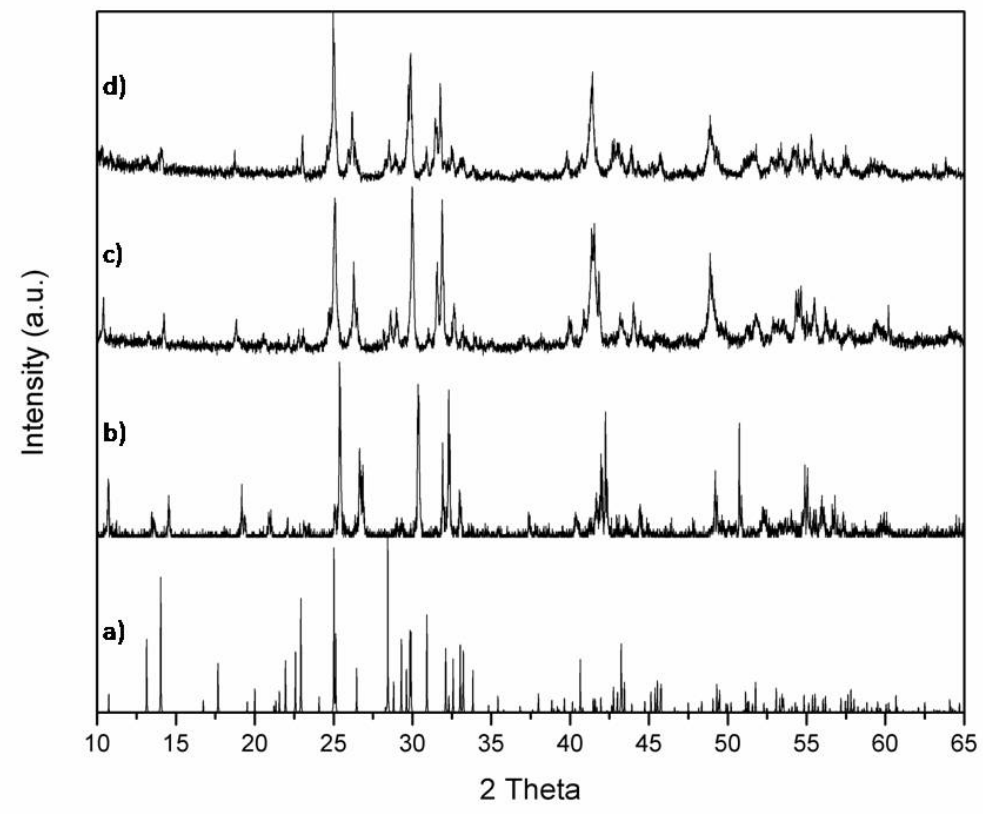

Figure 3.3: Powder diffraction patterns of hydrothermally grown $Ba_2RE_2Si_4O_{12}F_2$ crystals: a) Calculated diffraction pattern of $Ba_2Lu_2Si_4O_{12}F_2$ based on single crystal structure analysis, b-d) As-grown Lu, Tm, and Er analogs, respectively. Figure reused with permission from IUCr (http://journals.iucr.org/10.1107/S2052520617009544).

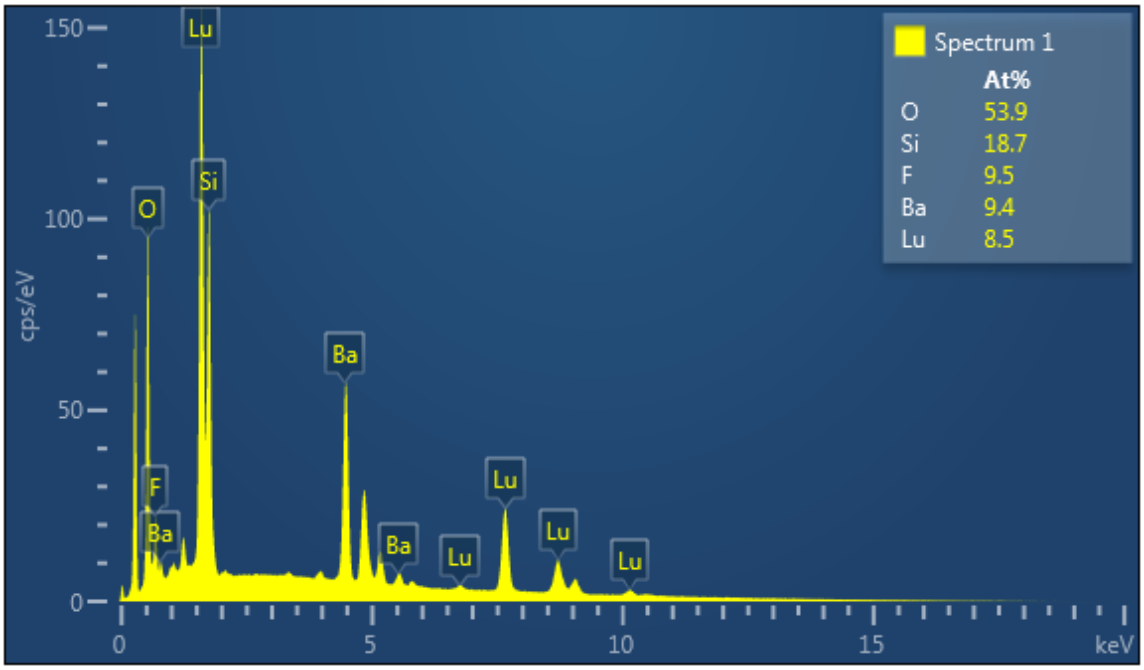

Figure 3.4: EDX spectrum of $Ba_2Lu_2Si_4O_{12}F_2$. Figure reused with permission from IUCr (http://journals.iucr.org/10.1107/S2052520617009544).

The terminal oxygen atoms of the $[Si_4O_{12}]$ group (O(2), O(4), O(5), and O(6)) display shorter Si–O bond lengths over the bridging oxygen atoms, and are shared by the $RE_2O_8F_2$ dimers such that one tetrasilicate connects to four dimers (and one dimer connects to four tetrasilicates), as shown in **Figure 3.1a**. This connectivity establishes sheets that propagate in the *ab*-plane and are separated by Ba atoms, **Figure 3.2**. The barium atoms can be described as nine-coordinate BaO_6F_3 polyhedra. The fluorine atoms were unequivocally determined via bond valence considerations (as all oxygen atoms are bound to at least one silicon atom), and they display shorter bond lengths to the rare-earth atoms than do the oxygen atoms. The fluorine atoms are terminal on the rare-earth dimers, and they provide connectivity to the layers of barium atoms. As expected, the observed average RE–O and RE–F interatomic distances scale appropriately with the size of the rare-earth element. The bridging RE–O bonds of the dimer are slightly elongated compared to the RE–O bonds that extend to the silicate units. The bridging RE–O–RE bond angles between edge-shared rare-earth dimers are 104.4(3)° for Er^{3+}, 104.70(12)° for Tm^{3+}, 104.86(13)° for Yb^{3+}, and 104.8(2)° for Lu^{3+}.

Bridging fluorine atoms have also been reported for connecting rare-earth and actinide chains in the literature of rare-earth silicate structures including tetrasilicates like $Rb_2Lu(Si_4O_{10})F$,[22] $Cs_2Y(Si_4O_{10})F$,[23] $Rb_2Sc(Si_4O_{10})F$,[24] $K_2Sc(Si_4O_{10})F$,[25] $Rb_3Sc_2(Si_4O_{10})F_5$,[26] and $K_2Th(Si_4O_{10})F_2$.[27] Long interactions between rare-earth and fluorine atoms are found in the tetrameric rare-earth units of $K_5La_4(SiO_4)_4F$[26] and $Na_5Y_4(SiO_4)_4F$,[28] while fluorine coordinates only alkali metal cations as a salt inclusion lattice in the $K_9RE_3(Si_{12}O_{32})F_2$ (RE = Y^{3+}, Eu^{3+}, Sm^{3+}) system.[22,29] An interesting comparison can be made between the

$Ba_2RE_2Si_4O_{12}F_2$ series here and $K_5Eu_2(Si_4O_{13})$,[30] which possesses fluorine-corner-shared $Eu_2O_{10}F$ dimers connected by finite $[Si_4O_{13}]$ chains (where we note the silicate unit is also similar to that in the $Ba_2RE_2Si_4O_{13}$ series described below). In $K_5Eu_2(Si_4O_{13})F$, the bridging rare-earth to fluorine bonds in the $Eu_2O_{10}F$ dimer are longer than the terminal bonds to oxygen, and the resulting rare-earth silicate network is a three-dimensional framework, compared to the shorter terminal fluorine bonds and two dimensional nature of the $RE_2O_8F_2$ dimers in the rare-earth silicate network in $Ba_2RE_2Si_4O_{12}F_2$. The RE–F bonds point generally outward from the rare-earth silicate layer to interact weakly with the Ba^{2+} ion, and it thus seems that terminal fluorine atoms may be a structural director of lower dimensionality. PXRD of the as-grown powder confirmed that the $Ba_2RE_2Si_4O_{12}F_2$ family can be grown in a phase pure manner, **Figure 3.3**

Crystal Structure of Monoclinic $Ba_2RE_2Si_4O_{13}$ (RE=Sm^{3+}-Ho^{3+})

Interestingly, a distinct change in the synthetic chemistry occurs based on the size of the rare-earth element used in otherwise identical hydrothermal reactions. Compared to the formation of $Ba_2RE_2Si_4O_{12}F_2$ for the smaller rare-earths (Er^{3+}-Lu^{3+}), the larger rare-earths Sm-Ho result in the formation of the monoclinic tetrasilicate $Ba_2RE_2Si_4O_{13}$. The initial member of this family $Ba_2Gd_2Si_4O_{13}$ was synthesized previously using flux growth techniques,[10] and the present study extends the series of this structure type to both larger and smaller lanthanides (for $Ba_2Gd_2Si_4O_{13}$, a = 12.896(3) Å, b = 5.2120(10) Å, c = 17.549(4) Å, β = 104.08(3)°; <Gd–O = 2.388(3) Å; R_1 = 0.026). **Tables 3.4 and 3.5** include the crystallographic data and selected interatomic distances and angles pertaining to these derivatives. It should be noted that two polymorphs are reported for the general $Ba_2RE_2Si_4O_{13}$ composition, as an earlier report on the structure of $Ba_2Nd_2Si_4O_{13}$ places that compound in the triclinic crystal system through flux growth.[31] In our hands, the hydrothermal reactions involving the larger lanthanides, La^{3+}-Pr^{3+} likewise result in triclinic $Ba_2RE_2Si_4O_{13}$ described below.

Table 3.4: Crystallographic data of the monoclinic $Ba_2RE_2Si_4O_{13}$ (RE = Sm^{3+}-Ho^{3+}) series determined by single crystal X-ray diffraction. Table reused with permission from IUCr (http://journals.iucr.org/10.1107/S2052520617009544).

empirical formula	**$Ba_2Sm_2Si_4O_{13}$**	**$Ba_2Eu_2Si_4O_{13}$**	**$Ba_2Tb_2Si_4O_{13}$**	**$Ba_2Dy_2Si_4O_{13}$**	**$Ba_2Ho_2Si_4O_{13}$**
formula weight (g/mol)	895.74	896.96	912.88	920.04	924.90
temperature (K)	293	293	293	293	293
crystal size (mm)	0.22 x 0.15 x 0.15	0.18 x 0.16 x 0.13	0.16 x 0.16 x 0.06	0.25 x 0.20 x 0.18	0.15 x 0.14 x 0.13
crystal system	monoclinic	monoclinic	monoclinic	monoclinic	monoclinic
space group	*C*2/*c* (No. 15)	*C*2/*c* (No. 15)	*C*2/*c* (No. 15)	*C*2/*c* (No. 15)	*C*2/*c* (No. 15)
a, Å	12.9961(9)	12.9545(13)	12.8568(5)	12.8478(9)	12.8127(7)
b, Å	5.2355(7)	5.2311(8)	5.2019(2)	5.2020(6)	5.1934(5)
c, Å	17.626(3)	17.595(5)	17.5243(7)	17.525(3)	17.514(3)
β, °	104.148(18)	104.23(2)	104.1469(15)	104.077(15)	103.971(12)
volume ($Å^3$)	1162.9(3)	1155.7(4)	1136.48(8)	1136.1(3)	1130.9(2)
Z, calcd density ($\mu g/m^3$)	4, 5.116	4, 5.166	4, 5.335	4, 5.379	4, 5.432
absorption coefficient (mm^{-1})	17.117	17.915	19.626	20.337	21.208
F(000)	1584	1592	1608	1616	1624
Tmax, Tmin	1.0000, 0.4490	1.0000, 0.3821	1.0000, 0.8387	1.0000, 0.4051	1.0000, 0.5231
Θ range for data	3.16 – 26.73	2.39-26.73	2.46-33.12	2.40-26.73	2.40-26.72
reflections collected	4506	4857	6944	4778	4762
data/restraints/parameters	1174/0/97	1196/0/97	1177/0/97	1190/0/97	1182/0/97
goodness-of-fit on F^2	1.177	1.111	1.194	1.162	1.130
R_1, wR_2 ($I \geq 2\sigma(I)$)	0.0490, 0.1447	0.0435, 0.1149	0.0170, 0.0393	0.0431, 0.1283	0.0345, 0.1004
R_1, wR_2 (all data)	0.0509, 0.1464	0.0485, 0.1191	0.0200, 0.0485	0.0446, 0.1304	0.0366, 0.1026

Table 3.5: Selected interatomic distances (Å) and angles (°) of the monoclinic $Ba_2RE_2Si_4O_{13}$ (RE=Sm^{3+}-Ho^{3+}) series. Table reused with permission from IUCr (http://journals.iucr.org/10.1107/S2052520617009544).

	$Ba_2Sm_2Si_4O_{13}$	**$Ba_2Eu_2Si_4O_{13}$**	**$Ba_2Tb_2Si_4O_{13}$**	**$Ba_2Dy_2Si_4O_{13}$**	**$Ba_2Ho_2Si_4O_{13}$**
$RE(1)O_7$					
RE(1)−O(1)	2.639(6)	2.631(6)	2.620(3)	2.615(5)	2.606(5)
RE(1)−O(2)	2.309(7)	2.307(6)	2.285(3)	2.268(6)	2.261(6)
RE(1)−O(3)	2.323(5)	2.313(5)	2.292(3)	2.274(6)	2.274(5)
RE(1)−O(3)	2.508(6)	2.495(6)	2.470(3)	2.469(5)	2.457(5)
RE(1)−O(4)	2.332(6)	2.317(6)	2.278(3)	2.272(6)	2.260(5)
RE(1)−O(6)	2.357(6)	2.341(6)	2.318(4)	2.300(6)	2.295(5)
RE(1)−O(7)	2.395(6)	2.392(6)	2.366(3)	2.351(6)	2.345(5)
$Si(1)O_4$					
Si(1)−O(1)	1.691(6)	1.695(6)	1.695(3)	1.690(6)	1.686(5)
Si(1)−O(2)	1.624(7)	1.619(6)	1.624(4)	1.627(7)	1.620(6)
Si(1)−O(3)	1.658(6)	1.660(6)	1.642(4)	1.650(6)	1.648(5)
Si(1)−O(4)	1.602(6)	1.595(6)	1.596(4)	1.597(6)	1.595(5)
$Si(2)O_4$					
Si(2)−O(1)	1.683(6)	1.670(6)	1.662(3)	1.667(6)	1.677(5)
Si(2)−O(5)	1.658(4)	1.651(4)	1.647(2)	1.652(4)	1.654(3)
Si(2)−O(6)	1.594(7)	1.586(7)	1.589(4)	1.582(6)	1.588(6)
Si(2)−O(7)	1.600(6)	1.600(6)	1.603(4)	1.609(6)	1.604(5)
<RE−O>	2.409(7)	2.399(6)	2.376(3)	2.364(6)	2.357(6)
<Si−O>	1.639(7)	1.634(7)	1.632(4)	1.634(7)	1.634(6)
Si(1)−O(1)−Si(2)	124.6(4)	124.8(4)	125.0(2)	125.0(4)	124.7(3)
Si(2)−O(5)−Si(2)	141.8(6)	142.6(6)	143.7(3)	144.7(6)	144.8(5)

The monoclinic $Ba_2RE_2Si_4O_{13}$ structure forms a three-dimensional, rare-earth silicate framework with barium atoms occupying channels extending along the *b-axis* of the framework (**Figures 3.5a** and **3.6**). The structure again consists of rare-earth dimers, but this time the dimers are based on seven-coordinate REO_7 units that share an edge to form the RE_2O_{12} units (**Figure 3.5b**). The tetrasilicate unit in $Ba_2RE_2Si_4O_{13}$ also differs from that in $Ba_2RE_2Si_4O_{12}F_2$, as it is present as a finite zigzag $[Si_4O_{13}]$ chain (**Figure 3.3c**). Similar chains are observed for samples in the structures of $Ag_{10}Si_4O_{13}$,[32] $Ag_{18}(SiO_4)_2(Si_4O_{13})$,[33] $K_5Eu_2Si_4O_{13}F$,[30] and $Na_4Sc_2Si_4O_{13}$[34] for example. Alternatively, the $[Si_4O_{13}]$ tetrasilicate has also been shown to take on a branched chain, or island-like arrangement in the $Pb_{21}(Si_7O_{22})(Si_4O_{13})$[35] and $NaBa_3RE_3(Si_4O_{13})(Si_2O_7)$ (RE = Y, Nd, Sm, Eu, Gd) structure types,[36–38] and a horseshoe-like arrangement in $La_6(Si_4O_{13})(SiO_4)_2$.[39] Each silicate unit in $Ba_2RE_2Si_4O_{13}$ shares oxygen corners with four RE_2O_{12} dimers to create the framework.

In comparison to the $Ba_2RE_2Si_4O_{12}F_2$ structure type above, it is clear that the presence of only oxygen atoms in the dimers of $Ba_2RE_2Si_4O_{13}$, as opposed to terminal fluorine atoms, presents a more favorable bond valence capacity for corner sharing to silicon atoms, and this in turn enables extension of the rare-earth silicate network to three dimensions. The apparent dependence of the structure type on the size of the rare-earth element might be reconciled using the monoclinic $Ba_2RE_2Si_4O_{13}$ series as a starting point. Contraction of the average RE–O bond distances with decreasing size of the rare-earth elements (2.409(7) Å for Sm^{3+}, 2.399(6) Å for Eu^{3+}, 2.376(3) Å for Tb^{3+}, 2.364(6) Å for Dy^{3+}, and 2.357(6) Å for Ho^{3+}) is also accompanied by a decrease in the Ba–O bond

distances. In particular, an already relatively short Ba(1)–O(7) interaction is reduced to only 2.659(5) Å in the case of the Ho^{3+} analog. As the system is extended to still smaller rare-earth elements we postulate a significant structural rearrangement is needed to mitigate further structural strain, particularly in the short Ba–O interaction, and the $Ba_2RE_2Si_4O_{12}F_2$ structure type is then preferred. For comparison, the shortest bond length about Ba^{2+} in $Ba_2Er_2Si_4O_{12}F_2$ is the Ba(1)–F(1) bond at 2.685(6) Å, which is more reasonable given the smaller size of the F^- anion compared to O^{2-}. Alternatively, it may also be reasonable that the RE_2O_{12} dimer is a less-stable building block for smaller rare-earth elements, and the $RE_2O_8F_2$ dimer with lower anion coordination number about the rare-earth ion is preferable. PXRD of the hydrothermally-grown powder confirms this family can be grown in a phase pure manner with no indication of impurities, **Figure 3.8**. A sample of hydrothermally grown $Ba_2Ho_2Si_4O_{13}$ is shown in **Figure 3.7**.

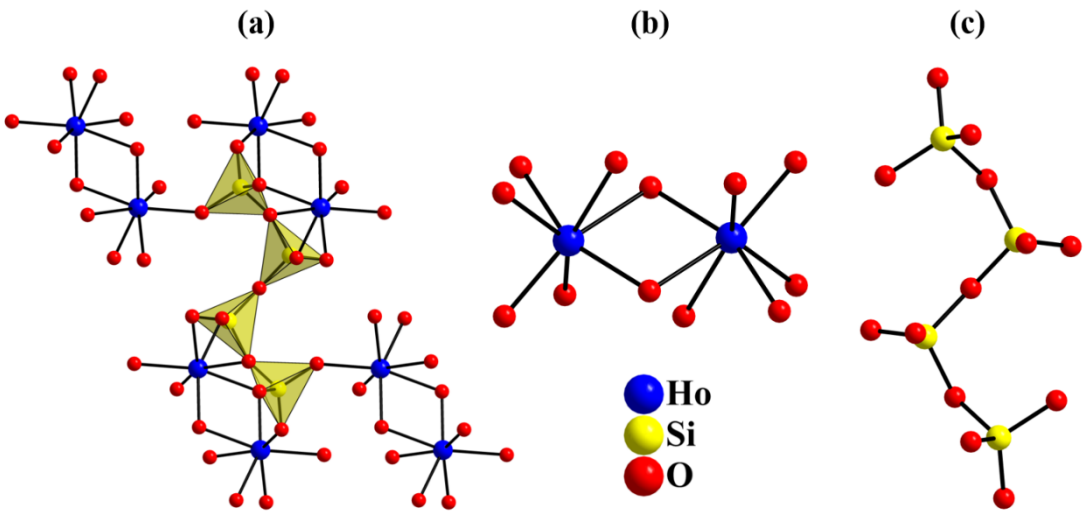

Figure 3.5: Connectivity between the Ho_2O_{12} dimers and Si_4O_{13}-chains in monoclinic $Ba_2RE_2Si_4O_{13}$ viewed along [010] projection. (a) Each Ho_2O_{12} dimer connects to four Si_4O_{13}-chains. (b) Ho_2O_{12} dimers in $Ba_2Ho_2Si_4O_{13}$. (c) Si_4O_{13}-chains formed from $Si(1)O_4$ and $Si(2)O_4$ tetrahedra units via corner sharing. Figure reused with permission from IUCr (http://journals.iucr.org/10.1107/S2052520617009544).

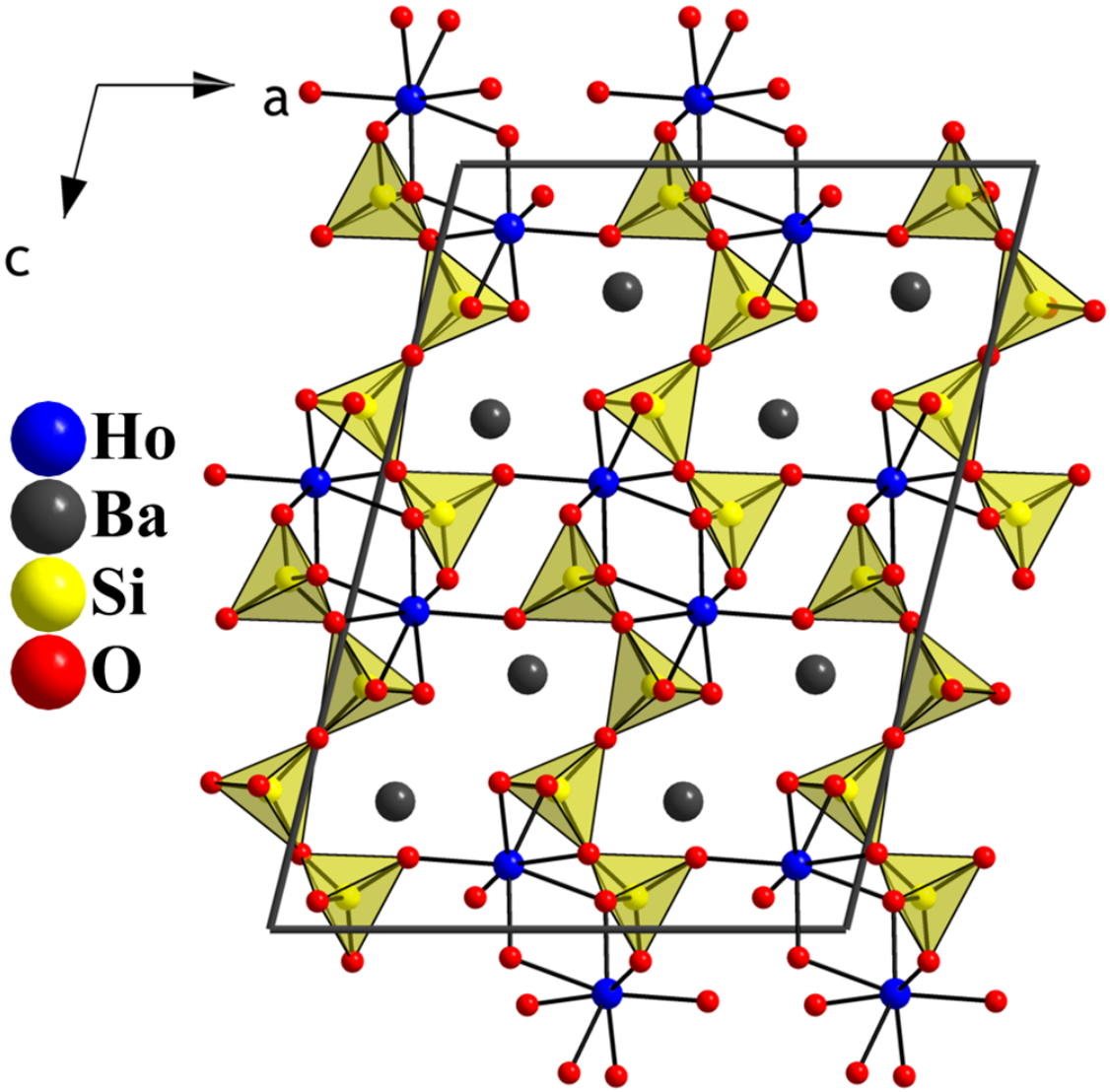

Figure 3.6: $Ba_2Ho_2Si_4O_{13}$along the [010] projection showing Si_4O_{13} finite zigzag chains and Ho_2O_{12} dimers forming a channel structure where the Ba^{2+}-ions reside. Figure reused with permission from IUCr (http://journals.iucr.org/10.1107/S2052520617009544).

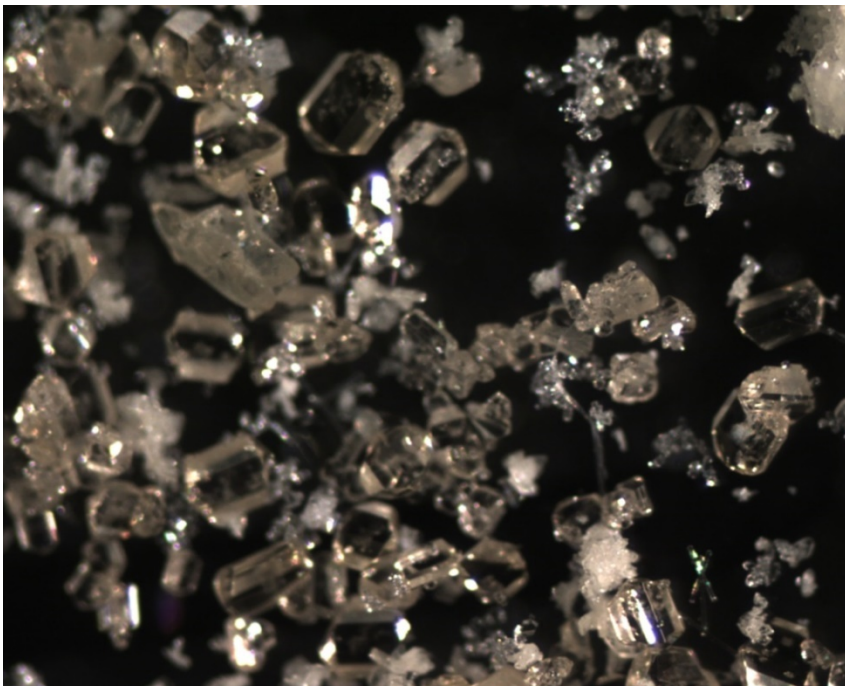

Figure 3.7: Quality of sample growth of $Ba_2Ho_2Si_4O_{13}$ single crystals.

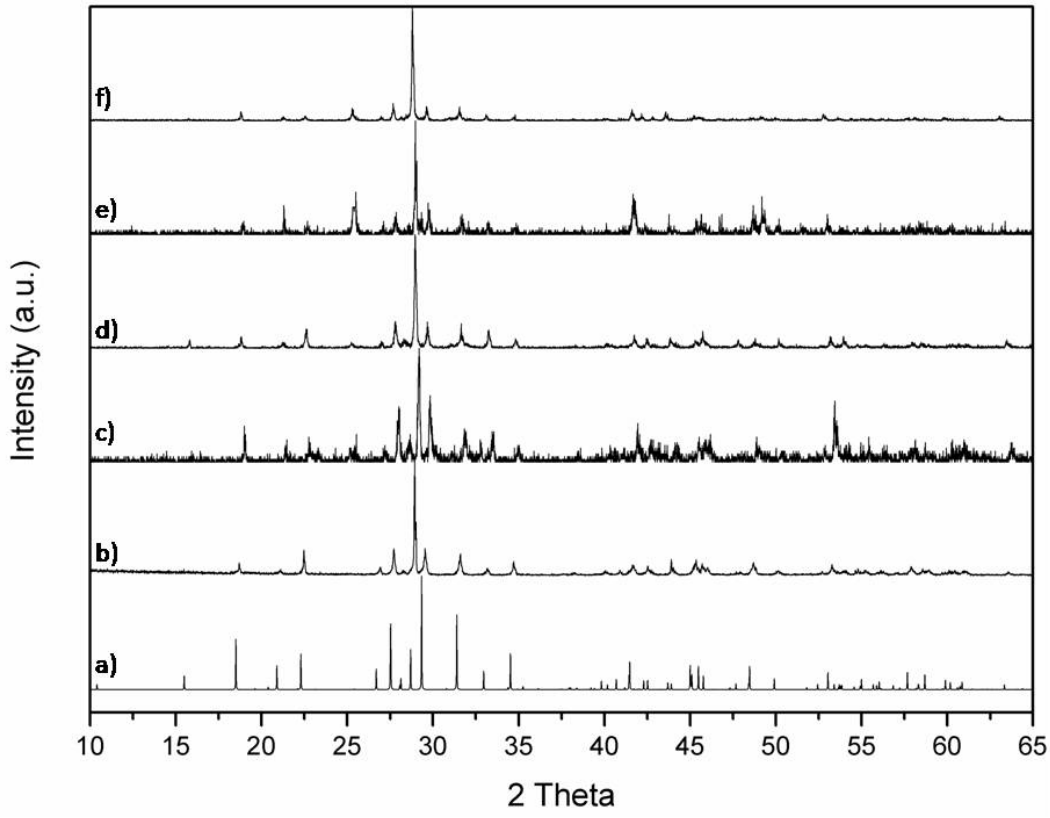

Figure 3.8: Powder diffraction patterns of hydrothermally grown $Ba_2RE_2Si_4O_{13}$ crystals: a) Simulated PXRD of $Ba_2Ho_2Si_4O_{13}$, b-f) As-grown Ho, Dy, Tb, Eu, Sm analogs, respectively. Figure reused with permission from IUCr (http://journals.iucr.org/10.1107/S2052520617009544).

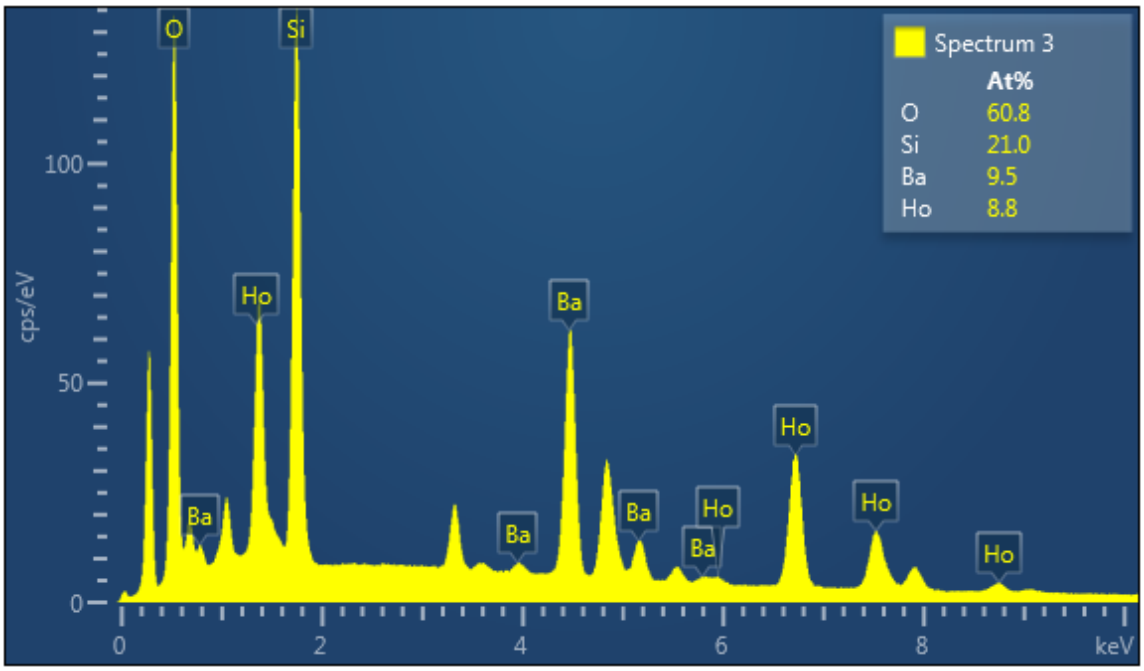

Figure 3.9: EDX spectrum of $Ba_2Ho_2Si_4O_{13}$. Figure reused with permission from IUCr (http://journals.iucr.org/10.1107/S2052520617009544).

Crystal Structure of triclinic $Ba_2RE_2Si_4O_{13}$ (RE=La^{3+}-Nd^{3+})

In the spirit of understanding the fundamental crystal chemistry of rare-earths with tetrasilicate units, the largest rare-earth ions (La^{3+}-Nd^{3+}) were also investigated. A transition to another structure type results as the rare-earth size is increased in these larger f-block ions, wherein a triclinic polymorph of $Ba_2RE_2Si_4O_{13}$ is obtained (**Tables 3.6 and 3.7**), consistent with the $Ba_2Nd_2Si_4O_{13}$ structural type in space group *P-1* (for $Ba_2Nd_2Si_4O_{13}$, a = 6.657(1), b = 8.924(2), c = 10.084(1), α = 86.44(1)°, β = 73.58(1)°, γ = 86.24(1)°, R_1 = 0.067).[31] Indeed, we observe this triclinic polymorph to persist for the remaining larger lanthanides (La^{3+}-Nd^{3+}), though in our particular reactions the phase is only obtained as a minor side product relative to the apatite phase, $KRE_9(SiO_4)_6O_2$.[16] Nevertheless, extension to the largest rare-earth ion La^{3+} establishes a range for this structural type, and triclinic $Ba_2La_2Si_4O_{13}$ can be used as a surrogate of this family (**Figures 3.10 and 3.11**) to make crystal chemical comparisons to the monoclinic polymorph.

Unlike the $Ba_2RE_2Si_4O_{12}F_2$ and monoclinic $Ba_2RE_2Si_4O_{13}$ (*C*2/*c*) structural types, triclinic $Ba_2RE_2Si_4O_{13}$ (*P*-1) contains planar sheets of rare-earth oxide polyhedra that are connected by finite [Si_4O_{13}] chains acting as pillars (**Figure 3.10a**). Within the rare-earth sheets eight-coordinate lanthanum oxide units are connected via oxygen edge-sharing (**Figure 3.10b**). Both unique LaO_8 units form distorted square antiprisms. Within the present study, it appears that the transition from six-coordinate REO_5F and seven-coordinate REO_7 to eight-coordinate REO_8 units is driven by the size of the rare-earth,

and it enables the formation of an extended rare-earth oxide network in triclinic $Ba_2RE_2Si_4O_{13}$ as opposed to isolated dimers in $Ba_2RE_2Si_4O_{12}F_2$ and monoclinic $Ba_2RE_2Si_4O_{13}$. Rare-earth oxide sheets are parallel to (111). Like the monoclinic polymorph, triclinic $Ba_2RE_2Si_4O_{13}$ possesses finite $[Si_4O_{13}]$ chains (**Figure 3.10c**). These connect the rare-earth oxide sheets along [111], again forming a three dimensional rare-earth silicate framework. Barium atoms reside in gaps between the rare-earth sheets and silicate chains (**Figure 3.11**), and are aligned in narrow channels that propagate along the *c*-axis.

The smaller Si(2)–O(13)–Si(3) bond angle in the triclinc polymorph compared to the Si(2)–O(5)–Si(2) angle in the monoclinic polymorph gives the Si_4O_{13} units in the former a more kinked appearance. This is also supported by the Si–Si–Si angles within the chains, consistent with the comparison of $Ba_2Gd_2Si_4O_{13}$ and $Ba_2Nd_2Si_4O_{13}$ made previously.[10] However, in both polymorphs very little change occurs in the Si–Si–Si angles of the $[Si_4O_{13}]$ chains as a function of rare-earth ion within the given structure type. Thus, the rare-earth ion size acts more as a broad structural director of the polymorphs by establishing each particular $[Si_4O_{13}]$ chain in rather rigid geometries with a distinct structural variation, as opposed to imparting a gradual distortion in the $[Si_4O_{13}]$ chains.

Table 3.6: Crystallographic data of triclinic $Ba_2RE_2Si_4O_{13}$(RE =La^{3+}-Pr^{3+}) determined by single crystal X-ray diffraction. Table reused with permission from IUCr (http://journals.iucr.org/10.1107/S2052520617009544).

empirical formula	**$Ba_2La_2Si_4O_{13}$**	**$Ba_2Ce_2Si_4O_{13}$**	**$Ba_2Pr_2Si_4O_{13}$**
formula weight (g/mol)	872.86	875.28	876.86
temperature (K)	295(2)	295(2)	300(2)
crystal size (mm)	0.09 x 0.10 x 0.11	0.06 x 0.06 x 0.07	0.06 x 0.06 x 0.07
crystal system	triclinic	triclinic	triclinic
space group	*P*-1	*P*-1	*P*-1
a, Å	6.7327(3)	6.7062(3)	6.6880(3)
b, Å	8.9894(4)	8.9719(4)	8.9530(4)
c, Å	10.2191(4)	10.1565(5)	10.1324(4)
α, °	86.6588(12)	86.6118(16)	86.5023(13)
β, °	73.5660(12)	73.5658(15)	73.5481(13)
γ, °	86.5873(13)	86.4609(16)	86.2929(15)
volume ($Å^3$)	591.62(4)	584.45(5)	580.07(4)
Z, calcd density ($\mu g/m^3$)	2, 4.900	2, 4.974	2, 5.020
absorption coefficient (mm^{-1})	14.118	14.770	15.434
F(000)	772	776	780
Tmax, Tmin	1.000, 0.7877	1.000, 0.6802	1.000, 0.7739
Θ range for data	2.08-26.00	2.09-26.50	2.28-25.99
reflections collected	10742	22454	11990
data/restraints/parameters	2309/0/190	2433/0/190	2269/0/190
goodness-of-fit on F^2	1.172	1.122	1.165
R_1, wR_2 (I≥ 2σ(I))	0.0203, 0.0501	0.0185, 0.0437	0.0205, 0.0500
R_1, wR_2 (all data)	0.0216, 0.0508	0.0206, 0.0445	0.0222, 0.0507

Table 3.7: Selected interatomic distances (Å) and angles (°) of the $Ba_2RE_2Si_4O_{13}$RE=(La^{3+}-Pr^{3+}) series. Table reused with permission from IUCr (http://journals.iucr.org/10.1107/S2052520617009544).

	$Ba_2La_2Si_4O_{13}$	**$Ba_2Ce_2Si_4O_{13}$**	**$Ba_2Pr_2Si_4O_{13}$**
RE(1)O_8			
RE(1)−O(1)	2.492(3)	2.473(3)	2.467(3)
RE(1)−O(2)	2.531(3)	2.522(3)	2.506(3)
RE(1)−O(4)	2.492(3)	2.473(3)	2.463(3)
RE(1)−O(4)	2.523(3)	2.501(3)	2.491(3)
RE(1)−O(7)	2.718(3)	2.700(3)	2.693(3)
RE(1)−O(7)	2.835(3)	2.855(3)	2.844(3)
RE(1)−O(9)	2.479(3)	2.444(3)	2.431(3)
RE(1)−O(11)	2.385(3)	2.355(3)	2.345(3)
RE(2)O_8			
RE(2)−O(1)	2.504(3)	2.490(3)	2.471(3)
RE(2)−O(2)	2.455(3)	2.435(3)	2.425(3)
RE(2)−O(3)	2.536(3)	2.514(3)	2.502(3)
RE(2)−O(3)	2.540(3)	2.533(3)	2.522(3)
RE(2)−O(8)	2.725(3)	2.719(3)	2.711(3)
RE(2)−O(8)	2.753(3)	2.751(3)	2.746(3)
RE(2)−O(10)	2.516(3)	2.482(3)	2.463(3)
RE(2)−O(12)	2.531(3)	2.510(3)	2.493(3)
Si(1)O_4			
Si(1)−O(2)	1.619(3)	1.618(3)	1.617(3)
Si(1)−O(4)	1.617(3)	1.622(3)	1.617(3)
Si(1)−O(5)	1.677(3)	1.672(3)	1.675(3)
Si(1)−O(7)	1.624(3)	1.619(3)	1.619(3)
Si(2)O_4			
Si(2)−O(5)	1.664(3)	1.669(3)	1.666(3)
Si(2)−O(9)	1.595(3)	1.594(3)	1.588(3)
Si(2)−O(12)	1.599(3)	1.596(3)	1.598(3)
Si(2)−O(13)	1.645(3)	1.641(3)	1.642(3)
Si(3)O_4			
Si(3)−O(6)	1.670(3)	1.672(3)	1.670(3)
Si(3)−O(10)	1.592(3)	1.591(3)	1.591(3)
Si(3)−O(11)	1.590(3)	1.584(3)	1.586(3)
Si(3)−O(13)	1.647(3)	1.649(3)	1.644(3)
Si(4)O_4			
Si(4)−O(1)	1.622(3)	1.616(3)	1.620(3)
Si(4)−O(3)	1.629(3)	1.628(3)	1.629(3)
Si(4)−O(6)	1.662(3)	1.660(3)	1.658(3)
Si(4)−O(8)	1.625(3)	1.621(3)	1.619(3)
<RE−O>	2.563(3)	2.547(3)	2.536(3)
<Si−O>	1.630(3)	1.628(3)	1.627(3)
Si(2)−O(13)−Si(3)	135.1(2)	135.08(18)	134.88(19)
Si(4)−O6)−Si(3)	124.18(19)	123.66(18)	123.57(18)
Si(2)−O(5)−Si(1)	124.30(19)	124.05918)	123.98(18)

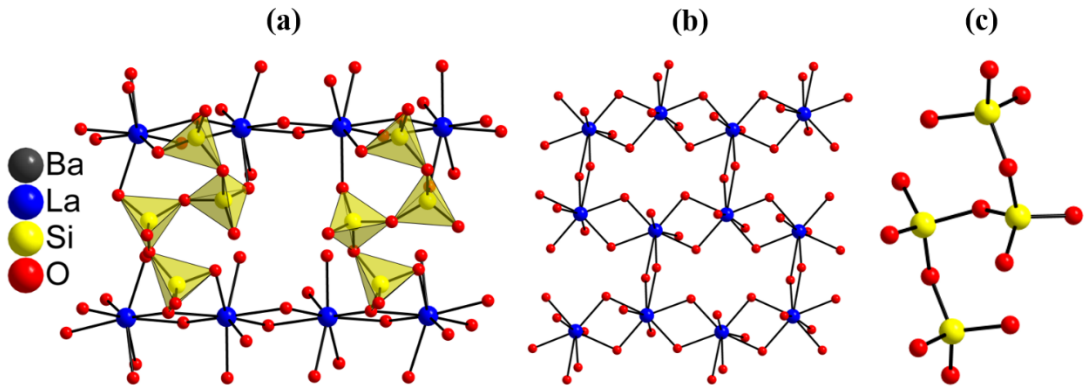

Figure 3.10: a) $Ba_2La_2Si_4O_{13}$ structure highlighting the Si_4O_{13} chains linking the sheets of lanthanum oxide polyhedra. b) LaO_8 sheets propagating in the (111) plane through edge sharing of oxygen atoms. c) Silicate arrangement of the $[Si_4O_{13}]^{-10}$ unit. Figure reused with permission from IUCr (http://journals.iucr.org/10.1107/S2052520617009544).

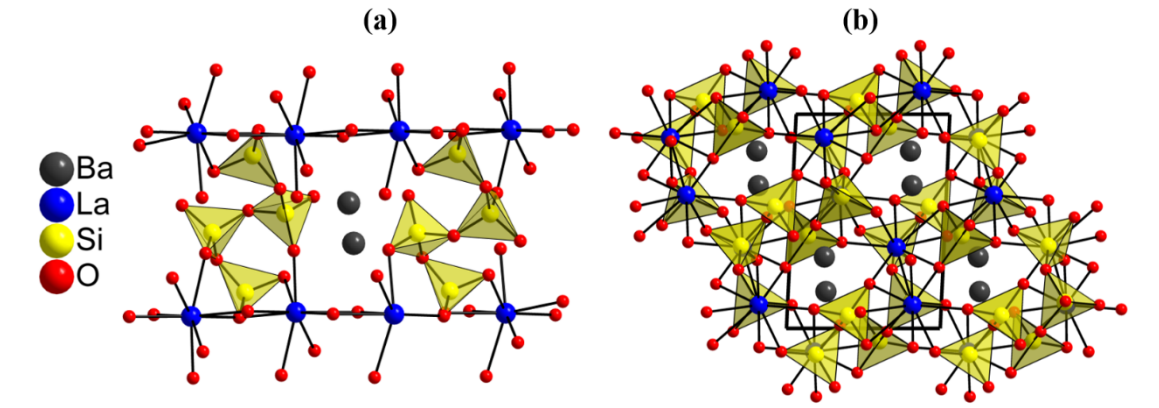

Figure 3.11: a) $Ba_2La_2Si_4O_{13}$ structure highlighting the Ba atom arrangement relative to the planar rare-earth oxide polyhedra in the (111) plane. b) View along [001] indicating prominence of Ba atoms aligned in narrow channels within the silicate framework. Figure reused with permission from IUCr (http://journals.iucr.org/10.1107/S2052520617009544).

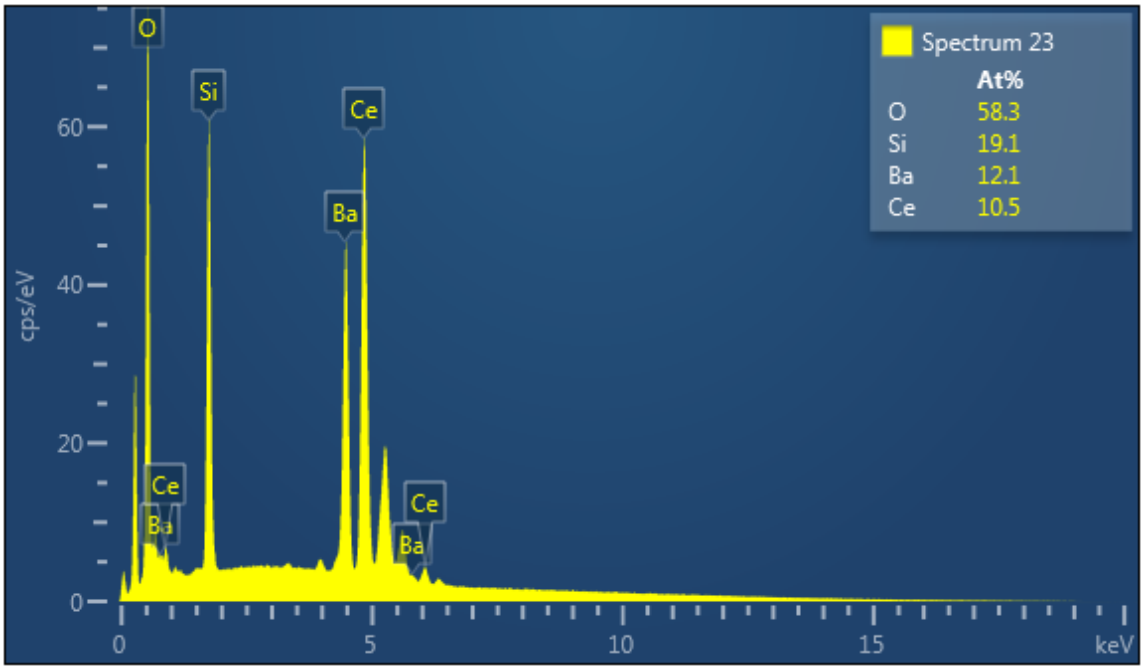

Figure 3.12: EDX spectrum of $Ba_2Ce_2Si_4O_{13}$. Figure reused with permission from IUCr (http://journals.iucr.org/10.1107/S2052520617009544).

Hydrothermal Crystal Growth of $KSrRESi_3O_9$ Single Crystals (RE = Tb-Yb)

The success and chemical knowledge attained during our investigation of the ternary silicate system BaO + RE_2O_3 + SiO_2 in the presence of a mixed hydroxide/ fluoride mineralizer (6 M KF/1 M KOH), led to a current study involving reactions involving SrO + RE_2O_3 + SiO_2. The objective was to observe the structural changes that result from introduction of a slightly smaller alkaline earth metal oxide under conditions of high-temperature and high-pressure hydrothermal growth. The hydrothermal growth technique has been used to synthesize several alkali metal rare-earth silicates including $Na_3RESi_6O_{15}$, $Na_3RESi_3O_9$ and $K_3RESi_3O_8(OH)_2$.[40–42] While the flux growth technique has been widely used to synthesize a number of alkali/ alkaline earth silicates, we find that in our hands the hydrothermal growth technique leads to a rich area of new materials to examine as new possible scintillators. [7,9,43] In this section, a report of the high-temperature synthesis of $KSrRESi_3O_9$, which is in a new structure type, is described. There have been two previously reported rare-earth silicates with the general formula type $ABRESi_3O_9$: $RbBaScSi_3O_9$[44] and $NaBaEuSi_3O_9$[38] where A is an alkali metal ion and B is a alkaline-earth ion. Despite the presence of a common trisilicate [Si_3O_9] ring as the primary building block, all three have different structures. A trisilicate ring is reasonably well known in naturally occurring mineral systems containing transition metals, such as wadeite ($K_2ZrSi_3O_9$)[45] and benitoite ($BaTiSi_3O_9$)[46] as well as several synthetic systems prepared hydrothermally such as $Cs_2ThSi_3O_9$.[27]

Synthesis and Crystallization of $KSrRESi_3O_9$ (RE = Tb-Yb) Single Crystals

Single crystals in this study were synthesized by a high-temperature, high-pressure hydrothermal synthesis method. Reactions consisted of component oxides that were mixed in welded silver ampoules also containing an aqueous mineralizer, 6*M* KF/1*M* KOH. Reaction ampoules were welded shut, loaded into a Tuttle cold seal autoclave and heated to 650 ˚C for 7 d. The autoclave was subsequently cooled and the contents were filtered and washed with DI water. Specific synthetic details of the rare-earth silicate families are described below.

As a representative of the general class of $KSrRESi_3O_9$, $KSrTbSi_3O_9$ will be used as a surrogate to describe the synthetic details of this family. Colorless hexagonal plates of $KSrTbSi_3O_9$ were synthesized using a mixture of SrO (Alfa Aesar 99.9%), SiO_2 (Alfa Aesar 99.9%) and Tb_4O_7 (HEFA Rare-earth 99.9%) in a 3:1.5:6 molar ratio. The reaction was heated for 7 d at 650 °C, generating 207 MPa (30 kpsi) pressure. Crystals of this family containing the other rare-earth ions (Dy-Yb) were grown in a similar fashion using the appropriate oxide components as starting materials in a similar 3:1.5:6 molar ratio. In most of these cases, the rare-earth trisilicate phase was present as the majority product (~70%) with the rest forming the minor product of $K_9RE_2Si_{12}O_{32}F_2$ (RE = Dy, Ho, Er, Tm), which crystallizes as rectangular plates. A reaction summary is included in **Table 3.10**.

Table 3.8: Crystallographic data of $KSrRESi_3O_9$ determined by single crystal X-ray diffraction.

Empirical formula	**$KSrTbSi_3O_9$**	**$KSrDySi_3O_9$**	**$KSrHoSi_3O_9$**	**$KSrErSi_3O_9$**	**$KSrYbSi_3O_9$**
Formula weight	513.91	517.49	519.92	522.25	528.03
Crystal System	Monoclinic	Monoclinic	Monoclinic	Monoclinic	Monoclinic
Space group	$P2_1/n$ (#14)	$P2_1/n$ (#14)	$P2_1/n$ (#14)	$P2_1/n$ (#14)	$P2_1/n$ (#14)
a (Å)	6.7778(3)	6.7983(5)	6.7570(3)	6.7481(3)	6.7253(3)
b (Å	18.1478(8)	18.1073(14)	18.0524(8)	18.0158(9)	17.9539(8)
c (Å)	6.8426(3)	6.8067(5)	6.8205(3)	6.8103(3)	6.7841(3)
β (deg)	102.660(1)	102.645(2)	102.597(1)	102.567(1)	102.484(1)
V ($Å^3$)	821.20(5)	817.57(11)	811.94(6)	808.15(6)	799.78(6)
Z	4	4	4	4	4
D_{calc} (Mg/m^3)	4.157	4.204	4.253	4.293	4.385
Parameters	136	137	136	136	137
μ (mm^{-1})	16.012	16.572	17.229	17.905	19.292
F(000)	944	948	952	956	964
θ range (deg)	2.24-28.35	2.25-25.99	2.26-26.50	2.26-25.99	2.27-25.98
Indices (min)	[-8, -22, -8]	[-8, -22, -8]	[-8, -22, -8]	[-8, -22, -8]	[-8, -21, -8]
(max)	[8, 22, 8]	[8, 22, 8]	[8, 22, 8]	[8, 22, 8]	[7, 22, 8]
Reflections					
Collected	1717	1603	1691	1581	1564
Independent	1662	1576	1524	1547	1497
Observed [I≥2σ(I)]	0.0136	0.0197	0.0211	0.018	0.0255
R(int)	0.0337	0.0406	0.0509	0.0385	0.0346
Final R (obs data)[a]					
R_1	0.0190	0.0167	0.0278	0.0237	0.0179
wR_2	0.0489	0.0482	0.0477	0.0691	0.0458
Final R (all data)					
R_1	0.0200	0.0170	0.0341	0.0269	0.0194
wR_2	0.0494	0.0484	0.0489	0.0919	0.0478
Goodness of fit on F^2	1.168	1.052	1.261	1.121	1.091

[a] $R_1 = [\sum \| F_o | - | F_c \| / \sum | F_o |$; $wR_2 = \{[\sum w[(F_o)^2 - (F_c)^2]^2]\}^{1/2}$

Table 3.9: Selected interatomic distances (Å) and angles (°) of the $KSrRESi_3O_9$ series.

	$KSrTbSi_3O_9$	$KSrDySi_3O_9$	$KSrHoSi_3O_9$
K(1)O_8	2.708-3.240(3)	2.704-3.231(4)	2.710-3.235(5)
RE(1)O_6	2.231-2.388(3)	2.207-2.373(4)	2.208-2.365(4)
Sr(1)O_9	2.535-3.237(3)	2.518-3.227(5)	2.527-3.208(5)
Si(1)O_4	1.606-1.665(3)	1.607-1.658(4)	1.607-1.665(5)
Si(2)O_4	1.588-1.664(3)	1.593-1.671(4)	1.585-1.662(5)
Si(3)O_4	1.587-1.685(3)	1.589-1.689(4)	1.583-1.683(5)
RE(1)−O(1)−RE(1)	102.03(11)	101.54(15)	101.43(16)
Si(2)−O(9)−Si(3)	124.83(18)	125.2(3)	125.2(3)
Si(2)−O(7)−Si(1)	122.18(18	121.7(2)	121.5(3)
Si(1)−O(6)−Si(3)	124.20(18)	124.6(3)	124.5(3)
	$KSrErSi_3O_9$	$KSrTmSi_3O_9$	$KSrYbSi_3O_9$
K(1)O_8	2.708-3.234(6)	2.714-3.223(4)	2.723-3.214(4)
RE(1)O_6	2.198-2.354(6)	2.182-2.343(4)	2.171-2.335(3)
Sr(1)O_9	2.518-3.207(6)	2.516-3.189(4)	2.512-3.180(4)
Si(1)O_4	1.602-1.665(6)	1.591-1.668(4)	1.608-1.673(4)
Si(2)O_4	1.586-1.670(6)	1.608-1.668(4)	1.590-1.663(4)
Si(3)O_4	1.583-1.683(6)	1.583-1.682(4)	1.582-1.681(4)
RE(1)−O(1)−RE(1)	101.3(2)	101.28(15)	100.99(13)
Si(2)−O(9)−Si(3)	125.2(4)	124.8(3)	125.2(2)
Si(2)−O(7)−Si(1)	121.2(4)	121.4(3)	120.9(2)
Si(1)−O(6)−Si(3)	124.9(4)	125.2(3)	125.0(2)

Crystal Structure of $KSrRESi_3O_9$ (RE = Tb^{3+} - Yb^{3+})

Crystallographic data and selected interatomic distances and angles of the $KSrRESi_3O_9$ (RE = Tb^{3+}-Yb^{3+}) series of compounds are shown in **Tables 3.8 and 3.9**, respectively. The crystals reported here are a new member of the $ABRESi_3O_9$ class, in this case containing unique K^+, Sr^{2+} and Ln^{3+} ions. Like the flux grown $RbBaScSi_3O_9$, the title structures are in the centrosymmetric *P21/n* space group, which is in contrast to $NaBaEuSi_3O_9$, which crystallizes in the acentric space group $P2_12_12_1$. One interesting aspect of rare-earth silicates is that the rare-earth ion is often octahedrally (or near-octahedrally) coordinated, in contrast to many other rare-earth complexes where the metal is in a higher and more irregularly coordinated environment. Within the new $ABRESi_3O_9$ (RE = Tb-Yb) class we are mainly going to focus on the Ho^{3+} structure as Ho^{3+} is a good prototype rare-earth ion due to its intermediate size and with an f^{10} electronic configuration it may have rich spectroscopic and magnetic behavior.

$KSrRESi_3O_9$ (RE = Tb-Yb) crystallizes in the monoclinic space group *P21/n* within a range of cell dimensions from a = 6.725-6.798(3) Å, b = 17.954-18.148(8) Å, c = 6.784-6.843(3) Å, β = 102.484-102.660(1)°. This new structural type appears to be unrelated to $NaBaNdSi_3O_9$ and $NaBaEuSi_3O_9$, which crystallize in the acentric space group $P2_12_12_1$. $RbBaScSi_3O_9$ also crystallizes in *P21/n* but with unit cell parameters of a = 6.957(1) Å, b = 10.199(2) Å, c = 11.881(2) Å, β = 90.07(3)°, there is no clear correlation based on unit cell dimensions. Additionally, there appears to be no correlation to $Na_3RESi_3O_9$ (RE = Y and Er), while this family crystallizes in the orthorhombic space

group $P2_12_12_1$, the presence of a spiral radical silicate metachain $(Si_{12}O_{36})_\infty$ is unprecedented within the known alkali alkaline-earth rare-earth silicates.[38]

The structure of the $KSrRESi_3O_9$ series is an intricate three-dimensional framework. The principle building block is a $[Si_3O_9]$ cyclosilicate ring. The Si-O bond distances of the tetrahedra encompassing the $[Si_3O_9]$ group range from 1.651(5) to 1.689(5) Å for the three bridging O atoms and 1.582(5) to 1.619(5) Å for the six terminal O atoms. Within the cyclosilicate unit, O–Si–O bond angles vary from 100.9(3)–118.0(4)°, while $NaBaEuSi_3O_9$ and $RbBaScSi_3O_9$ contain internal angles ranging from 101.4(4)–117.7(4)° and 104.44(8)-131.11(1)°, respectively. Isolated $[Si_3O_9]$ building blocks are coordinated to heavy metals K^+, Sr^{2+} and RE^{3+} in a complicated framework, visible in **Figure 3.13**. Bridging O atoms within the $[Si_3O_9]$ group connect to K^+ and Sr^{2+} and are unbound to the $[RE_2O_{10}]$ dimers, while terminal O atoms bind to all three metals. K^+ displays an 8-coordinate environment with K–O bonds ranging from 2.704(5)–3.240(5) Å. Sr^{2+} displays a 9-coordinate environment with Sr-O bonds ranging from 2.512(5)–3.237(5) Å. SrO_9 polyhedra interconnect to each other through edge sharing of O5, O6, O8, and O9 to form finite sheets propagating along the *ac-plane*. KO_8 additionally interconnects through edge sharing of O4 and O7 in a zigzag chain extending along the *a-axis*, visible in **Figure 3.13b**. SrO_9 and KO_8 are linked through edge sharing of the O2, O3, and O8 atoms and through this connectivity K^+ links to five $[Si_3O_9]$ groups, while Sr^{2+} links to four, each through corner sharing of O atoms. RE^{3+} adopts a 6-coordinate environment with O atoms in a nearly ideal octahedron. RE–O bonds range from 2.171(4)-2.388(4) Å for terminal O atoms and 2.306(4)-2.388(4) Å for bridging of

O1. In this structure, RE^{3+} forms $[RE_2O_{10}]$ dimers that edge share through O1. Each $[RE_2O_{10}]$ dimer coordinates to eight $[Si_3O_9]$ groups, six through terminal O atoms and two through bridging O1 atoms. Dimer formation is in marked contrast to the other $ABRESi_3O_9$ structures, which contain isolated REO_6 octahedra. Most of the other members of the general class of A^+-B^{2+} rare-earth silicates also contain only isolated REO_6 octahedra.

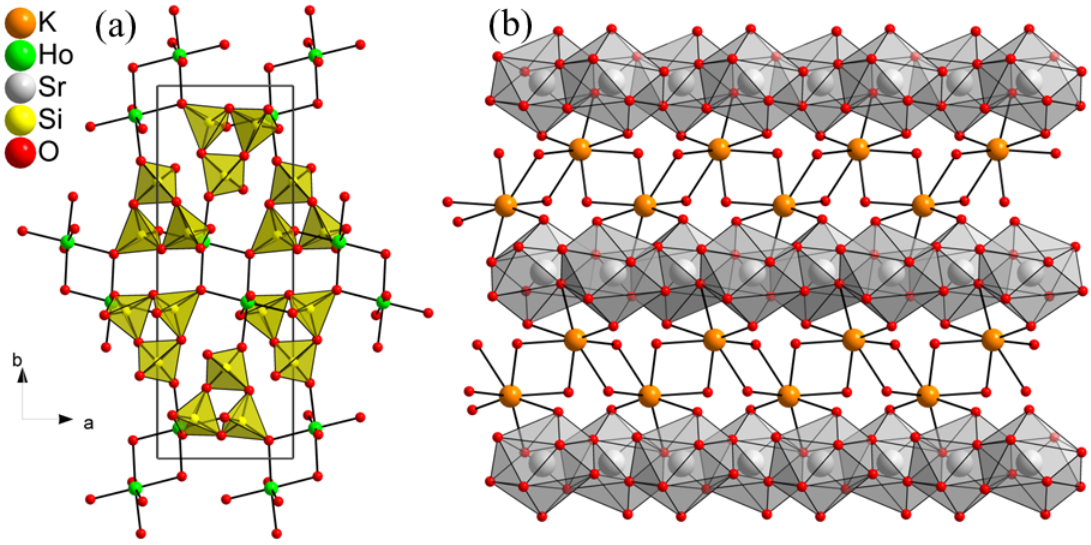

Figure 3.13: Projection of $KSrHoSi_3O_9$ structure viewed along the [001] direction. a) highlighting the Si_3O_9 trimeric units and Ho_2O_{10} dimers. (b) Layered KO_8 and SrO_9 connectivity.

Interestingly, the three reported $ABRESi_3O_9$ structures each contain different alkali metal ions. Previous reports with this nominal formula contain Ba^{2+} as the alkaline earth ion. In this case the Ba^{2+} is irregularly six coordinate for $NaBaEuSi_3O_9$ while it is seven coordinate in $RbBaScSi_3O_9$ and eight coordinate in $KSrHoSi_3O_9$.[38] Of the three Si_3O_9 structures, two have been prepared by high-temperature and high-pressure hydrothermal synthesis. $RbBaScSi_3O_9$ was prepared by Wierzbicka by a high-temperature molybdenum oxide (MoO_3) flux in Pt crucibles at temperatures exceeding 1000 °C with resulting crystals on the order of 100 μm.[44] Herein, we report single crystal growth of $KSrHoSi_3O_9$ on the order of 0.25-0.45 mm. Clearly, the hydrothermal technique provides unsurpassed availability to solubilize even the most recumbent metal oxides for the use in larger single crystal growth. From repeated PXRD experiments with the $KSrRESi_3O_9$ system, there is a clear preferred crystallographic growth direction as seen by the (060) reflection in the experimental PXRD pattern shown in **Figure 3.14**. This fact is not surprising when considering the plate like habit of the hydrothermally as-grown crystals. The absence of hydroxide is supported by the IR spectrum of $KSrHoSi_3O_9$, as shown in **Figure 3.15**.

It is clear from examining $RbBaScSi_3O_9$ and $KSrHoSi_3O_9$, that the latter is a new structural type. First, $RbBaScSi_3O_9$ displays pseudo-hexagonal symmetry when viewed along the [010] direction. In addition, the authors mention that the crystal habit is pseudo-hexagonal in shape, while neither is true for $KSrHoSi_3O_9$. $RbBaScSi_3O_9$ contains isolated REO_6 environments, while $KSrHoSi_3O_9$ contains dimer units of $[Ho_2O_{10}]$. Ba^{2+} and Rb^+ are alternating along the [010] in the void of the Si_3O_9 groups for $RbBaScSi_3O_9$. As

mentioned earlier, KO_8 and SrO_9 exhibit layering of zigzag chains and sheets, respectively, viewed along the [001] direction for $KSrHoSi_3O_9$. No direct structural correlation between $KSrHoSi_3O_9$ and $RbBaScSi_3O_9$ has been found, though both contain isolated Si_3O_9 groups and appear isoformulaic. Continuation into larger rare-earth ions (RE = La-Gd), resulted in formation of the well-established apatite structure, $KRE_9(SiO_4)_6O_2$.[16] $K_9RE_2Si_{12}O_{32}F_2$ in *P-1* is a new structural type currently being pursued by the group at the time of this write-up.

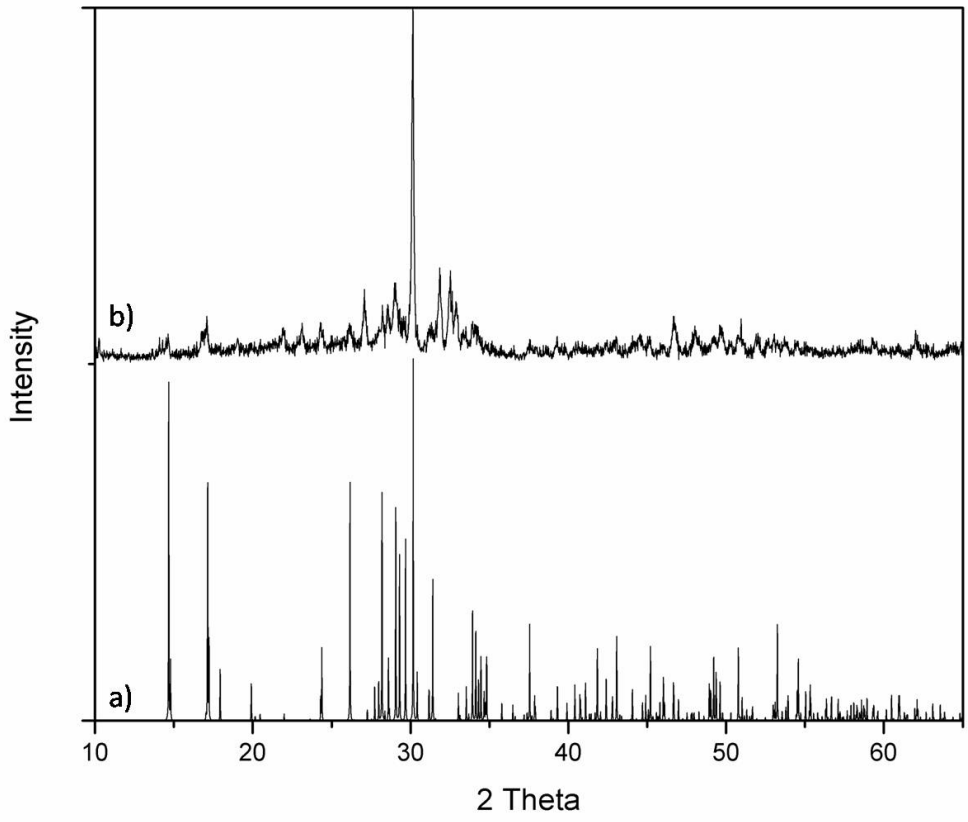

Figure 3.14: a) Simulated powder pattern of $KSrHoSi_3O_9$ from crystal data. b) Experimental powder pattern of ground powder from reaction producing $KSrHoSi_3O_9$.

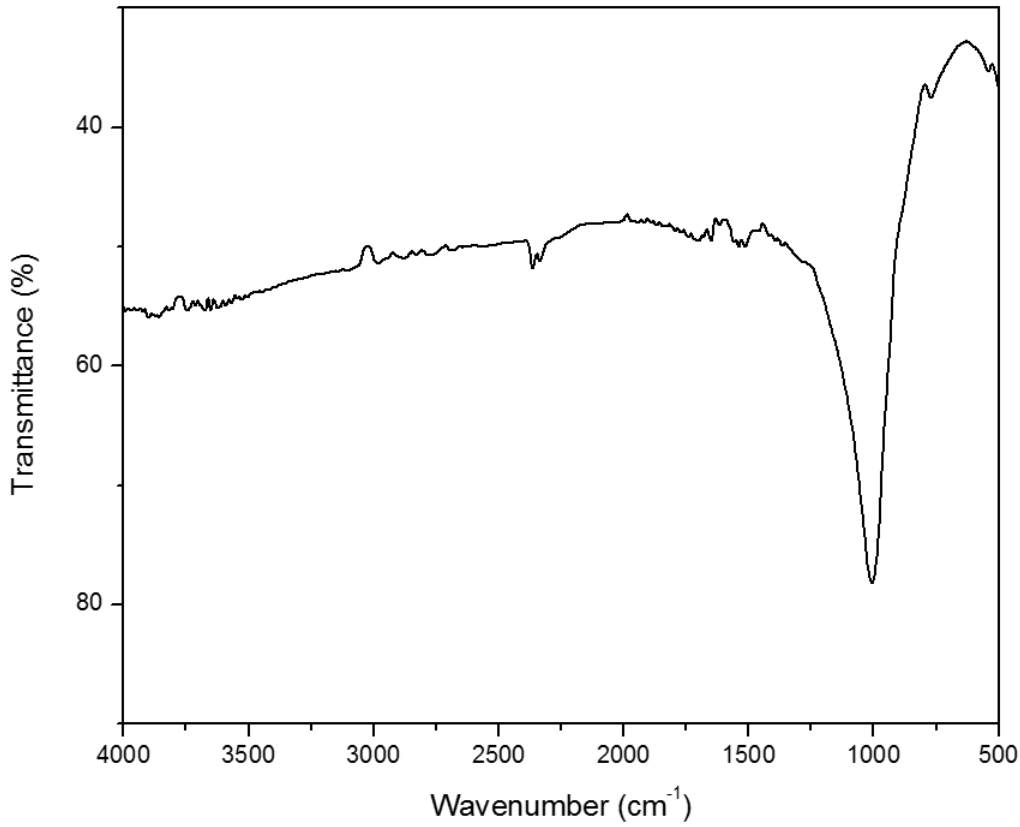

Figure 3.15: IR spectrum of $KSrHoSi_3O_9$.

Table 3.10: Summary of product formation from high-temperature hydrothermal growth: $SrO + RE_2O_3 + SiO_2$+ 6 *M* KF/1 *M* KOH at 650 °C for 7 days.

RE^{+3}	Products
Tb^{3+}	$KSrTbSi_3O_9$ (*P21/n*)
Dy^{3+}	$KSrDySi_3O_9$ (*P21/n*)
	$K_9Dy_2Si_{12}O_{32}F_2$ (*P-1*)
Ho^{3+}	$KSrHoSi_3O_9$ (*P21/n*)
	$K_9Ho_2Si_{12}O_{32}F_2$ (*P-1*)
Er^{3+}	$KSrErSi_3O_9$ (*P21/n*)
	$K_9Er_2Si_{12}O_{32}F_2$ (*P-1*)
Tm^{3+}	$KSrTmSi_3O_9$ (*P21/n*)
	$K_9Tm_2Si_{12}O_{32}F_2$ (*P-1*)
Yb^{3+}	$KSrYbSi_3O_9$ (*P21/n*)

Hydrothermal Crystal Growth of Wadeite Mineral Type $A_2M^{+4}B_3O_9$: $K_2TiSi_3O_9$ $K_2SnSi_3O_9$, $Rb_2USi_3O_9$, $Cs_2HfGe_3O_9$, and $Cs_2ZrGe_3O_9$

In the spirit of fundamental crystal growth and basic science, the hydrothermal growth of several wadeite structures is reported and described. A group of tetravalent refractory metal oxides has been investigated by high-temperature and high-pressure reactions to elucidate their relative solubility and chemical reactivity in concentrated basic hydroxide and fluoride mineralizers. Metal oxides TiO_2, SnO_2, UO_2, HfO_2, and ZrO_2 represent a highly refractory class of oxides that are prevalent as prime candidates for hydrothermal crystal growth. Tetravalent oxides of UO_2, HfO_2 and ZrO_2 have melting points exceeding 2500 °C, while SnO_2 is known to sublime before reaching a melting point near 1800 °C.[47] Herein, a careful examination of the limits to the wedeite structure type $A_2M^{+4}B_3O_9$ are discussed where A represents an alkali metal (K, Rb, Cs), M^{4+} represents a tetravalent metal oxide (Ti, Sn, Zr, U, Hf), and B represents a tetravalent tetrahedral metal (Si or Ge). For completion, $Cs_2HfGe_3O_9$, and $Cs_2ZrGe_3O_9$ were synthesized. While these structures are not silicate-based frameworks, they display similar structural and solution chemistry. A detailed synopsis of hydrothermal growth with rare-earth germanates will be elucidated in Chapter 3.

The wadeite-type structure is based on the $K_2ZrSi_3O_9$ structural type.[48] The presence of several tetravalent cations in the literature lead to the conclusion the family contains a high degree of flexibility to incorporate a variety of alkali and tetravalent metals: $K_2SiSi_3O_9$,[49] $K_2TiSi_3O_9$,[48] $K_2ZrSi_3O_9$,[48] $K_2SnSi_3O_9$,[50] $Rb_2ThSi_3O_9$, and $Cs_2ThSi_3O_9$.[27] Of the known wadeite germanate structural types $A_2M^{4+}Ge_3O_9$ (A = Tl, K, Rb, Cs) (M^{4+} = Sn or Ti), all have been prepared by sintering of metal oxide powders to

less than satisfactory convergenace.[50] To date, $K_2SiSi_3O_9$ (V = 360.11 Å^3) and $Cs_2ThSi_3O_9$ (V = 516.34 Å^3) represent the current end limits of this family of compounds. Additionally, the first U^{4+} wadeite is reported, which could lead to interesting optical characterization of the S = 1 configuration.

Experimental Method for Growth of Hydrothermal Wadeite Single Crystals

Single crystals of the wadeite structure were synthesized via the high-temperature and high-pressure hydrothermal method. Reactants were heated in fine silver ampoules (99.9% fine silver) for 7 days at 650 °C. Upon completion, the ampoules were opened, and single crystals were filtered and washed with DI water. Each reaction represents a 1 : 3 stoichiometric ratio of M^{4+}: Si^{4+} or M^{4+}: Ge^{4+}. The exact amount of metal oxides is described below. For $K_2TiSi_3O_9$, TiO_2 (46 mg, 0.577 mmol) and SiO_2 (104 mg, 1.73 mmol) powders were reacted with 0.4 mL of 10 M KOH. For $K_2SnSi_3O_9$, SnO_2 (68 mg, 0.453 mmol) and SiO_2 (82 mg, 1.36 mmol) powders were reacted with 10 M KOH. For $Rb_2USi_3O_9$, UO_2 (90 mg, 0.333 mmol) and SiO_2 (60 mg, 0.999 mmol) were reacted. For $Cs_2HfGe_3O_9$, HfO_2 (60 mg, 0.286 mmol) and GeO_2 (90 mg, 0.858 mmol) were treated with 0.4 mL of 6 M CsF. For $Cs_2ZrGe_3O_9$, ZrO_2 (42 mg, 0.343 mmol) and GeO_2 (108 mg, 1.03 mmol) were treated with 0.4 mL of 6 M CsF. For preparation of UO_2 powder, uranium acetate ($UO_2(C_2H_3O_2)_2 + 2H_2O$) was decomposed at 500 °C for 6 hours. The resultant black chunky powder was ground and pressed into a pellet using a hydraulic pellet press. The pellet was subsequently heated again at 500 °C for 6 hours. This powder was treated hydrothermally with SiO_2 in the presence of 0.4 mL of 6 M RbF/ 1 M RbOH to form $Rb_2USi_3O_9$ black/dark green single crystals (0.25 mm). These crystals were

subsequently treated hydrothermally as seed crystals to grow larger $Rb_2USi_3O_9$ crystals under identical reactions for possible magnetic measurements. The resultant crystals were characterized as $Rb_2USi_6O_{15}$ which has been synthesized and reported by Morrison and co-workers.[20] Additionally, the formation of yellow $Rb_2U_2O_7$ created an oxidizing environment in which the silver ampoules were oxidized and destroyed. Due to the oxidizing conditions of this system, follow-up characterization was not pursued. However, a single crystal structure was collected and reported herein.

Table 3.11: Crystallographic parameters of $A_2M^{4+}B_3O_9$ determined by single crystal X-ray diffraction.

empirical formula	**$K_2TiSi_3O_9$**	**$K_2SnSi_3O_9$**	**$Rb_2USi_3O_9$**	**$Cs_2HfGe_3O_9$**	**$Cs_2ZrGe_3O_9$**
formula weight (g/mol)	354.37	425.16	637.24	806.08	718.81
temperature (K)	293	293	293	293	293
crystal system	Hexagonal	Hexagonal	Hexagonal	Hexagonal	Hexagonal
space group	*P6/3m*	*P6/3m*	*P6/3m*	*P6/3m*	*P6/3m*
Unit cell parameters					
a, Å	6.7819	6.8753(10)	7.2516(10)	7.3475(8)	7.3630(3)
c, Å	9.938(2)	10.038(2)	10.554(2)	10.6319(12)	10.6838(5)
volume ($Å^3$)	395.86(14)	410.92(14)	480.65(13)	497.07(12)	501.61(5)
Z, calcd density ($\mu g/m^3$)	2, 2.973	2, 3.436	2, 4.403	2, 5.386	2, 4.759
absorption coefficient (mm^{-1})	2.618	4.591	27.347	26.633	17.090
F(000)	348	404	560	700	636
Tmax, Tmin	1.000-0.6637	1.000-0.6855	1.000-0.5585	1.000-0.8387	1.000-0.4357
Θ range for data	3.46-26.70	3.46-26.70	3.46-26.70	3.20-33.16	3.12-26.50
reflections collected	3482	3719	4660	21465	9304
data/restraints/parameters	282/0/28	290/0/28	361/0/28	346/0/29	369/0/28
goodness-of-fit on F^2	1.156	1.181	1.156	1.198	1.043
R_1, wR_2 ($I \geq 2\sigma(I)$)	0.0243, 0.0616	0.0177, 0.0433	0.0265, 0.0623	0.0096, 0.0257	0.0197, 0.0477
R_1, wR_2 (all data)	0.0246, 0.0618	0.0180, 0.0436	0.0277, 0.0630	0.0096, 0.0257	0.0199, 0.0479

Table 3.12: Select bond distances (Å) and angles (°) in the wadeite family: $A_2M^{4+}B_3O_9$

	$K_2TiSi_3O_9$	**$K_2SnSi_3O_9$**	**$Rb_2USi_3O_9$**	**$Cs_2HfGe_3O_9$**	**$Cs_2ZrGe_3O_9$**
M-O(2) x6	1.9467(17)	2.0332(19)	2.252(4)	2.071(2)	2.082(3)
B(1)-O(1) x2	1.5953(17)	1.597(2)	1.601(4)	1.712(2)	1.716(3)
B(1)-O(2)	1.645(2)	1.645(3)	1.649(6)	1.758(3)	1.765(4)
B(1)-O(2)	1.657(2)	1.656(3)	1.652(6)	1.783(3)	1.785(4)
B(1)-O(1)-B(1)	133.70(16)	133.65(18)	133.7(4)	132.3(2)	131.7(3)

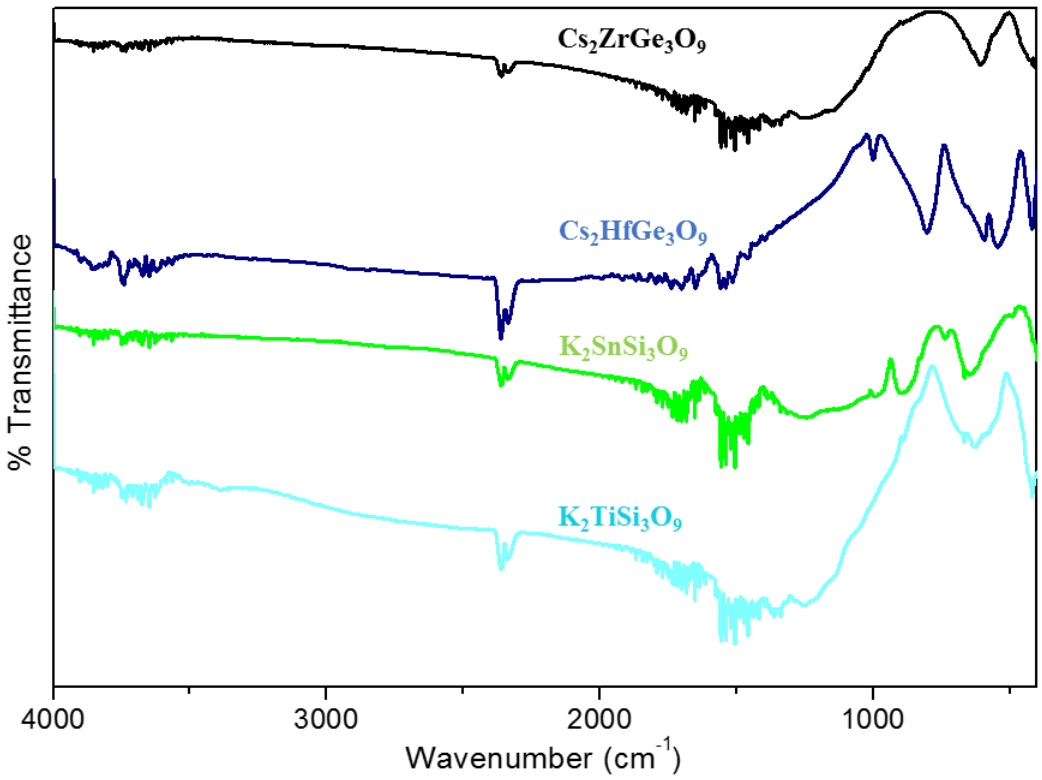

Figure 3.16: IR spectrum of hydrothermally grown wadeite structures.

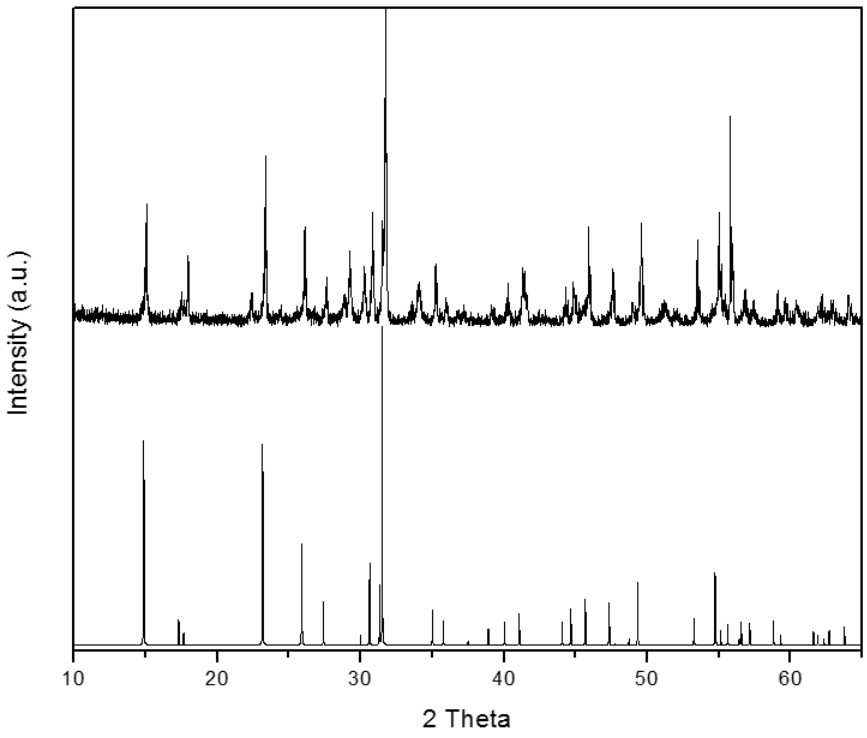

Figure 3.17: (Bottom) Simulated powder pattern of $K_2SnSi_3O_9$. (Top) Hydrothermally grown powder of $K_2SnSi_3O_9$.

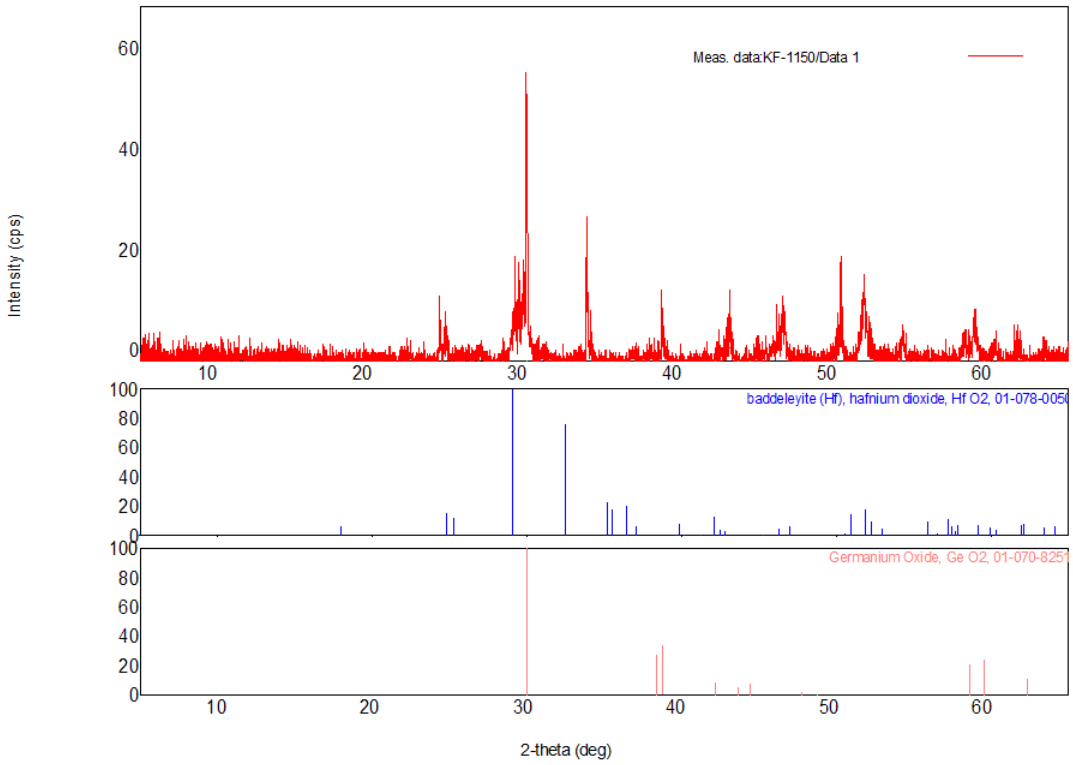

Figure 3.18: Hydrothermally grown powder of $Cs_2HfGe_3O_9$ showing a mixture of products consisting of starting material powder (HfO_2, GeO_2) and wadeite $Cs_2HfGe_3O_9$.

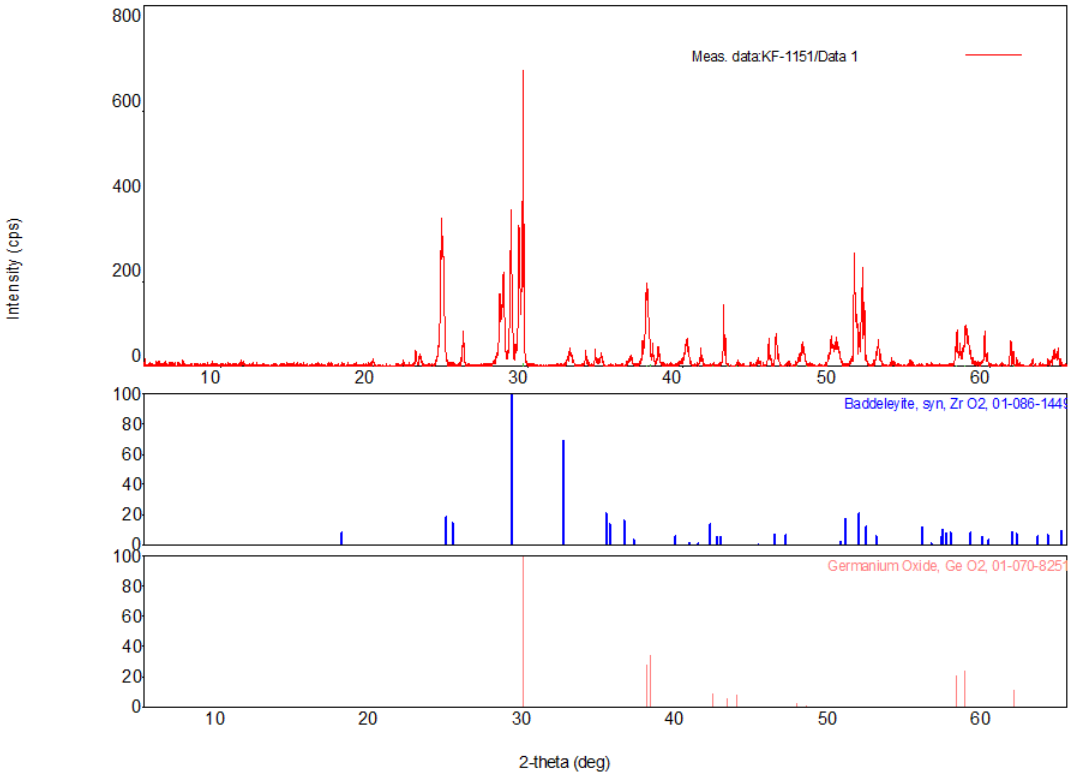

Figure 3.19: Hydrothermally grown powder of $Cs_2ZrGe_3O_9$ showing a mixture of products consisting of starting material powder (ZrO_2, GeO_2) and wadeite $Cs_2ZrGe_3O_9$.

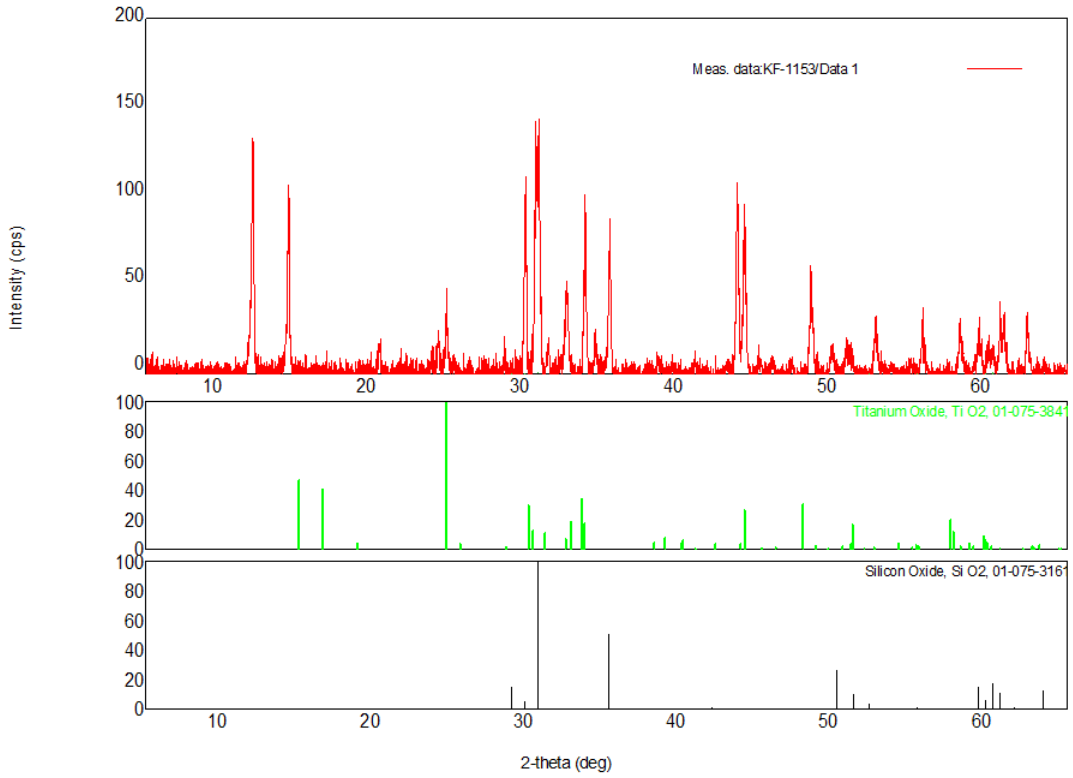

Figure 3.20: Hydrothermally grown powder of $K_2TiSi_3O_9$ showing a mixture of products consisting of starting material powder (TiO_2, SiO_2) and wadeite $K_2TiSi_3O_9$.

Crystal Structure of Wadeite Mineral Type $A_2M^{4+}B_3O_9$: $K_2TiSi_3O_9$ $K_2SnSi_3O_9$, $Rb_2USi_3O_9$, $Cs_2HfGe_3O_9$, and $Cs_2ZrGe_3O_9$

The compounds $K_2TiSi_3O_9$ $K_2SnSi_3O_9$, $Rb_2USi_3O_9$, $Cs_2HfGe_3O_9$, and $Cs_2ZrGe_3O_9$ crystallize in hexagonal space group *P6₃/m* (No. 176) and are consistent with known wadeite mineral types. The wadeite structure type is based on the $K_2ZrSi_3O_9$ crystal structure.[48] Of the reported crystal structures, $Cs_2ThSi_3O_9$ represents the largest unit cell volume (516.34(15) Å^3) and $K_2SiSi_3O_9$ as the smallest (360.11 Å^3).[27] Of the reported structures conducted in this study, all remain within the current unit cell limits of the family. Even with incorporation of a larger tetrahedral tetravalent building block (GeO_2), $Cs_2ZrGe_3O_9$ is 2.9% smaller via unit cell parameters in comparison with $Cs_2ThSi_3O_9$. Unit cell parameters and selected bond distances and angles are listed in **Tables 3.11 and 3.12**.

To discuss the structural features of this mineral class, $K_2SnSi_3O_9$ will be used as a surrogate example. The wadeite structure type is based on a nearly-ideal octahedra [MO_6] with building blocks of cyclosilicate [Si_3O_9] or cyclogermanate [Ge_3O_9] and charge balancing alkali metals (K^+, Rb^+ or Cs^+). The [Si_3O_9] building block consists of Si(1)-O(1)-Si(1) internal angles of 133.65(18)° and a range of 133.70(16) to 131.7(3)° for the reported structures with decreasing torsion angles with increasing unit cell parameters. The cyclosilicate is linked through O(2) to SnO_6 as shown in **Figure 3.21**. Each SnO_6 polyhedra coordinates six [Si_3O_9] units in the *ab*-plane (3 above and 3 below the plane), **Figure 3.22**). For SnO_6 a near-ideal octahedral environment is realized with Sn(1)-O(2) bond distances of 2.0332(19) Å. Potassium ions coordinate oxygen atoms above and below the [Si_3O_9] unit to complete the solid-state framework and provide the

necessary charge balance, **Figure 3.23**. PXRD of the as-grown wadeite structures revealed that a mixture of starting material (MO_2, BO_2) (M = Zr, Hf, Ti) (B = Si or Ge) with wadeite mineral type was prevalent for all compounds, excluding $K_2SnSi_3O_9$, **Figures 3.17-3.20**. For $Rb_2USi_3O_9$, as described in the experimental methods, subsequent reactions involving $Rb_2USi_3O_9$ as seed crystals resulted in formation of $Rb_2USi_3O_9$ and $Rb_2U_2F_7$ single crystals. The ability for uranium to form multiple stable oxidation states under hydrothermal conditions led to conditions where the silver ampoules could be oxidized during these reactions. For this reason, further pursuit of this material for supporting characterization was not pursued at this time. It is believed that changing to more stable platinum ampoules could lead to further reactions of this interesting U^{4+} compound.

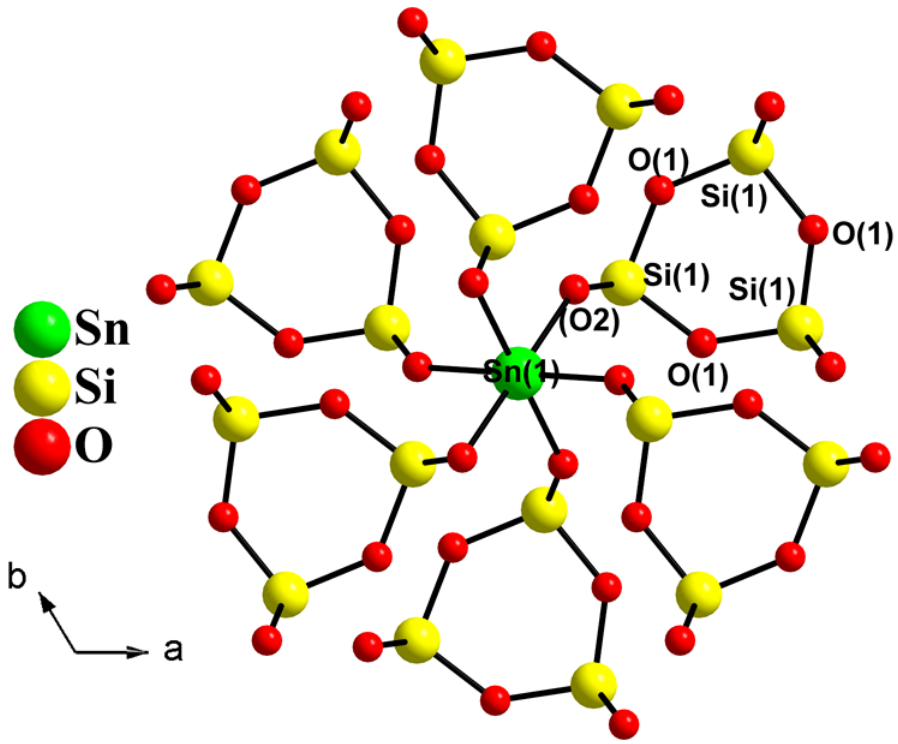

Figure 3.21: SnO_6 octahedra coordinating $[Si_3O_9]$ units in the *ab*-plane via corner-sharing of O(2) viewed along the [001] direction.

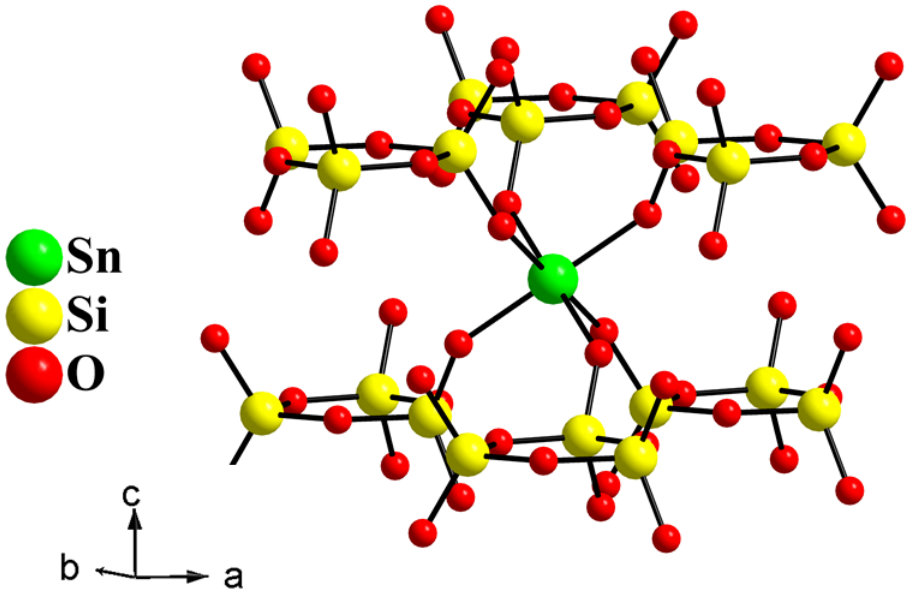

Figure 3.22: SnO_6 polyhedra coordination of six $[Si_3O_9]$ units, three above and three below the *ab*-plane.

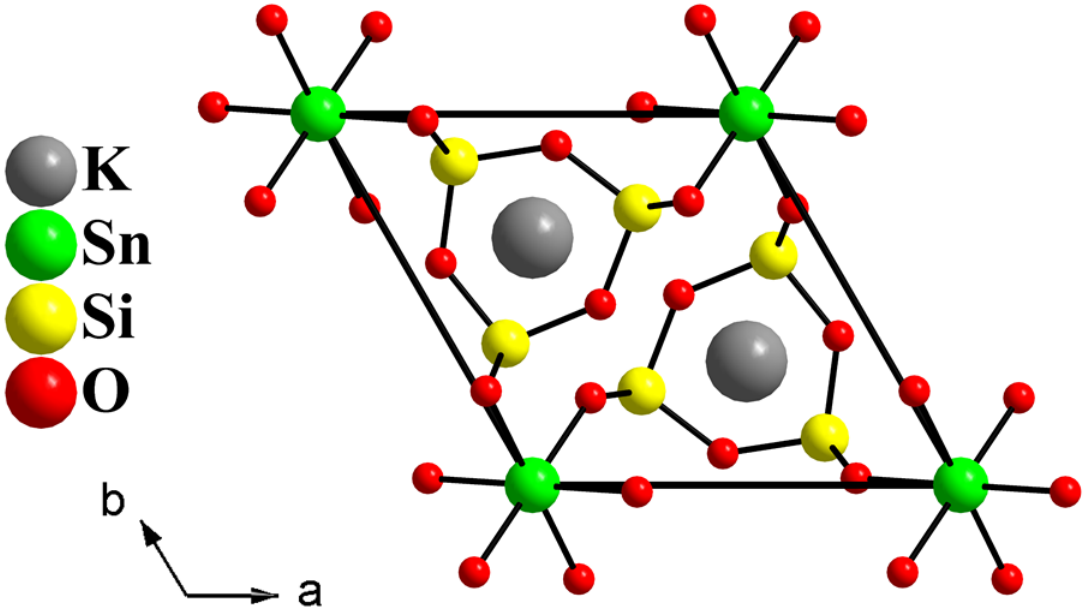

Figure 3.23: Unit cell projection of $K_2SnSi_3O_9$ along [001] direction.

Hydrothermal Crystal Growth of $K_2HfSi_2O_7$

In pursuit of refractory silicates grown under hydrothermal conditions, a new hafnium silicate, $K_2HfSi_2O_7$, has been synthesized and characterized. The potassium hafnium silicate was synthesized via a stoichiometric reaction of HfO_2 (96 mg, 0.454 mmol) and SiO_2 (54 mg, 0.901 mmol) in the presence of 0.4 mL of 10 M KOH at 650 °C for 7 days. The resulting colorless polyhedral crystals were 0.25 mm on any given edge. The resulting crystals gave the false appearance of rhombohedral symmetry via examination with SCXRD. The unit cell symmetry was reduced to monoclinic symmetry where a satisfactory structural solution could be found in space group $P2_1/m$. Unit cell parameters for $K_2HfSi_2O_7$ are presented below in **Table 3.13**.

$K_2HfSi_2O_7$ is based on a pyrosilicate [Si_2O_7] building block and is most structurally similar to $NaBaScSi_2O_7$.[7] The unit cell parameters of $NaBaScSi_2O_7$ are a = 6.957(1) Å, b = 5.626(1) Å, c = 8.819(2) Å with β = 109.33(3)°. The asymmetric unit of $K_2HfSi_2O_7$ consists of K(1), K(2), Hf(1), Si(1), Si(2), O(1), O(2), O(3), O(4), O(5), and O(5a). O(5) and O(5a) are split atoms and each are set to 0.5 occupancy on two general *4f* Wyckoff positions. The pyrosilicate building block [Si_2O_7] contains an internal Si(1)-O(4)-Si(2) angle of 144.6(5)°, similar to that of $NaBaScSi_2O_7$. Hf(1) occupies a six-coordinate environment with Hf(1)-O bond distances ranging from 2.050(7)-2.085(6) Å. The $Hf(1)O_6$ polyhedra are isolated from one another and coordinate six [Si_2O_7] units via corner-sharing of O(1) x2, O(2), O(3), O(5) and O(5a), **Figure 3.24**. $Si(1)O_4$ bond distances range from 1.606(7) to 1.695(10) Å and $Si(2)O_4$ bond distances range from 1.589(6) to 1.612(7) Å. Two [Si_2O_7] units and two $Hf(1)O_6$ in the (-110) plane to form

distorted channels. Potassium ions reside off-center in these channels to complete the solid-state framework and provide the necessary charge balance, **Figure 3.25**. PXRD confirms that this phase can be grown in a phase pure manner, **Figure 3.26**. IR of the hydrothermally-grown powder shows no presence of hydroxide in the material, **Figure 3.27.**

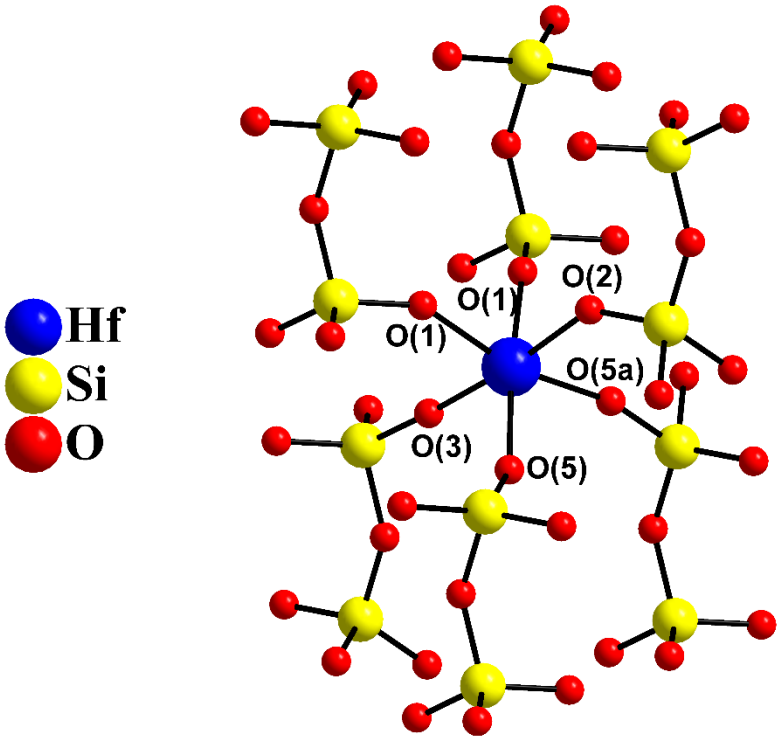

Figure 3.24: $Hf(1)O_6$ polyhedra coordinating six $[Si_2O_7]$ units in $K_2HfSi_2O_7$.

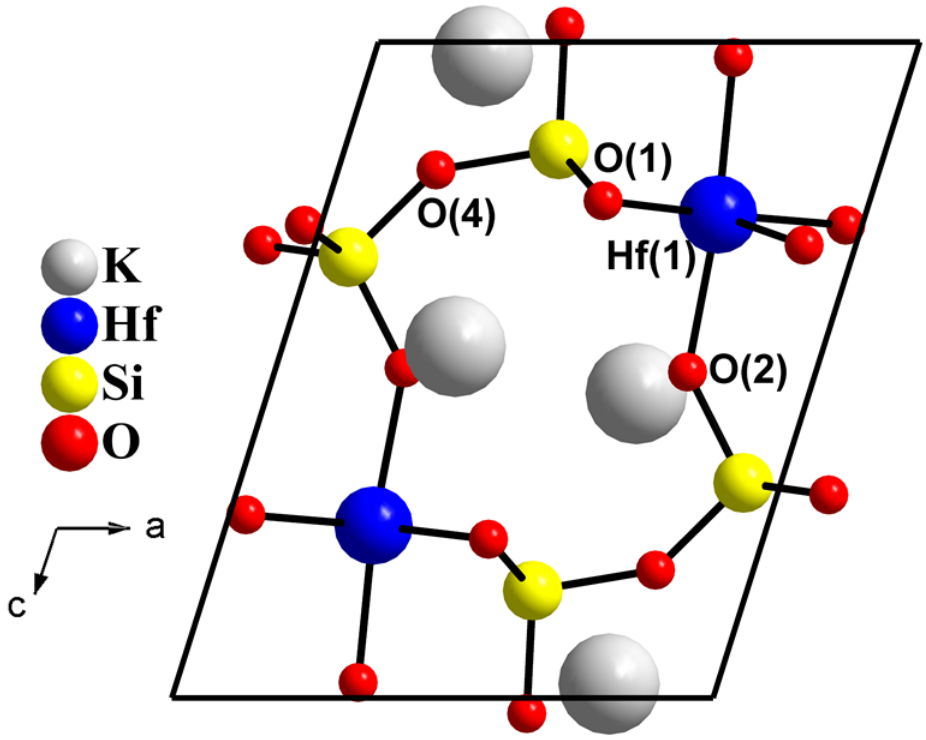

Figure 3.25: Unit cell representation of $K_2HfSi_2O_7$ viewed along the [010] direction.

Table 3.13: Crystallographic parameters for $K_2HfSi_2O_7$.

empirical formula	**K2HfSi2O7**
formula weight (g/mol)	**849.74**
temperature (K)	**293**
crystal system	**monoclinic**
space group	**P21/m**
Unit cell parameters	
a, Å	**7.0172(4)**
b, Å	**5.5193(3)**
c, Å	**8.9373(5)**
β, °	**107.4460(10)**
volume (Å3)	**330.22(3)**
Z, calcd density (µg/m3)	**1, 4.273**
absorption coefficient (mm-1)	**17.411**
F(000)	**388**
Tmax, Tmin	**1.000-0.6437**
Θ range for data	**3.04-26.41**
reflections collected	**13901**
data/restraints/parameters	**743/0/71**
goodness-of-fit on F2	**1.216**
R1, wR2 (I≥ 2σ(I))	**0.0214, 0.0517**
R1, wR2 (all data)	**0.0214, 0.0517**

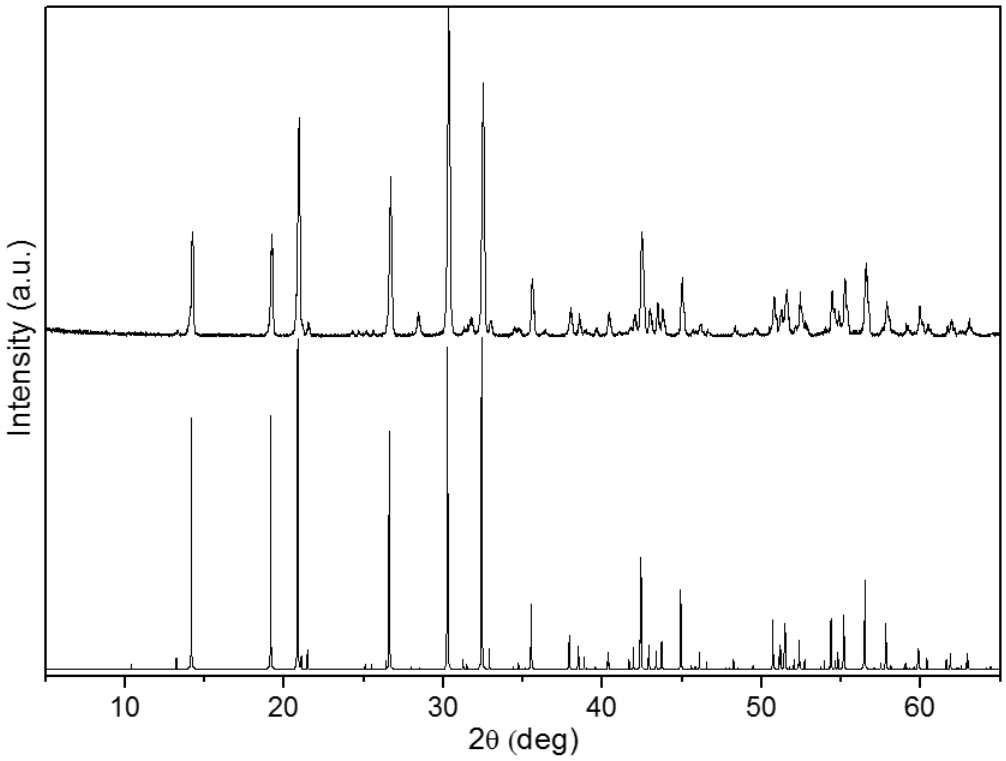

Figure 3.26: (Bottom) Simulated powder pattern of $K_2HfSi_2O_7$ in monoclinic $P2_1/m$.

(Top) Hydrothermally-grown powder of $K_2HfSi_2O_7$.

Conclusions for Hydrothermally Grown Silicates and Select Germanates

A number of new and existing silicates have been synthesized via high-temperature and high-pressure hydrothermal solutions. The Ba-RE-Si exploration led to three primary phases: $Ba_2RE_2Si_4O_{12}$ (RE = La-Er), $Ba_2RE_2Si_4O_{13}$ (monoclinic)(RE = Ho-Sm), and $Ba_2RE_2Si_4O_{13}$ (triclinic) (RE = Nd-La) in the presence of a mixed hydroxide fluoride mineralizer, 6 M KF/ 1 M KOH. In a supplementary investigation of the Sr-RE-Si phase space, a new formation of a cyclosilicate, $KSrRESi_3O_9$ (RE = Yb-Tb) in the presence of the same mixed hydroxide/fluoride mineralizer 6 M KF/ 1 M KOH. In addition to the refractory rare-earth oxides, RE_2O_3 (RE = La-Lu), a number of refractory tetravalent metal oxides were examined under hydrothermal conditions. The oxides of SnO_2, HfO_2, UO_2, ZrO_2 and TiO_2 all show solubility under hydrothermal conditions which led to the investigation of wadeite mineral type $A_2M^{+4}B_3O_9$: $K_2TiSi_3O_9$ $K_2SnSi_3O_9$, $Rb_2USi_3O_9$, $Cs_2HfGe_3O_9$, and $Cs_2ZrGe_3O_9$. These compounds were synthesized under basic mineralizers of 10 M KOH, 6 M RbF/ 1 M KOH or 6 M CsF solutions. In the investigation of these compounds, the crystal structure of a hafnium pyrosilicate, $K_2HfSi_2O_7$, was solved after initial attempts to resolve the crystal structure in rhombohedral symmetry were unsuccessful. A proper assignment of monoclinic symmetry in space group $P2_1/m$ was in good agreement with the as-grown powder. From these results, and the phase spaces observed during the study, a number of conclusions can be drawn.

As initially predicted, the presence of silica, SiO_2, introduces an ideal building block to hydrothermal solutions. Due to the basic mineralizers utilized in this study,

(hydroxides, fluorides, and mixtures therein), SiO_2 can act as a Lewis acid and create diverse chemistry in the presence of refractory oxides. In this Chapter, several different configurations of silicate frameworks have been realized: pyrosilicate Si_2O_7, cyclo-trisilicate Si_3O_9, cyclo-tetrasilicate Si_4O_{12}, and linear Si_4O_{13} chains. The ability to adopt a number of different arrangements increases the likelihood that new and interesting materials can be grown. While SiO_2 is considered a rigid tetravalent tetrahedral molecule, its relatively small crystallographic radius, coupled with high solubility in hydrothermal solutions, had led to an array of new and existing materials.

Second, the presence of a variety of basic hydrothermal mineralizers leads to increased solubility of refractory oxides. In this chapter, hydrothermal temperatures ranging from 650-700 °C were investigated. Investigation of refractory rare-earth and tetravalent oxides well below their reported melting points indicates an important role for hydrothermal mineralizers in the increased solubility of these compounds. For general purposes, it is noteworthy to mention that a mixed hydroxide/fluoride combination results in the best overall solubility. It is believed that the presence of fluoride aids in driving the solubility of refractory oxides into solution, while the presence of hydroxide aids in initializing nucleation of crystals.[51]

Lastly, the success of refractory oxides and silica under hydrothermal solutions will lead to an investigation involving germanium oxide, GeO_2, in the subsequent Chapter.

References

(1) Adachi, G.; Imanaka, N. The Binary Rare Earth Oxides. *Chem. Rev.* **1998**, *98* (4), 1479–1514.

(2) McMillen, C. D.; Mann, M.; Fan, J.; Zhu, L.; Kolis, J. W. Revisiting the Hydrothermal Growth of YAG. *J. Cryst. Growth* **2012**, *356*, 58–64.

(3) Kasamatsu, T.; Sekita, H.; Kuwano, Y. Temperature Dependence and Optimization of 970-Nm Diode-Pumped Yb:YAG and Yb:LuAG Lasers. *Appl. Opt.* **1999**, *38* (24), 5149–5153.

(4) Felsche, J. The Crystal Chemistry of the Rare-Earth Silicates. In *Rare Earths*; Springer: Berlin, Heidelberg, 1973; pp 99–197.

(5) Laudise, R. A. Hydrothermal Synthesis of Single Crystals. *Prog. Inorg. Chem.* **1962**, *3*, 1–47.

(6) Fulle, K.; Sanjeewa, L. D.; McMillen, C.; Kolis, J. W. Crystal Chemistry of the Discrete Tetrasilicate Units with Rare Earth Dimers: $Ba_2RE_2Si_4O_{12}F_2$ (RE = Er-Lu) and $Ba_2RE_2Si_4O_{13}$ (RE = Pr-Sm). *Acta Cryst. B.* **2017**, *73*, 907-915.

(7) Wierzbicka-Wieczorek, M.; Kolitsch, U.; Tillmanns, E. Synthesis and Structural Study of Five New Trisilicates, $BaREE_2Si_3O_{10}$ (REE = Gd, Er, Yb, Sc) and $SrY_2Si_3O_{10}$, Including a Review on the Geometry of the Si_3O_{10} Unit. *Eur. J. Mineral.* **2010**, *22* (2), 245–258.

(8) Wierzbicka-Wieczorek, M.; Kolitsch, U.; Lenz, C.; Giester, G. Structural and Photoluminescence Properties of Doped and REE-Endmember Mixed-Framework Rare-Earth Sorosilicates. *J. Lumin.* **2015**, *168*, 207–217.

(9) Wierzbicka-Wieczorek, M.; Göckeritz, M.; Kolitsch, U.; Lenz, C.; Giester, G. Crystallographic and Spectroscopic Investigations on Nine Metal–Rare-Earth Silicates with the Apatite Structure Type. *Eur. J. Inorg. Chem.* **2015**, *2015* (6), 948–963.

(10) Wierzbicka-Wieczorek, M.; Kolitsch, U.; Tillmanns, E. Ba2Gd2(Si4O13): A Silicate with Finite Si_4O_{13} Chains. *Acta Crystallogr. C* **2010**, *66* (3), i29–i32.

(11) Guo, H.; Zhang, H.; Li, J.; Li, F. Blue-White-Green Tunable Luminescence from $Ba_2Gd_2Si_4O_{13}$:Ce^{3+},Tb^{3+} Phosphors Excited by Ultraviolet Light. *Opt. Express* **2010**, *18* (26), 27257–27262.

(12) Guo, H.; Zhang, H.; Wei, R.; Zheng, M.; Zhang, L. Preparation, Structural and Luminescent Properties of $Ba_2Gd_2Si_4O_{13}:Eu^{3+}$ for White LEDs. *Opt. Express* **2011**, *19* (102), A201–A206.

(13) Zhang, F.; Li, G.; Huang, Y.; Tao, Y. Excitation Wavelength Dependent Luminescence Properties for Eu^{3+}-Activated $Ba_2Gd_2Si_4O_{13}$ Phosphor. *J. Mater. Sci.* **2015**, *50* (13), 4772–4778.

(14) Zhang, F.; Wang, Y.; Tao, Y. VUV Spectroscopic Properties of $Ba_2Gd_2Si_4O_{13}:RE^{3+}$ (RE^{3+}=Ce^{3+}, Tb^{3+}, Dy^{3+}, Eu^{3+}, Sm^{3+}). *Mater. Res. Bull.* **2013**, *48* (5), 1952–1956.

(15) Zhou, H.; Wang, Q.; Jiang, M.; Jiang, X.; Jin, Y. A Novel Green-Emitting Phosphor $Ba_2Gd_2Si_4O_{13}:Eu^{2+}$ for near UV-Pumped Light-Emitting Diodes. *Dalton Trans.* **2015**, *44* (31), 13962–13968.

(16) Werner, F.; Kubel, F. Apatite-Type $Pr_9K(SiO_4)_6O_2$—a Potential Oxide Ion Conductor. *Mater. Lett.* **2005**, *59* (28), 3660–3665.

(17) Janczak, J.; Kubiak, R. Structure of the Cyclic Barium Copper Silicate $Ba_2Cu_2[Si_4O_{12}]$ at 300 K. *Acta Crystallogr. C* **1992**, *48* (1), 8–10.

(18) Crosnier, M. P.; Guyomard, D.; Verbaere, A.; Piffard, Y.; Tournoux, M. The Potassium Niobyl Cyclotetrasilicate $K_2(NbO)_2Si_4O_{12}$. *J. Solid State Chem.* **1992**, *98* (1), 128–132.

(19) Hartenbach, I.; Jagiella, S.; Schleid, T. The lanthanoid(III) Chloride Cyclo-Tetrasilicates $M_6Cl_{10}[Si_4O_{12}]$ (M=Sm, Gd–Dy): Synthesis, Structure and IR Investigations. *J. Solid State Chem.* **2006**, *179* (8), 2258–2264.

(20) Read, C. M.; Smith, M. D.; Withers, R.; zur Loye, H.-C. Flux Crystal Growth and Optical Properties of Two Uranium-Containing Silicates: A_2USiO_6 (A = Cs, Rb). *Inorg. Chem.* **2015**, *54* (9), 4520–4525.

(21) Machida, K.; Adachi, G.; Shiokawa, J.; Shimada, M.; Koizumi, M.; Suito, K.; Onodera, A. High-Pressure Synthesis, Crystal Structures, and Luminescence Properties of Europium (II) Metasilicate and Europium (II)-Activated Calcium and Strontium Metasilicates. *Inorg. Chem.* **1982**, *21* (4), 1512–1519.

(22) Kahlenberg, V.; Manninger, T. $K_9Y_3[Si_{12}O_{32}]F_2$. *Acta Crystallogr. Sect. E Struct. Rep. Online* **2014**, *70* (2), i11–i11.

(23) Schäfer, M. C.; Schleid, T. Synthese Und Kristallstruktur Des Fluorid-Ino-Oxosilicats $Cs_2YFSi_4O_{10}$. *Z. Anorg. Allg. Chem.* **2007**, *633* (7), 1018–1023.

(24) Kahlenberg, V.; Manninger, T. $Rb_2Lu[Si_4O_{10}]F$, a Tubular Chain Silicate. *Acta Crystallogr. Sect. E Struct. Rep. Online* **2014**, *70* (3), i14–i14.

(25) Kolitsch, U.; Tillmanns, E. The Structural Relation between the New Synthetic Silicate $K_2ScFSi_4O_{10}$ and Narsarsukite, $Na_2(Ti, Fe^{3+})(O, F)Si_4O_{10}$. *Eur. J. Mineral.* **2004**, *16* (1), 143–149.

(26) Schafer, M. C.; Schleid, T. $K_5La_4F[SiO_4]_4$: A Fluoride-Poor Quinary Lanthanum Neso-Oxosilicate. *Zeitschrift für anorganische und allgemeine Chemie*. **2010**, *636*(11), 2069.

(27) Mann, J. M.; McMillen, C. D.; Kolis, J. W. Crystal Chemistry of Alkali Thorium Silicates Under Hydrothermal Conditions. *Cryst. Growth Des.* **2015**, *15* (6), 2643–2651.

(28) Merinov, B. V.; Maksimov, B. A.; Ilyukhin, V. V.; Belov, N. V. The Crystal Structure of $NaYSiO_4$ NaF. *Soviet Phys. Dokl.* **1980**; *25*, 874.

(29) Tang, M.-F.; Chiang, P.-Y.; Su, Y.-H.; Jung, Y.-C.; Hou, G.-Y.; Chang, B.-C.; Lii, K.-H. Flux Synthesis, Crystal Structures, and Luminescence Properties of Salt-Inclusion Lanthanide Silicates: $[K_9F_2][Ln_3Si_{12}O_{32}]$ (Ln = Sm, Eu, Gd). *Inorg. Chem.* **2008**, *47* (19), 8985–8989.

(30) Chiang, P.-Y.; Lin, T.-W.; Dai, J.-H.; Chang, B.-C.; Lii, K.-H. Flux Synthesis, Crystal Structure, and Luminescence Properties of a New Europium Fluoride–Silicate: $K_5Eu_2FSi_4O_{13}$. *Inorg. Chem.* **2007**, *46* (9), 3619–3622.

(31) Tamazyan, R. A.; Malinovskij, Y. A. Crystal structure of $Nd_2Ba_2[Si_4O_{13}]$. *Dokl. Akad. Nauk SSSR* **1985**, *285* (1), 124–128.

(32) Jansen, M.; Keller, H.-L. $Ag_{10}Si_4O_{13}$—The First Tetrasilicate. *Angew. Chem. Int. Ed. Engl.* **1979**, *18* (6), 464–464.

(33) Heidebrecht, K.; Jansen, M. $Ag_{18}(SiO_4)_2(Si_4O_{13})$, Das Erste Silbersilicat Mit Gemischten Anionen. *Z. Anorg. Allg. Chem.* **1991**, *597* (1), 79–86.

(34) Maksimov, B. A.; Mel'nikov, O. K.; Zhdanova, T. A.; Ilyukhin, V. V.; Belov, N. V. Crystal structure of $Na_4Sc_2Si_4O_{13}$. *Dokl. Akad. Nauk SSSR* **1980**, *251* (1), 98–102.

(35) Siidra, O. I.; Zenko, D. S.; Krivovichev, S. V. Structural complexity of lead silicates: Crystal structure of $Pb_{21}[Si_7O_{22}]_2[Si_4O_{13}]$ and its comparison to hyttsjöite. *Am. Mineral* **2014**, *99*, 817-823.

(36) Malinovskii, I.; Baturin, S. V.; Bondareva, O. S. A New Insular Silicate Radical [SI_4O_{13}] in the Structure of $NaBa_3Nd_3$ [$SI_2O_7Si_4O_{13}$]. *Dokl. Akad. NAUK SSSR*, **1983**, *272* (4), 865–869.

(37) Sanjeewa, L. D.; Fulle, K.; McMillen, C. D.; Wang, F.; Liu, Y.; He, J.; Anker, J. N.; Kolis, J. W. Hydrothermal Synthesis, Structure, and Property Characterization of Rare Earth Silicate Compounds: $NaBa_3Ln_3Si_6O_{20}$ (Ln=Y, Nd, Sm, Eu, Gd). *Solid State Sci.* **2015**, *48*, 256–262.

(38) Heyward, C. C.; McMillen, C. D.; Kolis, J. W. Hydrothermal Growth of Lanthanide Borosilicates: A Useful Approach to New Acentric Crystals Including a Derivative of Cappelenite. *Inorg. Chem.* **2015**, *54* (3), 905–913.

(39) Müller—Bunz, H.; Schleid, T. $La_2Si_2O_7$ Im I—Typ: Gemäß $La_6[Si_4O_{13}][SiO_4]_2$ kein Echtes Lanthandisilicat. *Z. Anorg. Allg. Chem.* **2002**, *628* (3), 564–569.

(40) Haile, S. M.; Maier, J.; Wuensch, B. J.; Laudise, R. A. Structure of $Na_3YSi_6O_{15}$ – a Unique Silicate Based on Discrete Si_6O_{15} Units, and a Possible Fast-Ion Conductor. *Acta Crystallogr. B* **1995**, *51* (5), 673–680.

(41) Haile, S. M.; Wuensch, B. J.; Laudise, R. A. Hydrothermal Synthesis of New Alkali Silicates II. Sodium Neodymium and Sodium Yttrium Phases. *J. Cryst. Growth* **1993**, *131* (3), 373–386.

(42) Haile, S. M.; Wuensch, B. J.; Siegrist, T.; Laudise, R. A. Hydrothermal Synthesis of New Alkali Silicates I. Potassium Neodymium Phases. *J. Cryst. Growth* **1993**, *131* (3), 352–372.

(43) Wierzbicka-Wieczorek, M.; Kolitsch, U.; Panczer, G.; Giester, G.; Chanmuang, C.; Grzechnik, A. Crystal Structures and Photoluminescence Properties of Two Novel Sorosilicates with an Unprecedented Ratio of Di- and Trisilicate Groups: $Ba_2Ho_{10}(Si_2O_7)_3(Si_3O_{10})_2$ and Isotypic $Ba_2Er_{10}(Si_2O_7)_3(Si_3O_{10})_2$. *J. Solid State Chem.* **2017**, *252*, 33–42.

(44) Wierzbicka-Wieczorek, M.; Kolitsch, U.; Tillmanns, E. Synthesis and Structural Study of Five New Trisilicates, $BaREE_2Si_3O_{10}$ (REE = Gd, Er, Yb, Sc) and $SrY_2Si_3O_{10}$, Including a Review on the Geometry of the Si_3O_{10} Unit. *Eur. J. Mineral.* **2010**, *22* (2), 245–258.

(45) Orlando, A.; Thibault, Y.; Edgar, A. D. Experimental Study of the $K_2ZrSi_3O_9$ (wadeite)–$K_2TiSi_3O_9$ and $K_2(Zr,Ti)Si_3O_9$–phlogopite Systems at 2–3 GPa. *Contrib. Mineral. Petrol.* **2000**, *139* (2), 136–145.

(46) Fisher, K. Crystal Structure Determination of Benitoite $BaTi(Si_3O_9)$. *Z Kristallogr*. **1969**, *129*, 222–243.

(47) Schneider, S. J. Compilation of the Melting Points of the Metal Oxides https://digital.library.unt.edu/ark:/67531/metadc70451/ (accessed Sep 1, 2017).

(48) Henshaw, D. E. The Structure of Wadeite. *Mineral. Mag*. **1955**, *30* (228), 585–595.

(49) Swanson, D. K.; Prewitt, C. T. The Crystal Structure of $K_2SVISi_3IVO_9$. *Am. Mineral*. **1983**, *68* (5–6), 581–585.

(50) Choisnet, J.; Deschanvres, A.; Raveau, B. Evolution Structurale de Nouveaux Germanates et Silicates de Type Wadéïte et de Structure Apparentée. *J. Solid State Chem*. **1973**, *7* (4), 408–417.

(51) D. McMillen, C.; W. Kolis, J. Hydrothermal Synthesis as a Route to Mineralogically-Inspired Structures. *Dalton Trans*. **2016**, *45* (7), 2772–2784.

CHAPTER FOUR

HYDROTHERMAL GROWTH OF RARE-EARTH GERMANATES

Introduction

This Chapter centers on a unique investigation of rare-earth germanates with interesting oxidative states and structural properties. "Some content of this Chapter is used as a reprint (adapted) from permission from Fulle, K.; Sanjeewa, L. D.; McMillen, C. D., Wen, Y., Rajamanthrilage, A. C., Anker, J. N., Chumanov, G., Kolis, J. W. One-Pot Hydrothermal Synthesis of $Tb^{III}_{13}Ge_6O_{31}(OH)$ and $K_2Tb^{IV}Ge_2O_7$: Preparation of a Stable Terbium(4+) Complex. *Inorg. Chem.* **2017**, *56*, 6044-6047.[1] Copyright 2017 American Chemical Society." A duplicate of the copyright permission is located in Appendix.

The rare-earth germanates are a structurally rich class of solids that have several potential applications.[2,3] They can find use as hosts for luminescence or lasing, or act as models for long-term nuclear waste storage. They tend to be dense and have high refractive indices. Germanium oxide, GeO_2, can be viewed as a slightly larger tetravalent ion (0.53 Å) compared to Si^{4+}, which have the capability to act as a Lewis acid in the presence of concentrated basic hydroxide and fluoride mineralizers under hydrothermal conditions. Unlike silica, germanium oxide has a less predictable geometry that can adapt 4-, 5-, and 6-coordinate geometries. The germanates most obviously stand in direct

comparison to the metal silicates. They have not been studied nearly as intensely as the metal silicates,[4,5] but they do display a very rich chemistry that often is unique to themselves. One important structural aspect of metal germanate chemistry is that germanates sometimes adopt higher coordination numbers.[6,7] This contrasts with silicates, which only adopt octahedral coordination at extremely high-pressures.[8] As such, the octahedral metal germanates may act as surrogate models for deep earth silicate structures.[9]

Although metal germanates have been isolated from melts and fluxes,[10-13] like the silicates, the melts tend to be somewhat viscous, so hydrothermal growth has been explored as a potentially attractive alternative route to single crystals.[14] The advantages of the hydrothermal method in metal germanate crystal growth have been discussed thoroughly,[3] and the method is sensitive to reaction conditions and has a rich structural chemistry.[15] Previously our group developed a convenient high-temperature hydrothermal route to a variety of both transition metal and rare-earth germanates.[16-19] Most earlier work focused on reactions performed at somewhat lower temperatures (ca. 500 ˚C) and more modest mineralizer concentrations. In our more recent work, observations centered on the fact that at higher temperatures (650-700 ˚C) the chemistry changes considerably, while increasing the OH^- mineralizer concentration to high values such as 10-20 *M* induces growth of high quality single crystals of large size. Now a systematic examination of the reaction of the rare-earth ions with germanates in high concentrations of aqueous base at high-temperatures and pressure (650-700 ˚C/200 MPa).

Despite the emergence of germanate crystals $Bi_4Ge_3O_{12}$ (BGO) and $BiY_{1-x}RE_xGeO_5$ (RE = Eu^{3+}) as potential scintillators and emitters some years ago, investigation of rare-earth (RE = La-Lu, Y) germanates has not received as much attention as rare-earth silicates.[20,21] It should be noted however, that a number of interesting new alkali rare-earth germanates, including but not limited to $NaEu_3(GeO_4)_2(OH)_2$, $NaREGeO_4$ (RE = Sm-Lu), $KLa_9(GeO_4)_6O_2$, $Na_5RE_4F(GeO_4)_4$ (RE = Pr, Nd), $Na_5Nd_4Ge_4O_{16}(OH)$, $Na_2NdGeO_4(OH)$, $K_2TbGe_2O_7$, $KEuGe_2O_6$, and $Na_3ErSi_3O_9$ have been prepared recently by solid-state and hydrothermal techniques.[22–31] In general, the differences in structural chemistry between the silicates and germanates can be significant, certainly different enough to justify a detailed comparative study of their respective chemistries.[32]

Of the reported alkaline rare-earth germanates, $Ca_2Gd_2Ge_2O_9$, $Ca_3RE_2Ge_3O_{12}$ (RE = Pr^{3+}-Gd^{3+}, Dy^{3+}), $CaEu_2Ge_3O_{10}$, $CaRE_2Ge_4O_{12}$ (RE = Eu^{3+}-Lu^{3+}), $MgLa_2GeO_6$, $Be_2RE_2GeO_7$ (RE = La^{3+}-Er^{3+}) and well-studied rare-earth oxy-apatites, no synthetic details of barium rare-earth germanate oxides or oxy-hydroxides have been reported to date, to our knowledge.[25,33–39] The optical properties of the rare-earth germanates are of particular interest. For example, the 1.54 μm luminescence of Er^{3+} ($4f^{11}$) from spin-orbit levels $^4I_{13/2}\rightarrow{}^4I_{15/2}$ is well sought for eye-safe emission.[40] Additionally, upconversion of Ho^{3+} ($4f^{10}$) in transparent glass ceramics have been linked to transitions from spin-orbit levels $^5F_5\rightarrow{}^5I_8$ which are viable alternatives for production of red emission (650 nm) in solid-state displays.[41] These optically active ions have been co-doped into bismuth germanate glasses to allow energy transfer from Er^{3+} $^4I_{13/2}$ state to Ho^{3+} $^5I_7$ state for

subsequent emission of 2 μm lasing in the eye-safe region.[42] Typically, these samples are prepared by conventional solid-state techniques in the form of powders. For detailed studies and optimized performance, it is often desirable to prepare the materials has high quality single crystals. As such, it is be desirable to undertake a systematic effort to develop a reliable route to single crystals of rare-earth germanates. For the most part metal germanate single crystals have been synthesized using either a flux growth or a hydrothermal method similar to the growth of rare-earth silicates. The hydrothermal technique is a particularly attractive method for the examination of germanates because amphoteric oxides tend to grow well in the presence of basic mineralizers. In a previous study, a systematic study of rare-earth and refractory oxide silicates has paid dividends and that mentality is being extended into the germanates.

In this first section, a description of the use of a high-temperature hydrothermal growth method to prepare single crystals of the first in a series of several new rare-earth germanates is reported. The investigation centers on holmium and erbium as the initial rare-earth ions because of their interesting optical activity. The introduction of barium ions in the reaction was also included to ascertain the role of counterions in new phases. The presence of an innocent divalent ion performs several functions. It provides a divalent prototype ion that may be systematically replaced with other divalent ions of different size to expand the structural possibilities of this class of new phases. The ions can also be subsequently replaced with a more active metal such as a divalent first row transition metal with different magnetic and optical properties. Herein, a report of the hydrothermal crystal growth, crystal structure, and supporting characterization of two

new rare-earth germanate phases, $BaREGeO_4(OH)$ and $BaRE_{10}(GeO_4)_4O_8$ ($RE=Ho^{3+}$-Er^{3+}), both of which display interesting new layered structure types, is given.

Experimental Methods for Barium Rare-Earth Germanates

The title compounds $BaREGeO_4(OH)$ and $BaRE_{10}(GeO_4)_4O_8$ ($RE=Ho^{3+}$-Er^{3+}) were prepared through direct reaction of BaO, RE_2O_3 and GeO_2 powders via high-temperature and high-pressure hydrothermal synthesis. As a typical example, $BaHoGeO_4(OH)$ and $BaHo_{10}(GeO_4)_4O_8$ were prepared by combining BaO (36 mg, 233 mmol; Alfa Aesar, 99.0%), Ho_2O_3 (74 mg, 195 mmol; HEFA Rare Earth, 99.99%) and GeO_2 (41 mg, 389 mmol; Alfa Aesar, 99.9%) in a 3:2.5:5 ratio, respectively. The starting materials were reacted isothermally at 650 °C for 7 days in welded silver (99.9%) (1/4" x 2.5") ampoules loaded into a Tuttle cold seal autoclave constructed from Inconel 718 material. The ampoules were loaded with the appropriate component oxide feedstock and weld sealed from both ends after addition of 0.4 mL of 6 *M* CsOH as a mineralizer. Upon completion of reaction, the silver ampoules were opened and washed with DI water. In each reaction, $BaREGeO_4(OH)$, $BaRE_{10}(GeO_4)_4O_8$ crystals constituted an approximate 5/95 ratio of products, respectively. Single crystals of $BaREGeO_4(OH)$ were produced as polyhedral crystals approximately 0.25-0.45 mm in size and were distinguished by SCXRD unit cell determinations. The compound $BaRE_{10}(GeO_4)_4O_8$ constituted the majority crystalline product and was identified as thick hexagonal plate crystals, with some striations on the surface, ranging from 0.15-0.35 mm in size, **Figure 4.1**.

Table 4.1: Crystallographic data of rare-earth germanates and germanate hydroxides determined by single crystal X-ray diffraction.

empirical formula	**$BaHo_{10}(GeO_4)_4O_8$**	**$BaEr_{10}(GeO_4)_4O_8$**	**$BaHoGeO_4(OH)$**	**$BaErGeO_4(OH)$**
formula weight (g/mol)	2461.00	2484.30	455.87	458.20
crystal system	monoclinic	monoclinic	orthorhombic	orthorhombic
space group, *Z*	*C2/m* (no.12), *2*	*C2/m* (no.12), *2*	*Pbca* (no.61), *8*	*Pbca* (no.61*), 8*
temperature, K	298(2)	298(2)	298(2)	298(2)
crystal size (mm)	0.08 x 0.1 x 0.1	0.07 x 0.07 x 0.07	0.02 x 0.05 x 0.07	0.08 x 0.08 x 0.09
a, Å	12.4972(5)	12.4533(8)	5.7175(2)	5.7100(2)
b, Å	7.2444(3)	7.2008(5)	10.1556(5)	10.1511(5)
c, Å	12.0170(5)	12.0034(8)	16.6189(9)	16.5766(8)
β, °	100.249(2)	100.183(2)	---	---
volume, $Å^3$	1070.60(8)	1059.43(12)	964.97(8)	960.83(7)
calculated density ($\mu g/m^3$)	7.634	7.788	6.276	6.335
absorption coefficient (mm^{-1})	43.891	46.619	30.420	31.550
F(000)	2092	2112	1568	1576
Tmax, Tmin	0.2642, 1.0000	0.2191, 1.000	0.6135, 1.000	0.5321, 1.0000
Θ range for data	3.26-30.58	3.28-28.29	4.01-26.50	4.02-26.49
reflections collected	2443	1790	7359	8926
data/restraints/parameters	2443/6/107	1790/12/107	1002/1/77	993/1/77
final R [$I > 2\sigma(I)$] R1, wR2	0.0362, 0.0785	0.0440, 0.1184	0.0213, 0.0382	0.0161, 0.0316
final R (all data) R1, wR2	0.0425, 0.0810	0.0483, 0.1216	0.0296, 0.0404	0.0195, 0.0325
goodness-of-fit on F^2	1.131	1.087	1.102	1.196
largest diff. peak/hole, e/ $Å^3$	3.831, -2.448	3.605, -2.855	0.893, -1.076	0.628, -1.073

Table 4.2: Bond distances for $BaHoGeO_4(OH)$ and $BaErGeO_4(OH)$.

$BaHoGeO_4(OH)$		**$BaErGeO_4(OH)$**	
$Ho(1)O_7$		**$Er(1)O_7$**	
Ho(1)−O(1)	2.290(4)	Er(1)−O(1)	2.285(3)
Ho(1)−O(2)	2.388(4)	Er(1)−O(2)	2.376(3)
Ho(1)−O(3)	2.286(4)	Er(1)−O(3)	2.274(3)
Ho(1)−O(4)	2.262(4)	Er(1)−O(4)	2.254(3)
Ho(1)−O(4)	2.433(4)	Er(1)−O(4)	2.422(3)
Ho(1)−O(5)	2.291(4)	Er(1)−O(5)	2.287(3)
Ho(1)−O(5)	2.356(4)	Er(1)−O(5)	2.338(3)
$Ba(1)O_{10}$		**$Ba(1)O_{10}$**	
Ba(1)−O(1)	2.822(4)	Ba(1)−O(1)	2.818(3)
Ba(1)−O(1)	3.039(4)	Ba(1)−O(1)	3.036(3)
Ba(1)−O(1)	3.077(4)	Ba(1)−O(1)	3.082(3)
Ba(1)−O(2)	2.579(4)	Ba(1)−O(2)	2.580(3)
Ba(1)−O(2)	2.969(4)	Ba(1)−O(2)	2.962(3)
Ba(1)−O(2)	3.041(4)	Ba(1)−O(2)	3.042(3)
Ba(1)−O(3)	2.857(4)	Ba(1)−O(3)	2.857(3)
Ba(1)−O(3)	2.992(4)	Ba(1)−O(3)	2.988(3)
Ba(1)−O(3)	3.241(4)	Ba(1)−O(3)	3.230(3)
Ba(1)−O(5)	2.791(4)	Ba(1)−O(5)	2.793(3)
$Ge(1)O_4$		**$Ge(1)O_4$**	
Ge(1)−O(1)	1.751(4)	Ge(1)−O(1)	1.748(3)
Ge(1)−O(2)	1.754(4)	Ge(1)−O(2)	1.758(3)
Ge(1)−O(3)	1.742(4)	Ge(1)−O(3)	1.749(3)
Ge(1)−O(4)	1.771(4)	Ge(1)−O(4)	1.771(3)

Table 4.3: Bond distances for $BaHo_{10}(GeO_4)_4O_8$ and $BaEr_{10}(GeO_4)_4O_8$,

$BaHo_{10}(GeO_4)_4O_8$		**$BaEr_{10}(GeO_4)_4O_8$**	
$Ho(1)O_7$		**$Er(1)O_7$**	
Ho(1)−O(3) x 2	2.366(7)	Er(1)−O(3) x 2	2.343(17)
Ho(1)−O(4)	2.224(10)	Er (1)−O(4)	2.184(15)
Ho(1)−O(5)	2.196(10)	Er (1)−O(5)	2.16(2)
Ho(1)−O(6)	2.377(10)	Er (1)−O(6)	2.35(2)
Ho(1)−O(7) x 2	2.425(7)	Er (1)−O(7) x 2	2.437(17)
$Ho(2)O_7$		**$Er(2)O_7$**	
Ho(2)−O(2) x 2	2.313(6)	Er(2)−O(2) x 2	2.290(15)
Ho(2)−O(2) x 2	2.410(7)	Er(2)−O(2) x 2	2.413(15)
Ho(2)−O(4)	2.350(10)	Er(2)−O(4)	2.33(2)
Ho(2)−O(5)	2.254(9)	Er(2)−O(5)	2.276(14)
Ho(2)−O(9)	2.341(10)	Er(2)−O(9)	2.35(3)
$Ho(3)O_7$		**$Er(3)O_7$**	
Ho(3)−O(1)	2.333(6)	E(1)−O(1)	2.310(12)
Ho(3)−O(2)	2.253(6)	Er(3)−O(2)	2.259(12)
Ho(3)−O(3)	2.352(7)	Er(3)−O(3)	2.328(14)
Ho(3)−O(5)	2.187(5)	Er(3)−O(5)	2.178(11)
Ho(3)−O(6)	2.428(6)	Er(3)−O(6)	2.421(13)
Ho(3)−O(7)	2.475(7)	Er(3)−O(7)	2.503(14)
Ho(3)−O(8)	2.490(7)	Er(3)−O(8)	2.472(12)
$Ho(4)O_6$		**$Er(4)O_6$**	
Ho(4)−O(2) x 2	2.285(7)	Er(4)−O(2) x 2	2.266(14)
Ho(4)−O(4) x 2	2.220(6)	Er(4)−O(4) x 2	2.231(13)
Ho(4)−O(9) x 2	2.367(6)	Er(4)−O(9) x 2	2.344(16)
$Ba(1)O_8$		**$Ba(1)O_8$**	
Ba(1)−O(1) x 2	3.201(10)	Ba(1)−O(1) x 2	3.191(17)
Ba(1)−O(7) x 4	2.797(7)	Ba(1)−O(7) x 4	2.739(13)
Ba(1)−O(8) x 2	2.778(9)	Ba(1)−O(8) x 2	2.767(17)
$Ge(1)O_4$		**$Ge(1)O_4$**	
Ge(1)−O(1)	1.734(9)	Ge(1)−O(1)	1.757(19)
Ge(1)−O(3) x 2	1.744(7)	Ge(1)−O(3) x 2	1.750(14)
Ge(1)−O(9)	1.740(9)	Ge(1)−O(9)	1.740(15)
$Ge(2)O_4$		**$Ge(2)O_4$**	
Ge(2)−O(6)	1.751(9)	Ge(2)−O(6)	1.761(15)
Ge(2)−O(7) x 2	1.741(7)	Ge(2)−O(7) x 2	1.766(12)
Ge(2)−O(8)	1.748(9)	Ge(2)−O(8)	1.760(17)

Table 4.4: Bond valence sum calculations for $BaHoGeO_4(OH)$ and $BaErGeO_4(OH)$.

$BaHoGeO_4(OH)$		**$BaErGeO_4(OH)$**	
$Ho(1)O_7$	**Σ3.10**	**$Er(1)O_7$**	**Σ3.10**
Ho(1)−O(1)	0.486	Er(1)−O(1)	0.476
Ho(1)−O(2)	0.373	Er(1)−O(2)	0.372
Ho(1)−O(3)	0.491	Er(1)−O(3)	0.490
Ho(1)−O(4)	0.524	Er(1)−O(4)	0.517
Ho(1)−O(4)	0.330	Er(1)−O(4)	0.328
Ho(1)−O(5)	0.485	Er(1)−O(5)	0.473
Ho(1)−O(5)	0.407	Er(1)−O(5)	0.412
$Ba(1)O_{10}$	**Σ1.94**	**$Ba(1)O_{10}$**	**Σ1.94**
Ba(1)−O(1)	0.237	Ba(1)−O(1)	0.240
Ba(1)−O(1)	0.132	Ba(1)−O(1)	0.133
Ba(1)−O(1)	0.119	Ba(1)−O(1)	0.118
Ba(1)−O(2)	0.458	Ba(1)−O(2)	0.457
Ba(1)−O(2)	0.160	Ba(1)−O(2)	0.163
Ba(1)−O(2)	0.131	Ba(1)−O(2)	0.131
Ba(1)−O(3)	0.216	Ba(1)−O(3)	0.216
Ba(1)−O(3)	0.150	Ba(1)−O(3)	0.152
Ba(1)−O(3)	0.077	Ba(1)−O(3)	0.079
Ba(1)−O(5)	0.258	Ba(1)−O(5)	0.257
$Ge(1)O_4$	**Σ3.93**	**$Ge(1)O_4$**	**Σ3.91**
Ge(1)−O(1)	0.992	Ge(1)−O(1)	1.000
Ge(1)−O(2)	0.984	Ge(1)−O(2)	0.973
Ge(1)−O(3)	1.016	Ge(1)−O(3)	0.997
Ge(1)−O(4)	0.940	Ge(1)−O(4	0.940

Table 4.5: Bond valence sum calculations for $BaHo_{10}(GeO_4)_4O_8$ and $BaEr_{10}(GeO_4)_4O_8$.

$BaHo_{10}(GeO_4)_4O_8$		**$BaEr_{10}(GeO_4)_4O_8$**	
$Ho(1)O_7$	**Σ3.06**	**$Er(1)O_7$**	**Σ3.13**
Ho(1)−O(3) x 2	0.791	Er(1)−O(3) x 2	0.813
Ho(1)−O(4)	0.581	Er (1)−O(4)	0.625
Ho(1)−O(5)	0.627	Er (1)−O(5)	0.667
Ho(1)−O(6)	0.384	Er (1)−O(6)	0.399
Ho(1)−O(7) x 2	0.675	Er (1)−O(7) x 2	0.631
$Ho(2)O_7$	**Σ2.99**	**$Er(2)O_7$**	**Σ2.92**
Ho(2)−O(2) x 2	0.913	Er(2)−O(2) x 2	0.938
Ho(2)−O(2) x 2	0.703	Er(2)−O(2) x 2	0.673
Ho(2)−O(4)	0.413	Er(2)−O(4)	0.421
Ho(2)−O(5)	0.536	Er(2)−O(5)	0.487
Ho(2)−O(9)	0.423	Er(2)−O(9)	0.399
$Ho(3)O_7$	**Σ2.94**	**$Er(3)O_7$**	**Σ2.89**
Ho(3)−O(1)	0.433	E(1)−O(1)	0.444
Ho(3)−O(2)	0.537	Er(3)−O(2)	0.510
Ho(3)−O(3)	0.411	Er(3)−O(3)	0.423
Ho(3)−O(5)	0.642	Er(3)−O(5)	0.635
Ho(3)−O(6)	0.335	Er(3)−O(6)	0.329
Ho(3)−O(7)	0.295	Er(3)−O(7)	0.264
Ho(3)−O(8)	0.283	Er(3)−O(8)	0.287
$Ho(4)O_6$	**Σ2.95**	**$Er(4)O_6$**	**Σ2.91**
Ho(4)−O(2) x 2	0.985	Er(4)−O(2) x 2	1.001
Ho(4)−O(4) x 2	1.174	Er(4)−O(4) x 2	1.101
Ho(4)−O(9) x 2	0.789	Er(4)−O(9) x 2	0.811
$Ba(1)O_8$	**Σ1.72**	**$Ba(1)O_8$**	**Σ1.91**
Ba(1)−O(1) x 2	0.171	Ba(1)−O(1) x 2	0.175
Ba(1)−O(7) x 4	1.016	Ba(1)−O(7) x 4	1.189
Ba(1)−O(8) x 2	0.535	Ba(1)−O(8) x 2	0.551
$Ge(1)O_4$	**Σ4.08**	**$Ge(1)O_4$**	**Σ3.99**
Ge(1)−O(1)	1.039	Ge(1)−O(1)	0.976
Ge(1)−O(3) x 2	2.022	Ge(1)−O(3) x 2	1.989
Ge(1)−O(9)	1.022	Ge(1)−O(9)	1.022
$Ge(2)O_4$	**Σ4.03**	**$Ge(2)O_4$**	**Σ3.84**
Ge(2)−O(6)	0.992	Ge(2)−O(6)	0.965
Ge(2)−O(7) x 2	2.038	Ge(2)−O(7) x 2	1.905
Ge(2)−O(8)	1.000	Ge(2)−O(8)	0.968

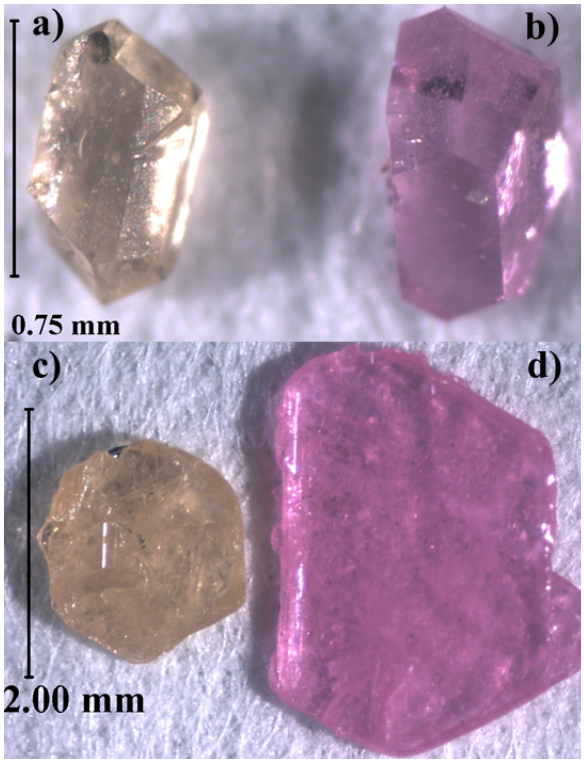

Figure 4.1: Sample growth of new barium rare-earth germanate oxides and oxy-hydroxides. a) $BaHoGeO_4(OH)$, b) $BaErGeO_4(OH)$, c) $BaHo_{10}(GeO_4)_4O_8$, and d) $BaEr_{10}(GeO_4)_4O_8$ single crystals.

Crystal Structure of $BaREGeO_4(OH)$ ($RE=Ho^{3+}$-Er^{3+})

The $BaREGeO_4(OH)$ ($RE = Ho^{3+}$-Er^{3+}) compounds in the current study crystallize in the orthorhombic space group *Pbca* (No. 61). The two compounds are isostructural, with the Er^{3+} analog exhibiting slightly contracted cell parameters compared to Ho^{3+}, **Table 4.1**. $BaHoGeO_4(OH)$ is used as a representative of the family with cell parameters of a = 5.7175(2) Å, b = 10.1556(5) Å, c = 10.6189(9) Å and V = 964.97(8) $Å^3$. Bond distances for $BaHoGeO_4(OH)$ and $BaErGeO_4(OH)$ are reported in **Table 4.2**, with bond valence sums for metal oxide coordination in **Table 4.4**. The structure is based on seven-coordinate HoO_7, BaO_{10} and isolated GeO_4 tetrahedra, **Figure 4.2**. All atoms reside on general crystallographic positions with *8c* Wyckoff symmetry. As seen in **Figure 4.2**, infinite zigzag chains of HoO_7 polyhedra run parallel to the *a*-axis via edge sharing of O(4) and O(5) atoms and are the key structural component to the framework. Each GeO_4 unit coordinates four HoO_7 polyhedra via corner-sharing of O(1) and O(3), and edge-sharing of O(2) and O(4) oxygen atoms, and each HoO_7 polyhedra likewise coordinates four GeO_4 units to form a three-dimensional framework **Figure 4.3**.

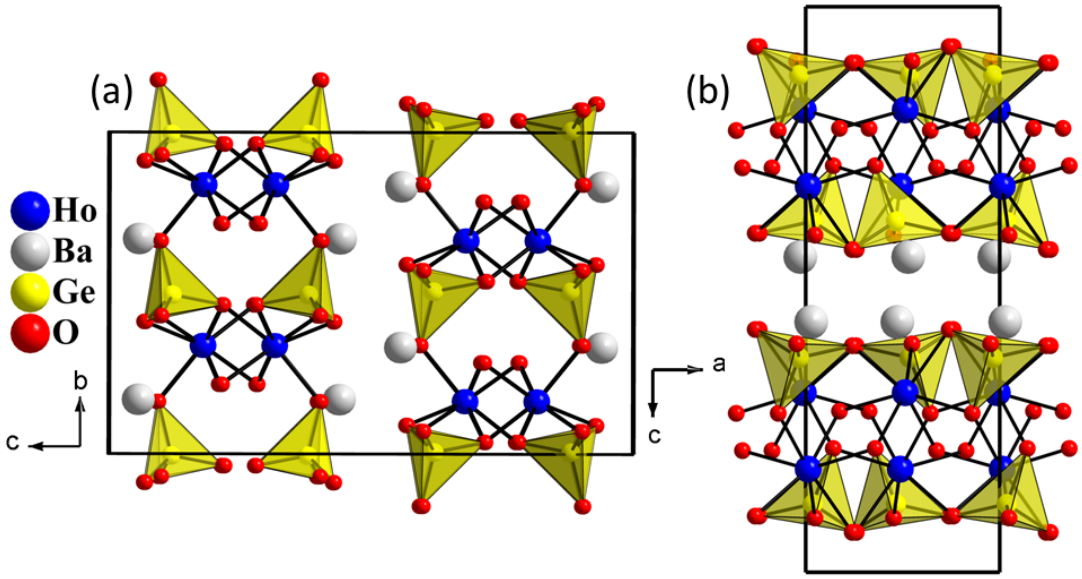

Figure 4.2: a) Isolated GeO_4 units connect holmium polyhedra in the (001) plane with barium atoms residing between layers. **b)** Holmium oxide polyhedra extending along the [100] direction through edge sharing of oxygen atoms to form a one-dimensional rare-earth oxide chain.

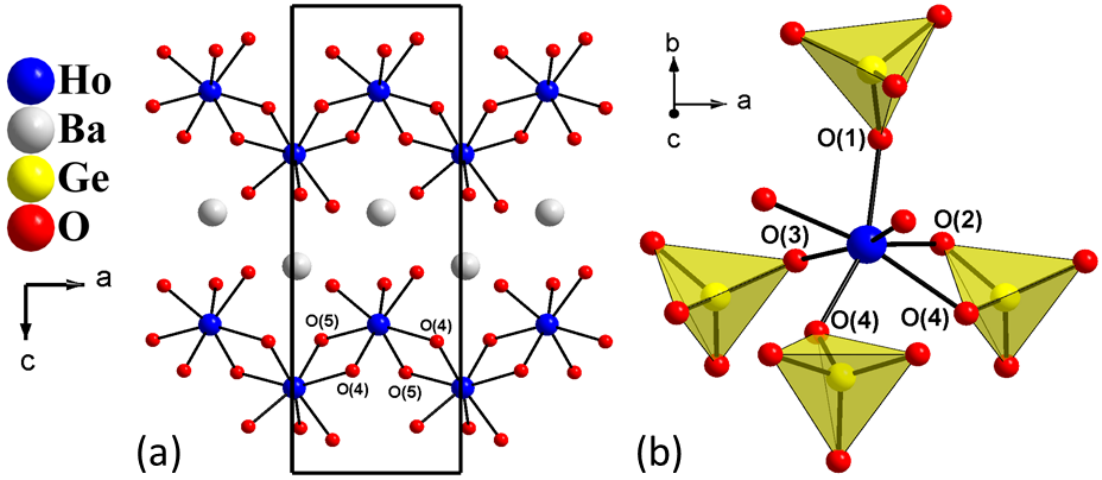

Figure 4.3: **a)** Ho(1)O_7 polyhedra forming infinite chains separated by interstitial barium atoms and connected via edge-sharing of O(4) and O(5) oxygen atoms in the (010) plane. **b)** Each Ho(1)O_7 polyhedra coordinates four GeO_4 units through corner-sharing of O(1), O(3), O(4), and edge-sharing of O(2)/O(4) oxygen atoms, shown just off [001] direction.

This framework forms alternating layers of HoO_7 polyhedra and GeO_4 units. Additionally, GeO_4 units orient relative to the *b*-axis in an alternating fashion as is visible in **Figure 4.2**. Thus, this layered framework is built up by the corner and edge-shared HoO_7 and GeO_4 polyhedra, between which the barium atoms reside to maintain charge balances. The HoO_7 polyhedra form distorted trigonal prismatic, square-face mono-capped geometry with Ho-O bond distances ranging from 2.262(4)—2.433(4) Å with an average of 2.33 Å. GeO_4 tetrahedra exhibit bond distances ranging from 1.742(4)—1.771(4) Å with an average distance of 1.75 Å. The existence of barium atoms in the framework creates an intricate three-dimensional network. The barium atoms exist as irregular polyhedra with Ba—O distances between 2.579(4)—3.241(4) Å and averaging 2.94 Å. Bond valence sum calculations resulted in values of 1.94, 3.10, and 3.93 for Ba^{2+}, Ho^{3+}, and Ge^{+4}, respectively, consistent with the assigned oxidation states.[43,44] Oxygen atom O(5) is suspected as the hydroxide by bond valence sum considerations and O(5) being the only non-bonding germanium oxygen. Bond valence sum of the O(5) atom is 1.15, and other oxygen atoms exhibit values of 1.79—2.11, supporting the assignment of OH^- and O^{2-}, respectively **Table 4.4**. The hydroxide group points generally toward the vacancy formed between germanate and holmium polyhedra. The presence of hydroxide is supported by IR and Raman of $BaHoGeO_4(OH)$ and $BaErGeO_4(OH)$ with single crystal Raman indicating a strong stretching mode at 3420 cm^{-1} for $BaHoGeO_4(OH)$, (**Figure 4.7 and/or Figure 4.17**). Semi-quantitative elemental analysis (EDX) was used to support the 1:1:1 ratio of metals and supports the assignment of Ba^{2+} over Cs^+ in the framework, with no evidence of a mixed metal site, (**Figure 4.4).**

The formula of this new barium rare-earth oxy-hydroxides discussed herein are somewhat reminiscent of the sodium rare-earth germanate species $Na_2NdGeO_4(OH)$, synthesized by mild hydro-flux of sodium hydroxide.[27] Both structures exhibit one-dimensional zigzag chains of rare-earth polyhedra. However, these structures are not isostructural as $Na_2NdGeO_4(OH)$ chains interconnect via corner sharing of O(4) atoms forming an intricate rare-earth framework, while $BaREGeO_4(OH)$ exhibits truly isolated one-dimensional chains interconnected through isolated GeO_4 building blocks.

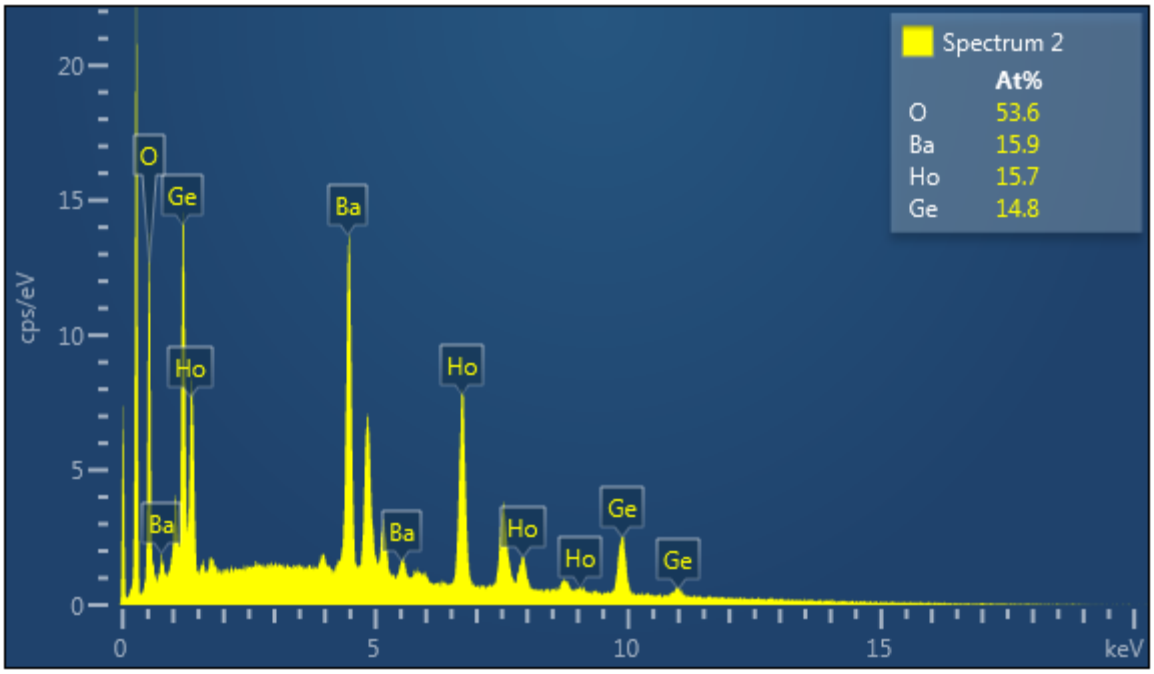

Figure 4.4: EDX spectrum of $BaHoGeO_4(OH)$.

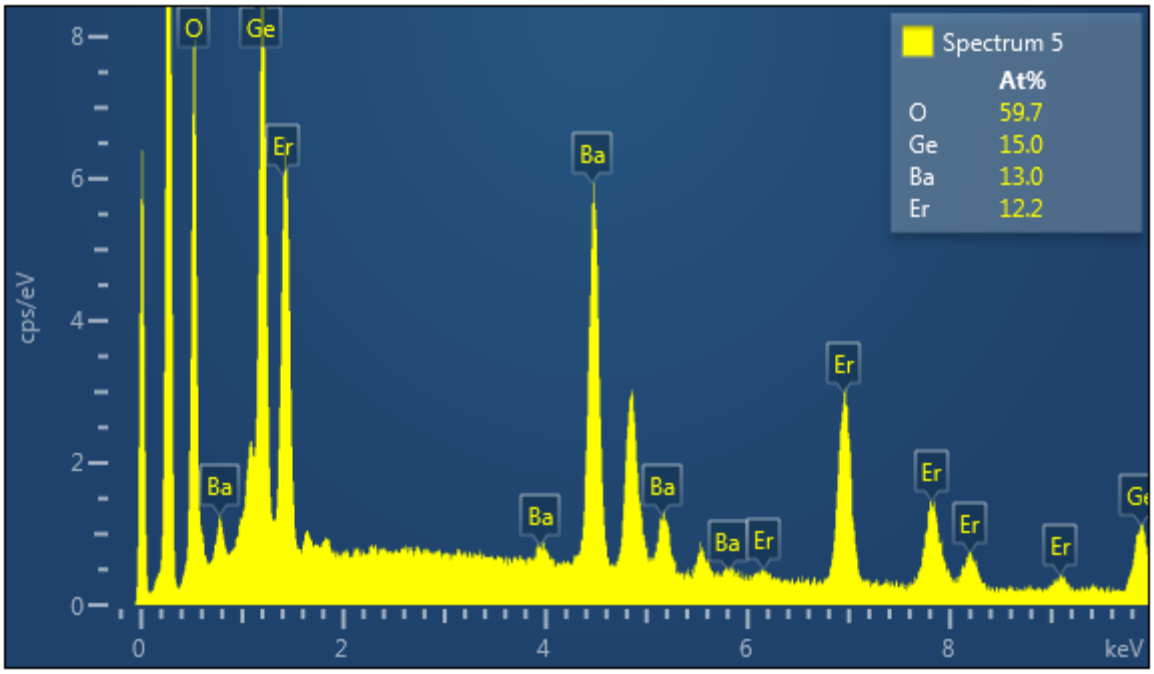

Figure 4.5. EDX spectrum of $BaErGeO_4(OH)$.

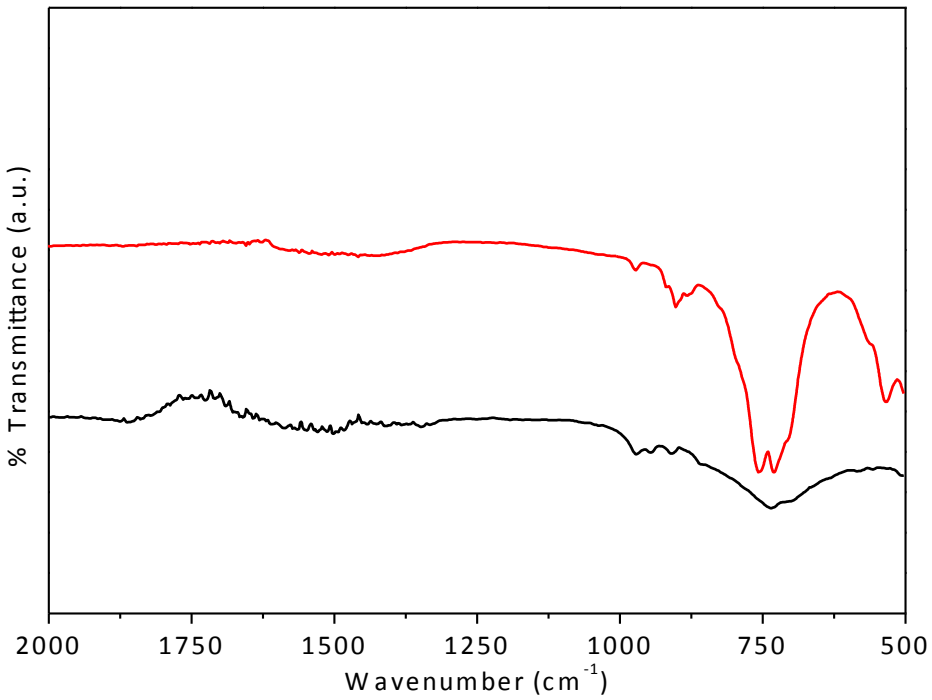

Figure 4.6: IR spectrum of $BaErGeO_4(OH)$ (red) and $BaErGeO_4(OH)$ (black) single crystals collected from 2000-500 cm^{-1}.

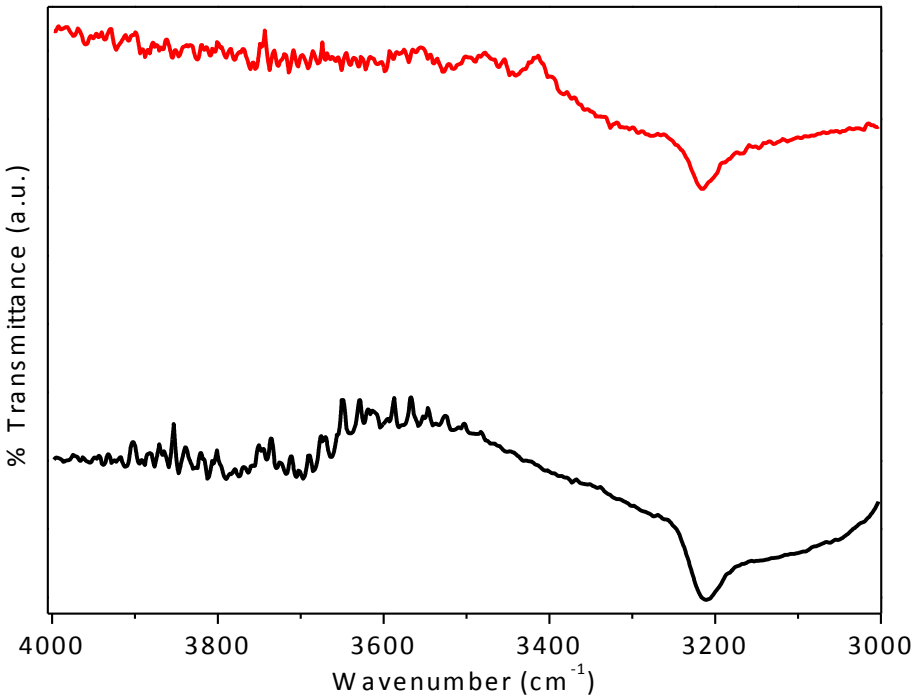

Figure 4.7: IR spectrum of $BaErGeO_4(OH)$ (red) and $BaErGeO_4(OH)$ (black) single crystals collected from 4000-3000 cm^{-1}.

Crystal Structure of $BaRE_{10}(GeO_4)_4O_8$ ($RE=Ho^{3+}$-Er^{3+})

The crystal structure of $BaRE_{10}(GeO_4)_4O_8$ ($RE=Ho^{3+}$-Er^{3+}) represents the first barium rare-earth germanate oxide with BaO_8, HoO_6, HoO_7, and GeO_4 building blocks. The structures are isostructural with the Er^{3+} unit cell parameters being slightly constricted as expected, **Table 4.1**. $BaHo_{10}(GeO_4)_4O_8$ is used as a representative of this structure type with cell parameters of a = 12.4533(8) Å, b = 7.2008(5) Å, c = 12.0034(8) Å, β = 100.183(2) ° and V = 1059.43(12) $Å^3$.

The use of concentrated CsOH as a mineralizer required a systematic approach and support to accurately assign $BaRE_{10}(GeO_4)_4O_8$ over $CsRE_{10}(GeO_4)_4O_7(OH)$. The use of energy dispersive X-ray spectroscopy (EDX), IR, and single-crystal Raman spectroscopy were employed to deduce the final structural assignment. The absence of cesium from EDX of single crystals of $BaHo_{10}(GeO_4)_4O_8$ and $BaEr_{10}(GeO_4)_4O_8$, in addition to, an absence of hydroxide stretching modes in IR and Raman spectroscopy, leaves no ambiguity to the reported barium rare-earth oxides, **Figures 4.11, 4.12, 4.16, 4.17**.

The structural type contains four unique crystallographic Ho^{3+} sites: $Ho(1)O_7$ (*4i*), $Ho(2)O_7$ (*4i*), $Ho(3)O_7$ (*8j*), and $Ho(4)O_6$ (*4g*) with Ho(1)/Ho(2) residing on mirror planes and Ho(4) inhabiting a 2-fold symmetry site. The Ho-O bond distances range from 2.187(5)—2.490(7) Å for the four holmium polyhedra. The compound forms a complex framework of HoO_6 and HoO_7 polyhedra that form sheets propagating along the *ab*-plane, **Figure 4.8a**.

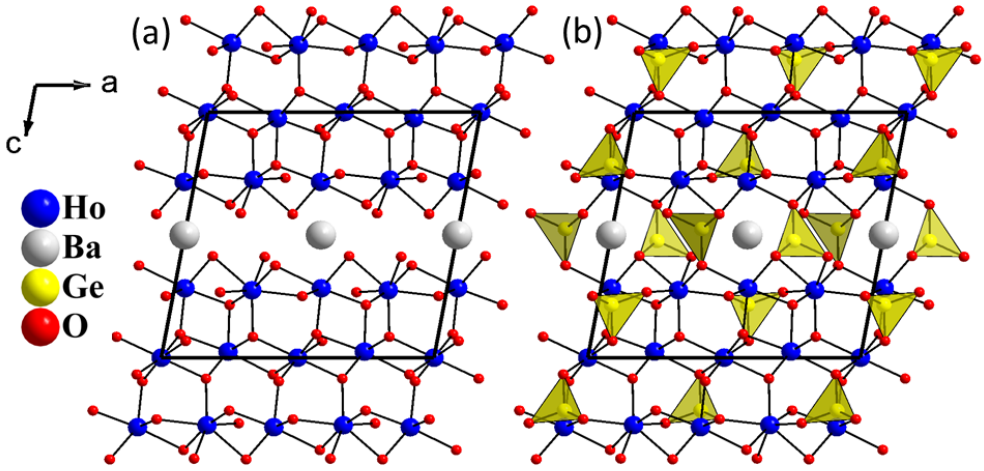

Figure 4.8: $BaHo_{10}(GeO_4)_4O_8$ view along the [010] projection. **(a)** Sheet-like arrangement of holmium oxide polyhedra extending in the *ab*-plane with Ba^{2+} ions occupying void between layers. (**b)** Isolated GeO_4 units stabilize the rare-earth framework and encapsulate the Ba^{2+} ions in channels along [010] direction.

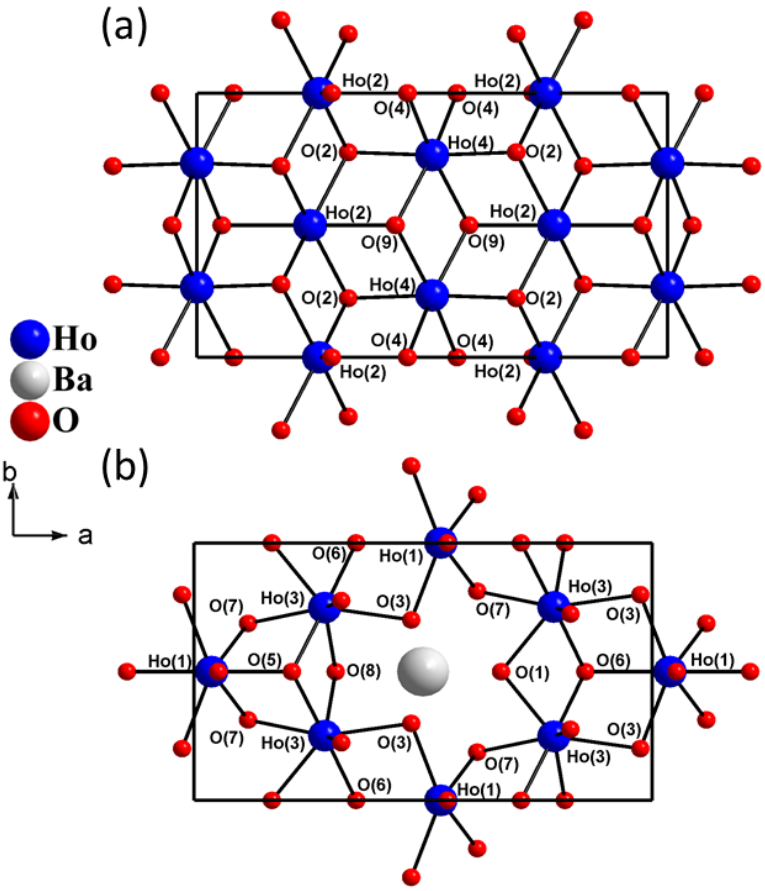

Figure 4.9: (a) Ho(2) and Ho(4) polyhedra forming a honeycomb-type of arrangement visible along the [001] direction. **(b)** Ho(1) and Ho(3) polyhedra creating distorted channels with Ba^{2+} ions coordinating the center to provide additional structural support and charge balance.

Within the rare-earth oxide framework, two distinct connectivities are observed. The first framework is built up of Ho(4) polyhedra that interconnect through edge-sharing of alternating O(4) and O(9) atoms in the *ab*-plane, **Figure 4.9a**. These chains interconnect through Ho(2) polyhedra coordinating through μ3-bridging of O(2), O(4), and O(9) to construct a honeycomb-type lattice, also shown in **Figure 4.9a.** Simultaneously, Ho(1) and Ho(3) polyhedra form a planar network constructed from edge sharing of O(1), O(3), O(7), and O(8) with μ_3 bridging of O(5) and O(6), **Figure 4.9b**. Ho(1) and Ho(3) polyhedra form a planar network consisting of distorted channels along the *c*-axis in which barium atoms coordinate, **Figure. 4.9b**. The Ho(1) and Ho(3) polyhedra form a cap with the Ho(2)/Ho(4) honeycomb lattice residing within this cap and interconnecting through μ_4 bridging of O(2) and O(4) This framework of Ho^{3+} polyhedra forms a sheet that propagates in the *ab*-plane with barium atoms separating the layers **Figure 4.8a** and provides the necessary charge balance.

Isolated GeO_4 tetrahedra support the solid-state framework, **Figure 4.10.** Two crystallographically distinct germanium sites, $Ge(1)O_4$ and $Ge(2)O_4$, reside on *4i* Wyckoff sites with mirror symmetry. The Ge-O bond distances range from 1.734(9)—1.748(9) Å for the two germanium sites. $Ge(1)O_4$ coordinates nine holmium polyhedra and resides within the holmium oxide framework, **Figure 4.10a**. $Ge(1)O_4$ coordinates a trimeric unit of Ho(2) and Ho(4) x2 through μ_4-bridging of O(9) above the tetrahedral site in the *ab*-plane. Additionally, $Ge(1)O_4$ coordinates six holmium centers, (four Ho(3) and two Ho(1) atoms), through corner-shared O(1) and O(3) x2 oxygen atoms below the *ab*-plane, **Figure 4.10a**. The $Ge(1)O_4$ tetrahedra link the two distinct rare-earth frameworks

while $Ge(2)O_4$ tetrahedra coordinate the void between layers to create distorted channels where barium atoms reside. The $Ge(2)O_4$ tetrahedra coordinate two trimeric units, (two Ho(3) and one Ho(1) atoms), in the *ab*-plane through μ_4 bridging of O(6) above the tetrahedral site and below through edge-sharing of O(7) and O(8) atoms, **Figure 4.10b**. The $Ge(2)O_4$ tetrahedra resides between the rare-earth layers with neighboring barium atoms, thus strengthening the layered structure. $Ge(2)O_4$ alternates up/down direction relative to the *c*-axis while propagating throughout the *ab*-plane, **Figure 4.8b**.

Bond valence sum calculations resulted in values of 1.72, 3.06, 2.99, 2.94, 2.95, 4.08, and 4.03 for Ba(1), Ho(1), Ho(2), Ho(3), Ho(4), Ge(1), and Ge(2), respectively, and are consistent with the assigned oxidation states. The absence of hydroxide is supported by IR as well as single crystal Raman which indicate no observation of potential OH^- stretches in the region from 3600-3200 cm^{-1} in $BaHo_{10}(GeO_4)_4O_8$, **Figure 4.17**. Semi-quantitative elemental analysis (EDX) was used to support the ratio of metals and supports the assignment of Ba^{2+} in the framework, with no evidence of Cs^+ ions in the structure, **Figures 4.11 and 4.12.**

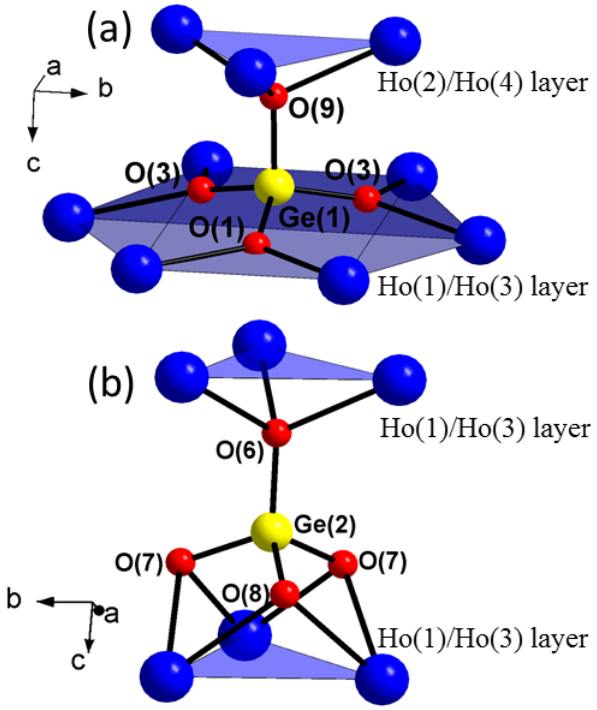

Figure 4.10:. Holmium polyhedra omitted for clarity. **(a)** $Ge(1)O_4$ coordination highlighting bridging between Ho(2)/Ho(4) and Ho(1)/Ho(3) layers. **(b)** $Ge(2)O_4$ coordination between Ho(1)/Ho(3) layers just off [100] direction.

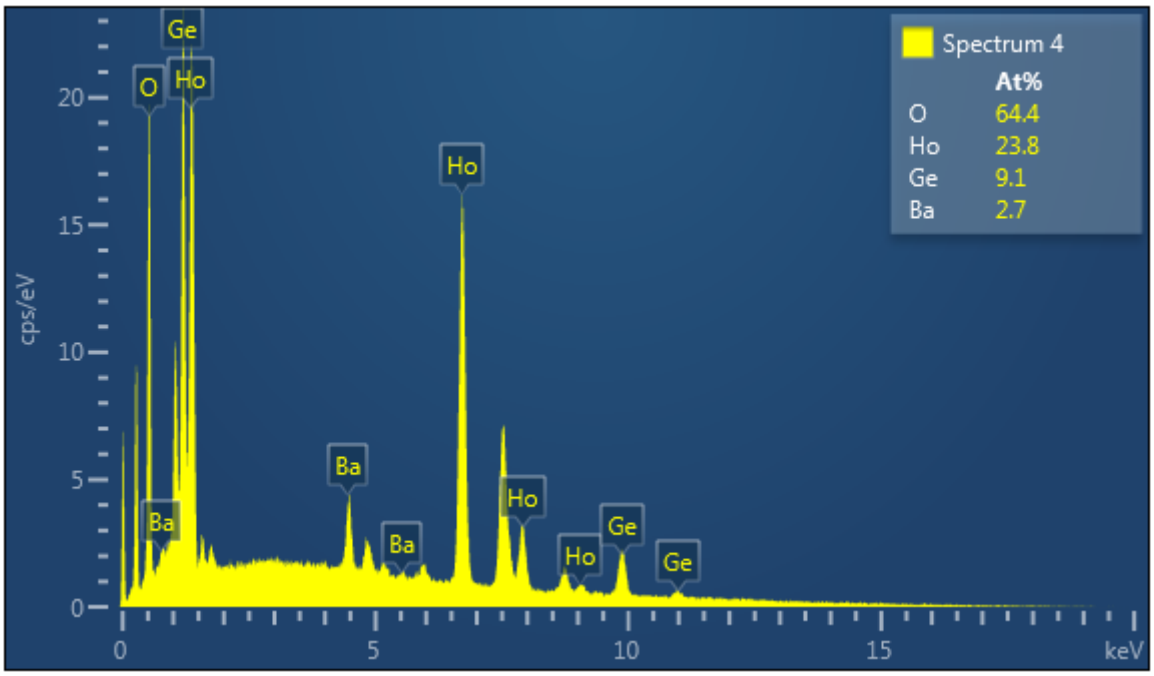

Figure 4.11: EDX spectrum of $BaHo_{10}(GeO_4)_4O_{8.}$

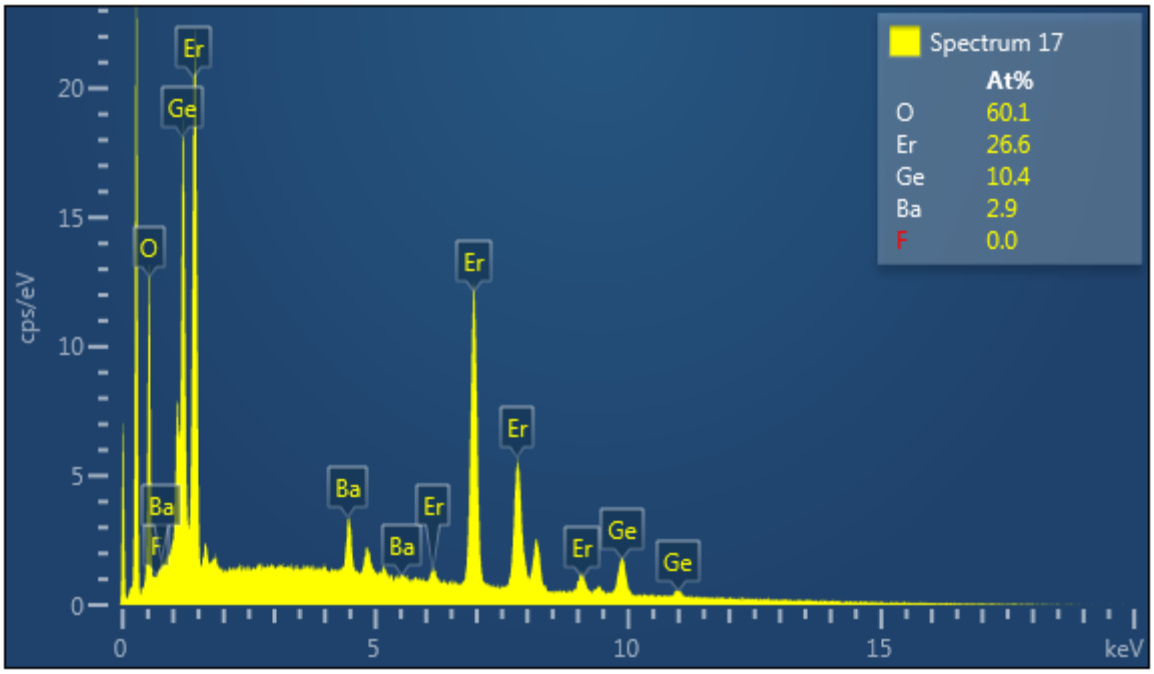

Figure 4.12: EDX spectrum of $BaEr_{10}(GeO_4)_4O_8$.

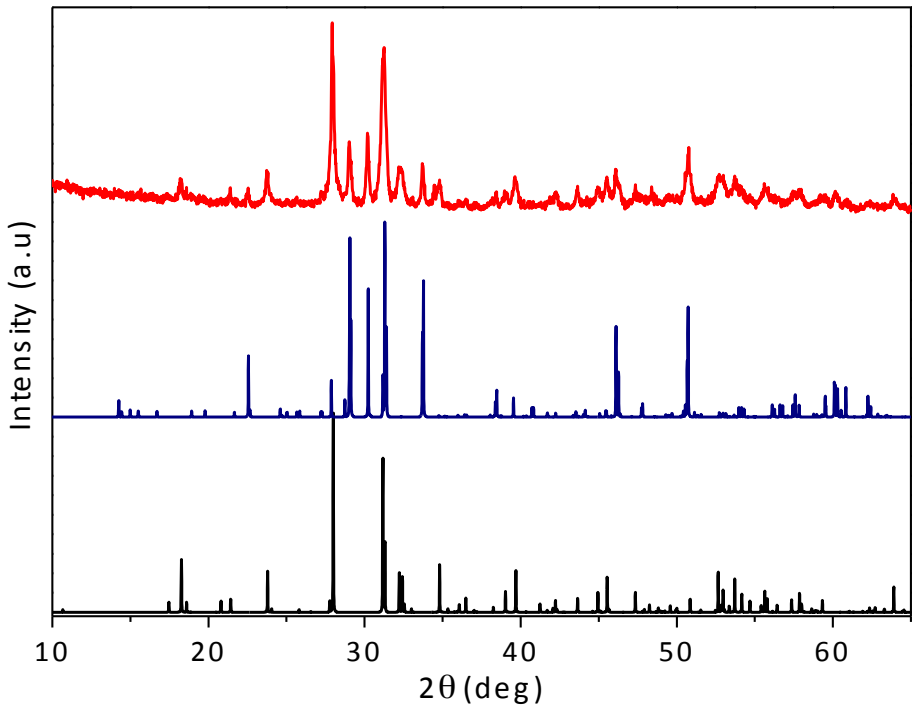

Figure 4.13: Simulated powder X-ray diffraction of $BaErGeO_4(OH)$ simulated in space group *Pbca* in black (Bottom). Simulated powder X-ray diffraction of $BaEr_{10}(GeO_4)_4O_8$) simulated in space group *C2/m* in blue (Middle). Hydrothermally grown powder of $BaErGeO_4(OH)$ and $BaEr_{10}(GeO_4)_4O_8$) shown in red (Top) revealing a mixture of phases with the aid of CsOH mineralizers.

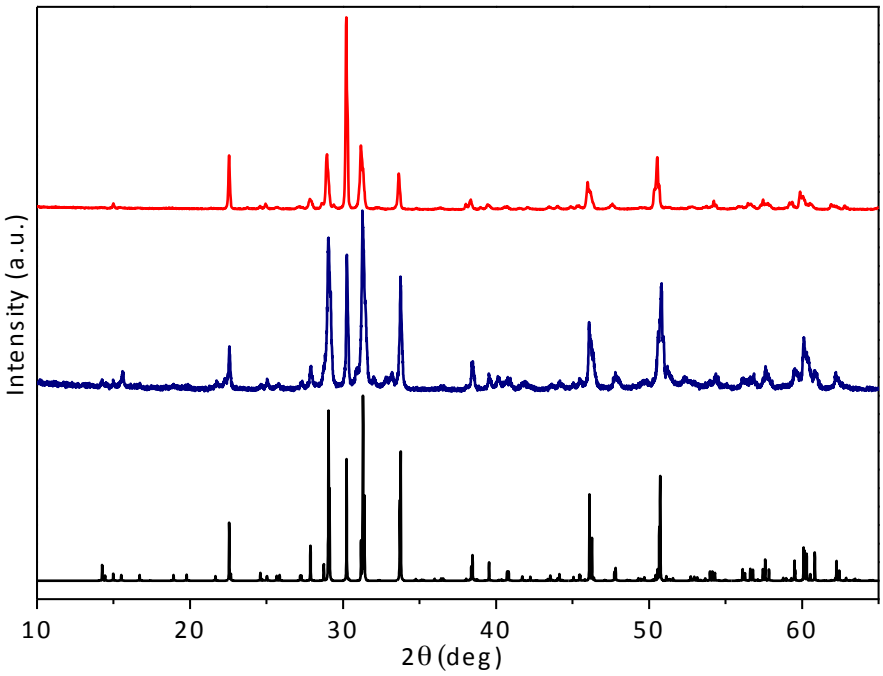

Figure 4.14: Simulated powder X-ray diffraction of $BaEr_{10}(GeO_4)_4O_8$ simulated in space group *C2/m* in black (Bottom). Hydrothermally grown powder of $BaEr_{10}(GeO_4)_4O_8$ shown in blue (Middle). Hydrothermally grown powder of $BaHo_{10}(GeO_4)_4O_8$ shown in red (Top). No ambiguous reflections in the as-grown powder were identified.

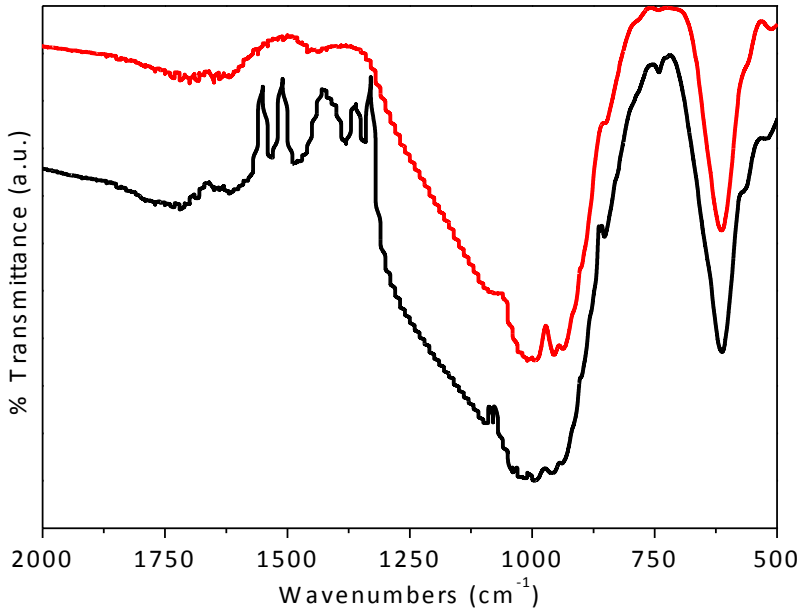

Figure 4.15: IR spectrum of $BaEr_{10}(GeO_4)_4O_8$ (red) and $BaHo_{10}(GeO_4)_4O_8$ (black) single crystals collected from 2000-500 cm^{-1}.

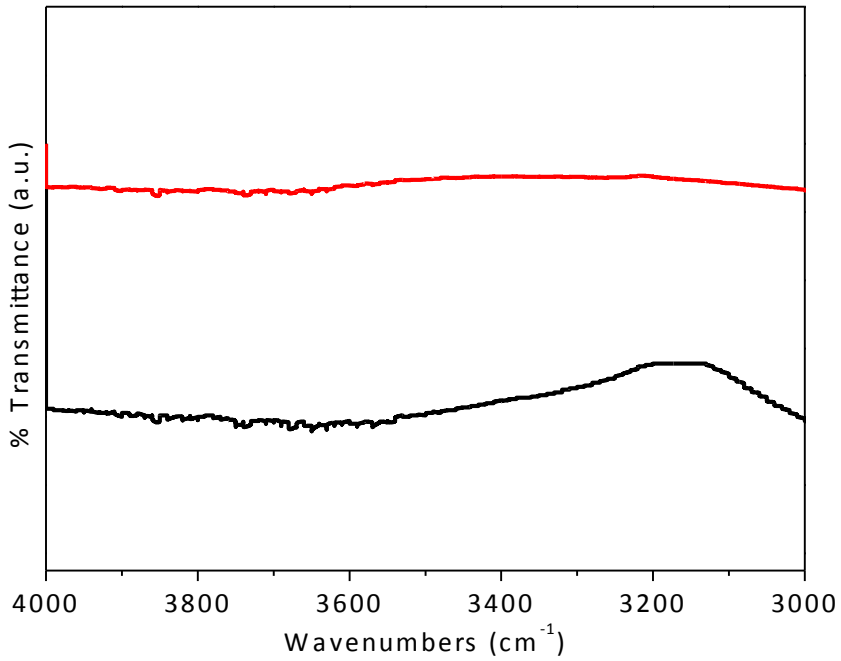

Figure 4.16: IR spectrum of $BaEr_{10}(GeO_4)_4O_8$ (red) and $BaHo_{10}(GeO_4)_4O_8$ (black) single crystals collected from 4000-3000 cm^{-1}.

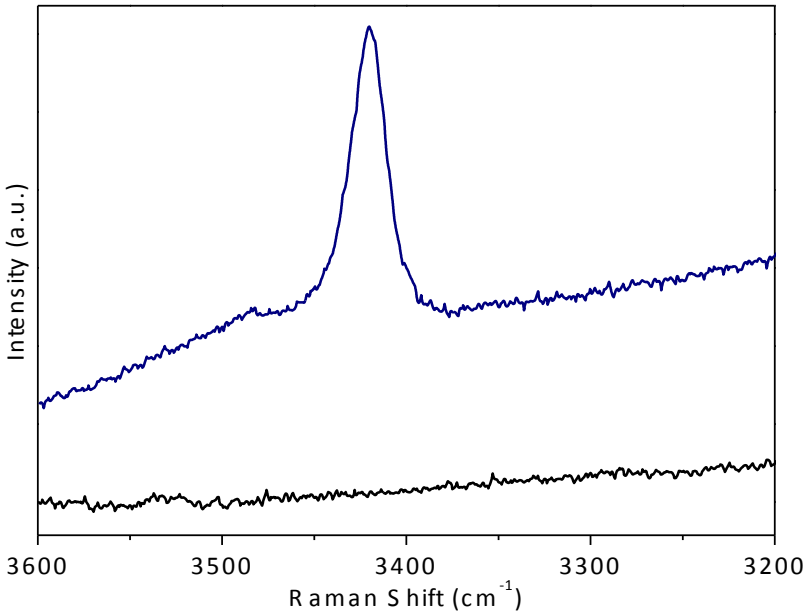

Figure 4.17: Single crystal Raman scattering of $BaHoGeO_4(OH)$ (blue) and $BaHo_{10}(GeO_4)_4O_8$ (black) from 3600-3200 cm^{-1}. A strong hydroxide stretching mode for $BaHoGeO_4(OH)$ was detected at 3420 cm^{-1}, while no hydroxide stretching modes were detected for $BaHo_{10}(GeO_4)_4O_8$.

Single Crystal Raman Characterization

Let us now examine simple phonon properties of the barium rare-earth germanates. $BaHoGeO_4(OH)$ and $BaHo_{10}(GeO_4)_4O_8$ are examined as representatives of each new structural type by single-crystal Raman scattering. Factor group analysis for $BaHoGeO_4(OH)$ orthorhombic structure (*Pbca*, $Z = 8$), factor group D_{2h}^{15}, reveals that the normal modes are distributed among the following irreducible representations for the elementary unit cell: $27A_g + 27A_u + 27B_{1g} + 27B_{1u} + 27B_{2g} + 27B_{2u} + 27B_{3g} + 27B_{3u}$. Here, B_{1u}, B_{2u} and B_{3u} can be assigned to acoustic modes, $26B_{1u} + 26B_{2u} + 26B_{3u}$ to IR active modes, and $27A_g + 27B_{1g} + 27B_{2g} + 27B_{3g}$ to Raman active modes. Since the Ge—O bonds are much stronger than the Ho—O bonds, and exhibit distortion away from ideal T_d symmetry, simplification of the Raman active modes to focus on the $[GeO_4]^{4-}$ tetrahedra is appropriate.

For each free $[GeO_4]^{3-}$ anion, nine internal Raman vibrational modes are expected from the general formula $3N$-6. The $[GeO_4]^{4-}$ anions in $BaHoGeO_4(OH)$ and $BaHo_{10}(GeO_4)_4O_8$ adopt C_1 point group symmetry, and internal vibrations can be described by A Raman active modes. $BaHoGeO_4(OH)$ exhibits a strong Raman signal at 785 cm^{-1} which has been assigned to the symmetric υ_1 stretching modes and asymmetric ν_3 stretching modes observed for bands from 700-800 cm^{-1}, **Figure 4.19a**. Bands in the 400-500 cm^{-1} region have been assigned to the ν_4 bending internal modes of the $[GeO_4]^{4-}$ building block.

Factor group analysis of monoclinic $BaHo_{10}(GeO_4)_4O_8$ (*C2/m*, $Z = 2$), factor group C_{2h}^3, reveals the normal modes are distributed among the following irreducible

representations for the elementary unit cell: $33A_g + 24A_u + 24B_g + 36B_u$. From these modes, two modes should be classified as acoustic ($A_u + 2B_u$). The IR active modes are $23A_u + 34B_u$, while $33A_g + 24B_g$ represent Raman active modes. **Figure 4.19b** reveals three distinct peaks from 700-810 cm^{-1}, with an intense Raman peak at 765 cm^{-1}. Again, these peaks have been assigned to symmetric υ_1 stretching modes and asymmetric v_3 stretching modes with peaks at 400-500 cm^{-1} region being assigned to the v_4 bending internal modes of the germanate. This is commensurate with known rare-earth apatite $La_{8+x}Ba_{2-x}(GeO_4)_6O_{2+x/2}$ (x= 0 and 1.2) structural types, which also display isolated $[GeO_4]^{4-}$ building blocks, and scattering bands were assigned these corresponding modes.[45,46]

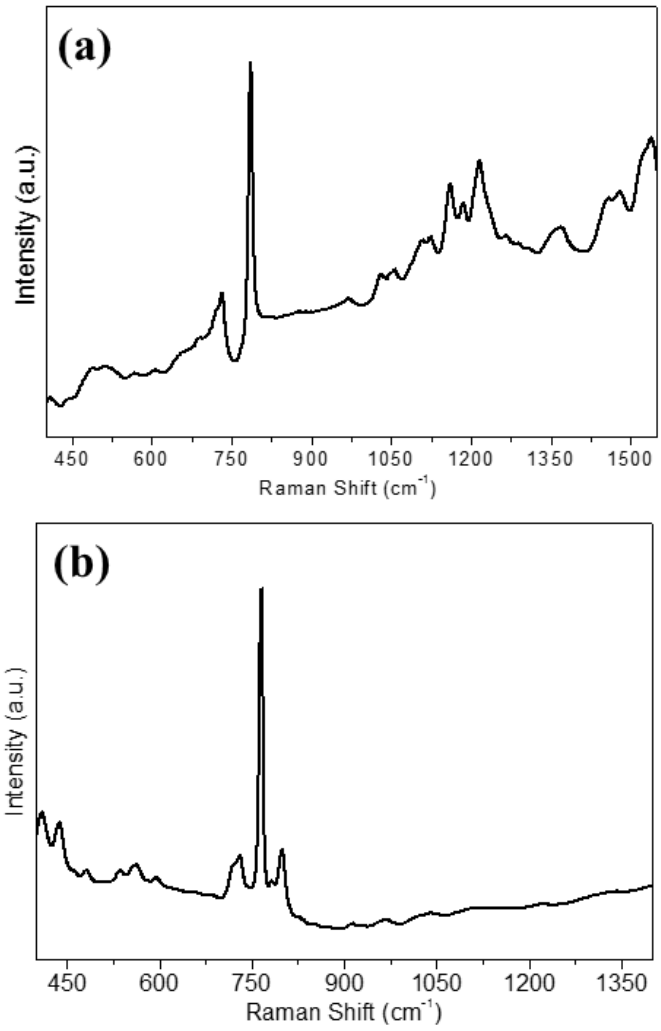

Figure 4.19: Single crystal Raman scattering of (a) $BaHoGeO_4(OH)$ and (b) $BaHo_{10}(GeO_4)_4O_8$.

Photoluminescent studies of $BaHo_{10}(GeO_4)_4O_8$ and $BaEr_{10}(GeO_4)_4O_8$

Photoluminescent spectra of $BaREGeO_4(OH)$ and $BaRE_{10}(GeO_4)_4O_8$ ($RE=Ho^{3+}$-Er^{3+}) crystals collected using 457.9 nm laser excitation are shown in **Figure 4.20**. The emission spectrum in **Figure 4.20a** depicts an intense peak in the green spectral range (between 550 – 570 nm) which is characteristic of Er^{3+} ions present in the $BaEr_{10}(GeO_4)_4O_8$ crystal. This peak can be associated with the $^4S_{3/2}$ to $^4I_{15/2}$ transition of Er^{3+} ions. The peaks centered at around 540 nm and 675 nm can be associated with $^2H_{11/2}$ to $^4I_{15/2}$ and $^4F_{9/2}$ to $^4I_{15/2}$ transitions of Er^{3+} ions, respectively. Similar emission patterns were observed for Er^{3+} ions in silicate frameworks containing barium ions. **Figure 4.20b** shows characteristic emission peaks of Ho^{3+} ions present in the $BaHo_{10}(GeO_4)_4O_8$ crystal. The dominant peak in the red spectral region (630 – 675 nm) is associated with the $^5F_3$ to $^5I_7$ transition. A similar peak pattern is observed for Ho^{3+} containing silicate crystals containing barium ions.[47]

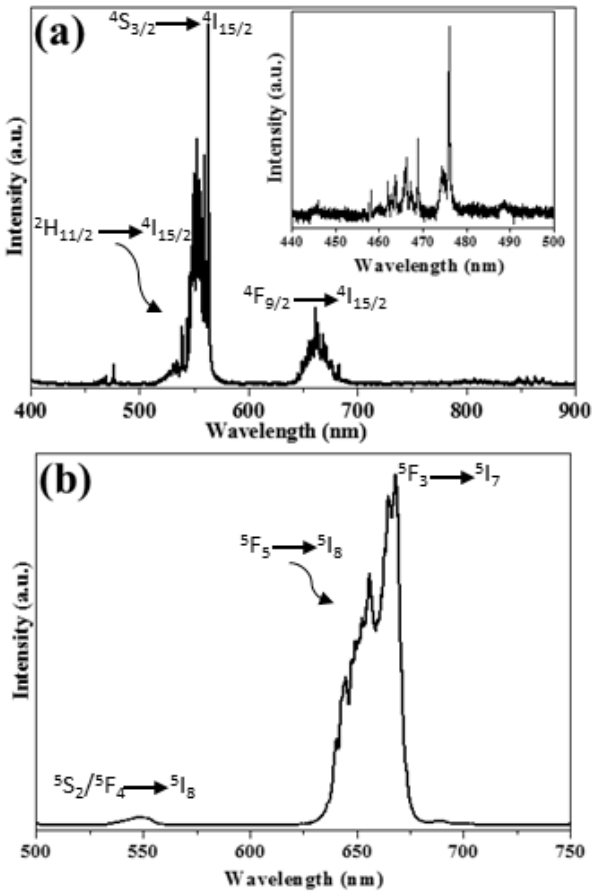

Figure 4.20: Solid-phase photoluminescent studies of (a) $BaEr_{10}(GeO_4)_4O_8$ and (b) $BaHo_{10}(GeO_4)_4O_8$ crystals using 457.9 nm laser excitation.

$Tb_{13}(GeO_4)_6O_7(OH)$ and $K_2TbGe_2O_7$ Crystal Structures and Characterization

In this section, a description of initial reactions of germanates with terbium oxide, Tb_4O_7, to generate large high quality single crystals of two new terbium germanates. The reaction of mixed-valent Tb(III)/Tb(IV) Tb_4O_7 with GeO_2 in high-temperature hydrothermal hydroxide fluids led to two new crystals, one of which is a Tb^{3+} complex and the other is a Tb^{4+} complex.

Although the Tb^{4+} oxidation state is known it is generally considered a very oxidizing ion. Thus, very few well-characterized, purely tetravalent, terbium examples exist due to the high oxidation potential of Tb^{4+}. The binary fluorides TbF_4 and oxides TbO_2 are quite unstable and their synthetic and characterization difficulties are well described in the older literature.[48-51] Most of the well characterized structures are anionic salts of either alkali terbium fluorides[52-54] or alkali or alkaline earth oxides, predominantly perovskite derivatives.[55-59] The high redox potential of Tb^{4+} is such that it appears to only be stabilized in solution by strong base (OH^- and/or CO_3^{2-}). In this way, it has been investigated as a surrogate to high potential tetravalent actinides such as Cm^{4+} and Bk^{4+}.[60-61] It appears that there is no previous single crystal structural characterization of any Tb^{4+} complex with any oxyanion ligand. The work reported herein may be the first steps in studying high oxidation potential f-element ions in oxyanion matrices such as silicates, titanates or germanates. The crystal structure of select $RE_{13}(GeO_4)_6O_7(OH)$ (RE = Gd, Er, Tm) compounds is reported for completeness of the family.

Experimental Methods for Terbium Germanates

The compounds of the present study were prepared from the hydrothermal reaction of Tb_4O_7 with GeO_2 starting materials in a 1:4 molar ratio, using 20 M KOH as a mineralizer at 700 °C. The resultant crystals were identified by single crystal X-ray diffraction (**Tables 4.6, 4.7**), and other supporting characterization (Figures **4.21-4.28**), as $Tb_{13}(GeO_4)_6O_7(OH)$ containing Tb^{3+}, and $K_2TbGe_2O_7$ containing Tb^{4+}. In this case, both products were isolated as large, colorless crystals (~1 mm^3) from the same reaction, and contain Tb^{3+} and Tb^{4+}, respectively. The crystals were most readily distinguishable from one another under long wave UV light (380 nm), where crystals of $Tb_{13}(GeO_4)_6O_7(OH)$ exhibited a strong green luminescence (535 nm) characteristic of Tb^{3+}, while crystals of $K_2TbGe_2O_7$ did not luminesce significantly (**Fig. 4.21 and 4.28**).

Single crystals of $Tb_{13}(GeO_4)_6O_7(OH)$ and $K_2TbGe_2O_7$ were grown isothermally at 700 °C for 7 days using 20 *M* KOH mineralizer. The feedstock consisted of Tb_4O_7 (129 mg, 0.172 mmol; HEFA Rare-Earth 99.99%) and GeO_2 (71 mg, 0.687 mmol; Alfa Aesar 99.9%) in a 1:4 molar ratio, respectively. These components and 0.4 mL of the KOH mineralizer were loaded into a 99.9% fine silver ampule (2.5" long) that was weld sealed. Two independent band heaters were strapped to the outside of the autoclave to maintain the isothermal 700 °C system, and autogenously generating 200 MPa pressure. After the reaction period the autoclave was cooled to room temperature over a period of 12 hours. Single crystals of $RE_{13}(GeO_4)_6O_7(OH)$ (RE = Gd-Yb) were grown from identical stoichiometric reactions in comparison to $Tb_{13}(GeO_4)_6O_7(OH)$.

Although crystals of $K_2TbGe_2O_7$ were formed in comparable size to $Tb_{13}(GeO_4)_6O_7(OH)$, the yield of $Tb_{13}(GeO_4)_6O_7(OH)$ was far greater, appearing in > 90% yield in multiple reactions. In general, we find hydrothermal synthesis provides somewhat reducing conditions, in this case leading to a lower yield of $K_2TbGe_2O_7$. This may be improved in the future through the addition of an oxidant and the use of a platinum reaction vessel. Nevertheless, the UV light was used to isolate a few single crystals of $K_2TbGe_2O_7$ for further characterization. The presence of both species under hydrothermal conditions indicates both compounds are thermodynamically stable in highly basic conditions.

Table 4.6: Crystallographic data for $Tb_{13}(GeO_4)_6O_7(OH)$ and $K_2TbGe_2O_7$.

	$Tb_{13}(GeO_4)_6O_7(OH)$	**$K_2TbGe_2O_7$**
FW	3014.51	494.30
crystal system	trigonal	monoclinic
crystal dimension, mm	0.05 x 0.05 x 0.04	0.06 x 0.05 x 0.04
space group, Z	*R-3*, 3	*C2/c*, 4
T, °C	25	25
a, Å	15.8667(6)	10.2720(4)
b, Å	15.8667(6)	5.7273(2)
c, Å	9.5266(4)	13.3584(6)
β, °	---	105.6890(10)
V, $Å^3$	2077.02(18)	756.61(5)
dcalc, g cm^{-3}	7.230	4.339
2θ range, °	2.26-25.99	3.17-28.30
Tmin/Tmax	0.6483/1.0000	0.7382/1.0000
Reflns coll./unique/obs.	5974/908/814	8694/946/915
μ (Mo Kα), mm^{-1}	39.218	18.233
data/restraints/param.	908/1/79	946/0/58
R1, wR2 (obs. data [I> 2σ(I)])	0.0267, 0.0598	0.0148, 0.0367
R1, wR2 (all data)	0.0323, 0.0621	0.0158/0.0370
S	1.069	1.183

Table 4.7: Selected interatomic distances (Å) and angles (°) for $Tb_{13}(GeO_4)_6O_7(OH)$ and $K_2TbGe_2O_7$.

$Tb_{13}(GeO_4)_6O_7(OH)$ (I)		**$K_2TbGe_2O_7$ (II)**	
$Tb(1)O_7$		**$Tb(1)O_6$**	
Tb(1)−O(1)	2.551(7)	Tb(1)−O(1) x2	2.2505(17)
Tb(1)−O(2)	2.345(7)	Tb(1)−O(3) x2	2.2691(18)
Tb(1)−O(3)	2.211(7)	Tb(1)−O(4) x2	2.3745(17)
Tb(1)−O(4)	2.685(7)	**$K(1)O_9$**	
Tb(1)−O(5)	2.304(7)	K(1)−O(1)	2.691(2)
Tb(1)−O(5)	2.328(7)	K(1)−O(1)	2.8499(19)
Tb(1)−O(6)	2.3205(5)	K(1)−O(1)	3.357(2)
$Tb(2)O_7$		K(1)−O(2)	2.7897(19)
Tb(2)−O(1)	2.304(7)	K(1)−O(3)	2.9157(19)
Tb(2)−O(1)	2.468(7)	K(1)−O(3)	2.9617(19)
Tb(2)−O(2)	2.369(7)	K(1)−O(3)	3.1360(19)
Tb(2)−O(3)	2.211(7)	K(1)−O(4)	3.102(2)
Tb(2)−O(3)	2.254(7)	K(1)−O(4)	3.2287(19)
Tb(2)−O(4)	2.336(7)	**$Ge(1)O_4$**	
Tb(2)−O(4)	2.638(8)	Ge(1)−O(1)	1.7324(16)
$Tb(3)O_6$		Ge(1)−O(2)	1.7901(13)
Tb(3)−O(3) x6	2.339(7)	Ge(1)−O(3)	1.7182(17)
$Ge(1)O_4$		Ge(1)−O(4)	1.7719(18)
Ge(1)−O(1)	1.765(7)		
Ge(1)−O(2)	1.733(7)	Ge(1)−O(2)−Ge(1)	121.56(14)
Ge(1)−O(4)	1.762(7)		
Ge(1)−O(5)	1.746(7)		
Tb(2)−O(3)−Tb(3)	103.7(3)		
Tb(2)−O(3)−Tb(3)	102.3(3)		
Tb(1)−O(5)−Tb(1)	122.9(3)		

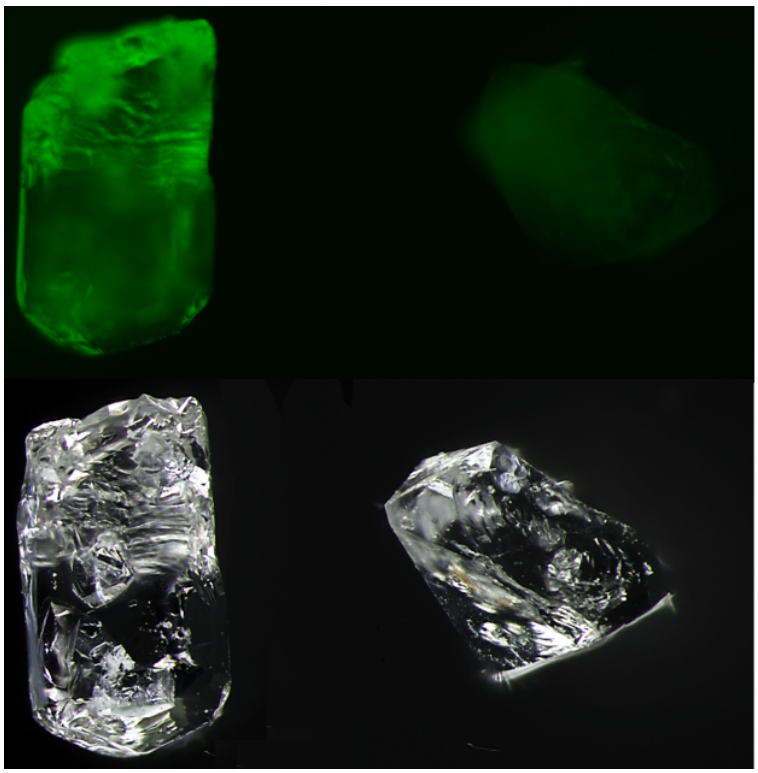

Figure 4.21: $Tb_{13}(GeO_4)_6O_7(OH)$ (**I**) (left) and $K_2TbGe_2O_7$ (**II**) (right) crystals under UV (top) and white (bottom) light. Faint luminescence from **II** likely results from very low levels of Tb^{3+} impurities associated with OH^- deposited on the crystal surface during cool-down (similar to what is observed for $K_2ZrGe_2O_7$) or trace substitution of Tb^{3+} impurities in the bulk. Crystals are approximately 0.5 mm in size.

Crystal Structure of $RE_{13}(GeO_4)_6O_7(OH)$ (RE = Gd-Yb,Y)

As a surrogate of this crystal family, $Tb_{13}(GeO_4)_6O_7(OH)$ will be used to describe the structural features and characterization. The crystal structure data for several isostructural rare-earth analogues is given in **Table 4.8**. Crystal quality and habit are shown in **Figure 4.29** for rare-earth analogues Gd-Yb. The crystal structure of the high density $Tb_{13}(GeO_4)_6O_7(OH)$ is similar to that of $Er_{13}Ge_6O_{31}(OH)$ and $Gd_{13}Ge_6O_{31}F$ which were briefly reported some years ago in the noncentrosymmetric and potentially ferroic space group *R*3.[34,35] Some doubt was cast upon the original space group assignment in favor of the centrosymmetric space group *R*-3 based on the observed physical properties, but no additional studies have followed.[36] The structure refinement of the hydrothermally grown crystals from our lab leaves little doubt that the correct solution is the centrosymmetric *R*-3 assignment (**Table 4.6, Figure 4.24**), as test refinements in *R*3 led to unsatisfactory anisotropic displacement parameters and a Flack parameter of 0.5.

The structure is a complex three-dimensional network of terbium oxide ($[Tb(1)O_7]$, $[Tb(2)O_7]$, and $[Tb(3)O_6]$) polyhedra and germanate tetrahedra. The individual terbium polyhedra form interesting subunits that ultimately build the three-dimensional structure. The $[Tb(2)O_7]$ units are edge-sharing with one another through O(3) and O(4) atoms, forming a ring of six Tb atoms. At the center of this ring is Tb(3), which forms the angularly-distorted octahedral $[Tb(3)O_6]$ unit to stabilize the ring with connectivity to O(3) (**Figure 4.22a**). This arrangement is reminiscent of half-units of the polyoxometalate class.[37] Neighboring units are connected through edge-sharing of O(1).

Germanium atoms coordinate all of the oxygen atoms on the cluster except O(3) (**Figure 4.27**).

The O(3) site serves as a tetrahedral vertex with terbium atoms, also bridging to a different structural subunit formed by [Tb(1)O_7] groups. These groups connect to one another to form a trimer unit through μ-3 bridging of O(6). Two staggered trimers are fused along the c-axis by corner sharing of O(5) (**Figure 4.22b**).

The Tb(2)/Tb(3) units each containing seven Tb^{3+} ions are linked to each other via oxy bridges, forming diagonal layers connected into a framework **(Figure 4.23a, 4.23b**). Unlike the Tb(2)/Tb(3) network, the Tb(1)-containing subunits possess only six Tb^{3+} ions and are not further connected to one another. They do fill gaps in the Tb(2)/Tb(3) network (**Figure 4.23c, 4.23d**) and occur in diagonal layers stacked along the *c*-axis. The Tb(1) and Tb(2)/Tb(3) subunits occur in alternating fashion along the c-axis. All of these units are decorated by [GeO_4] tetrahedra (**Figure 4.23e**), which fill the remaining space and generate a complex layered three-dimensional structure. The O(6) atom was identified as underbonded (1.377 bvs) and geometrically capable of supporting a hydrogen atom assignment. The H(6) atom is half-occupied based on charge balance, bond valence, and geometric considerations, and contained within the Tb(1) cluster subunit. The presence of hydroxide is supported by IR and single crystal Raman analysis in which a strong hydroxyl stretching mode was observed at 3468 cm^{-1} (**Figure 4.34, 4.35**). Also, the crystals exhibit characteristic Raman scattering in the single crystal Raman spectra (**Figure 4.26**).

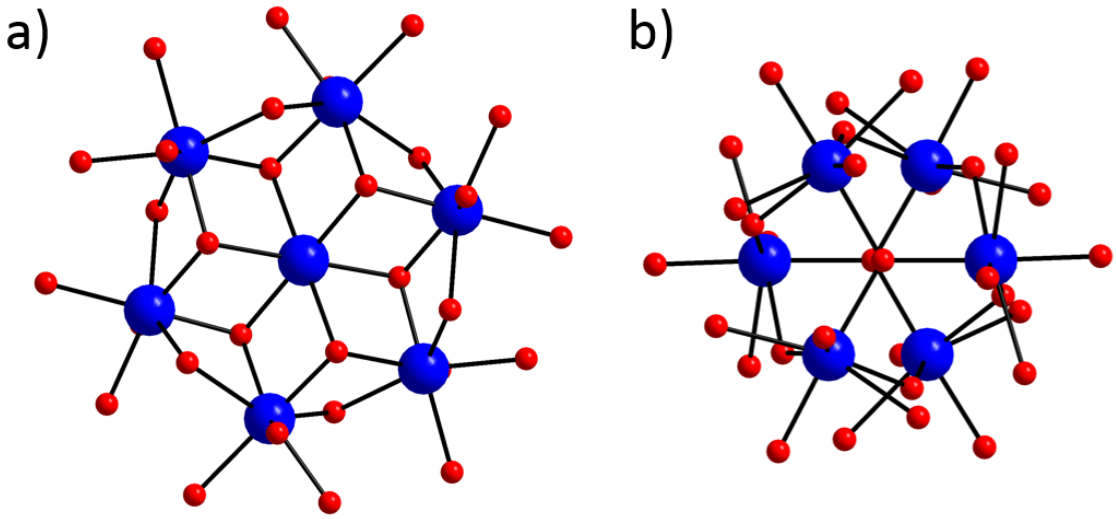

Figure 4.22: Terbium oxide subunits in **I**: a) Tb(2)/Tb(3) subunit; b) Tb(1) subunit.

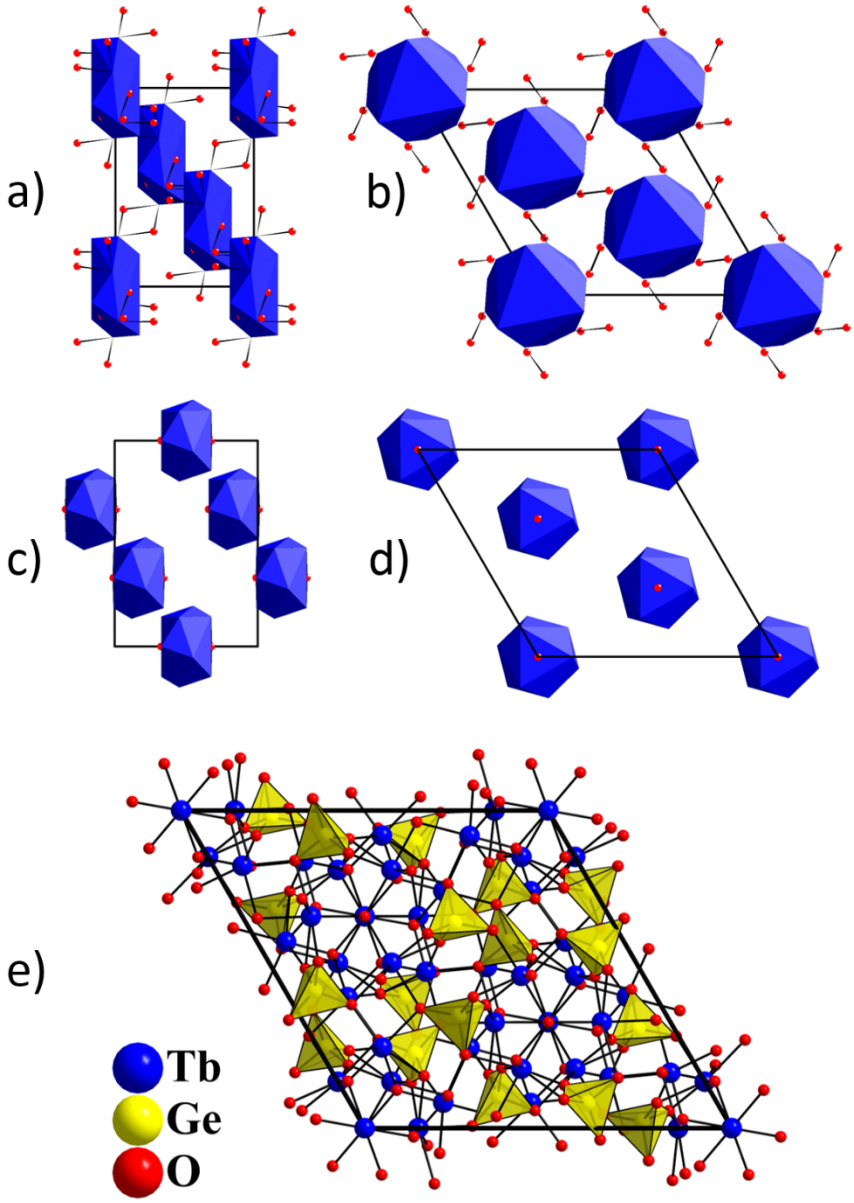

Figure 4.23: Alternating arrangement of Tb(2)/Tb(3) and Tb(1) subunits in **I**: a) Tb(2)/Tb(3) subunits viewed along *a*; b) the same Tb(2)/Tb(3) subunits viewed along *c*; c) Tb(1) subunits viewed along *a*; d) the same Tb(1) subunits viewed along *c*; e) stacking of subunits along c, including the total unit cell contents.

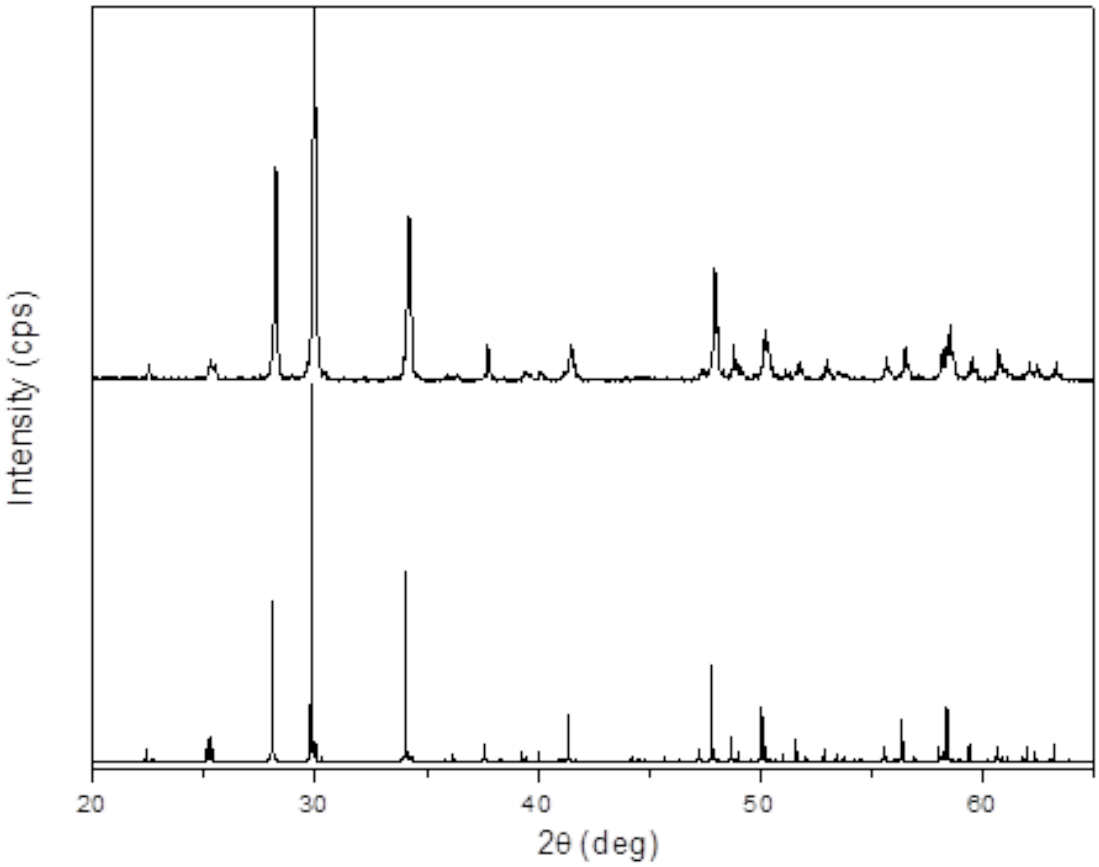

Figure 4.24: PXRD of $Tb_{13}(GeO_4)_6O_7(OH)$. (Top) Powder diffraction pattern of as-grown $Tb_{13}(GeO_4)_6O_7(OH)$. (Bottom) Simulated powder diffraction pattern of $Tb_{13}(GeO_4)_6O_7(OH)$ in space group *R-3*. Hydrothermally grown powder analysis was performed via the bulk material.

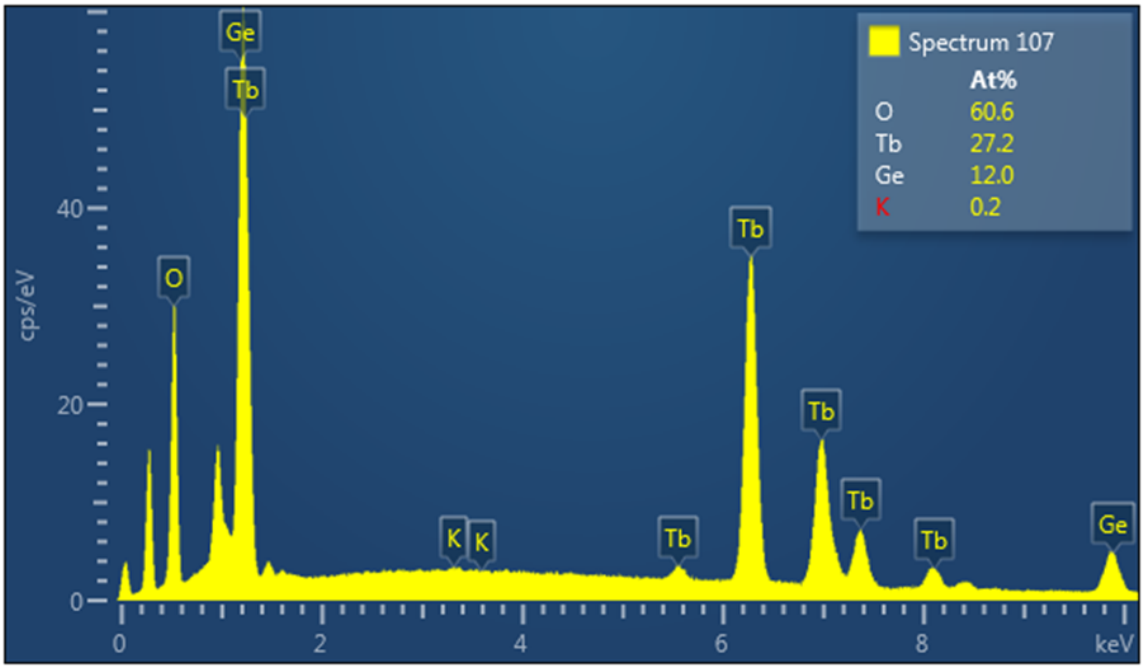

Figure 4.25: EDX analysis of $Tb_{13}(GeO_4)_6O_7(OH)$.

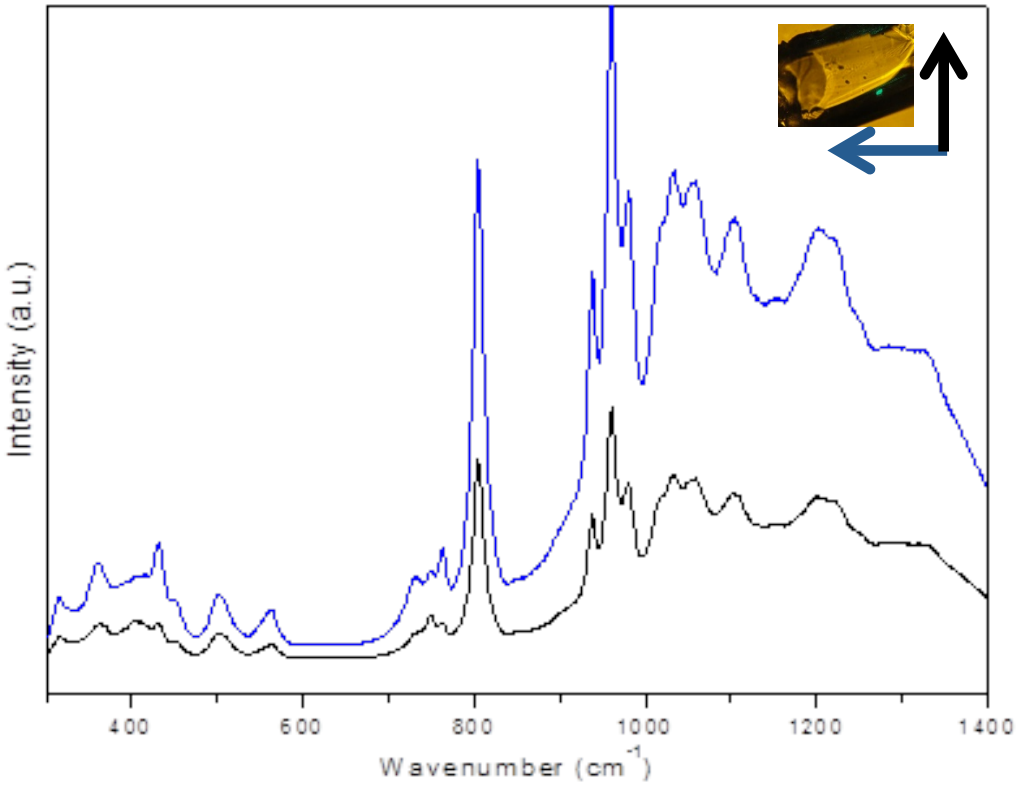

Figure 4.26: Single crystal Raman scattering of $Tb_{13}(GeO_4)_6O_7(OH)$ from 300-1400 cm^{-1}. The intensity ratio of the bands at 749 and 763 cm^{-1} changes as a function of the direction of polarization. Blue indicates polarization left while black indicates polarization up, indicated by direction of arrows.

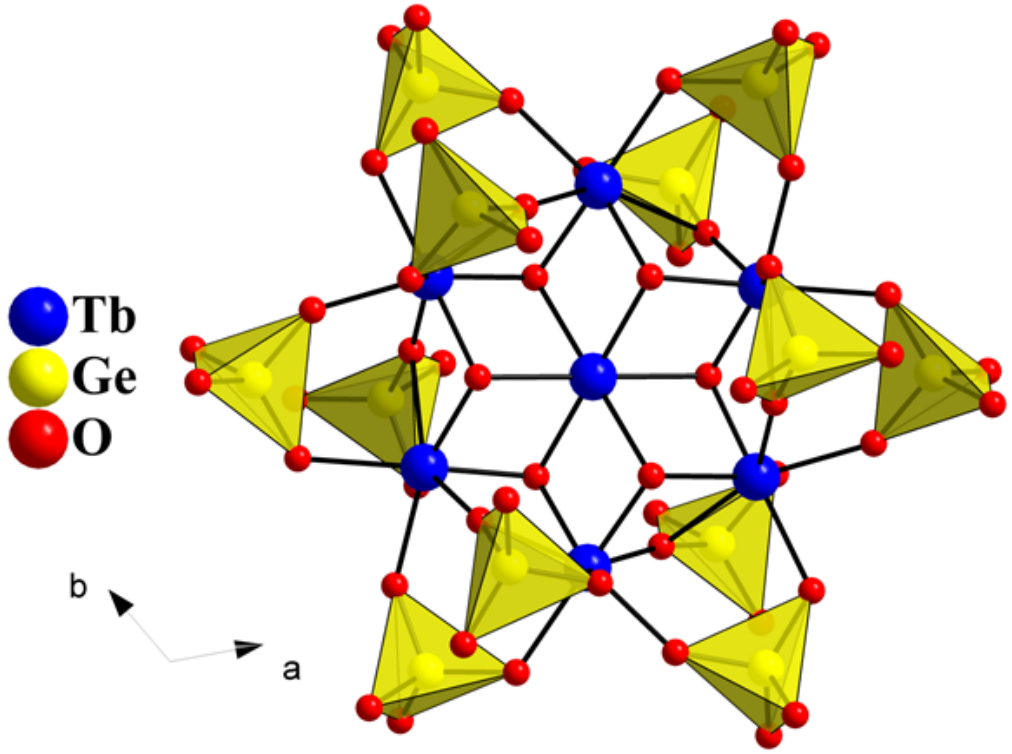

Figure 4.27: Tb(2)/Tb(3) cluster decorated with isolated GeO_4 units viewed along [001] direction.

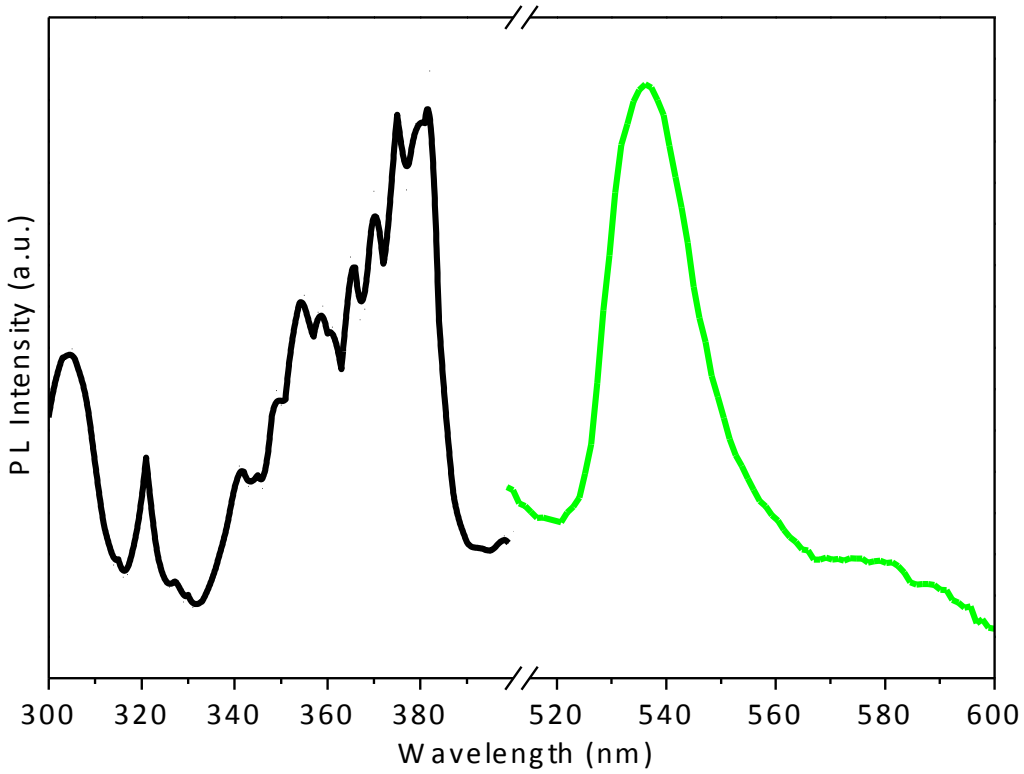

Figure 4.28: Photoluminescence excitation and emission of $Tb_{13}(GeO_4)_6O_7(OH)$. Excited was measured from 300-400 nm and is shown in black. Emission was measured from 510-600 nm and is shown in green at an excitation of 380 nm. Most intense emission peak occurs as 542 nm consistent with the green luminescence observed in **Figure 4.21**.

Table 4.8: Crystallographic data for select $RE_{13}(GeO_4)_6O_7(OH)$ (RE = Gd, Er, and Tm) compounds.

empirical formula	**$Gd_{13}(GeO_4)_6O_7(OH)$**	**$Er_{13}(GeO_4)_6O_7(OH)$**	**$Tm_{13}(GeO_4)_6O_7(OH)$**
formula weight (g/mol)	2992.80	3122.93	3144.64
crystal system	Trigonal	Trigonal	Trigonal
space group, *Z*	R-3, 3	R-3, 3	R-3, 3
temperature, K	298(2)	298(2)	298(2)
crystal size (mm)	0.055 x 0.058 x 0.068	0.054 x 0.058 x 0.068	0.060 x 0.080 x 0.180
***a*, Å**	15.9541(6)	15.6777(7)	15.591(2)
***c*, Å**	9.5898(4)	9.4218(4)	9.3862(19)
volume, $Å^3$	2113.90(18)	2005.5(2)	1975.9(7)
calculated density ($\mu g/m^3$)	7.053	7.757	7.928
absorption coefficient (mm^{-1})	36.504	47.033	50.106
F(000)	3843	3999	4038
Θ range for data	2.553-28.279	2.631-26.465	2.613-25.984
reflections collected	1160	912	867
data/restraints/parameters	1160/0/79	912/0/79	867/0/79
final R [$I > 2\sigma(I)$] R1, wR2	0.0384, 0.1067	0.0428, 0.0883	0.0334, 0.0798
final R (all data) R1, wR2	0.0401, 0.1090	0.0496, 0.0908	0.0362, 0.0820
goodness-of-fit on F^2	1.045	1.120	1.102
largest diff. peak/hole, e/ $Å^3$	10.143/ -16.357	6.815/ -10.553	6.296/ -8.398

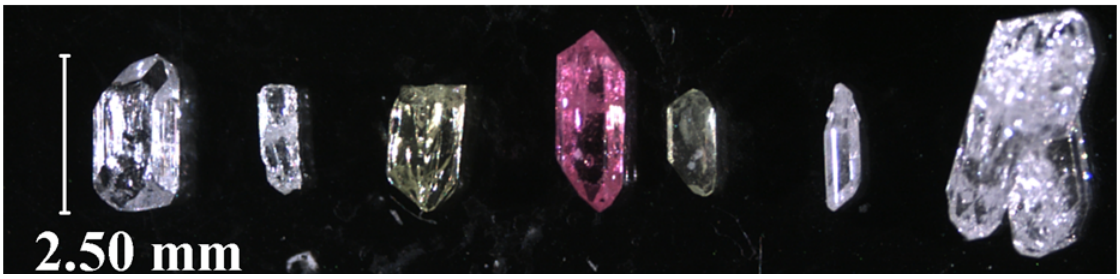

Figure 4.29: Hydrothermally grown crystals of $RE_{13}(GeO_4)_6O_7(OH)$ structure type. From left to right, crystals of rare-earth ions Gd^{3+}, Tb^{3+}, Dy^{3+}, Er^{3+}, Tm^{3+}, Y^{3+} and Yb^{3+}.

Crystal Structure of $K_2TbGe_2O_7$

The compound $K_2TbGe_2O_7$, is a Tb^{4+} pyrogermanate that is isostructural with $K_2ZrGe_2O_7$ and structurally similar to $Na_2ZrGe_2O_7$.[38-40] The building blocks of $K_2TbGe_2O_7$ are the pyrogermanate [Ge_2O_7] unit and a six-coordinate [TbO_6] unit. Each [TbO_6] unit is coordinated by six pyrogermanate groups through O(1), O(3), and O(4) vertices, and each [Ge_2O_7] group likewise coordinates six [TbO_6] units to form the 3-D framework (**Figure 4.30**). The framework has a channel-like arrangement with potassium ions providing charge balance and alternating off-center in the channels. $K_2TbGe_2O_7$ departs somewhat from $K_2ZrGe_2O_7$ in that it exhibits a wider range of Ge-O and Tb-O bond lengths, as well as O-Tb-O bond angles.

The Tb^{4+}–O bonds in $K_2TbGe_2O_7$ range from 2.2505(18)–2.3744(18) Å, which compares to Zr–O bonds ranging from 2.048(6)–2.113(5) Å for the analogous $K_2ZrGe_2O_7$. The average Tb^{4+}–O bond length in $K_2TbGe_2O_7$ (2.2980(19) Å) is shorter than the average Tb^{3+}–O bond length in $Tb_{13}(GeO_4)_6O_7(OH)$ (Tb^{3+}–O = 2.366(7) Å), as would be expected. They are however, somewhat longer than the Tb^{4+}–O distances in the simple oxides (2.16 Å),[29] as the oxygen atoms are drawn more toward Ge^{4+} by Tb-O-Ge bridging in $K_2TbGe_2O_7$. While the O(4) site is slightly under-bonded (1.48 v.u.), the absence of hydroxyl group stretching modes around 3000-3600 cm^{-1} in the IR and single crystal Raman experiments (**Figure 4.34 and 4.35**), as well as the lack of significant UV luminescence, supports the primary presence of Tb^{4+}. Furthermore, electron density having a suitable geometry for hydrogen atom assignment could not be identified in this sterically-compact structure. Test refinements where oxygen atoms were partially

occupied to instead model $K_2TbGe_2O_7$ as a Tb^{3+} species via oxygen vacancy ($K_2TbGe_2O_{6.5}$) were unsuccessful, as this resulted in significantly higher R values and non-positive definite anisotropic displacement parameters on the partially-occupied atoms. Some Tb^{3+} impurity may indeed be present in the bulk, but would appear to occur at very low concentrations based on the comparatively weak UV luminescence, and since a suitable charge-balance mechanism could not be identified from the X-ray data. The PXRD pattern calculated from the single crystal structure refinement was in excellent agreement with the obtained experimental pattern (**Figure 4.31**). Semi-quantitative energy dispersive X-ray analysis measurements indicate a 2:1:2 ratio of K:Tb:Ge metals (**Figure 4.32**). Typical strong Ge–O stretching modes are observed at 830, 959, and 993 cm^{-1} in the single crystal Raman spectra (**Figure 4.33**).

The formation of the Tb^{4+} germanate reported here is somewhat surprising. It represents, to our knowledge, the first structurally characterized complex of Tb^{4+} with any oxyanion. The few previous reports are either simple fluoride or oxide salts. The compound shows no signs of thermal instability or tendency to decompose in ambient conditions. We postulate that the high oxidation state is initially stabilized in the strongly basic solution and is then subsequently trapped in germanate crystalline lattice. This raises the question of the ability of other oxyanions such as silicates, to stabilize higher oxidation state rare-earth and actinide cations. Given that the Tb^{4+} state has been investigated as a surrogate for tetravalent actinides, this question may take on added significance.

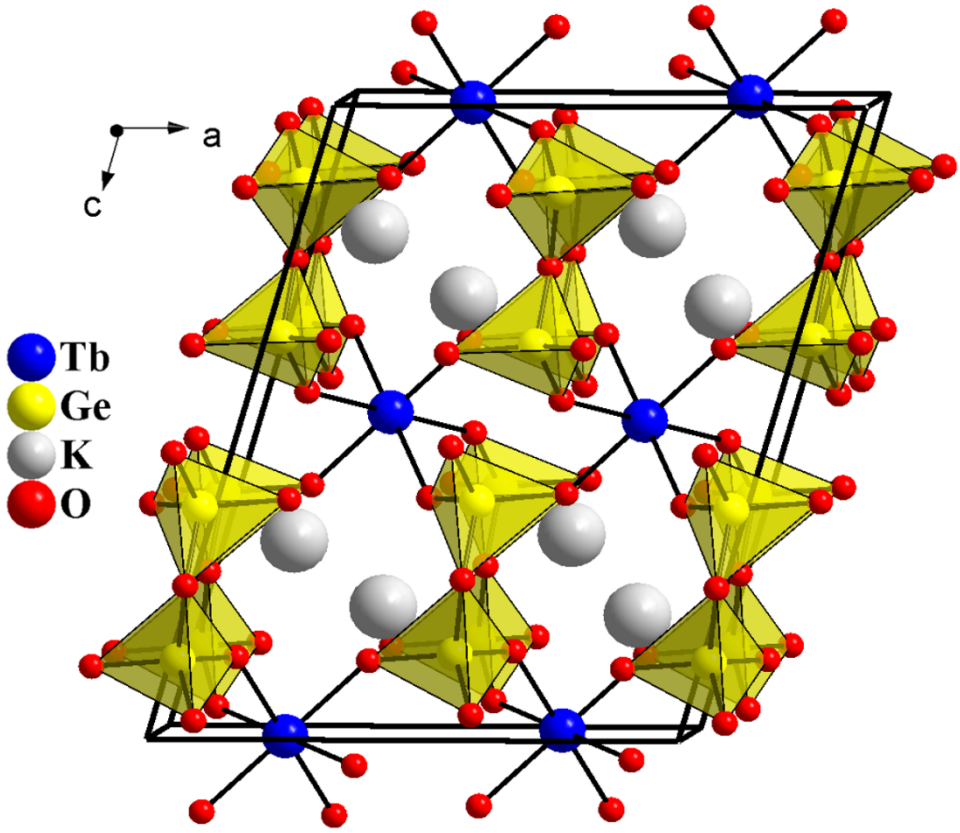

Figure 4.30: Channel-like arrangement of the $K_2TbGe_2O_7$ structure viewed off the *b*-axis.

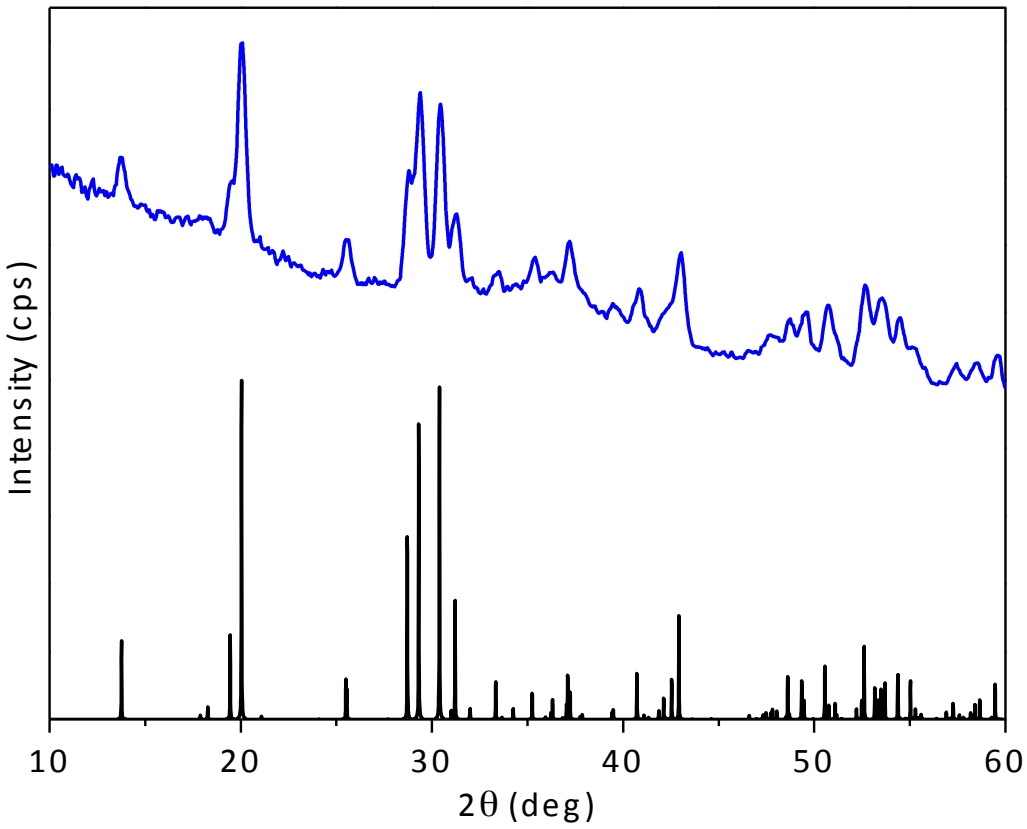

Figure 4.31: PXRD of $K_2TbGe_2O_7$ (Top) Powder diffraction pattern of as-grown $K_2TbGe_2O_7$. (Bottom) Simulated powder diffraction pattern of $K_2TbGe_2O_7$ in space group *C*2/*c*. Several single crystals of $K_2TbGe_2O_7$ were ground and data collected via an optimized algorithm for powder analysis on a Bruker D8 Venture single crystal diffractometer.

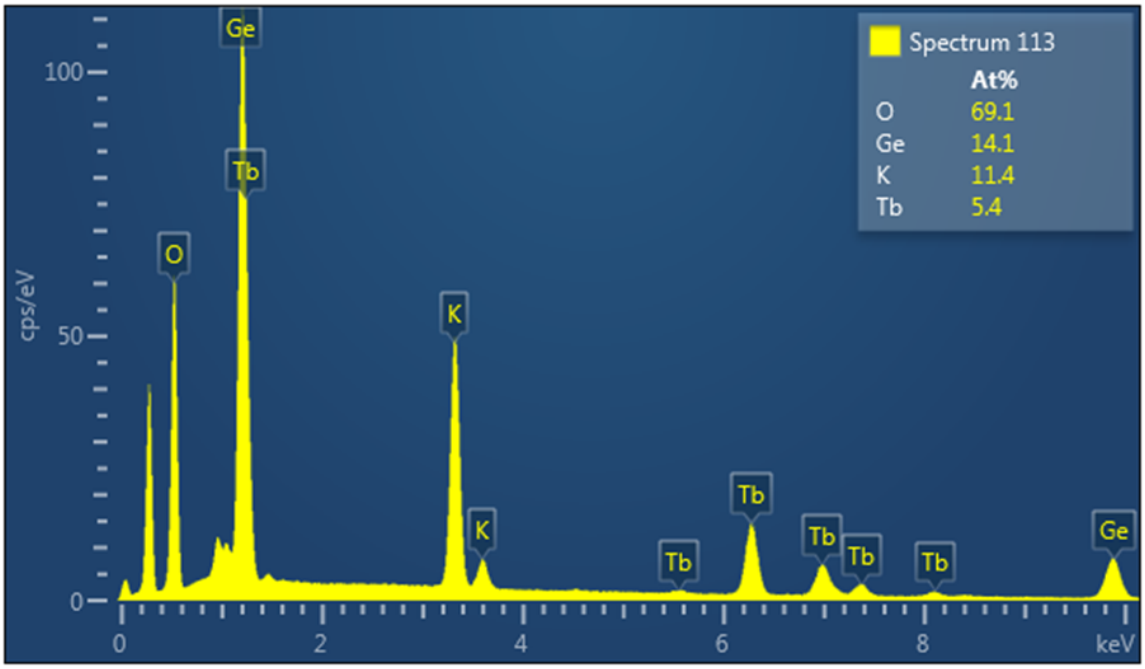

Figure 4.32: EDX analysis of $K_2TbGe_2O_7$.

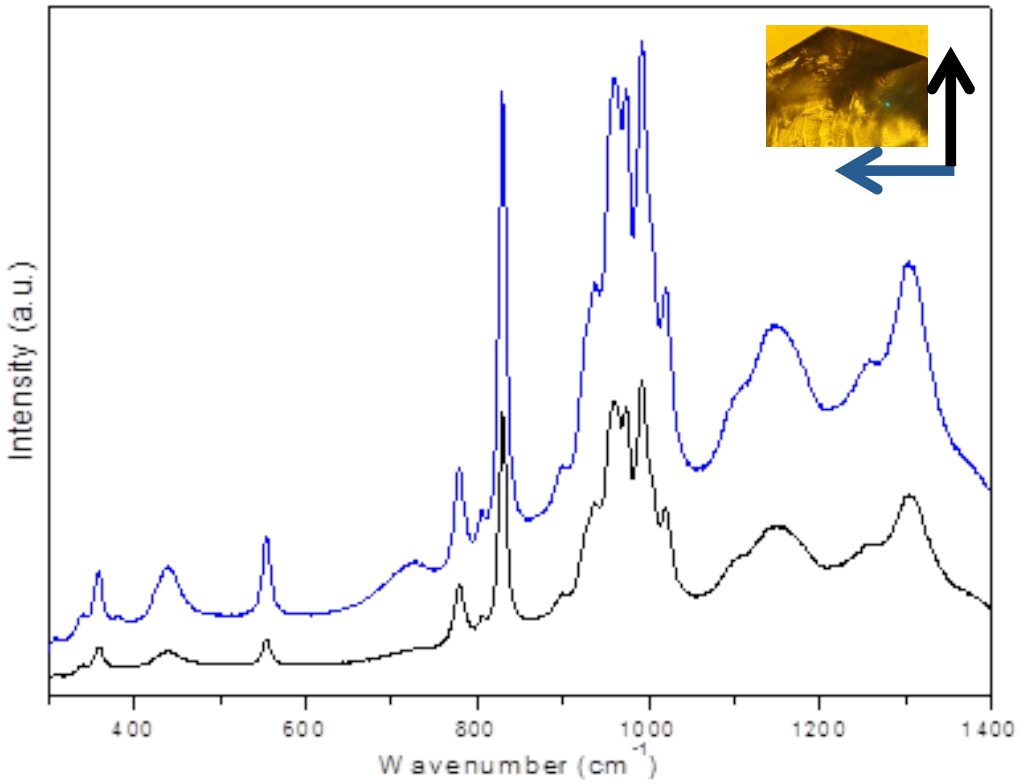

Figure 4.33: Single crystal Raman scattering of $K_2TbGe_2O_7$ from 300-1400 cm^{-1}. No significant changes were observed when the direction of polarization was changed. Blue indicates polarization left while black indicates polarization up, indicated by the direction of the arrows.

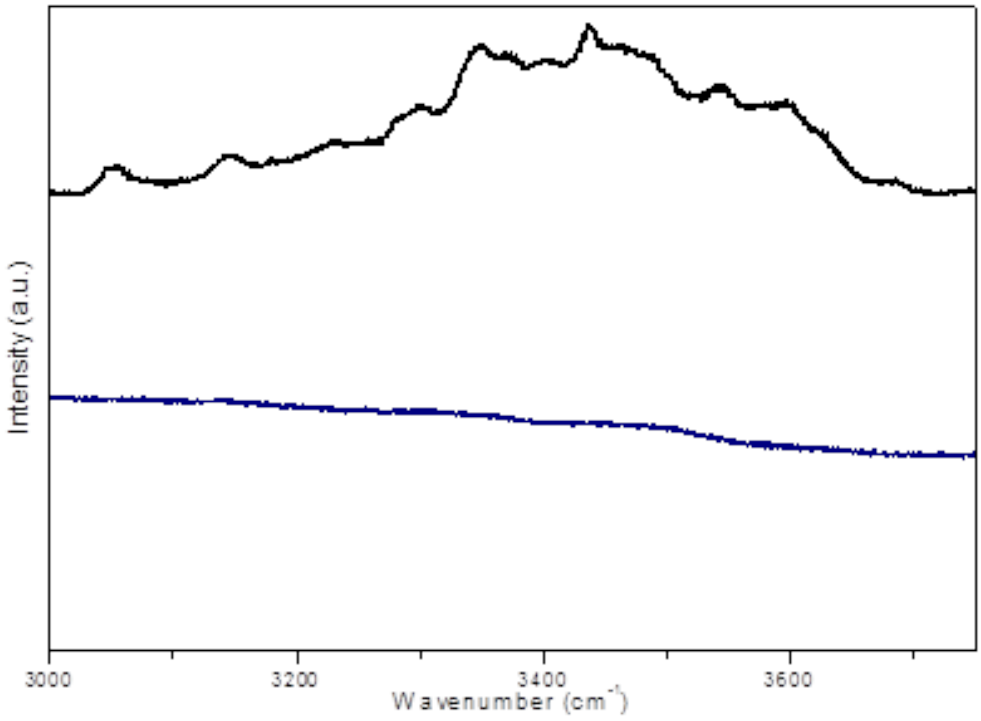

Figure 4.34: Single crystal Raman scattering of $Tb_{13}(GeO_4)_6O_7(OH)$ (black) and $K_2TbGe_2O_7$ (blue) from 3000-3750 cm^{-1}. No presence of hydroxide for $K_2TbGe_2O_7$ was detected. The strongest signal for the OH^- stretching mode for $Tb_{13}(GeO_4)_6O_7(OH)$ occurs at 3437 cm^{-1} in the Raman spectrum, consistent with the broad OH^- feature in the infrared spectrum.

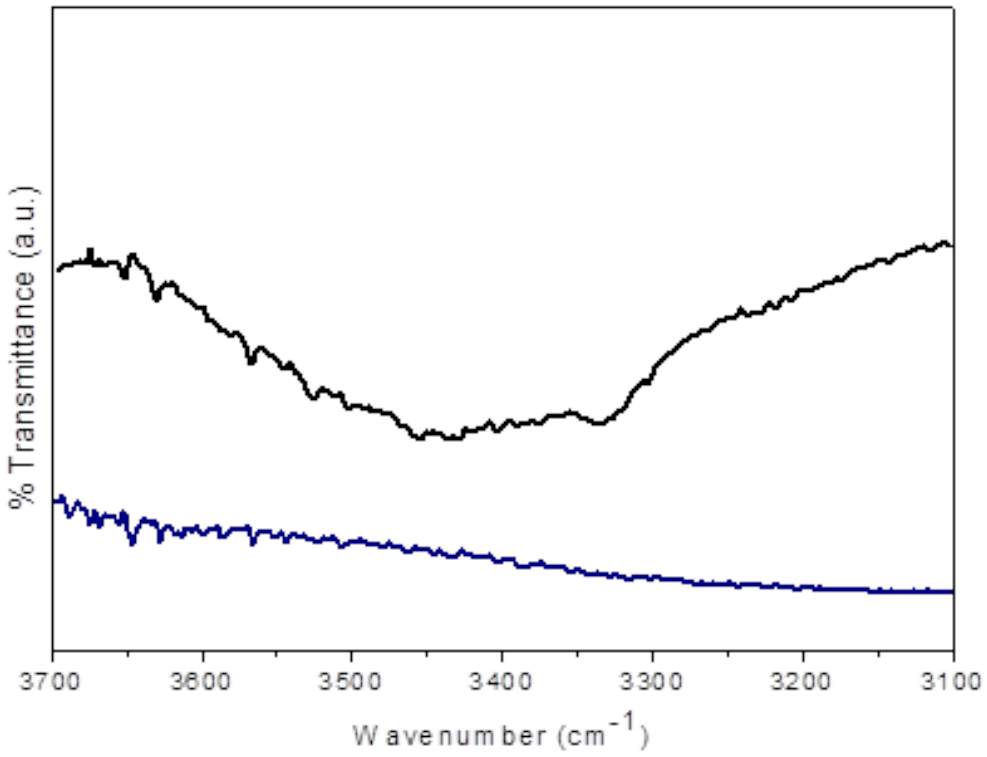

Figure 4.35: FTIR of the hydroxide stretching regions in $Tb_{13}(GeO_4)_6O_7(OH)$ (black) and $K_2TbGe_2O_7$ (blue) from 3700-3100 cm^{-1}.

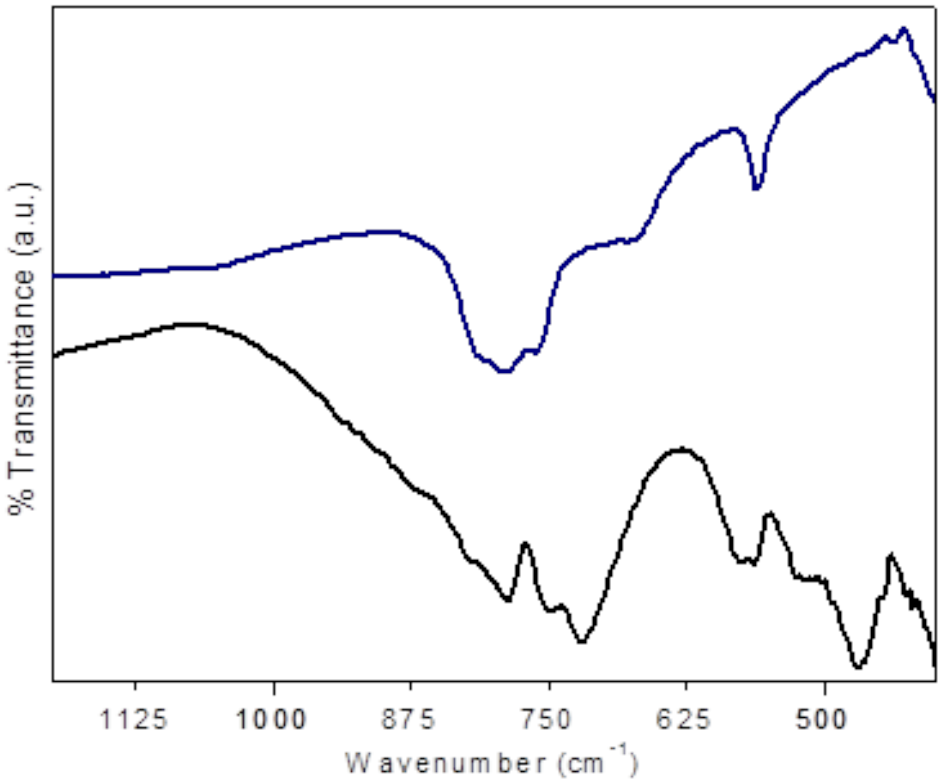

Figure 4.36: FTIR of germanate regions in $Tb_{13}(GeO_4)_6O_7(OH)$ (black) and $K_2TbGe_2O_7$ (blue) from 1200-400 cm^{-1}.

Hydrothermal Growth of $Cs_{0.5}RE_{13}(GeO_4)_6O_{3.5}F_{8.5}$ (RE = La-Sm)

As in extension of the rare-earth germanates into the larger rare-earth ions, the crystal structure of $Cs_{0.5}RE_{13}(GeO_4)_6O_{3.5}F_{8.5}$ (RE = La-Sm) has been synthesized and crystallographic data reported. Crystallographic data is reported below in **Table 4.9** with select bond distances reported in **Table 4.10**. This family is a salt-inclusion derivative of the $RE_{13}(GeO_4)_6O_7(OH)$ (RE = Gd-Yb) structural family reported also in this Chapter. Both structures contain very similar structural features that will be highlighted. Here, the pursuit of larger rare-earth ions causes a symmetry break from *R-3* to $P6_3/m$ and the larger rare-earth ions act as structural directors due to their larger coordination environments within the crystalline lattice.

Experimental Methods for $Cs_{0.5}RE_{13}(GeO_4)_6O_{3.5}F_{8.5}$ (RE = La-Sm)

Single crystals of the family $Cs_{0.5}RE_{13}(GeO_4)_6O_{3.5}F_{8.5}$ (RE = La-Sm) were grown from high-temperature and high-pressure hydrothermal conditions. The crystals display a rod-like habit and are typically between 2-3 mm in length after a 7 day reaction. This family of compounds can be grown in 6 *M* CsF at 650 °C to produce the target compounds. $Cs_{0.5}La_{13}(GeO_4)_6O_{3.5}F_{8.5}$ single crystals were grown from La_2O_3 (92 mg, 0.281 mmol) and GeO_2 (58 mg, 0.562 mmol). $Cs_{0.5}Pr_{13}(GeO_4)_6O_{3.5}F_{8.5}$ single crystals were grown from Pr_2O_3 (92 mg, 0.279 mmol) and GeO_2 (58 mg, 0.558 mmol). $Cs_{0.5}Nd_{13}(GeO_4)_6O_{3.5}F_{8.5}$ single crystals were grown from Nd_2O_3 (93 mg, 0.276 mmol) and GeO_2 (57 mg, 0.551 mmol). $Cs_{0.5}Sm_{13}(GeO_4)_6O_{3.5}F_{8.5}$ single crystals were grown from Sm_2O_3 (94 mg, 0.270 mmol) and GeO_2 (56 mg, 0.539 mmol). In each reaction a 2 : 1 stoichiometric ratio of RE^{3+} to Ge^{4+} was utilized. In each of these reactions, interaction

with the fluoride mineralizer causes incorporation of the salt in the crystalline lattice. EDX was used to confirm the trace amount of cesium and fluoride within the crystal structure.

Crystal Structure of $Cs_{0.5}RE_{13}(GeO_4)_6O_{3.5}F_{8.5}$ (RE = La-Sm)

As a representative of this structural class, $Cs_{0.5}La_{13}(GeO_4)_6O_{3.5}F_{8.5}$ will be used to discuss the structural features of this structure type. $Cs_{0.5}La_{13}(GeO_4)_6O_{3.5}F_{8.5}$ crystallizes in hexagonal space group $P6_3/m$ with unit cell parameters of a = 16.4087(8) Å and c = 7.2738(6) Å. It contains a complex lanthanide oxy-fluoride framework, ([La(1)O_6F_3], [La(2)O_7 or La(2)O_6F], [La(3)O_6F_2], and [La(4)O_3F_6]), and two distinct germanate sites [Ge(1)O_4] and [Ge(2)O_4]. Lanthanum oxide bond distances range from 2.413(4)-2.966(7) Å and La-F bond distances range from 2.3992(4)-2.848(6) Å. Germanium oxide tetrahedral units are isolated and display bond distances ranging from 1.704(5)-1.767(5) Å. The overall unit cell rendering is shown below in **Figure 4.38**. The structure has three types of crystallographic disorder within the lattice. First, O(8)/F(8) are split on a (0,0,z) *4e* Wkycoff position in which both positions are ¼ occupied. Second, a dynamic disorder of F(2), F(3), and Cs(1b) is occuring. F(2) and F(3) are 9/10 occupied and are present when Cs(1a) is present at bond distances of 2.8064(6) and 2.9010(7) Å, respectively. Cs(1b) is set at a site occupancy of 1/10 and is present when F(2) and F(3) are not. The presence of cesium and fluoride within the crystalline lattice was confirmed using EDX, **Table 4.11**. [La(3)O_6F_2] polyhedra are face-sharing with one another, through O(1), O(5), and O(7) atoms. At the same time each [La(3)O_6F_2] polyhedra is also edge-sharing O(1) and F(2) atoms. These units form a ring-like arrangement through edge-sharing of O(4)

atoms to form a network of six La(3) and 3 La(1) polyhedra. At the center of this ring is La(4), which forms the distorted [$La(4)O_3F_6$], and stabilizes the ring with connectivity to O(7) and F(2), **Figure 4.39**. Interestingly, the rings can be seen to propagate down the *c*-axis and interconnect via corner-sharing of O(2), O(6), and F(3) atoms to form foundational lanthanum oxy-fluoride columns, **Figure 4.41**. In this situation, a disordered Cs(1b) atom can fill the void space between rings when present in the lattice.

The O(8)/F(8) site serves as a unique trimeric vertex with lanthanum atoms. In this situation, one of two conformations is adapted at any given time: $La(2)O_7$ or $La(2)O_6F$. If O(8) is present, the $La(2)O_7$ is adapted. If F(8) is present, the $La(2)O_6F$ conformation is adapted. These groups connect to one another to form a trimer unit through μ-3 bridging of O(8)/F(8). These trimers are located at the corners of the unit cell and help to bridge the ring structures of La(1), La(3), and La(4) through corner-sharing of O(5) atoms.

Two distinct germanate sites serve as isolated building blocks that aid in holding the lanthanum framework together. Here, $Ge(1)O_4$ and $Ge(2)O_4$ can be seen to bridge the two distinct lanthanum subunits. $Ge(1)O_4$ is corner-sharing with La(1), La(2), and La(3) through O(4), O(5), O(6) atoms, **Figure 4.42a**. Ge(2)O4 is also corner-sharing with La(1), La(2), and La(3) polyhedra, but through O(4), **Figure 4.42b**.

Interestingly, unlike the $RE_{13}(GeO_4)_6O_7(OH)$ structure reported earlier, the $Cs_{0.5}RE_{13}(GeO_4)_6O_{3.5}F_{8.5}$ structure does not show evidence of a layered unit cell arrangement. The trimeric unit of $La(2)O_7$ or $La(2)O_6F$ can be seen to propagate along the [001] direction in **Figure 4.40**. The alternating trimeric units form columns along the

corner of the unit cell through corner-sharing of O(3) atoms. While the two structure types seem to be related by their architectural framework, the presence of cesium and fluoride within the $Cs_{0.5}RE_{13}(GeO_4)_6O_{3.5}F_{8.5}$ aids in stabilizing the larger rare-earth ions which are directors of dimensionality here. The larger rare-earth ion coordination causes a shift to lower symmetry and creating the column-like lanthanum framework reported.

PXRD was used to confirm the phase reported for the $Cs_{0.5}RE_{13}(GeO_4)_6O_{3.5}F_{8.5}$ (RE = La-Sm) family in which only the presence of rare-earth tri-fluorides (REF_3) was observed as a minor product, **Figure 4.37**. The absence of hydroxide within the crystalline lattice was confirmed by IR spectroscopy, reported in **Figure 4.43**. The pursuit to smaller rare-earth ions with 6 *M* CsF led to the synthesis of the structure type $RE_{13}(GeO_4)_6O_7(OH)$ (RE = Gd-Yb), which was reported earlier in this Chapter.

Table 4.9: Crystallographic data for $Cs_{0.5}RE_{13}(GeO_4)_6O_{3.5}F_{8.5}$ (RE = La-Pr).

empirical formula	**$Cs_{0.5}La_{13}(GeO_4)_6O_{3.5}F_{8.5}$**	**$Cs_{0.5}Pr_{13}(GeO_4)_6O_{3.5}F_{8.5}$**	**$Cs_{0.5}Nd_{13}(GeO_4)_6O_{3.5}F_{8.5}$**
formula weight (g/mol)	2909.33	2935.33	3036.57
crystal system	Hexagonal	Hexagonal	Hexagonal
space group, *Z*	*P63/m*, 2	*P63/m*, 2	*P63/m*, 2
temperature, K	298(2)	298(2)	298(2)
crystal size (mm)	0.04 x 0.045 x 0.5	0.055 x 0.065 x 0.062	0.040 x 0.045 x 0.052
***a*, Å**	16.4087(8)	16.2428(7)	16.1950(6)
***c*, Å**	7.2738(6)	7.1293(3)	7.0747(3)
volume, $Å^3$	1696.1(2)	1628.92(16)	1606.94(14)
calculated density ($\mu g/m^3$)	5.697	5.985	6.276
absorption coefficient (mm^{-1})	21.851	25.146	13.672
F(000)	2514	2566	1318
Θ range for data	2.482-30.559	2.508-28.318	2.515-30.532
reflections collected	1867	85537	23016
data/restraints/parameters	1867/0/113	1465/0/113	1759/0/113
final R [$I > 2\sigma(I)$] R1, wR2	0.0258, 0.0479	0.0205, 0.0441	0.0298, 0.0549
final R (all data) R1, wR2	0.0332, 0498	0.0234, 0.0450	0.0392, 0.0572
goodness-of-fit on F^2	1.092	1.125	1.143
largest diff. peak/hole, e/ $Å^3$	1.393/1.513	2.343/ -0.993	2.271/ -1.453

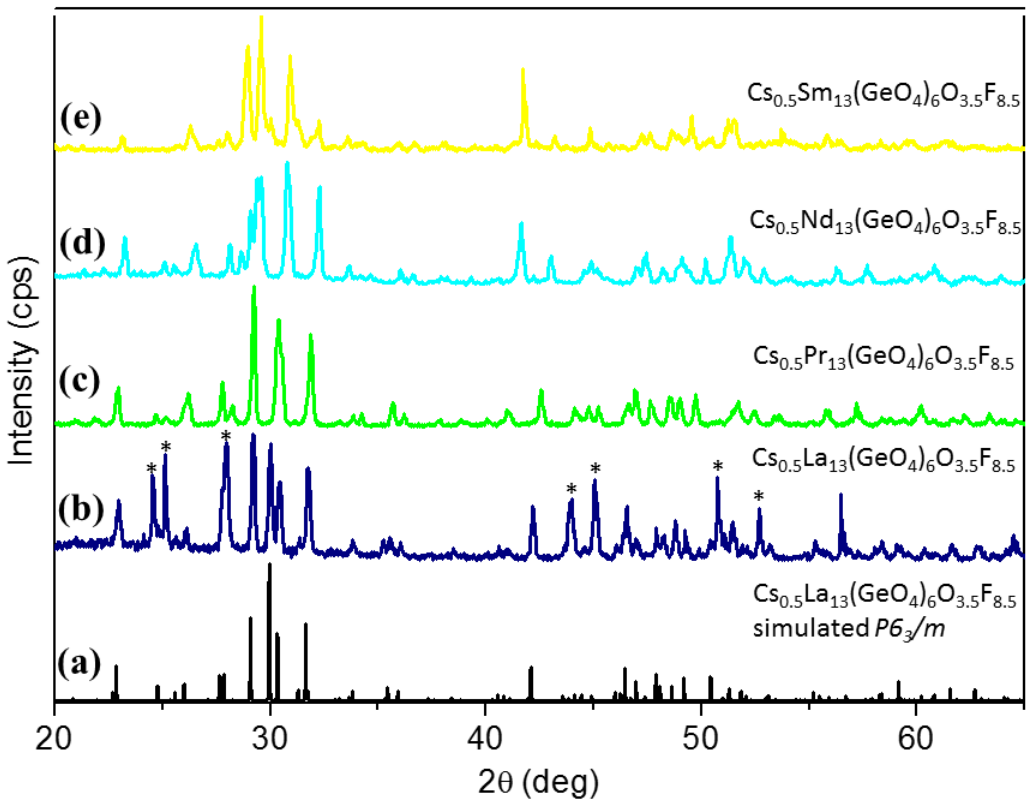

Figure 4.37: Powder overlay of reported $Cs_{0.5}RE_{13}(GeO_4)_6O_{3.5}F_{8.5}$ (RE = La-Sm) family. Reflections from minor product LaF_3 highlighted with (*).

Table 4.10: Select bond distances (Å) for reported $Cs_{0.5}RE_{13}(GeO_4)_6O_{3.5}F_{8.5}$ (RE = La-Nd).

$Cs_{0.5}La_{13}(GeO_4)_6O_{3.5}F_{8.5}$		**$Cs_{0.5}Pr_{13}(GeO_4)_6O_{3.5}F_{8.5}$**		**$Cs_{0.5}Nd_{13}(GeO_4)_6O_{3.5}F_{8.}$**	
La(1)O_6F_3		**Pr(1) O_6F_3**		**Nd(1) O_6F_3**	
La(1)−O(1)	2.512(5)	Pr(1)−O(1)	2.476(5)	Nd(1)−O(1)	2.460(6)
La(1)−O(4) x2	2.487(3	Pr(1)−O(4) x2	2.423(3)	Nd(1)−O(4) x2	2.416(4)
La(1)−O(4) x2	2.663(3)	Pr(1)−O(4) x2	2.632(3)	Nd(1)−O(4) x2	2.619(4)
La(1)−O(7)	2.481(4)	Pr(1)−O(7)	2.447(4)	Nd(1)−O(7)	2.424(5)
La(1)−F(2) x2	2.679(5)	Pr(1)−F(2) x2	2.649(4)	Nd(1)−F(2) x2	2.634(5)
La(1)−F(3)	2.848(6)	Pr(1)−F(3)	2.865(6)	Nd(1)−F(3)	2.914(7)
La(2)O_7 or La(2)O_6F		**Pr(2)O_7 or Pr(2)O_6F**		**Nd(2)O_7 or Nd(2)O_6F**	
La(2)−O(2)	2.967(7)	Pr(2)−O(2)	NA	Nd(2)−O(2)	NA
La(2)−O(3) x2	2.413(4)	Pr(2)−O(3) x2	2.352(5)	Nd(2)−O(3) x2	2.337(5)
La(2)−O(3) x2	2.639(5)	Pr(2)−O(3) x2	2.590(5)	Nd(2)−O(3) x2	2.555(6)
La(2)−O(5)	2.474(5)	Pr(2)−O(5)	2.432(5)	Nd(2)−O(5)	2.415(6)
La(2)−O(8) x2	2.4877(4)	Pr(2)−O(8) x2	2.4480(4)	Nd(2)−O(8) x2	2.4391(5)
La(2)−F(8) x2	2.3992(4)	Pr(2)−F(8) x2	2.3616(4)	Nd(2)−F(8) x2	2.3537(5)
La(3)O_6F_2		**Pr(3)O_8**		**Nd(3)O_8**	
La(3)−O(1)	2.549(4)	Pr(3)−O(1)	2.535(4)	Nd(3)−O(1)	2.495(4)
La(3)−O(2)	2.519(4)	Pr(3)−O(2)	2.463(4)	Nd(3)−O(2)	2.444(5)
La(3)−O(4)	2.727(3)	Pr(3)−O(4)	2.685(3)	Nd(3)−O(4)	2.671(4)
La(3)−O(5)	2.551(4)	Pr(3)−O(5)	2.535(4)	Nd(3)−O(5)	2.516(4)
La(3)−O(6)	2.428(4)	Pr(3)−O(6)	2.379(3)	Nd(3)−O(6)	2.372(4)
La(3)−O(7)	2.443(3)	Pr(3)−O(7)	2.390(3)	Nd(3)−O(7)	2.375(4)
La(3)−F(2)	2.537(4)	Pr(3)−F(2)	2.487(4)	Nd(3)−F(2)	2.478(5)
La(3)−F(3)	2.491(4)	Pr(3)−F(3)	2.435(4)	Nd(3)−F(3)	2.421(5)
La(4)O_3F_6		**Pr(4)O_9**		**Nd(4)O_9**	
La(4)−O(7) x3	2.541(4)	Pr(4)−O(7) x3	2.514(4)	Nd(4)−O(7) x3	2.501(5)
La(4)−F(2) x6	2.493(4)	Pr(4)−F(2) x6	2.444(4)	Nd(4)−F(2) x6	2.443(5)
Ge(1)O_4		**Ge(1)O_4**		**Ge(1)O_4**	
Ge(1)−O(1)	1.736(5)	Ge(1)−O(1)	1.736(5)	Ge(1)−O(1)	1.740(6)
Ge(1)−O(2)	1.720(5)	Ge(1)−O(2)	1.713(5)	Ge(1)−O(2)	1.711(6)
Ge(1)−O(3) x2	1.739(4)	Ge(1)−O(3) x2	1.739(5)	Ge(1)−O(3) x2	1.742(5)
Ge(2)O_4		**Ge(2)O_4**		**Ge(2)O_4**	
Ge(2)−O(4) x2	1.747(3)	Ge(2)−O(4) x2	1.749(3)	Ge(2)−O(4) x2	1.745(4)
Ge(2)−O(5)	1.767(5)	Ge(2)−O(5)	1.767(5)	Ge(2)−O(5)	1.774(6)
Ge(2)−O(6)	1.704(5)	Ge(2)−O(6)	1.702(5)	Ge(2)−O(6)	1.692(6)

* O(8) and F(2) are 0.25 SOF
* F(2)/F(3) are 0.9 SOF

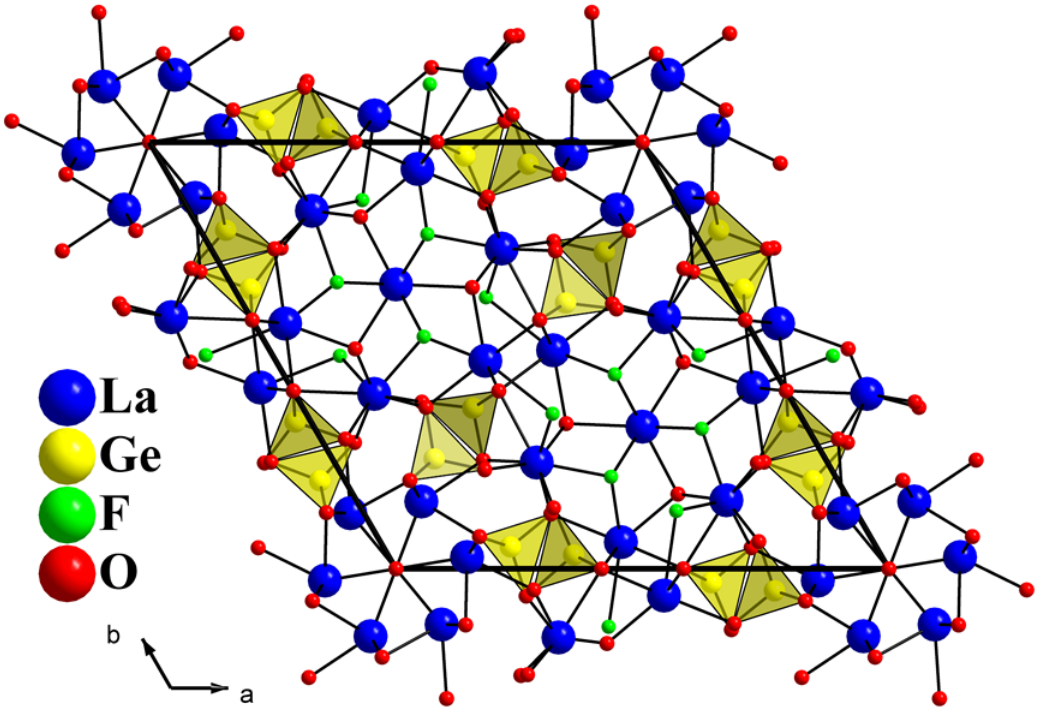

Figure 4.38: Unit cell rendering of $Cs_{0.5}La_{13}(GeO_4)_6O_{3.5}F_{8.5}$ viewed along the [001] direction.

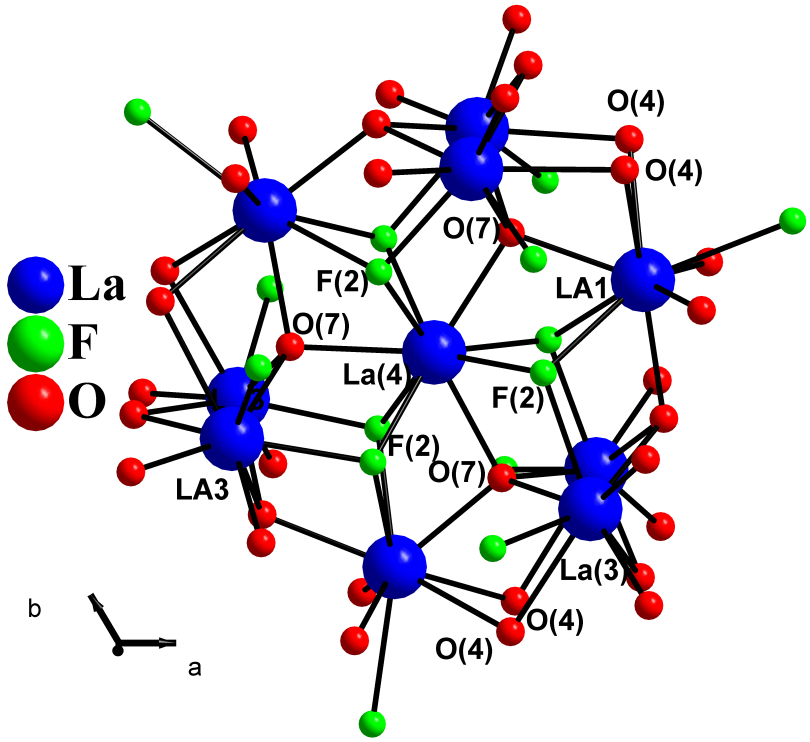

Figure 4.39: La(1), La(3), and La(4) connectivity viewed along the [001] direction.

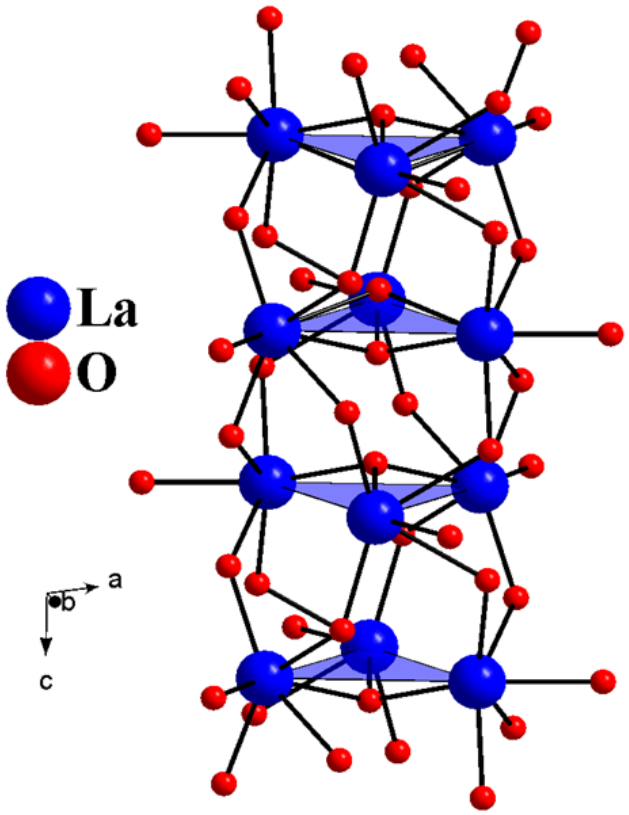

Figure 4.40: La(2) environment highlighting two distinct trimers alternating just off the [110] direction, forming a column within the lattice.

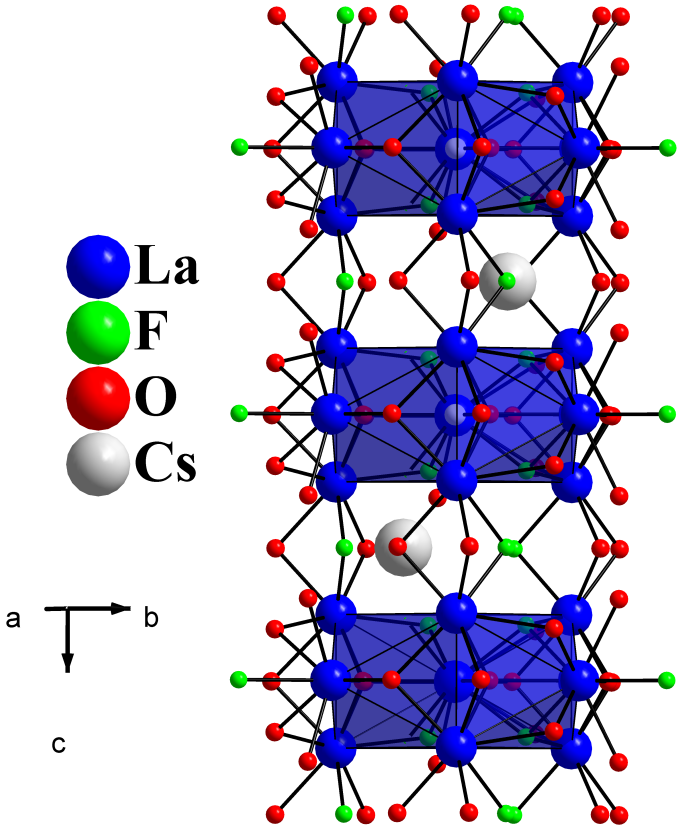

Figure 4.41: Ring structures of La(1), La(3), and La(4) forming columns along the [001] direction in which disordered Cs(1b) can reside when present.

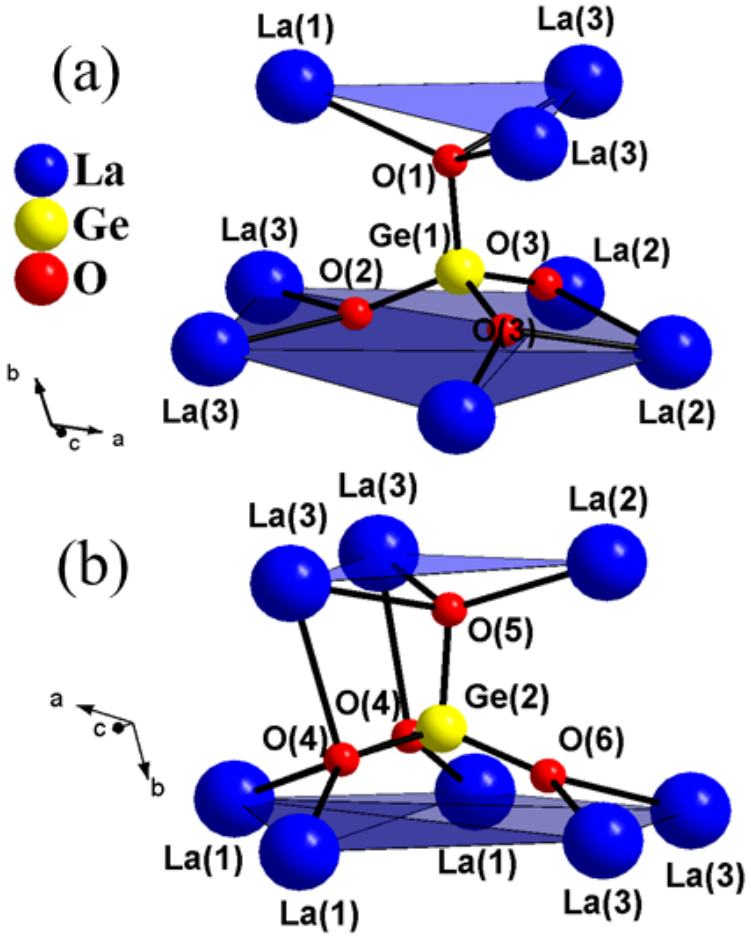

Figure 4.42: (a) Environment of $Ge(1)O_4$ highlighting connectivity to La(1), La(2) and La(3). (b) Highlighting $Ge(2)O_4$ connectivity also to La(1), La(2), and La(3). Germanium polyhedra interconnect the two distinct lanthanum sub-units within the lattice.

Table 4.11: EDX results for hydrothermally grown germanates: $Cs_{0.5}RE_{13}(GeO_4)_6O_{3.5}F_{8.5}$ (RE = La-Sm).

Compound	Experimental Results (atomic %)	Ideal Stoichiometric Results (atomic %)
$\mathbf{Cs_{0.5}La_{13}(GeO_4)_6O_{3.5}F_{8.5}}$	Cs-0.2 / La-24.9 / Ge-7.9 / O-32.3 / F-34.7	Cs-0.01 / La-23.4 / Ge-10.8 / O-49.5 / F-15.3
$\mathbf{Cs_{0.5}Pr_{13}(GeO_4)_6O_{3.5}F_{8.5}}$	Cs- 0.1/ Pr-23.5 / Ge-10.9 / O-55 / F-10.4	Cs-0.01 / Pr-23.4 / Ge-10.8 / O-49.5 / F-15.3
$\mathbf{Cs_{0.5}Nd_{13}(GeO_4)_6O_{3.5}F_{8.5}}$	Cs-0.7 / Nd-22.4 / Ge-8.8 / O-34 / F-16.6	Cs-0.01 / Nd-23.4 / Ge-10.8 / O-49.5 / F-15.3
$\mathbf{Cs_{0.5}Sm_{13}(GeO_4)_6O_{3.5}F_{8.5}}$	Cs-0.4 / Sm-19.4 / Ge-15.0 / O-59.5 / F-5.7	Cs-0.01 / Sm-23.4 / Ge-10.8 / O-49.5 / F-15.3

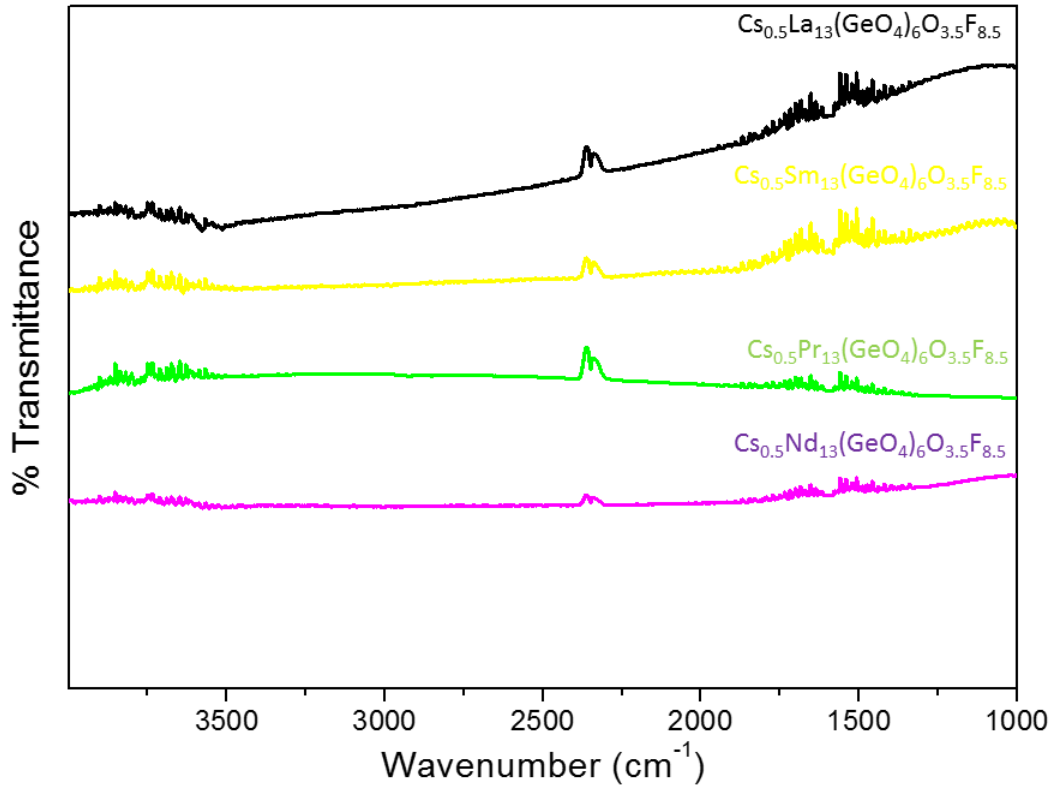

Figure 4.43: IR plots of reported rare-earth germanates: $Cs_{0.5}RE_{13}(GeO_4)_6O_{3.5}F_{8.5}$ (RE = La-Sm).

Conclusions about Hydrothermal Rare-Earth Germanate Reactions

While the rare-earth ions have often been viewed as a monotonic chemical block, their structural chemistry in the presence of oxyanion building blocks such as silicates and germanates indicates that this is not the case. [42] In particular, the chemistry across the f-block ion silicates in hydrothermal aqueous fluids has consistently shown an unexpectedly diverse behavior, leading to the emergence of a wide range new materials with interesting solid-state frameworks. In Chapter 3, an investigation into the chemistry of barium rare-earth silicates ($Ba_2RE_2Si_4O_{13}$) (RE = La^{3+}-Ho^{3+}) and barium rare-earth silicate fluorides ($Ba_2RE_2Si_4O_{12}F_2$) (RE = Er^{3+}-Lu^{3+}) in high-temperature and high-pressure hydrothermal conditions to determine the effect of rare-earth size on phase transitions between these structures was reported. [42] In tandem, a number of other rare-earth and refractory silicates was investigated including $KSrRESi_3O_9$ (RE = Tb-Yb) and wadeite mineral type $A_2M^{+4}B_3O_9$: $K_2TiSi_3O_9$ $K_2SnSi_3O_9$, $Rb_2USi_3O_9$, $Cs_2HfGe_3O_9$, and $Cs_2ZrGe_3O_9$. In a logical extension of this work, an investigation of the chemistry of rare-earth germanates in hydrothermal fluids, typically using aqueous bases, such CsOH as a mineralizer, was explored. The tetrahedral building blocks of silica and germanium oxide also show very different structural chemistry despite belonging to the same periodic group and displaying similar coordination chemistry. The structural chemistry of metal germanates is further complicated by the fact that, unlike silicates, germanates often display coordination environments other than tetrahedral (five- and six-coordinate), which makes the possible phase space even greater. [43]

Interestingly, although germanates show a very rich structural chemistry in Ge-O frameworks, there are fewer examples of germanates directly coordinated to rare-earth metal centers where the germanates are not just tetrahedra or polymeric tetrahedra like the silicates. There are a number of interesting uranium compounds with unusual polygermanate building blocks beyond the conventional tetrahedra that were synthesized using high-temperature hydrothermal methods.[44-45] These interesting compounds strongly suggest that rare-earth germanates with non-tetrahedral building blocks can be synthesized and isolated under appropriate hydrothermal conditions. A systematic examination of the phase space of rare-earth germanates under these typical high-temperature hydrothermal reaction conditions with the belief that a menu of isolated tetrahedral germanates, various polymeric germanate clusters and of non-tetrahedral germanate building blocks, along with a wide variety of coordination environments of the rare-earth ions, would combine to provide an almost infinite possibility of new structure types.

The reaction of barium oxide, select rare-earth oxides, and germanium oxide in hydrothermal fluids was done using a hydroxide mineralizer of 6 *M* CsOH. Two new stable products were isolated. $BaREGeO_4(OH)$ (RE = Ho, Er) single crystals formed as a minor hydrothermal product as good single crystals (0.25 mm). This new structure type displays an isolated one-dimensional chain of rare-earth polyhedra that are connected through edge sharing of oxygen atoms of isolated GeO_4 building blocks forming sheets with Ba^{2+} ions between layers. A second product major product $BaRE_{10}(GeO_4)_4O_8$

(RE=Ho, Er) displays a unique sheet-like arrangement involving four unique rare-earth sites separated by Ba^{2+} ions and coordinated by isolated GeO_4 units.

Compared to recently investigated rare-earth silicates, the phase stability of the rare-earth germanates appears much more complex. While the SiO_4 and GeO_4 building blocks display many of the same coordination features, the hydrothermal chemistry of these rare-earth building blocks thus far are quite different. The IR, Raman and photoluminescence spectroscopy also correlated well with the observed structures The introduction of barium ions in the chemistry provides an additional chemical and structural variability. To our knowledge this is the first example of a rare-earth germanate containing a barium ion. These preliminary results suggest that a wide range of new rare-earth germanates will isolated as large single crystals and their magnetic and optical properties can be studied.

The results of Tb_4O_7 in the presence of germanium oxide (GeO_2) and concentrated hydroxide mineralizer KOH led to the investigation of $Tb_{13}(GeO_4)_6O_7(OH)$ and Tb^{+4} compound, $K_2TbGe_2O_7$. These compounds indicate an ability to stabilize various rare-earth oxidation states in such a way that leads to unobserved solution chemistry to date. $Tb_{13}(GeO_4)_6O_7(OH)$ contains a complex network of terbium oxide units having three-fold symmetry, and previous uncertainty about the structure type has been resolved in the centrosymmetric space group *R-3*. $K_2TbGe_2O_7$ stabilizes the Tb^{4+} oxidation state that is rare for complexes other than fluorides or binary oxides. The behavior of Tb^{+4} is being studied to see if it is unique to this germanate system or if it can be extended to other oxyanions.

Pursuit of the larger rare-earth germanates led to the synthesis and crystallization of a new salt-inclusion rare-earth germanate oxy-fluoride, $Cs_{0.5}RE_{13}(GeO_4)_6O_{3.5}F_{8.5}$ (RE = La-Nd). This family of compounds has many structural rare-earth framework similarities to that of the $RE_{13}(GeO_4)_6O_7(OH)$ compounds. Here two distinct lanthanide oxy-fluoride frameworks are stabilized by the presence of tetravalent germanium oxide units and the inclusion of CsF into the lattice. The key in the structural diversity is the stabilization of the rare-earth ion in various connectivities. It was found that the rare-earth ions are directors of dimensionality not only in silicate, but also germanate based solid-state frameworks presented herein.

The results of the rare-earth germanates has shown that soluble tetravalent tetrahedral building blocks can be used in tandem with the high-temperature and high-pressure technique has an avenue to new material synthesis and characterization. With the results and knowledge gained in this Chapter we now move onto an investigation of a much less soluble pentavalent building block, Nb^{+5}. In Chapter Five an investigation into the use of Nb_2O_5 as a semi-soluble hydrothermal building block serves as a logical extension into the role of ionic building blocks as stabilizing participants for crystallization of new and existing rare-earth niobates.

References

(1) Fulle, K.; Sanjeewa, L. D.; McMillen, C. D., Wen, Y., Rajamanthrilage, A. C., Anker, J. N., Chumanov, G., Kolis, J. W. One-Pot Hydrothermal Synthesis of $Tb^{III}_{13}Ge_6O_{31}(OH)$ and $K_2Tb^{IV}Ge_2O_7$: Preparation of a Stable Terbium(4+) Complex. *Inorg. Chem.* **2017**, *56*, 6044-6047.

(2) Demianets, L. N.; Lobachev, A. N.; Emelchenko, G. A. Rare Earth Germanates. *Crystals: Growth Properties and Applications*. **1980**, *4*, 101-144.

(3) Demianets, L. N. Hydrothermal synthesis of new compounds. *Prog. Cryst. Growth and Charact.* **1990**, *21*, 299-355.

(4) Felsche, J. The Crystal Chemistry of the Rare-Earth Silicates. *Struct. Bond.* **1973**, *13*, 99-197.

(5) Wickleder, M. S. Inorganic Lanthanide Compounds with Complex Anions. *Chem Rev.* **2002**, *102*, 2011-2087.

(6) Li, H.; Eddaudi, M.; Yaghi, O. M. An Open Framework Germanate with Polycubane-Like Topology. *Angew. Chem. Int. Ed.* **1999**, *38*, 653-655.

(7) Nenoff, T. M.; Harrison, W. T. A.; Stucky, G. D. $Na_3H_x(H_2PO_4)_x[(GeO)_4(GeO_4)_3]\cdot 4H_2O$: A rhombohedrally-distorted germanium pharmacosiderite analog with anion/cation exchange capabilities. *Chem. Mater.* **1994**, *6*, 525-530.

(8) Hazen, R. M.; Downs, R. T.; Finger, L. W. High-Pressure Framework Silicates. *Science* **1991**, *272*, 1769-1771.

(9) Finger, L. W.; Hazen, R. M. Crystal Chemistry of Six-Coordinated Silicon: a Key to Understanding the Earth's Deep Interior. *Acta. Cryst.* **1991**, *B47*, 561-580.

(10) Chen, P.-L.; Chiang, P.-Y.; Yeh, H.-C.; Chang, B.-C.; Lii, K.-H. Synthesis, crystal structure, magnetic and luminescence properties of $KEuGe_2O_6$: a europium cyclogermanate containing infinite chains of edge-sharing Eu-O polyhedra. *Dalton Trans.* **2008**, *13*, 1721-1726.

(11) Yeon, J.; Hardaway, J. B.; Sefat, A. S.; Latshaw, A. M.; zur Loye, H.-C. Crystal growth, structures, magnetic and photoluminescent properties of $NaLnGeO_4$ (Ln= Sm, Eu, Gd, Tb). *Solid State Sci.* **2014**, *34*, 24-30.

(12) Liu, S.-P.; Chen, M.-L.; Chang, B.-C.; Lii, K.-H. Flux Synthesis, Crystal Structure, and Photoluminscence of a Heterometallic uranyl-Europium Germanate with U=O-Eu Linkage: $K_3[(UO_2)Eu_2(Ge_2O_7)_2]$. *Inorg. Chem.* **2013**, *52*, 3990-3994.

(13) Becker, U. W.; Felsche, J. Phases and structural relations of the rare earth germanates $RE_2Ge_2O_7$, RE= La-Lu. *J. Alloys Compd.* **1987**, *128*, 269-280.

(14) Byrappa, K; Yoshimura, M. *Handbook of Hydrothermal Technology*; Noyes Publications: Park Ridge, NJ, 2001.

(15) Emelchenko, G. A.; Demyanets, L. N.; Lobachev, A. N. Hydrothermal Crystal Synthesis in the $Ho_2O_3(Yb_2O_3)$-GeO_2-KF-H_2O Systems. *J. Solid State Chem.* **1975**, *14*, 209-215.

(16) Emirdag-Eanes, M.; Kolis, J. W. Hydrothermal synthesis, characterization and magnetic properties of $NaVGe_2O_6$ and $LiVGe_2O_6$. *Mat. Res. Bull.* **2004**, *39*, 1557-1567.

(17) Emirdag-Eanes, M.; Kolis, J. W. Hydrothermal synthesis and characterization of a new layered Li_2VGeO_5. *J. Alloys Compd.* **2004**, *370*, 90-93.

(18) Emirdag-Eanes, M.; Krawiec, M.; Kolis, J. W. Hydrothermal synthesis and structural characterization of $NaLnGeO_4$ (Ln=Ho, Er, Tb, Tm, Yb, Lu) family of lanthanide germanates. *J. Chem. Crystallogr.* **2001**, *31*, 281-285.

(19) Emirdag-Eanes, M.; Pennington, W. T.; Kolis, J. W. Synthesis, structural characterization, and magnetic properties of $NaRE_9(GeO_4)_6O_2$ (RE=Nd, Pr). *J. Alloys Compd.* **2004**, *366*, 76-80.

(20) Cascales, C.; Zaldo, C. Crystal-Field Analysis of Eu3+ Energy Levels in the New Rare-Earth R BiY1−xRxGeO$_5$ Oxide. *J. Solid State Chem.* **2003**, *171* (1), 262–267.

(21) Goyot, M.; Ille, B.; Lebrun, P.; Martin, J. P. Performances of a Preamplifier-Silicon Photodiode Readout System Associated with Large BGO Crystal Scintillators. *Nucl. Instrum. Methods Phys. Res. Sect. Accel. Spectrometers Detect. Assoc. Equip.* **1988**, *263* (1), 180–187.

(22) Zhao, X.; Yan, T.; Wang, K.; Yan, Y.; Zou, B.; Yu, J.; Xu, R. $NaEu_3(GeO_4)_2(OH)_2$: A High-Pressure-Stable Photoluminescent Lanthanide Germanate. *Eur. J. Inorg. Chem.* **2012**, *2012* (15), 2527–2532.

(23) Emirdag-Eanes, M.; Krawiec, M.; Kolis, J. W. Hydrothermal Synthesis and Structural Characterization of $NaLnGeO_4$ (Ln = Ho, Er, Tb, Tm, Yb, Lu) Family of Lanthanide Germanates. *J. Chem. Crystallogr.* **2001**, *31* (5), 281–285.

(24) Yeon, J.; Hardaway, J. B.; Sefat, A. S.; Latshaw, A. M.; zur Loye, H.-C. Crystal Growth, Structures, Magnetic and Photoluminescent Properties of $NaLnGeO_4$ (Ln=Sm, Eu, Gd, Tb). *Solid State Sci.* **2014**, *34*, 24–30.

(25) Lipina, O. A.; Surat, L. L.; Tyutyunnik, A. P.; Enyashin, A. N.; Chufarov, A. Y.; Zubkov, V. G. Structure and Optical Properties of $KLa_9(GeO_4)_6O_2$ and $KLa_{8.37}Eu_{0.63}(GeO_4)_6O_2$. *Chem. Phys. Lett.* **2017**, *667*, 9–14.

(26) Latshaw, A. M.; Wilkins, B. O.; Morrison, G.; Smith, M. D.; zur Loye, H.-C. $A_5RE_4X[TO_4]_4$ Crystal Growth: Fluoride Flux Synthesis of $Na_5Ln_4F[GeO_4]_4$ (Ln=Pr, Nd), the First Quaternary Germanate Oxyfluorides. *J. Solid State Chem.* **2016**, *239*, 200–203.

(27) Hughey, K.; Yeon, J.; zur Loye, H.-C. Crystal Growth and Structure Determination of the New Neodymium Germanate, $Na_2NdGeO_4(OH)$. *J. Chem. Crystallogr.* **2014**, *44* (6), 320–323.

(28) Hughey, K.; Yeon, J.; zur Loye, H.-C. Crystal Growth and Structure Determination of the New Neodymium Germanate, $Na_5Nd_4Ge_4O_{16}(OH)$. *J. Chem. Crystallogr.* **2014**, *44* (7), 376–379.

(29) Chen, P.-L.; Chiang, P.-Y.; Yeh, H.-C.; Chang, B.-C.; Lii, K.-H. Synthesis, Crystal Structure, Magnetic and Luminescence Properties of $KEuGe_2O_6$: A Europium Cyclogermanate Containing Infinite Chains of Edge-Sharing Eu–O Polyhedra. *Dalton Trans.* **2008**, *0* (13), 1721–1726.

(30) Ananias, D.; Rainho, J. P.; Ferreira, A.; Lopes, M.; Morais, C. M.; Rocha, J.; Carlos, L. D. Synthesis and Characterization of Er(III) and Y(III) Sodium Silicates: $Na_3ErSi_3O_9$, a New Infrared Emitter. *Chem. Mater.* **2002**, *14* (4), 1767–1772.

(31) Becker, U. W.; Felsche, J. Phases and Structural Relations of the Rare Earth Germanates $RE_2Ge_2O_7$, RE ≡ La-Lu. *J. Common Met.* **1987**, *128*, 269–280.

(32) Piccinelli, F.; Pedroni, M.; Cagliero, S.; Speghini, A.; Bettinelli, M. Structural Study of $Ca_2Gd_2Ge_2O_9$ and Optical Spectroscopy of the Eu^{3+} Dopant Ion. *J. Solid State Chem.* **2014**, *212*, 180–184.

(33) Piccinelli, F.; Lausi, A.; Bettinelli, M. Structural Investigation of the New $Ca_3Ln_2Ge_3O_{12}$ (Ln=Pr, Nd, Sm, Gd and Dy) Compounds and Luminescence Spectroscopy of $Ca_3Gd_2Ge_3O_{12}$ Doped with the Eu3+ Ion. *J. Solid State Chem.* **2013**, *205*, 190–196.

(34) Lipina, O. A.; Surat, L. L.; Melkozerova, M. A.; Tyutyunnik, A. P.; Leonidov, I. I.; Zubkov, V. G. Synthesis, Crystal Structure and Luminescence Properties of $CaY_{2-x}Eu_xGe_3O_{10}$ (x=0–2). *J. Solid State Chem.* **2013**, *206*, 117–121.

(35) Zubkov, V. G.; Tarakina, N. V.; Leonidov, I. I.; Tyutyunnik, A. P.; Surat, L. L.; Melkozerova, M. A.; Zabolotskaya, E. V.; Kellerman, D. G. Synthesis and Crystal Structure of $Ln_2M^{2+}Ge_4O_{12}$, Ln=rare-Earth Element or Y; M=Ca, Mn, Zn. *J. Solid State Chem.* **2010**, *183* (5), 1186–1193.

(36) Swaffer, M.; Slater, P. R.; Gover, R. K.; Matsumura, T.; Kanno, R.; Kamiyama, T. La_2MgGeO_6: A Novel Ge Based Perovskite Synthesized under Ambient Pressure. *ChemInform* **2002**, *33* (45), 17.

(37) Ochi, Y.; Morikawa, H.; Marumo, F.; Nozaki, H. Structures and Magnetic Properties of Rare Earth Compounds in the Melilite Group. *Yogyo-Kyokai-Shi* **1983**, *91*, 229–235.

(38) Berastegui, P.; Hull, S.; Garcı Garcı, F. J.; Grins, J. A Structural Investigation of $La_2(GeO_4)O$ and Alkaline-Earth-Doped $La_{9.33}(GeO_4)_6O_2$. *J. Solid State Chem.* **2002**, *168* (1), 294–305.

(39) Latshaw, A. M.; Hughey, K. D.; Smith, M. D.; Yeon, J.; zur Loye, H.-C. Photoluminescent and Magnetic Properties of Lanthanide Containing Apatites: $Na_xLn_{10-x}(SiO_4)_6O_{2-y}F_y$, $Ca_xLn_{10-x}(SiO_4)_6O_{2-y}F_y$ (Ln = Eu, Gd, and Sm), $Gd_{9.34}(SiO_4)_6O_2$, and $K_{1.32}Pr_{8.68}(SiO_4)_6O_{1.36}F_{0.64}$. *Inorg. Chem.* **2015**, *54* (3), 876–884.

(40) Bueno, L. A.; Gouveia-Neto, A. S.; Costa, E. B. da; Messaddeq, Y.; Ribeiro, S. J. L. Structural and Spectroscopic Study of Oxyfluoride Glasses and Glass-Ceramics Using Europium Ion as a Structural Probe. *J. Phys. Condens. Matter* **2008**, *20* (14), 145201.

(41) A.S. Gouveia-Neto, E.B. da Costa, L.A. Bueno, S.J.L. Ribeiro, Intense red upconversion emission in infrared excited holmium-doped $PbGeO_3$–PbF_2–CdF_2 transparent glass ceramic, *J. Lumin.* **2004**, *110*, 79–84.

(42) Ragin, T.; Kochanowicz, M.; Zmojda, J.; Dorosz, D. Spectroscopic properties of bismuth-germanate glasses co-doped with erbium and holmium ions. *SPIE* **2014**, *9228*, 92280C-1-92280C-8.

(43) Brese, N. E.; O'Keeffe, M. O. Bond-valence parameters for solids. *Acta Crystallogr. B.* **1991**, 47, 192–197.

(44) Brown, I. D.; Altermatt, D. Bond-valence parameters obtained from a systematic analysis of the Inorganic Crystal Structure Database. *Acta Crystallogr. B.* **1985**, *B41*, 244–247.

(45) Orera, A.; Sanjuan, M. L.; Kendrick, E.; Orera V. M.; Slater, P. R. Raman spectroscopy studies of apatite -type germanate oxide ion conductors: correlation with interstitial oxide ion location and conduction. *J. Mater. Chem.* **2010**, *20*, 2170–2175.

(46) Kroumova, E.; Aroyo, M. I.; Perez-Mato, J. M.; Kirov, A.; Capillas, C.; Ivantchev, S.; Wondratschek, H. Bilbao Crystallographic Server : Useful Databases and Tools for Phase-Transition Studies, Phase Transit. **2003**, *76*, 155–170.

(47) Wierzbicka-Wieczorek, M.; Kolitsch, U.; Panczer, G.; Giester, G.; Chanmuang, C.; Grzechnik, A. Crystal structures and photoluminescence properties of two novel sorosilicates with an unprecedented ratio of di- and trisilicate groups: $Ba_2Ho_{10}(Si_2O_7)_3(Si_3O_{10})_2$ and isotypic $Ba_2Er_{10}(Si_2O_7)_3(Si_3O_{10})_2$, *J. Solid State Chem.* **2017**, *252*, 33–42.

(48) Cunningham, B. B.; Feay, D. C. Rollier, M. A. "Terbium Tetrafluoride: Preparation and Properties" *J. Am Chem. Soc.* **1954**, *76*, 3361-3363.

(49) MacChesney, W.; Sherwood H. J.; Potter, J. F. Preparation and Low Temperature Magnetic Properties of the Terbium Oxides. *J. Chem. Phys.* **1966**, *44*, 596-601.

(50) Baenzinger, N. C. Eick, H. A. Schuldt, H. S. Eyring, L Terbium Oxides III. X-ray Diffraction Studies of Several Stable Phases. *J. Am, Chem.* Soc. **1961**, *83*, 2219-2223.

(51) El-Ghozzi, M.; Avignant, D. Crystal chemistry and magnetic structures of Tb(IV) fluorides. *J. Fluorine Chem.* **2001**, *107*, 229-233.

(52) Largeau, E.; El-Ghozzi, M.; Avignant, D. Synthesis and Crystal Structure of a New Mixed-Valent Terbium Fluoride, $KTb^{III}Tb^{IV}{}_2F_{12}$, and Related $KLn^{III}M^{IV}{}_2F_{12}$ Compounds (M^{IV}=Tb, Zr, Hf; Ln^{III}=Ce-Lu). *J. Solid State Chem.* **1998**, *139*, 248-258.

(53) Josse, M.; Dubois, M.; El-Ghozzi, M.; Avignant, D. Synthesis and crystal structures of new mixed-valence terbium (III/IV) fluorides with a random distribution between Tb^{+3} and Tb^{+4}. *J. Alloys Compd.* **2004**, *374*, 213-218.

(54) Tezuka, K.; Hinatsu, Y.; Shimojo, Y.; Morii, Y. Study in the Crystal and Magnetic Structures of $SrTbO_3$ and $BaTbO_3$ by Powder Neutron Diffraction. *J. Phys. Condens. Matter* **1998**, *10*, 11703-11712.

(55) Wolf, R.; Hoppe, R. "Über Na_2PrO_3 und Na_2TbO_3" *Z. Anorg. Allg. Chem.* **1988**, *556*, 97–108.

(56) Voigt, S., Werthmann, R. Hoppe, R. NeueVertreter des $K_2Li_{14}[Pb_3O_{14}]$-Typs $Cs_2Li_{14}[Tb_3O_{14}]$ und $K_2Li_{14}[Zr_3O_{14}]$. *Z. Anorg. Allg. Chem.* **1989**, *574*, 65-78.

(57) Doi, Y.; Wakeshima, M.; Hinatsu, Y.; Tabo, A.; Ohoyama, K.; Yamaguchi, Y. Magnetic and Calorimetric Studies on 6H-Perovskite $Ba_3TbRu_2O_9$. *J. Alloys and Compd.* **2002**, *344*, 166-169.

(58) Doi, Y.; Ninomiya, K.; Hinatsu, Y.; Ohoyama, K. Structure and Magnetic Properties of Two-Dimensional Antiferromagnetic Na_2TbO_3. *J. Phys. Condens. Matter* **2005**, *17*, 4393-4401.

(59) Hobart, D.E.; Samhoun, K.; Young, J.P.; Norvell, V.E.; Mamantov, G.; Peterson, J.R. Stabilization of Praseodymium (IV) and Terbium (IV) in Aquoues Carbonate Solution. *Inorg. Nucl. Chem. Lett.* **1980**, *16*, 321-328.

(60) Varlashkin, P.G.; Begun, G.M.; Peterson, J.R. On the Nature of Tetravalent Terbium in Carbonate Hydroxide Solutions. *J. Less Common Metals* **1985**, *109*, 123-134.

(61) Li, X.; Dong, W.; Qi, Y.; Wang, D.; Yang, R. Studies on the Stabilization of Terbium (IV) in Aqueous Tetrametaphosphate Solution. *Polyhedron* **1991**, *10*, 1479-1483.

CHAPTER FIVE

HYDROTHERMAL GROWTH OF RARE-EARTH TITANATES

Introduction

In this Chapter, an examination of the hydrothermal chemistry of the binary system RE_2O_3-TiO_2 (RE = La – Lu) will be examined in detail. It has been shown in previous Chapters that tetravalent tetrahedral ions like Si^{4+} and Ge^{4+} display new phase chemistry in the presence of rare-earth ions under high-temperature and high-pressure hydrothermal conditions. The ability to form various solid-state networks while simultaneously increasing the solubility of refractory rare-earth oxides in solution is key to the formation of high-quality single crystal grown. In the RE-Si and RE-Ge Chapters, an examination of the various structural formations with rare-earth oxides in the presence of tetravalent metal oxides led to a rich systematic chemistry study of new compounds. The key variable in all cases is finding a soluble, stable and predictable building block in hydrothermal conditions that can aid in the solubility of refractory oxides, which will lead to single crystal growth.

Herein, an examination of the hydrothermal phase space of RE ions with a tetravalent building block is detailed. The difference in this case is that it is a d-block ions with empty d-orbitals Unlike tetravalent building blocks of Si^{4+} and Ge^{4+}, Ti^{4+} readily adopts a 6-coordinate environment, in most cases. The Ti^{4+} ion is an excellent candidate as a hydrothermal building block for several reasons. In addition to adopting a Ti^{4+},

titanium can also adapt the reduced Ti^{3+} and Ti^{+2} oxidation states in certain environments. Additionally, Ti^{4+} can adopt a variety of coordination environments including 4, 5 and 6-coordinate. Coupling the flexible oxidation state and coordination environments of titanium with its relatively small crystallographic radius (0.88 Å) makes this RE-Ti binary system an ideal candidate to investigate under high-pressure and high-pressure conditions.

Rare-earth (*RE* = La-Lu, Y) titanates have a long history of study, particularly those exhibiting $RE_2Ti_2O_7$ pyrochlore-type structures.[1,2] These receive considerable attention due to their unusual magnetic behavior including spin frustration and spin ice behavior.[3–12] The rare-earth titanates have also been investigated for several other potential properties and applications, including ionic conductivity, actinide immobilization and high-temperature piezoelectricity.[13–21]

The cubic (*Fd-3m*) pyrochlore has become the most well-known and studied structure type of the rare-earth titanates.[1,2,16] Other polymorphs of the $RE_2Ti_2O_7$ formulation are also known, particularly those of the early rare-earths (La, Pr, Nd) with polar biaxial structures.[19,21–26] In addition, there are rare-earth titanates, such as $RETiO_3$,[27] RE_2TiO_5 (*RE* = Yb, Dy, Gd, Sm, Nd, La),[28–31] $La_4Ti_3O_{12}$,[32,33] and $CeTi_2O_6$,[34] in the literature that display complex three dimensional (3-D) frameworks with uses ranging from photo-catalysts to ceramics for electronic circuits.

Due to the high melting points of the rare-earth oxides (> 2000 °C) and the tendency of Ti^{4+} oxides to become reduced at high reaction temperatures to form defect structures,[35,36] the exploration of relatively lower reaction temperature techniques is of

interest. Many solid-state techniques employed in the synthesis of rare-earth titanates lead to formation of powder or poor single crystal quality due to oxygen defects, thermal strain and contaminations from crucibles at high-temperatures. The need for high quality single crystal is essential to study, for example, subtle but important effects such as site symmetry upon ordering in applied magnetic fields and complex frustrated structures.

The chemistry of this series of rare-earth titanates is summarized and the single crystal structures of the new species $La_5Ti_4O_{15}(OH)$ **I**, $Sm_3TiO_5(OH)_3$ **II**, $Lu_5Ti_2O_{11}(OH)$ **III** and $Ce_2Ti_4O_{11}$ **IV** are described. Additionally, the role of the mineralizer was examined by comparing products using concentrated hydroxide fluids to those obtained from concentrated fluorides. The structural classes appear to be a function of the size of the rare-earth ion as well. The synthetic techniques employed, crystal structure and other analysis will be discussed. Several of the compounds have unusual structural relationships with some seemingly unrelated materials and these structural relationships are additionally discussed.

Hydrothermal Crystal Growth and Reagents

A high-temperature (700 °C) hydrothermal technique was employed to synthesize new refractory rare-earth (*RE*) oxide and oxy-hydroxide materials. Representative crystals of the reported compounds are shown in **Figure 5.1**. In each reaction, approximately 0.2 g of reactants with 0.4 mL of either 20 *M* KOH or 30 *M* CsF mineralizer fluids were used. In the case of $Ce_2Ti_4O_{11}$, a 6 *M* CsF mineralizer was used to achieve the best quality single crystals, hydroxide mineralizers led to powder products only. All the reactions were performed in 6.4 cm long silver ampoules with an outer diameter of 0.64 cm. The weld-sealed silver ampoules were loaded into a Tuttle cold-seal style autoclave and filled with distilled water at 80% of free volume to provide suitable counter pressure. The autoclave was heated to 700 °C for seven days at a typical pressure of 150 MPa. After cooling to room temperature, the crystals were retrieved by washing the ampoule with deionized water. In most cases the final products were large, uniform single crystals with sizes ranging from 0.5-1 mm, although crystals as large as several millimeters could be obtained in some cases. Occasionally, some additional powder consisting of rare-earth oxide or oxy-hydroxide accompanied the product, but was a minor impurity. The stoichiometric ratios and amounts used are given in detail below. The chemicals used in this study were used as received, without further purification: La_2O_3 (Alfa Aesar, 99.999%), Ce_2O_3 (CERAC, 99.9%), Pr_2O_3 (Alfa Aesar, 99.99%), Nd_2O_3 (Alfa Aesar, 99.99%), Sm_2O_3 (Alfa Aesar, 99.99%), Eu_2O_3 (HEFA Rare Earth, 99.9%), Gd_2O_3 (HEFA Rare Earth, 99.9%), Tb_4O_7 (HEFA Rare Earth, 99.9%), Dy_2O_3 (STREM, 99.9%), Ho_2O_3 (HEFA Rare Earth, 99.9%), Er_2O_3 (Alfa Aesar, 99.99%),

Tm_2O_3 (HEFA Rare Earth, 99.9%), Yb_2O_3 (HEFA Rare Earth, 99.99%), Lu_2O_3 (Alfa Aesar, 99.9%), TiO_2(Alfa Aesar, 99.99%), CsF (Alfa Aesar, 99.9%), $CsOH{\cdot}xH_2O$ (Alfa Aesar, 99.9%) and KOH (Alfa Aesar, 99.98%).

Synthesis of $La_5Ti_4O_{15}OH$ and $Er_5Ti_4O_{15}OH$

The $La_5Ti_4O_{15}OH$ product was synthesized by a direct hydrothermal reaction of binary metal oxides La_2O_3 (134 mg, 0.412 mmol) and TiO_2 (66 mg, 0.823 mmol) in a 1 : 2 molar ratio with 0.4 mL of 20 *M* KOH and heated as described in the Experimental Section. The crystals were colorless needles with an average length of 0.5 mm. In the case of the $Er_5Ti_4O_{15}OH$ analog, Er_2O_3 (106 mg, 0.276 mmol) and TiO_2 (44 mg, 0.553 mmol) in a 1 : 2 molar ratio with 0.4 mL of 20 *M* KOH.

Synthesis of $Lu_5Ti_2O_{11}OH$, $Yb_5Ti_2O_{11}OH$ and $Tm_5Ti_2O_{11}OH$

$Lu_5Ti_2O_{11}OH$ was synthesized by a direct hydrothermal reaction of binary metal oxides Lu_2O_3 (143 mg, 0.358 mmol) and TiO_2 (57 mg, 0.717 mmol) in a 1 : 2 molar ratio with 0.4 mL of 20 *M* KOH and heated as described above. The resulting crystals were colorless plates with an average size of 0.5 mm. In the cases of $Yb_5Ti_2O_{11}OH$, Yb_2O_3 (107 mg, 0.271 mmol) and TiO_2 (43 mg, 0.541 mmol) and $Tm_5Ti_2O_{11}OH$, Tm_2O_3 (106 mg, 0.275 mmol) and TiO_2 (44 mg, 0.550 mmol); single crystals were synthesized in identical conditions to that of the Lu analog. Resultant single crystals were colorless plates for the Yb analog (0.45 mm) and pale yellow plates for the Tm analog (0.4 mm).

Synthesis of $Sm_3TiO_5(OH)$

The product was synthesized by a direct hydrothermal reaction of binary metal oxides Sm_2O_3 (169 mg, 485 mmol) and TiO_2 (31 mg, 385 mmol) in a 5 : 4 molar ratio, with 0.4

mL of 20 *M* KOH and heated as described above. The resulting crystals were yellow blocks with an average size of 1 mm.

Synthesis of $Ce_2Ti_4O_{11}$

The product was synthesized by a direct hydrothermal reaction of binary metal oxides Ce_2O_3 (101 mg, 0.352 mmol) and TiO_2 (84 mg, 1.06 mmol) in a 1 : 4 molar ratio, with a 0.4 mL of 6 *M* CsF and heated as described above. The resulting crystals were dark red polyhedra with an average size of 0.3 mm.

Cubic Pyrochlore (*Fd-3m*) Synthesis of $RE_2Ti_2O_7$ (RE = Lu – Gd) Single Crystals

Cubic pyrochlores ($RE_2Ti_2O_7$) were synthesized by direct reaction of the binary metal oxides under hydrothermal conditions as detailed in the Experimental Section. In the case of $Lu_2Ti_2O_7$-$Er_2Ti_2O_7$, single crystals were only realized while employing 30 *M* CsF concentrations. For $Gd_2Ti_2O_7$-$Ho_2Ti_2O_7$ single crystals can be grown from either 20 *M* KOH or 30 *M* CsF mineralizer solutions. For each reaction, a stoichiometric molar ratio of 1 : 2 (RE : Ti) was employed to give the pyrochlore crystals (Tb_4O_7 was a ratio of 1 : 4 RE : Ti). $Lu_2Ti_2O_7$ single crystals were synthesized by reacting Lu_2O_3 (107 mg, 0.269 mmol) and TiO_2 (43 mg, 0.538 mmol) powders were reacted. For the Yb analog, Yb_2O_3 (107 mg, 0.271 mmol) and TiO_2 (43 mg, 0.541 mmol) powders were reacted. For the Tm analog, Tm_2O_3 (106 mg, 0.275 mmol) and TiO_2 (44mg, 0.550 mmol) powders were reacted. For the Er analog, Er_2O_3 (106 mg, 0.277 mmol) and TiO_2 (44 mg, 0.553 mmol) powders were reacted. For the Ho analog, Ho_2O_3 (105 mg, 0.279 mmol) and TiO_2 (45 mg, 0.558 mmol) powders were reacted. For the Dy analog, Dy_2O_3 (105 mg, 0.281mmol) and TiO_2 (45 mg, 0.563 mmol) powders were reacted. For the Tb analog, Tb_4O_7 (105 mg,

0.140 mmol) and TiO_2 (45 mg, 0.562 mmol) powders were reacted. For the Gd analog, Gd_2O_3 (104 mg, 0.287 mmol) and TiO_2 (46 mg, 0.574 mmol) powders were reacted. Characteristic colors of the reported rare-earth titanates are shown in **Figure 5.1**.

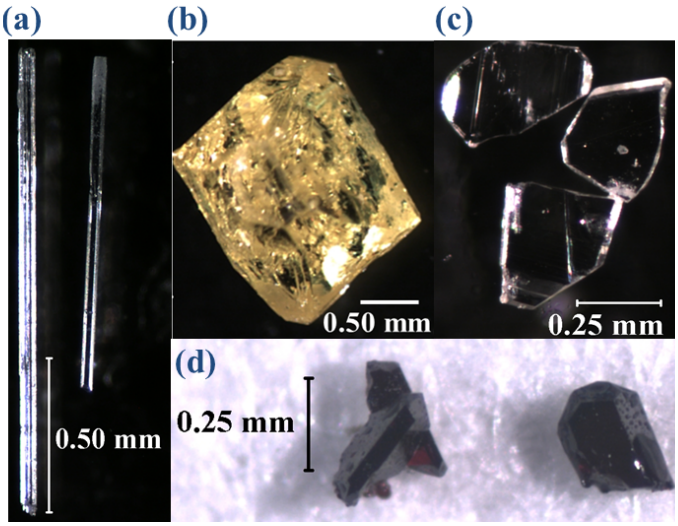

Figure 5.1: High-temperature and high-pressure hydrothermal growth of (**a**) $La_5Ti_4O_{15}(OH)$ (**b**) $Sm_3TiO_5(OH)_3$ (**c**) $Lu_5Ti_2O_{11}(OH)$ and (**d**) $Ce_2Ti_4O_{11}$ single crystals.

Structure Determination and Supporting Characterization

Single crystal structure characterization was conducted using a Bruker D8 Venture single crystal diffractometer with an Incoatec Mo Kα microfocus source and Photon 100 CMOS detector. In the case of $Lu_5Ti_2O_{11}(OH)$, *PLATON* was used to determine the twin law. In all of the structures studied, the thermal parameters of the metal sites in the crystallographic refinements suggested there was no mixing of Ti^{4+} and RE^{3+} at their respective sites. The results of the structure refinements are presented in **Table 5.1-5.2**, and selected bond lengths and bond valence sum calculations are given in **Tables 5.3-5.6**. Phase purity was studied using powder X-ray diffraction (PXRD). The PXRD data were collected using a Rigaku Ultima IV diffractometer equipped with Cu Kα radiation (λ = 1.5406 Å) in the range of 5-65° in 2θ with a scan speed of 0.25 degrees per minute and a step size of 0.02°.

Infrared (IR) spectroscopic analysis was used to confirm the presence of the hydroxide groups in the structures, **Figure 5.8**. Additionally, the elemental compositions of all the reported compounds were investigated using energy dispersive X-ray analysis (EDX), **Table 5.7**. IR spectra for selected compounds and elemental analysis are reported in the supporting information and are in good agreement with the structures determined by X-ray diffraction. Thermal Gravimetric Analysis (TGA) was employed to observe the evolution of water from the hydroxide containing rare-earth titantates reported herein. Here, nitrogen was used as the flowing gas at a flow rate of 100 mL/min and, at a heating and cooling rate of 10 °C/min from 25-800°C.

Table 5.1: Crystallographic data of rare-earth titanate hydroxides and titanates determined by single crystal X-ray diffraction.

	$La_5Ti_4O_{15}(OH)$ (I)	$Sm_3TiO_5(OH)_3$ (II)	$Lu_5Ti_2O_{11}(OH)$ (III)	$Ce_2Ti_4O_{11}$ (IV)
formula weight (g/mol)	1143.16	629.97	1163.62	647.84
crystal system	orthorhombic	monoclinic	monoclinic	monoclinic
space group, *Z*	*Pnnm* (no. 58), *4*	*$P2_1/m$* (no. 11*), 2*	*C2/m* (no. 12), *2*	*C2/c* (no. 15), *4*
Temperature (K)	298(2)	298(2)	298(2)	297(2)
Crystal size (mm)	0.27 x 0.04 x 0.03	0.04 x 0.05 x0.05	0.05 x 0.06 x 0.06	0.05 x 0.06 x 0.06
***a*, Å**	30.5152(12)	5.6066(2)	12.1252(9)	13.6875(7)
***b*, Å**	5.5832(2)	10.4622(4)	5.8243(4)	5.0955(3)
***c*, Å**	7.7590(3)	6.1258(2)	7.0407(5)	12.8592(7)
***β*, °**	----	104.7390(10)	106.939(3)	108.964(2)
volume ($Å^3$)	1321.92(9)	347.50(2)	475.65(6)	848.18(8)
D_{calc} (g/cm^3)	5.744	6.021	8.125	5.073
abs. coeff. (mm^{-1})	18.140	26.085	53.027	14.147
F(000)	2008	550	992	1168
Tmax, Tmin	1.0000, 0.6321	1.000, 0.7912	1.0000, 0.7013	1.0000, 0.7998
Θ range for data	2.709-26.498	3.439-28.309	3.024-26.498	3.147-26.490
Reflections collected	8894	8323	2796	7614
data/restraints/parameters	1452/0/129	914/2/69	552/48/58	874/0/78
final R [$I > 2\sigma(I)$] R1, wR2	0.0195, 0.0464	0.0148, 0.0314	0.0317, 0.0790	0.0180, 0.0476
final R (all data) R1, wR2	0.0203/0.0468	0.0158, 0.0318	0.0372, 0.0821	0.0203, 0.0747
goodness-of-fit on F^2	1.177	1.031	1.125	1.176
largest diff. pk/hl, e/ $Å^3$	1.124/-2.480	1.144/-1.041	1.739/-4.194	0.846/-1.135

Table 5.2: Crystallographic data for hydrothermally grown $Er_5Ti_4O_{15}(OH)$.

empirical formula	**$Er_5Ti_4O_{15}(OH)$ (V)**
formula weight (g/mol)	**1284.91**
crystal system	**orthorhombic**
space group, *Z*	***Pnnm* (no. 58), *4***
temperature, K	**273(2)**
crystal size (mm)	**0.12 x 0.08 x 0.02**
***a*, Å**	**29.7954(13)**
***b*, Å**	**5.3286(2)**
***c*, Å**	**7.4498(3)**
volume, $Å^3$	**1182.79(8)**
calculated density ($\mu g/m^3$)	**7.216**
absorption coefficient (mm^{-1})	**37.694**
F(000)	**2228**
Tmax, Tmin	**1.0000, 0.4169**
Θ range for data	**2.734-33.355**
reflections collected	**2349**
data/restraints/parameters	**2349/0/132**
final R [$I > 2\sigma(I)$] R1, wR2	**0.0244/0.0553**
final R (all data) R1, wR2	**0.0297/0.0566**
goodness-of-fit on F^2	**1.140**
largest diff. peak/hole, e/ $Å^3$	**2.241/-2.155**

Table 5.3: Bond distances (Å) of $La_5Ti_4O_{15}(OH)$ (I) and $Er_5Ti_4O_{15}(OH)$ (V).

$La_5Ti_4O_{15}(OH)$ (I)		**$Er_5Ti_4O_{15}(OH)$ (V)**	
$La(1)O_8$		**$Er(1)O_8$**	
La(1)−O(1) x 2	2.631(3)	**Er(1)−O(1) x 2**	2.418(4)
La(1)−O(4) x 2	2.567(3)	**Er(1)−O(4) x 2**	2.470(4)
La(1)−O(5) x 2	2.500(3)	**Er(1)−O(5) x 2**	2.353(4)
La(1)−O(6)	2.517(3)	**Er(1)−O(6)**	2.296(5)
La(1)−O(7)	2.586(4)	**Er(1)−O(7)**	2.342(5)
$La(2)O_7$		**$Er(2)O_7$**	
La(2)−O(2) x 2	2.360(4)	**Er(2)−O(2) x 2**	2.185(5)
La(2)−O(3)	2.567(4)	**Er(2)−O(3)**	2.308(5)
La(2)−O(4) x 2	2.471(3)	**Er(2)−O(4) x 2**	2.297(4)
La(2)−O(5) x 2	2.503(3)	**Er(2)−O(5) x 2**	2.443(4)
$La(3)O_8$		**$Er(3)O_8$**	
La(3)−O(2) x 2	2.366(3)	**Er(3)−O(2) x 2**	2.234(3)
La(3)−O(4) x 2	2.603(3)	**Er(3)−O(4) x 2**	2.494(4)
La(3)−O(5) x 2	2.605(3)	**Er(3)−O(5) x 2**	2.463(4)
La(3)−O(6) x 2	2.531(3)	**Er(3)−O(6) x 2**	2.380(3)
$La(4)O_9$		**$Er(4)O_8$**	
La(4)−O(1) x 2	2.652(3)	**Er(4)−O(1) x 2**	2.444(4)
La(4)−O(7)	2.528(4)	**Er(4)−O(7)**	2.301(5)
La(4)−O(8) x 2	2.567(3)	**Er(4)−O(8) x 2**	2.433(4)
La(4)−O(9)	2.811(4)	**Er(4)−O(9)**	NA
La(4)−O(10) x 2	2.504(3)	**Er(4)−O(10) x 2**	2.293(4)
La(4)−O(11)	2.457(4)	**Er(4)−O(11)**	2.234(5)
$La(5)O_9$		**$Er(5)O_8$**	
La(5)−O(3)	2.703(3)	**Er(5)−O(3)**	NA
La(5)−O(8) x 2	2.404(3)	**Er(5)−O(8) x 2**	2.244(4)
La(5)−O(9)	2.533(4)	**Er(5)−O(9)**	2.291(5)
La(5)−O(10) x 2	2.711(3)	**Er(5)−O(10) x 2**	2.242(4)
La(5)−O(10) x 2	2.758(3)	**Er(5)−O(10) x 2**	2.643(4)
La(5)−O(11)	2.512(4)	**Er(5)−O(11)**	2.253(5)
$Ti(1)O_6$		**$Ti(1)O_6$**	
Ti(1)−O(1)	2.267(3)	**Ti(1)−O(1)**	2.235(4)
Ti(1)−O(3)	1.9794(13)	**Ti(1)−O(3)**	1.9081(19)
Ti(1)−O(4)	1.803(3)	**Ti(1)−O(4)**	1.801(4)
Ti(1)−O(5)	1.866(3)	**Ti(1)−O(5)**	1.858(4)
Ti(1)−O(7)	2.107(3)	**Ti(1)−O(7)**	2.0142(17)
Ti(1)−O(8)	2.027(3)	**Ti(1)−O(8)**	2.043(4)
$Ti(2)O_6$		**$Ti(2)O_6$**	
Ti(2)−O(1)	1.827(3)	**Ti(2)−O(1)**	1.823(4)
Ti(2)−O(8)	1.920(3)	**Ti(2)−O(8)**	1.920(4)
Ti(2)−O(9)	1.968(3)	**Ti(2)−O(9)**	1.9118(15)
Ti(2)−O(10)	1.978(3)	**Ti(2)−O(10)**	1.9975(19)
Ti(2)−O(10)	2.184(3)	**Ti(2)−O(10)**	2.234(3)
Ti(2)−O(11)	1.998(3)	**Ti(2)−O(11)**	1.9975(19)

Table 5.4: Bond distances (Å) of $Sm_3TiO_5(OH)_3$ (II), $Lu_5Ti_2O_{11}(OH)$ (III), and $Ce_2Ti_4O_{11}$ (IV).

$Sm_3TiO_5(OH)_3$ (II)		$Lu_5Ti_2O_{11}(OH)$ (III)		$Ce_2Ti_4O_{11}$ (IV)	
$Sm(1)O_8$		**$Lu(1)O_7$**		**$Ce(1)O_8$**	
Sm(1)−O(1) x 2	2.403(3)	**Lu(1)−O(1) x 2**	2.227(10)	**Ce(1)−O(1)**	2.382(4)
Sm(1)−O(2) x 2	2.431(3)	**Lu(1)−O(1) x 2**	2.326(11)	**Ce(1)−O(2)**	2.408(4)
Sm(1)−O(3) x 2	2.558(3)	**Lu(1)−O(2) x 2**	2.335(12)	**Ce(1)−O(3)**	2.412(4)
Sm(1)−O(4)	2.431(5)	**Lu(1)−O(4)**	2.289(15)	**Ce(1)−O(3)**	2.439(4)
Sm(1)−O(5)	2.447(4)	**$Lu(2)O_7$**		**Ce(1)−O(4)**	2.450(4)
$Sm(2)O_7$		**Lu(2)−O(1) x 2**	2.258(11)	**Ce(1)−O(5)**	2.675(4)
Sm(2)−O(1)	2.375(3)	**Lu(2)−O(2) x 2**	2.278(12)	**Ce(1)−O(1)**	2.725(4)
Sm(2)−O(1)	2.444(3)	**Lu(2)−O(2) x 2**	2.333(12)	**$Ti(1)O_6$**	
Sm(2)−O(2)	2.296(3)	**Lu(2)−O(4)**	2.343(15)	**Ti(1)−O(1)**	1.961(4)
Sm(2)−O(2)	2.358(3)	**$Lu(3)O_6$**		**Ti(1)−O(2)**	2.039(4)
Sm(2)−O(3)	2.339(3)	**Lu(3)−O(2) x 4**	2.275(11)	**Ti(1)−O(4)**	1.879(4)
Sm(2)−O(3)	2.492(3)	**Lu(3)−O(3) x 2**	2.223(15)	**Ti(1)−O(4)**	1.932(4)
Sm(2)−O(5)	2.531(2)	**$Lu(4)O_6$**		**Ti(1)−O(5)**	1.928(4)
		Lu(4)−O(2) x 4	2.237(12)	**Ti(1)−O(6)**	2.139(3)
$Ti(1)O_5$		**Lu(4)−O(2) x 2**	2.151(14)	**$Ti(2)O_6$**	
Ti(1)−O(1) x 2	1.945(3)			**Ti(2)−O(1)**	1.918(4)
Ti(1)−O(2) x 2	1.926(3)	**$Ti(1)O_6$**		**Ti(2)−O(2)**	1.862(4)
Ti(1)−O(4)	1.764(5)	**Ti(1)−O(1) x 2**	1.917(9)	**Ti(2)−O(3)**	1.750(4)
		Ti(1)−O(3) x 2	1.908(10)	**Ti(2)−O(5)**	2.021(4)
		Ti(1)−O(4) x 2	2.041(10)	**Ti(2)−O(5)**	2.385(4)
				Ti(2)−O(6)	2.068(4)

Table 5.5: Bond Valence Calculations of Hydrothermally Grown $La_5Ti_4O_{15}(OH)$ (I) and $Er_5Ti_4O_{15}(OH)$ (V).

$La_5Ti_4O_{15}(OH)$ (I)		$Er_5Ti_4O_{15}(OH)$ (V)	
La(1)O_8		**Er(1)O_8**	
La(1)−O(1) x 2	0.578	**Er(1)−O(1) x 2**	0.616
La(1)−O(4) x 2	0.688	**Er(1)−O(4) x 2**	0.544
La(1)−O(5) x 2	0.824	**Er(1)−O(5) x 2**	0.746
La(1)−O(6)	0.394	**Er(1)−O(6)**	0.435
La(1)−O(7)	0.327	**Er(1)−O(7)**	0.384
ΣLa(1)	2.811	**ΣEr(1)**	2.734
La(2)O_7		**Er(2)O_7**	
La(2)−O(2) x 2	1.204	**Er(2)−O(2) x 2**	1.174
La(2)−O(3)	0.344	**ErLa(2)−O(3)**	0.421
La(2)−O(4) x 2	0.892	**Er(2)−O(4) x 2**	0.864
La(2)−O(5) x 2	0.818	**Er(2)−O(5) x 2**	0.586
ΣLa(2)	3.256	**ΣEr(2)**	3.048
La(3)O_8		**Er(3)O_8**	
La(3)−O(2) x 2	1.184	**Er(3)−O(2) x 2**	1.028
La(3)−O(4) x 2	0.624	**Er(3)−O(4) x 2**	0.510
La(3)−O(5) x 2	0.620	**Er(3)−O(5) x 2**	0.544
La(3)−O(6) x 2	0.758	**Er(3)−O(6) x 2**	0.694
ΣLa(3)	3.186	**ΣEr(3)**	2.785
La(4)O_9		**Er(4)O_9**	
La(4)−O(1) x 2	0.546	**Er(4)−O(1) x 2**	0.584
La(4)−O(7)	0.382	**Er(4)−O(7)**	0.429
La(4)−O(8) x 2	0.688	**Er(4)−O(8) x 2**	0.600
La(4)−O(9)	0.178	**Er(4)−O(9)**	NA
La(4)−O(10) x 2	0.816	**Er(4)−O(10) x 2**	0.878
La(4)−O(11)	0.463	**Er(4)−O(11)**	0.514
ΣLa(4)	3.072	**ΣEr(4)**	3.004
La(5)O_9		**Er(5)O_9**	
La(5)−O(3)	0.238	**Er(5)−O(3)**	NA
La(5)−O(8) x 2	1.068	**Er(5)−O(8) x 2**	1.002
La(5)−O(9)	0.377	**Er(5)−O(9)**	0.441
La(5)−O(10) x 2	0.466	**Er(5)−O(10) x 2**	1.006
La(5)−O(10) x 2	0.410	**Er(5)−O(10) x 2**	0.340
La(5)−O(11)	0.399	**Er(5)−O(11)**	0.489
ΣLa(5)	2.959	**ΣEr(5)**	3.278
Ti(1)O_6		**Ti(1)O_6**	
Ti(1)−O(1)	0.295	**Ti(1)−O(1)**	0.321
Ti(1)−O(3)	0.641	**Ti(1)−O(3)**	0.778
Ti(1)−O(4)	1.033	**Ti(1)−O(4)**	1.039
Ti(1)−O(5)	0.871	**Ti(1)−O(5)**	0.890
Ti(1)−O(7)	0.454	**Ti(1)−O(7)**	0.584
Ti(1)−O(8)	0.564	**Ti(1)−O(8)**	0.540
ΣTi(1)	3.858	**ΣTi(1)**	4.151
Ti(2)O_6		**Ti(2)O_6**	
Ti(2)−O(1)	0.968	**Ti(2)−O(1)**	0.979
Ti(2)−O(8)	0.753	**Ti(2)−O(8)**	0.753
Ti(2)−O(9)	0.661	**Ti(2)−O(9)**	0.770
Ti(2)−O(10)	0.644	**Ti(2)−O(10)**	0.611
Ti(2)−O(10)	0.369	**Ti(2)−O(10)**	0.322
Ti(2)−O(11)	0.610	**Ti(2)−O(11)**	0.611
ΣTi(2)	4.005	**ΣTi(2)**	4.045

Table 5.6: Bond Valence Calculations of Hydrothermally Grown $Sm_3TiO_5(OH)_3$ (II), $Lu_5Ti_2O_{11}(OH)$ (III), and $Ce_2Ti_4O_{11}$ (IV).

$Sm_3TiO_5(OH)_3$ (II)		**$Lu_5Ti_2O_{11}(OH)$ (III**		**$Ce_2Ti_4O_{11}$ (IV)**	
$Sm(1)O_8$		**$Lu(1)O_7$**		**$Ce(1)O_7$**	
Sm(1)−O(1) x 2	0.854	**Lu(1)−O(1) x 2**	1.002	**Ce(1)−O(1)**	0.536
Sm(1)−O(2) x 2	0.792	**Lu(1)−O(1) x 2**	0.766	**Ce(1)−O(2)**	0.499
Sm(1)−O(3) x 2	0.562	**Lu(1)−O(2) x 2**	0.748	**Ce(1)−O(3)**	0.494
Sm(1)−O(4)	0.396	**Lu(1)−O(4)**	0.423	**Ce(1)−O(3)**	0.459
Sm(1)−O(5)	0.379	**ΣLu(1)**	2.939	**Ce(1)−O(4)**	0.446
ΣSm(1)	2.981	**$Lu(2)O_7$**		**Ce(1)−O(5)**	0.243
$Sm(2)O_7$		**Lu(2)−O(1) x 2**	0.920	**Ce(1)−O(1)**	0.212
Sm(2)−O(1)	0.460	**Lu(2)−O(2) x 2**	0.872	**ΣCe(1)**	2.888
Sm(2)−O(1)	0.382	**Lu(2)−O(2) x 2**	0.752	**$Ti(1)O_6$**	
Sm(2)−O(2)	0.570	**Lu(2)−O(4)**	0.366	**Ti(1)−O(1)**	0.674
Sm(2)−O(2)	0.482	**ΣLu(2)**	2.911	**Ti(1)−O(2)**	0.546
Sm(2)−O(3)	0.507	**$Lu(3)O_6$**		**Ti(1)−O(4)**	0.841
Sm(2)−O(3)	0.336	**Lu(3)−O(2) x 4**	1.760	**Ti(1)−O(4)**	0.729
Sm(2)−O(5)	0.302	**Lu(3)−O(3) x 2**	1.012	**Ti(1)−O(5)**	0.737
ΣSm(2)	3.040	**ΣLu(3)**	2.771	**Ti(1)−O(6)**	0.417
$Ti(1)O_5$		**$Lu(4)O_6$**		**ΣTi(1)**	3.943
Ti(1)−O(1) x 2	1.408	**Lu(4)−O(2) x 4**	1.948	**$Ti(2)O_6$**	
Ti(1)−O(2) x 2	1.482	**Lu(4)−O(2) x 2**	1.230	**Ti(2)−O(1)**	0.757
Ti(1)−O(4)	1.148	**ΣLu(4)**	3.179	**Ti(2)−O(2)**	0.881
ΣTi(1)	4.037	**$Ti(1)O_6$**		**Ti(2)−O(3)**	1.192
		Ti(1)−O(1) x 2	1.518	**Ti(2)−O(5)**	0.573
		Ti(1)−O(3) x 2	1.556	**Ti(2)−O(5)**	0.214
		Ti(1)−O(4) x 2	1.086	**Ti(2)−O(6)**	0.505
		ΣTi(1)	4.159	**ΣTi(2)**	4.122

Synthesis and Phase Distribution

The title compounds were synthesized by employing a high-temperature hydrothermal method with 20 *M* KOH and 30 *M* CsF as mineralizers. In general, the stability of rare earth oxyhydroxide and trihydroxide species, REO(OH) and $RE(OH)_3$, in lower temperature (< 600˚C) hydrothermal conditions require that hydrothermal reactions be performed at higher temperature regimes (> 600˚C) to avoid formation of these solids as the dominant thermodynamic products regardless of mineralizer choice. The product distribution across the rare-earth oxide series in the present high-temperature study is displayed in **Scheme 5.1.** A wide variety of structures result, depending both upon the mineralizer identity and the size of the rare-earth cation. It is important to mention that, during the reactions, we maintained the stoichiometry between rare-earth oxide and the TiO_2 to 1:2 for all reactions. However, in some cases stoichiometric reactions of the precursors were subsequently used to prepare the target compounds in a higher yield after the preliminary reactions. The 20 *M* KOH reaction series has a very complicated phase distribution. The first compound isolated, $La_5Ti_4O_{15}(OH)$, **I**, represents a new structure type. However, this phase did not persist across the other lanthanide ions to form other derivatives of $La_5Ti_4O_{15}(OH)$, apart from $Er_5Ti_4O_{15}(OH)$. Reactions of Pr_2O_3 and Nd_2O_3 with TiO_2 resulted $Pr_2Ti_2O_7$ and $Nd_2Ti_2O_7$ which crystalize in the polar monoclinic space group $P2_1$.[26,52] In a similar fashion, reactions from Gd_2O_3 to Ho_2O_3 produced cubic pyrochlore-type $RE_2Ti_2O_7$ structures.[1,2] In the case of Sm, yellow crystals of $Sm_3TiO_5(OH)_3$, **II**, were formed (~ 2 mm, **Figure 5.1**) and found to be isostructural with the $RE_3MO_5(OH)_3$ (M = V^{+4}, Ge^{+4}) structure type (see structure discussion of

$Sm_3TiO_5(OH)_3$). As a separate series, the reactions from Tm_2O_3 to Lu_2O_3 with TiO_2 generally formed crystals of the $RE_2Ti_2O_{11}(OH)$ structure type, which shares similar structural features with rare-earth molybdates, ruthenates and rhenates ($RE_5X_2O_{12}$, X = Mo, Ru, Re) reported in the literature.[53–57,67,68] Moreover, synthesis of the $RE_5Ti_2O_{11}(OH)$ (*RE* = Tm-Lu) series was accomplished in good yield in all cases, producing thick colorless crystals with well-defined edges. Additionally, separate hydrothermal reactions investigating the mineralizer effects on the $RE_5Ti_2O_{11}(OH)$ system revealed a direct correlation between the mineralizer choice and the quality of crystal produced. For example, better quality crystals of $RE_5Ti_2O_{11}(OH)$ (*RE* = Tm-Lu) were isolated using CsOH compared to KOH. Phase formation of $Tm_5Ti_2O_{11}(OH)$ and $Yb_5Ti_2O_{11}(OH)$ were confirmed using PXRD (**Figure 5.14**), and no ambiguous reflections from additional phases were observed.

The observation that the reaction of Ce_2O_3 and TiO_2 in 20 *M* KOH did not produce any rare-earth titanate crystals led us to explore other mineralizer systems. These high-temperature hydrothermal reactions between rare-earth oxides and TiO_2 with concentrated fluoride solutions also showed an interesting phase distribution, **Scheme 5.1**. Herein, the ability of 30 M CsF to mineralize both the rare-earth oxide and titanium oxide starting materials was confirmed in the reactive chemistry. The use of 30 *M* CsF with the same 1:2 stoichiometric ratio between RE_2O_3 (*RE* = Gd-Lu) and TiO_2 resulted primarily in cubic pyrochlore $RE_2Ti_2O_7$ structures with average crystal size of ~ 0.5. The formation of monoclinic $RE_2Ti_2O_7$ pyrochlores in space group $P2_1$ were also observed

with larger rare-earth oxide cations such as La, Pr and Nd which is somewhat similar to the reaction chemistry of 20 *M* KOH.

Interestingly, the reaction between Ce_2O_3 and TiO_2 with 30 *M* CsF resulted in the formation of $Ce_2Ti_4O_{11}$, **IV**, which is isostructural with $Nd_2Ti_4O_{11}$ crystals grown by chemical transport at high-temperature (1000 °C) with the aid of chlorine gas as a transport catalyst.[58] Further, compound **IV** can be also grown using various concentrations of CsF ranging from 6 *M* with higher concentrations producing the best quality crystals with higher yield. Powders of cerium titanate adopting the brannerite-type structure ($CeTi_2O_6$) are of interest in catalysis, but a very limited number of well-characterized single crystals are reported for cerium titanates in general.[59,60] Other cerium titanate powders were prepared by ceramic methods and characterized by powder diffraction, while Ce_2TiO_5, Ce_2TiO_7 and $Ce_4Ti_9O_{24}$ types represent, to our knowledge, the only single crystal growth and structure characterization reported in the literature.[61]

Changing the rare-earth oxide to Sm_2O_3 and Eu_2O_3 in CsF mineralizer, did not produced any oxide materials, but rather resulted in the formation of rare-earth fluoride compounds, $CsRE_2F_7$.[61] Therefore, it confirms that, highly concentrated fluoride solutions are an effective route to obtain refractory oxide materials that do not contain hydroxide groups. This complements the studies with extremely high concentrated hydroxide that were very useful in obtaining a variety of new structure types. The versatility of the hydrothermal technique to support interchangeable mineralizer schemes thus makes it a valuable tool for the preparation of high quality single crystals of targeted materials (such as the pyrochlores) as well as engaging in exploratory chemistry.

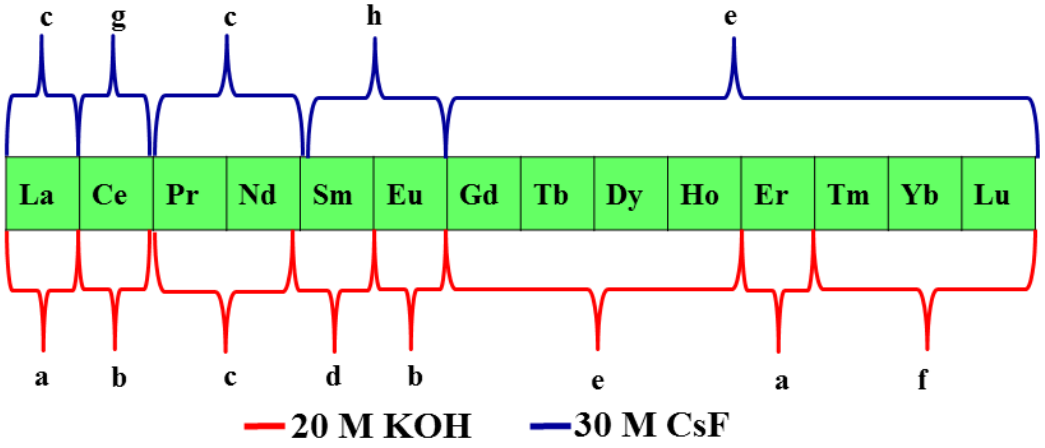

Scheme 5.1: Product distribution (a-h) of the hydrothermal reaction (650-700 °C) over the mineralizers of 20 *M* KOH and 30 *M* CsF: (a) $RE_5Ti_4O_{15}(OH)$; (b) *RE*O(OH); (c) $RE_2Ti_2O_7$-$P2_1$; (d) $RE_3TiO_5(OH)_3$; (e) $RE_2Ti_2O_7$-cubic pyrochlore; (f) $RE_5Ti_2O_{11}(OH)$; (g) $RE_2Ti_4O_{11}$; (h) $CsRE_2F_7$.

Crystal Structure of $RE_5Ti_4O_{15}(OH)$ (*RE*= La and Er), I

$La_5Ti_4O_{15}(OH)$ and $Er_5Ti_4O_{15}(OH)$ are isostructural and crystallize in orthorhombic crystal system in space group *Pnnm* (no.58). The structure of $La_5Ti_4O_{15}(OH)$ will be discussed in detail from here (**Table 5.1**), with crystallographic data for $Er_5Ti_4O_{15}(OH)$ summarized in (**Table 5.2**). The unit cell parameters of $La_5Ti_4O_{15}(OH)$ are a = 30.516(4) Å, b = 5.5837(7) Å , c = 7.7593(10) Å, V = 1322.1(3) $Å^3$ and Z = 4. Selected bond lengths and bond valence sum calculations are given in **Tables 5.3-5.6**, respectively. The crystal structure of $La_5Ti_4O_{15}(OH)$ can be best described as a complex three-dimensional framework consisting of seven distinct metal sites (five La^{3+} sites and two Ti^{+4} sites), and represents a new structure type, **Figure 5.2**. The structural framework consists of $La(1)O_8$, $La(2)O_7$, $La(3)O_8$, $La(4)O_9$ and $La(5)O_9$ coordination environments with La–O bond distances ranging from 2.360(4) to 2.811(4) Å, and averaging 2.553(4) Å. The LaO_n polyhedra form a three-dimensional (3D) framework built from two unique two-dimensional (2D) La–O–La slabs in the bc plane (**Figure 5.3**). The two unique Ti^{4+} sites both adopt an octahedral geometry (TiO_6) and form their own Ti–O–Ti sublattice of thick 2D slabs (**Figure 5.4**). The Ti–O–Ti sublattice is embedded inside the 3D La–O–La framework to form a very complex and dense structure. The Ti–O bond distances range from 1.803(3) to 2.267(3) Å for $Ti(1)O_6$ and 1.827(3) to 2.184(3) Å for $Ti(2)O_6$ suggesting a highly distorted octahedral environment in both TiO_6 units. The TiO6 octahedra also exhibit angular distortion with trans-O-Ti-O angles of 164.21(17)° to 174.99(12)° and cis-O-Ti-O angles of 80.12(12)° to 102.72(13)°.

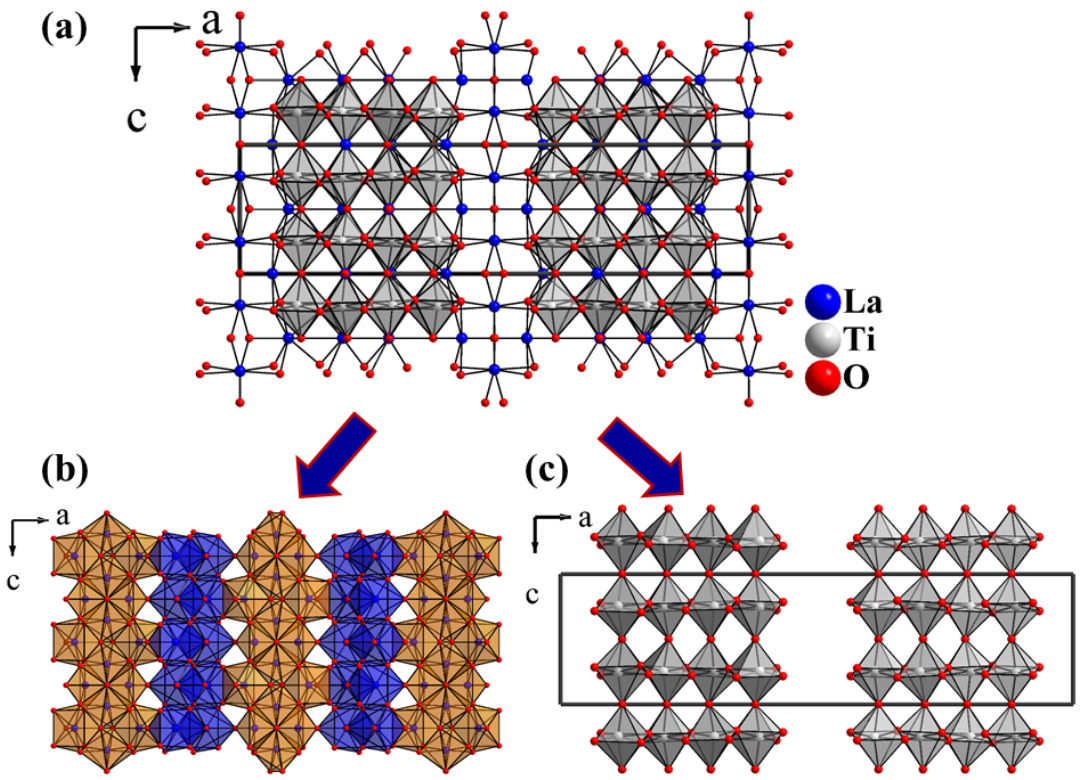

Figure 5.2: Crystal structure of $La_5Ti_4O_{15}(OH)$ viewing along the *b*-axis. (a) Partial polyhedral view showing the complex nature of the 3D La–O–Ti lattice; (b) Polyhedral view of the 3D La–O–La lattice, where orange and blue colored polyhedra distinguish the two different 2D La–O–La slabs in the *bc* plane, and alternating along the *a*-axis; (c) Construction of the Ti–O–Ti sublattice within the $La_5Ti_4O_{15}(OH)$ unit cell.

The nature of the 3D La–O–La lattice is worth further comment. As shown in **Figure 5.2b**, two La–O–La substructures are highlighted using orange (La–O–La slab 1) and blue (La–O–La slab 2) polyhedra and these substructures interconnect with each other along the *a*-axis to form the 3D La–O–La lattice which is the longest axis in the unit cell (30.516(4) Å). The first sublattice (orange color polyhedra in **Figure 5.2b** is formed by $La(1)O_8$, $La(2)O_9$ and $La(3)O_9$ polyhedra. Here, the $La(3)O_8$ polyhedra form edge sharing chains along the *c*-axis, that are bracketed by the $La(1)O_8$ and $La(2)O_7$ polyhedra also through edge-sharing (**Figure 5.3**). Meanwhile, slab 2 is formed by $La(4)O_9$ and $La(5)O_9$ polyhedra connected in alternating, edge-sharing fashion as shown in **Figure 5.3**. The overall La–O–La framework is established by corner and edge sharing oxygen atoms joining the slabs along the *a*-axis. The O(6) oxygen atom was found to be under-bonded based on its bond valence sum, as it possesses only three bonds to lanthanum atoms. Electron density in an appropriate geometry for a hydrogen atom attached to O(6) was identified from the difference electron density map, and assigned as such to satisfy the bond valence of O(6) and provide charge neutrality in the structure. The hydrogen atom occupies a small gap in the center of slab 1 of the lanthanum oxide framework.

The structural complexity of this material is also reflected in the titanium environments, **Figure 5.4**. Two distinct titanium environments generate a four-octahedron thick (along *a*) slab arrangement extending along the *bc*-plane with the thickness seen in the *ac*-plane in **Figure 5.2c and 5.6**. The thick layer is formed by corner sharing $Ti(1)O_6$ and $Ti(2)O_6$ octahedra, defined by intersecting chains of

Ti(1)–O(1)–Ti(2)–O(10)–Ti(2)–O(8)–Ti(1) connectivity in the *ab*-plane, and Ti(1)–O(3)–Ti(1), Ti(1)–O(7)–Ti(1), Ti(2)–O(9)–Ti(2), and Ti(2)–O(11)–Ti(2) connectivity along c **Figure 5.4**. The complex La–O–Ti framework is formed through a number of edge- and corner-sharing interactions where the Ti–O–Ti and La–O–La sublattices are interpenetrating, **Figure 5.5**. A phase pure crystallization product can be grown under hydrothermal conditions as shown in **Figure 5.7**. The presence of hydroxide was confirmed in the single crystal Raman spectrum as shown in **Figure 5.8**, with other products in this Chapter.

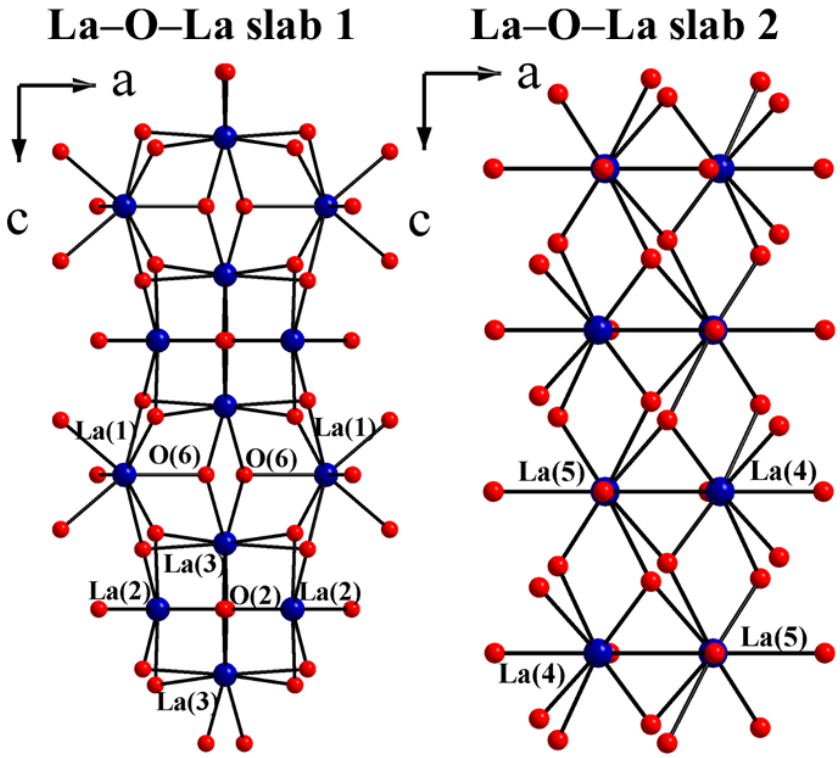

Figure 5.3: Partial structure of two La–O–La sublattices. Sublattice 1 is formed by $La(1)O_8$, $La(2)O_9$ and $La(3)O_9$ polyhedra and sublattice 2 is formed by $La(4)O_9$ and $La(5)O_9$. These two sublattices interconnect along the *a*-axis to form overall 3D La–O–La lattice.

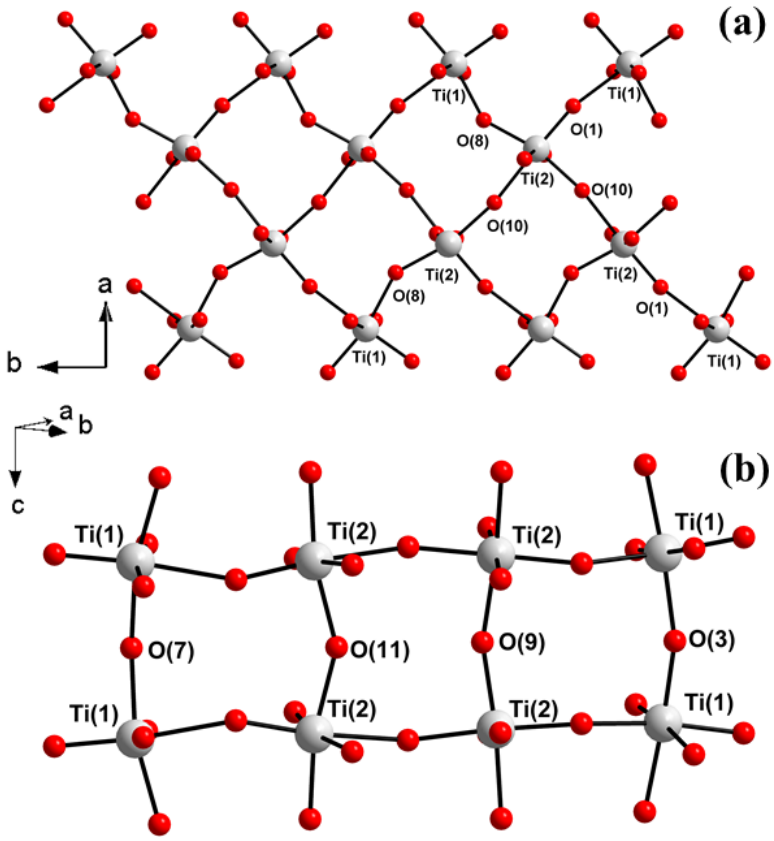

Figure 5.4: (a) basic building unit in the Ti–O–Ti lattice along the *c*-axis and it represents the thickness of the lattice; (b) shows the connectivity between the Ti(1)O_6 and Ti(2)O_6 units within the Ti–O–Ti lattice.

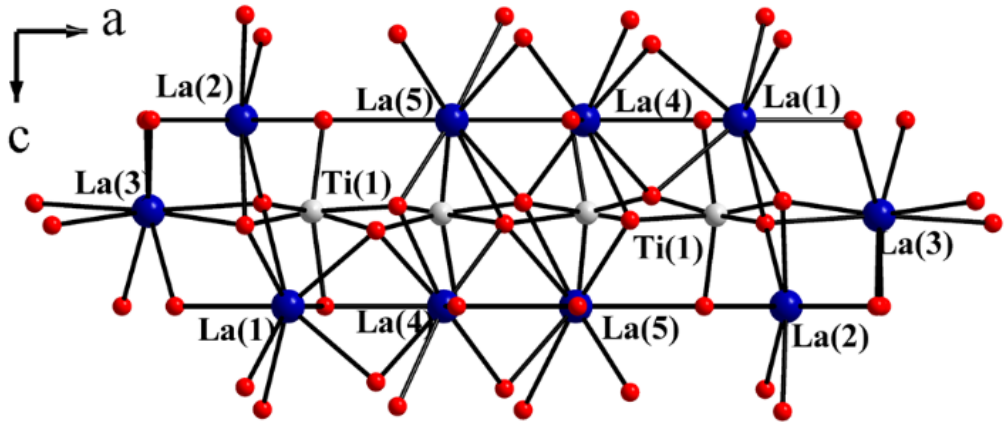

Figure 5.5: Shows the connectivity between LaO_n polyhedral and TiO_6-octahedra in $La_5Ti_4O_{15}(OH)$.

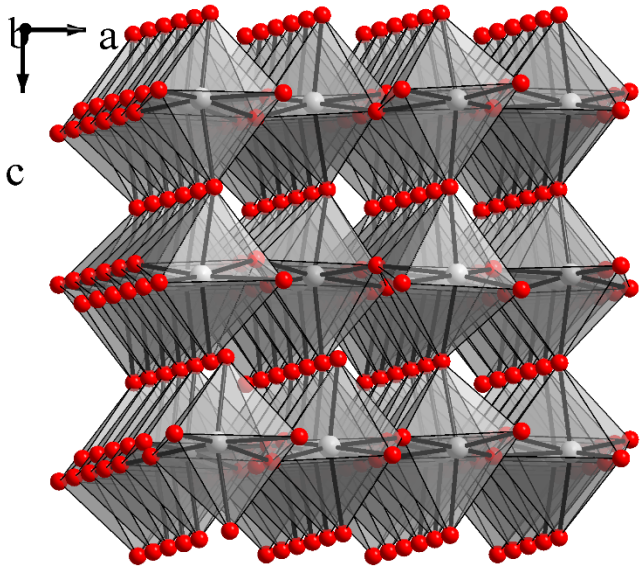

Figure 5.6: Ti–O–Ti lattice in $La_5Ti_4O_{15}(OH)$. (a) A polyhedral view of the Ti–O–Ti lattice showing the thickness of the lattice along the *a*-axis and lattice continue to grow along the *b*- and *c*-axis.

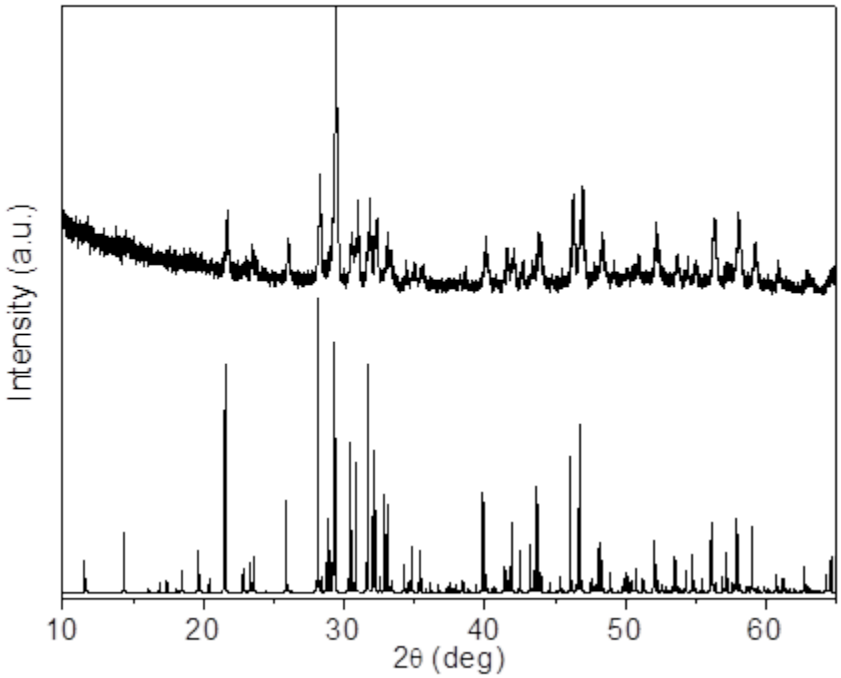

Figure 5.7: PXRD pattern of $La_5Ti_4O_{15}(OH)$. (Bottom) Simulated powder pattern of $La_5Ti_4O_{15}(OH)$; (Top) observed PXRD of $La_5Ti_4O_{15}(OH)$.

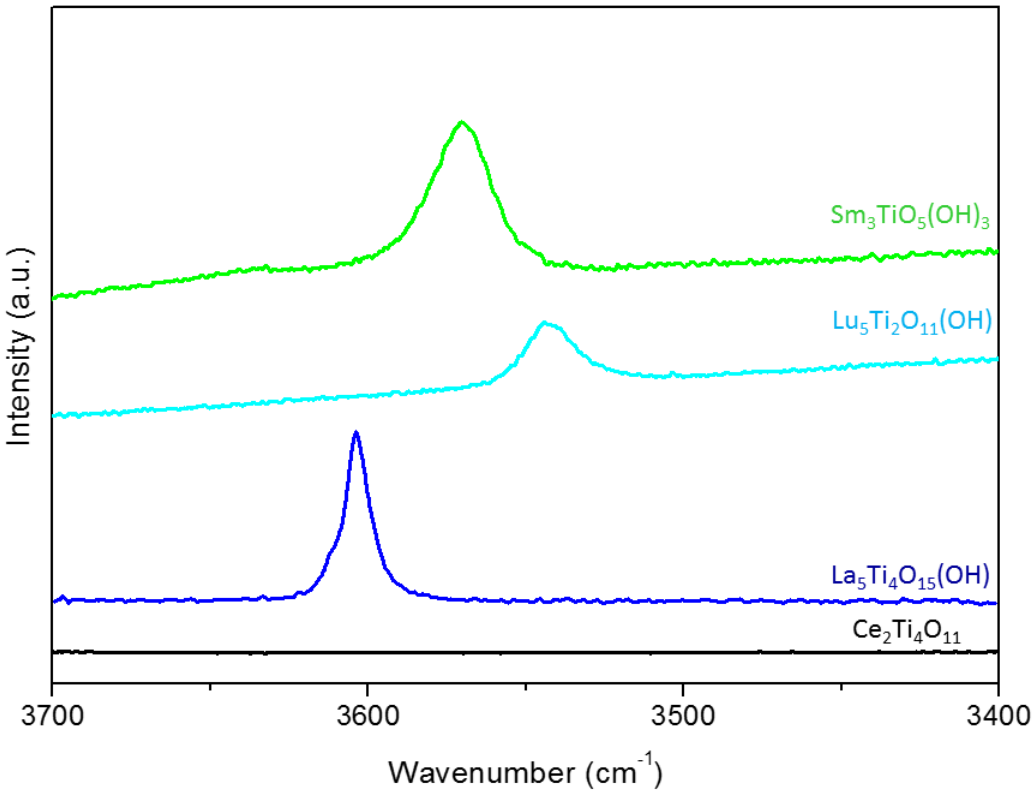

Figure 5.8: Single crystal Raman plots of $Ce_2Ti_4O_{11}$, $La_5Ti_4O_{15}(OH)$, $Lu_5Ti_2O_{11}(OH)$, and $Sm_3TiO_5(OH)_3$ compounds from bottom to top, respectively.

Table 5.7: EDX of reported rare-earth titanates with experimental and expected RE:Ti ratios.

	RE/Ti EDX ratio (%)	**Exp. ratio**	**Ideal ratio**
$La_5Ti_4O_{15}(OH)$	22.1/23.5	0.94:1	1.25:1
$Er_5Ti_4O_{15}(OH)$	18.6/16.5	1.13:1	1.25:1
$Ce_2Ti_4O_{11}$	9.8/20.7	0.47:1	0.5:1
$Sm_3TiO_5(OH)_3$	34.3/11.7	2.93:1	3:1
$Tm_5Ti_2O_{11}(OH)$	22.8/9.7	2.35:1	2.5:1
$Yb_5Ti_2O_{11}(OH)$	27/12	2.25:1	2.5:1
$Lu_5Ti_2O_{11}(OH)$	29.7/10.8	2.75:1	2.5:1

Crystal Structure of $Sm_3TiO_5(OH)_3$, II

Compound **II** crystallizes in the monoclinic crystal system in space group $P2_1/m$, with unit cell parameters of a = 5.6066(2) Å, b = 10.4622(4) Å, c = 6.1258(2) Å and β = 104.7390(10)°, V = 347.50(2) Å^3 and Z = 2. $Sm_3TiO_5(OH)_3$ is a titanyl structure type that is a structural analog of other $RE_3MO_5(OH)_3$ (M = V^{4+}, Ge^{4+}) compounds based on tetravalent building blocks.[62–65] The structure of $Sm_3TiO_5(OH)_3$ is comprised of two crystallographically distinct SmO_n polyhedra ($Sm(1)O_8$ and $Sm(2)O_7$) and one $Ti(1)O_5$ group, forming a 3D framework (**Figures 5.10-5.12**). The $Sm(1)O_8$ and $Sm(2)O_7$ units form an interesting 3D rare-earth sublattice, where chains of alternating $Sm(1)O_8$ and $Sm(2)O_7$ units connected by edge-sharing propagate along the b-axis, and are interconnected to neighboring chains also by oxygen edge-sharing to form the Sm–O–Sm sublattice. All oxygen atoms except O(4) are μ_3 oxo-bridging oxygen atoms within the rare-earth framework, creating numerous triangular lanthanide interactions. Of these oxygen atoms, O(3) and O(5) do not bridge to the TiO_5 units, and instead support the hydrogen atoms of the structure. The O(5)-H(5)---O(4) interaction exhibits a favorable distance and geometry for hydrogen bonding, while the O(3)-H(3) group appears to be a terminal hydroxide ligand. The hydrogen atom assignments to O(3) and O(5) significantly improves their bond valence. The Sm–O bond distances range from 2.296(3) to 2.555(3) Å, consistent with the analogous germanates and vanadates of this same structure type.[62–65]

The TiO_5 group exhibits a square pyramidal geometry (**Figure 5.10**) with Ti–O bond lengths of 1.763(5) Å to the apical O(4) atom and 1.925(3) to 1.944(3) Å to the

basal O(1) and O(2) atoms. The base of the pyramid exhibits some angular distortion, with cis-O-Ti-O angles of 81.62(17) ° to 86.82(12)°. The apical Ti–O(4) bond in compound **II** exhibits some titanyl character, and is slightly elongated relative to the titanyl bonds of 1.698(3) Å in $Li_2TiOSiO_4$, probably due to the additional bridging nature of O(4) to Sm^{3+} (Sm(1)) in the present structure.[66,67] As expected, the Ti–O(4) bond is slightly longer than that of the vanadyl bond in $Y_3VO_5(OH)_3$ (1.697(5) Å), **Table 5.8**. Despite the similarity of the Ti-O and Ge-O apical bond lengths in the structural analogs (**Table 5.8**), there is a much greater difference in apical vs. basal bond length for the respective MO_5 units in $Sm_3TiO_5(OH)_3$ compared to $Sm_3GeO_5(OH)_3$, also supporting the concept of a titanyl bond. The corresponding rare-earth vanadates, however, exhibit a greater degree of *M*=O character using this metric. Although O(4) only possesses bonds to Ti(1) and Sm(1), it maintains a reasonable bond valence of 1.544 (**Table 5.6**) given the titanyl character of the Ti-O(4) bond. The role of O(4) as a hydrogen bond acceptor as described above further stabilizes this site. The TiO_5 units are isolated relative to one another, but are integrated into the overall 3D framework by Ti-O-Sm bridging. This occurs by corner-sharing of the apical oxygen atoms and edge-and corner-sharing of the basal oxygen atoms of the TiO_5 units by Sm atoms. $Sm_3TiO_5(OH)_3$ can be grown as a hydrothermally pure product as represented by the PXRD pattern of as-grown material and simulated powder pattern, **Figure 5.13**. The presence of hydroxide was confirmed in the single crystal Raman spectrum of the as-grown material, shown in **Figure 5.8**. DSC of as-grown material of $Sm_3TiO_5(OH)_3$ is assumed to undergo continues loss of water, as

shown in **Figure 5.14**. The single crystals of $Sm_3TiO_5(OH)_3$ display a brilliant yellow color (**Figure 5.1**), indicative of samarium ions in a crystalline lattice.

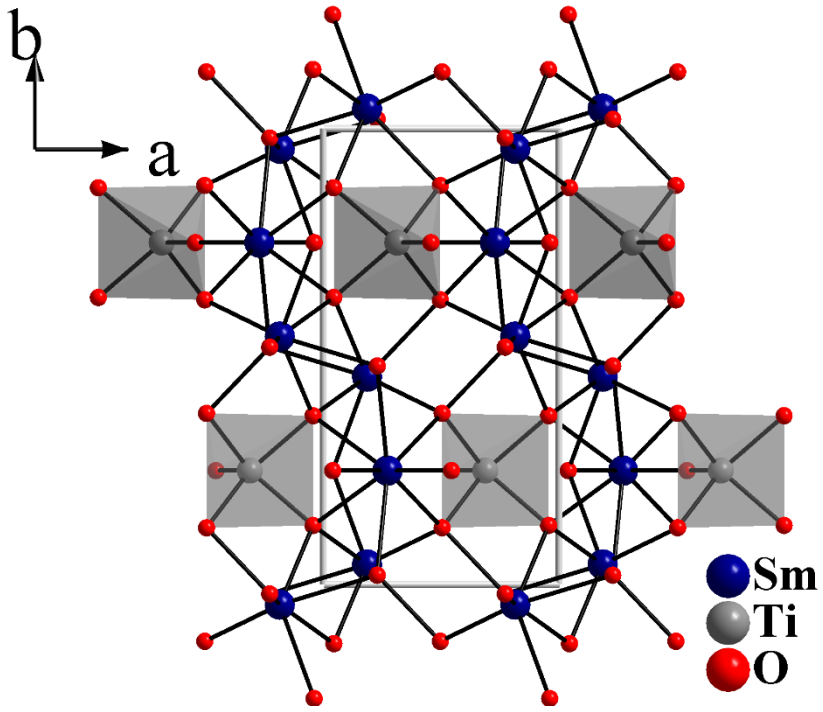

Figure 5.10: Extended structure of $Sm_3TiO_5(OH)_3$ viewed along [001].

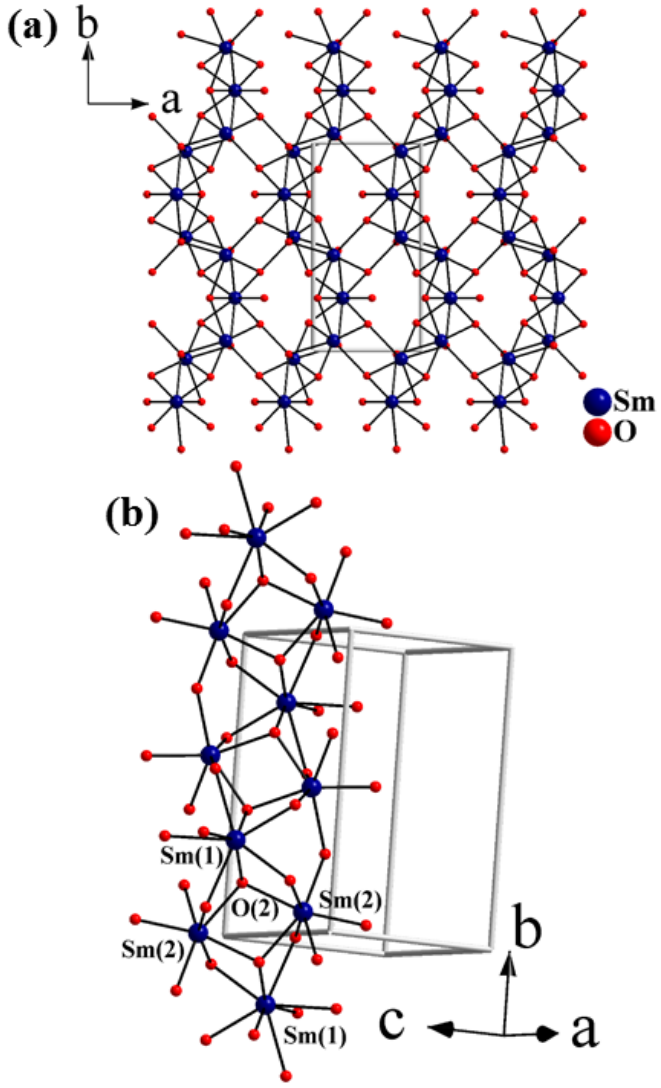

Figure 5.11: (a) Sm–O–Sm lattice of $Sm_3TiO_5(OH)_3$ along ab-plane which display the propagation of Sm–O–Sm lattice along the a- and b-axis; (b) partial structure of Sm–O–Sm wavy chains in the $Sm_3TiO_5(OH)_3$ and forms a triangular unit made from one Sm(1) and two Sm(2) centers.

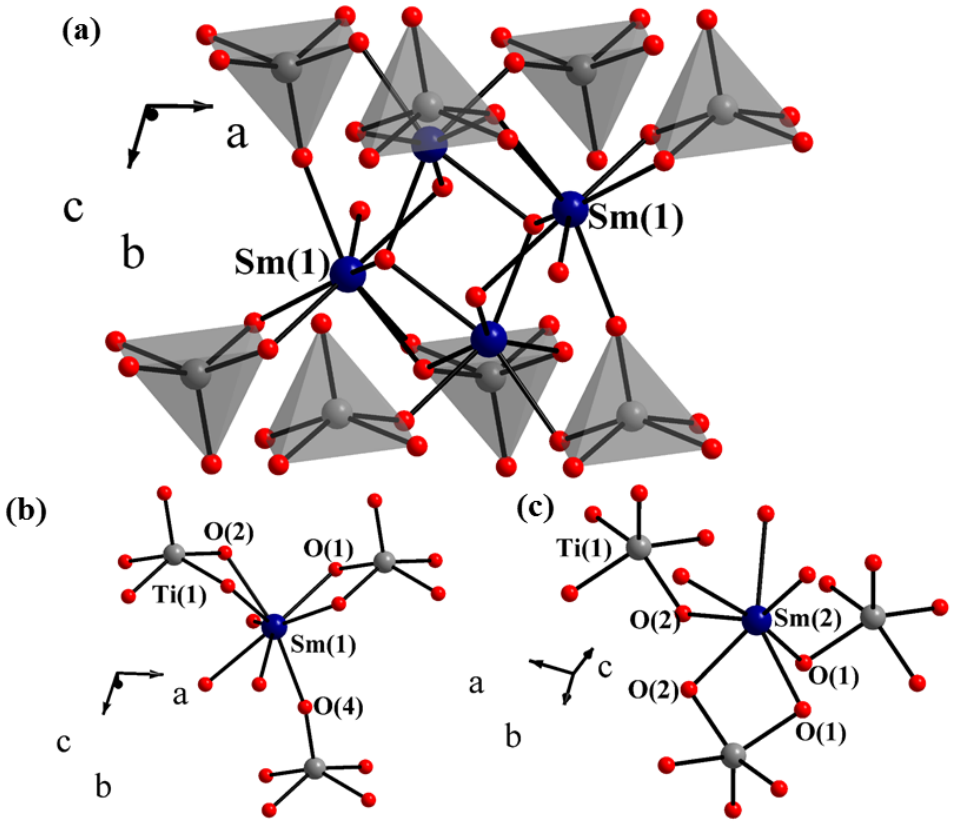

Figure 5.12: Connectivity between $Sm(1)O_8$, $Sm(2)O_7$ and $Ti(1)O_5$ units in $Sm_3TiO_5(OH)_3$.

Table 5.8: Summary of *M*=O bond distances for $RE_3MO_5(OH)_3$ ($M = V^{+4}, Ge^{+4}, Ti^{+4}$).

Structure Type ($RE_3MO_5(OH)_3$)	M=O bond distance Å	Average basal oxygen distance Å	Δ (basal avg. -M=O) Å	Reference
$La_3VO_5(OH)_3$	1.673(12)	1.931	0.258	62
$Dy_3VO_5(OH)_3$	1.670(2)	1.920	0.250	62
$Y_3VO_5(OH)_3$	1.697(5)	1.919	0.222	62
$Sm_3TiO_5(OH)_3$	1.764(4)	1.936	0.172	this work
$Sm_3GeO_5(OH)_3$	1.768(20)	1.863	0.095	65
$Dy_3GeO_5(OH)_3$	1.779(16)	1.860	0.081	64
$Y_3GeO_5(OH_{0.5}F_{0.5})_3$	1.794(28)	1.846	0.052	63

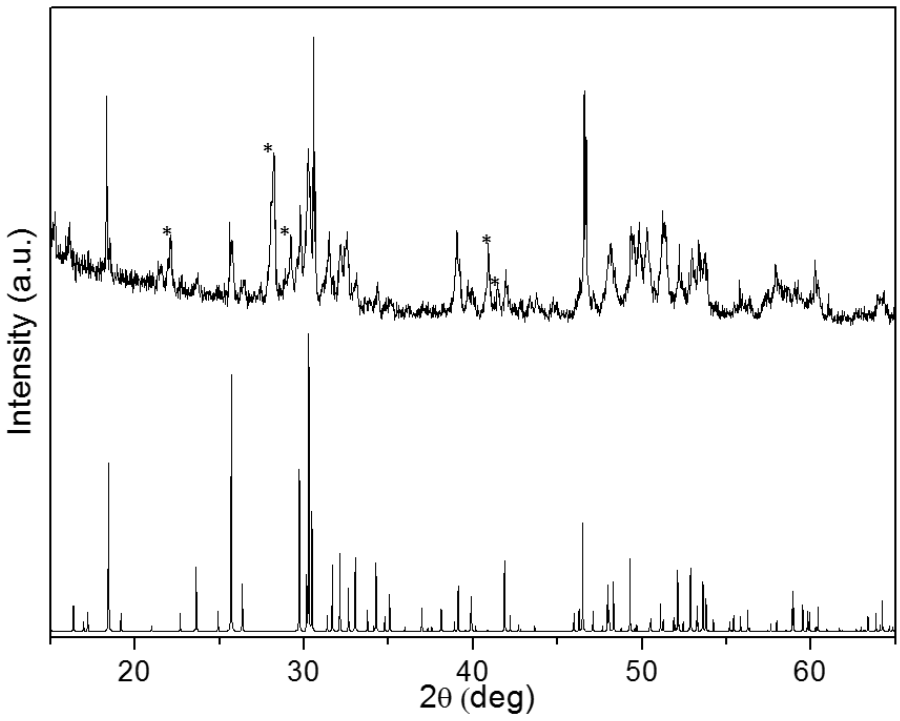

Figure 5.13: PXRD pattern of $Sm_3TiO_5(OH)_3$. (Bottom) Simulated powder pattern of $Sm_3TiO_5(OH)_3$. (Top) Hydrothermally grown $Sm_3TiO_5(OH)_3$ powder. Reflections from impurities $Sm(OH)_3$ 00-006-0117 and SmO(OH) 00-013-0168 (*) indicated above.

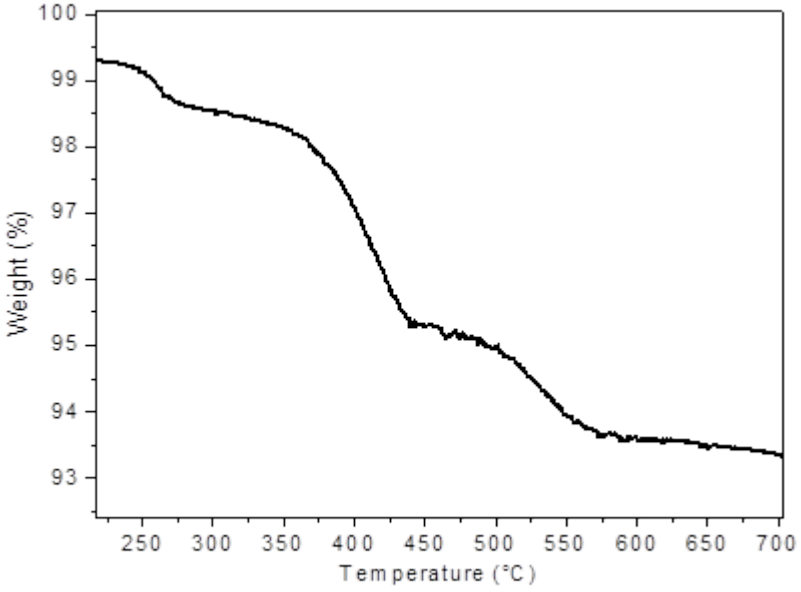

Figure 5.14: Decomposition of $Sm_3TiO_5(OH)_3$ occurs via continuous water loss from the OH^- groups upon heating in air from 23-283 °C(1.43% expected mass loss, 1.40% observed mass loss).

Crystal Structure of $RE_5Ti_2O_{11}(OH)$ (RE = Tm–Lu), III

The crystal structure of $RE_5Ti_2O_{11}(OH)$ (RE = Tm–Lu) type **III**, is monoclinic with $C2/m$ (no. 12) space group symmetry and a = 12.1252(9) Å, b = 5.8243(4) Å, c = 7.0407(5) Å, β = 106.939(3) ° and V = 475.65(6) Å^3. Selected bond lengths and angles are summarized in **Table 5.4**. Like the previous compounds, $Lu_5Ti_2O_{11}(OH)$ also possesses a complex 3-D framework. The rare-earth ions form their own 3D framework of by edge-shared oxygen atoms. An interesting feature of this rare-earth framework are periodic channels that are occupied by Ti^{4+}–O–Ti^{4+} chains propagating along the b-axis. The chains have alternating short (2.799(8) Å) and long (3.026(8) Å) interatomic distances between Ti^{4+} ions, **Figure 5.15**.

This structure type is analogous with a series of rare-earth containing rhenates and ruthenates, $RE_5M_2O_{12}$ (M = Re, Mo, Ru)[53–56] summarized in **Table 5.9**. These compounds have been studied due to their interesting magnetic and electric properties.[68] Crystals of these compounds are often twinned and disordered, and **III** also displays these tendencies due to the plate morphology of the crystals. The alternating shorter and longer M–M interatomic distances in the $RE_5M_2O_{12}$ structures are attributed to the formation of M–M bonds along the M–O–M chains, enabled by the presence of unpaired electrons in the extended d orbitals in 4d or 5d transition metals (rhenium and ruthenium) leading to metal-metal bond formation. However, the appearance of shorter Ti···Ti distance in compound **III** cannot be justified using the same concept as in the case of $RE_5M_2O_{12}$ compounds. Having said that, compound **III** is completely colorless (**Figure 5.1**) which confirms the presence of Ti^{4+} since any Ti^{3+} present in the lattice would be expected to be

strongly chromophoric. Moreover, lutetium has no reasonable oxidation state other than the empty shell Lu^{3+}, so these factors combine to rule out any electronic effects to cause the shorter titanium distances. Therefore, we can conclude that the alternating distances in **III** are only caused due to packing effects of the LuO_n polyhedra within the unit cell. Furthermore, $Lu_5Ti_2O_{11}(OH)$ exhibits a smaller difference in short versus long M-M distances compared to the Ru and Re analogs, where the attractive effects of M-M bond formation are pronounced. (See **Table 5.9**)

The overall Lu–O–Lu lattice is similar to the previously reported $RE_5M_2O_{12}$ structures.[69] Charge balance in the $RE_5M_2O_{12}$ series is accomplished by mixed-valent M^{4+}/M^{5+} at the transition metal sites (M = Re, Mo, Ru). In **III**, the presence of the OH stretching vibration in the infrared spectrum (**Figure 5.8**) and the water clear appearance of the crystals suggests charge balance should be accomplished according to the formula $Lu_5Ti_2O_{11}(OH)$ rather than any unexpected lower valence of Ti or RE. This formula is consistent with the mass loss observed by TGA in the region of 120-180 °C due to decomposition of the OH group, **Figure 5.17**. The O(2) atom was assigned as the OH group, on the basis of its lower bond valence sum, and its location within the framework capable of sterically supporting the hydrogen atom in ¼ occupancy on the general position. Single crystals of $RE_5Ti_2O_{11}(OH)$ (RE = Tm–Lu) were grown under hydrothermal conditions, as previously described, and phase purity was confirmed through PXRD measurements, **Figure 5.16**. Single crystal Raman scattering was used to confirm the presence of hydroxide, **Figure 5.8**.

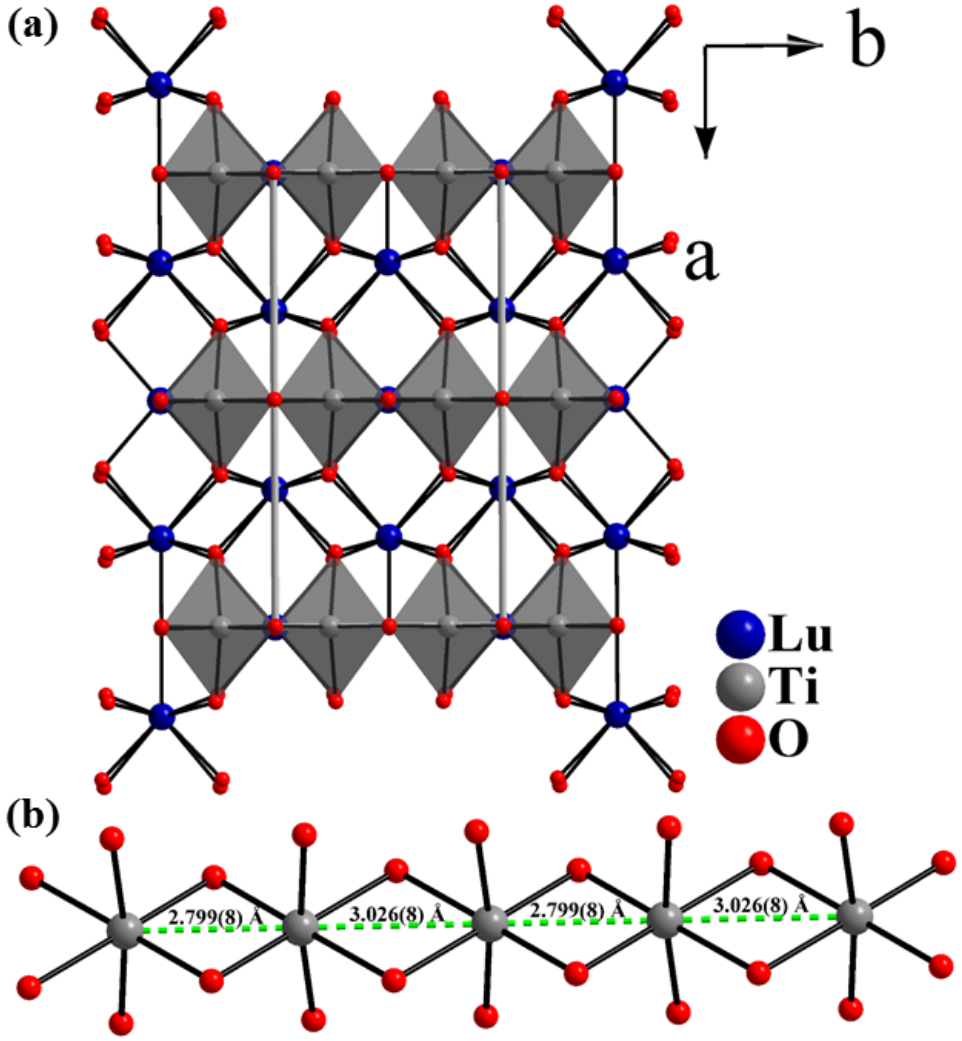

Figure 5.15: $Lu_5Ti_2O_{11}(OH)$ viewed along [001] direction revealing infinite titanium oxide chains propagating along the [010] direction; **(b)** one dimensional chains of Ti-O-Ti along the *b*-axis.

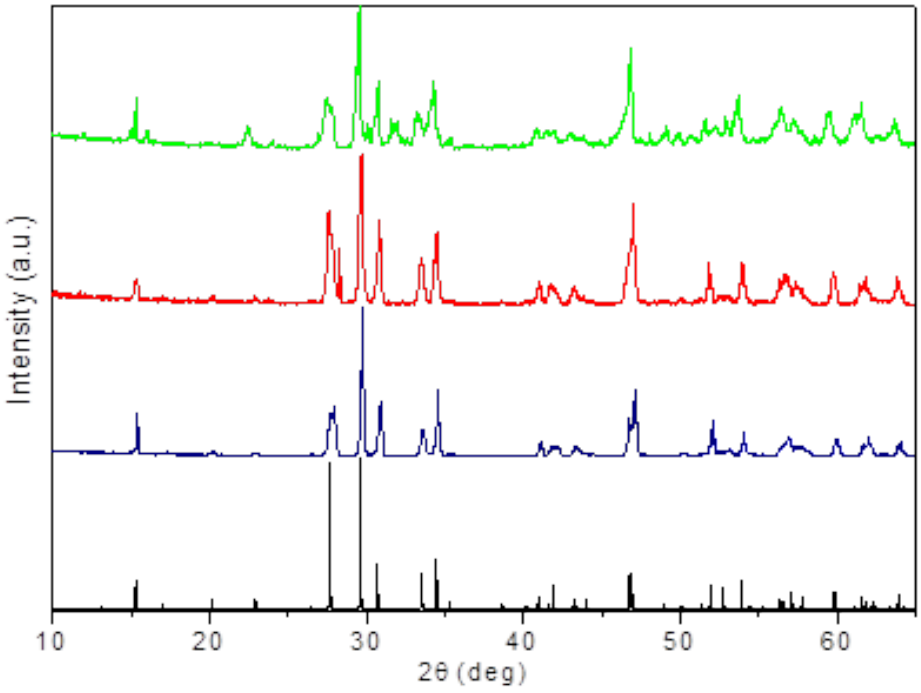

Figure 5.16: PXRD pattern of $Lu_5Ti_2O_{11}(OH)$. (Black) Simulated powder pattern of $Lu_5Ti_2O_{11}(OH)$; (Blue) Hydrothermally grown $Lu_5Ti_2O_{11}(OH)$ powder, (Red) Hydrothermally grown $Yb_5Ti_2O_{11}(OH)$ powder, (Green) Hydrothermally grown $Tm_5Ti_2O_{11}(OH)$ powder.

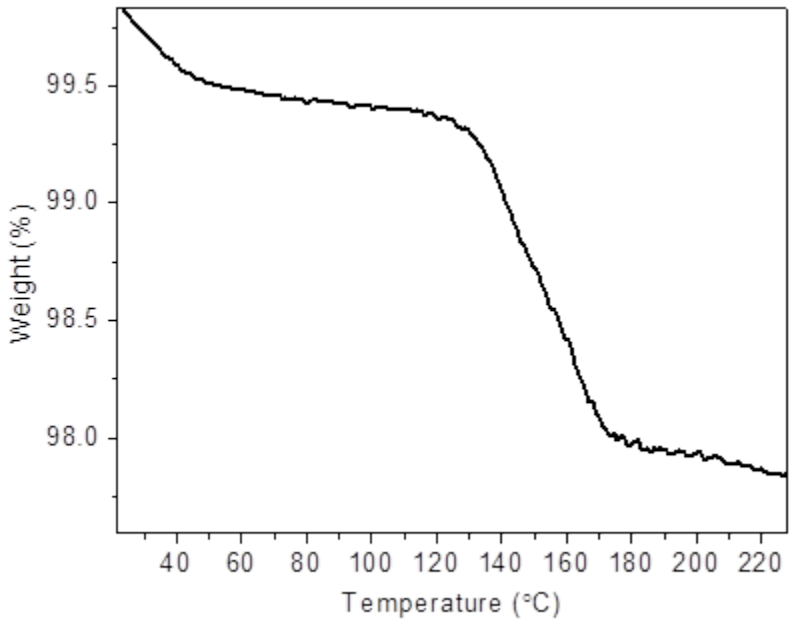

Figure 5.17: Decomposition of $Lu_5Ti_2O_{11}(OH)$ occurs via water loss from the OH^- groups upon heating in air from 23-128 °C(0.77% expected mass loss, 0.71% observed mass loss).

Table 5.9: Summary of *M*–*M* bond distances for $RE_5M_2O_{12}$ (*M* = Ru, Re) and $RE_5Ti_2O_{11}(OH)$ compounds.

Structure Type ($RE_5M_2O_{12}$)	M–M bond distance (short) (Å)	M–M bond distance (long) (Å)	Reference
$Pr_5Ru_2O_{12}$	2.8038(11)	3.1450(11)	53
$Eu_5Ru_2O_{12}$	2.780(2)	3.091(2)	53
$Gd_5Ru_2O_{12}$	2.774(3)	3.084(3)	53
$Tb_5Ru_2O_{12}$	2.7765(11)	3.0649(11)	53
$Y_5Re_2O_{12}$	2.4466(5)	3.2138(5)	54
$Tm_5Re_2O_{12}$	2.455(1)	3.219(1)	55
$Ho_5Re_2O_{12}$	2.436(2)	3.201(2)	56
$Lu_5Ti_2O_{11}(OH)$	2.799(8)	3.026(8)	this work

Crystal Structure of $Ce_2Ti_4O_{11}$, IV

Compound **IV**, $Ce_2Ti_4O_{11}$, crystallizes in the monoclinic space group *C*2/*c* with unit cell parameters of a = 13.6875(7) Å, b = 5.0955(3) Å, c = 12.8592(7) Å, β = 108.964(2)° and V = 848.18(8) Å^3 with Z = 4. The complex 3-D framework features three distinct metal sites, each residing on a general position. Viewed along the *b*-axis (**Figure 5.18**), the structure can be described as a framework of corrugated layers featuring sheets of cerium and titanium oxides condensed through common oxygen atoms. Each 2D layer propagates along the *bc*-plane, as viewed in **Figure 5.18b and 5.18c**. The cerium oxide sheet is built of one unique Ce atom that is edge- and corner-sharing with neighboring symmetry related Ce sites. Cerium is in an eight-coordinate environment with Ce–O bond lengths ranging from 2.382(4) to 2.725(4) Å. Two unique titanium atoms, Ti(1) and Ti(2) comprise the titanium oxide layer. The Ti(1) atom adopts a distorted octahedral environment with Ti(1)–O bond distances ranging from 1.879(4) to 2.139(3) Å. The Ti(2) site has a distorted octahedral geometry with an approximate titanyl configuration. Four equatorial bonds to oxygen range from 1.862(4) to 2.068(4) Å, while the opposing axial bonds to oxygen are 1.750(4) Å to O(3) and 2.385(4) Å to O(5) across the 170.13(17)° bond angle. The two TiO_6 octahedra possess a complex connectivity to form the layer, as shown in **Figure 5.18**. Two Ti(1)O_6 octahedra form a dimer by edge-sharing O(4) atoms, while two Ti(2)O_6 octahedra form their own dimer through an interesting face sharing connectivity by sharing two O(5) and one O(6) atoms, **Figure 5.19**. The respective dimer units share edges with one another, placing O(6) as a common vertex between four Ti atoms as a μ_4-oxo bridging atom. The face sharing nature of the two

$Ti(2)O_6$ octahedra, brings the two Ti(2) centers into a fairly close proximity of 2.869(2) Å. This structure type was previously reported for $Nd_2Ti_4O_{11}$,[58] but represents a one of few examples of structurally characterized cerium titanates other than $CeTi_2O_6$.[34] A mixed crystalline product of $Ce_2Ti_4O_{11}$ and $Ce(OH)_3$ was found to result under hydrothermal conditions (**Figure 5.20**). These two crystalline products are easily separated by crystal habit. Single crystals of $Ce_2Ti_4O_{11}$ grow as dark-red polyhedral crystals (**Figure 5.1**), while $Ce(OH)_3$ grows as large flat plats that are also dark-red in color. No presence of hydroxide groups was detected in the as-grown powder, as shown in the IR spectrum in **Figure 5.8**.

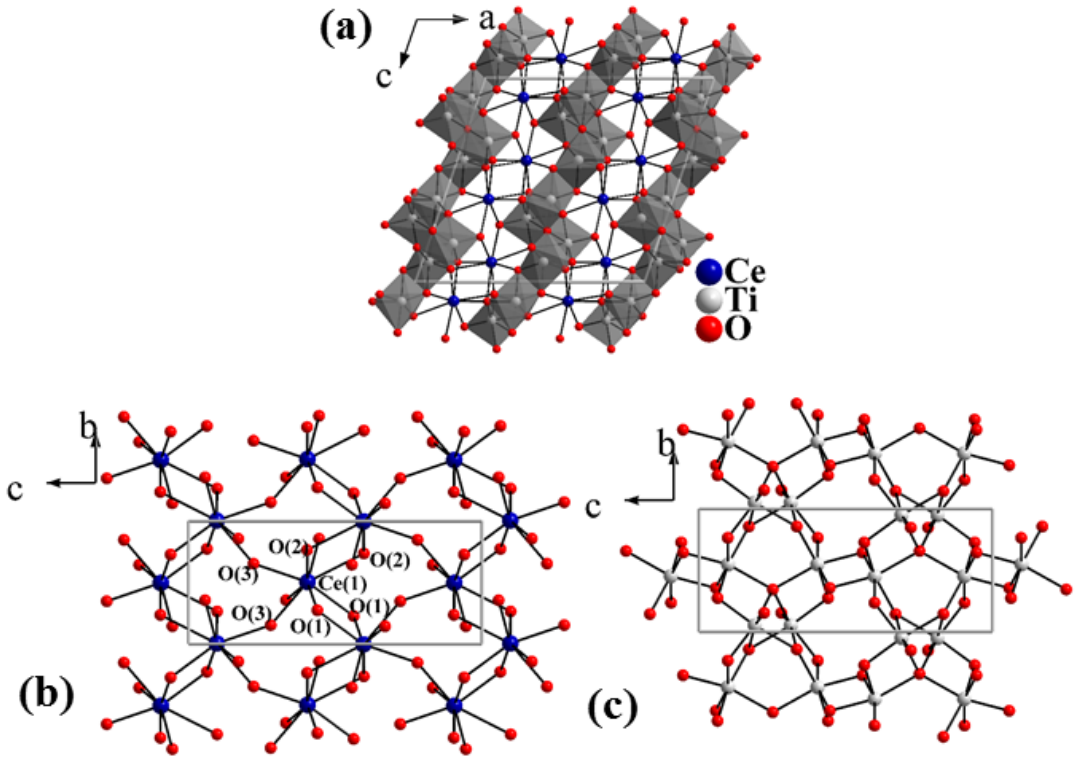

Figure 5.18: (a) $Ce_2Ti_4O_{11}$ viewed along [010] direction highlighting slabs of alternating rare-earth and titanium oxide polyhedral; **(b)** and **(c)** The 2D Ce–O–Ce and Ti–O–Ti lattices along *a*-axis, respectively.

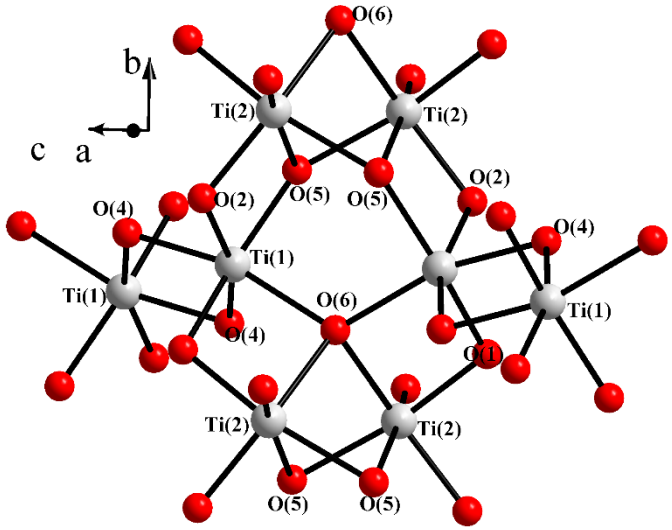

Figure 5.19: Detail drawing of 2D Ti–O–Ti lattice showing the complex connectivity between $Ti(1)O_6$ and $Ti(2)O_6$ octahedra.

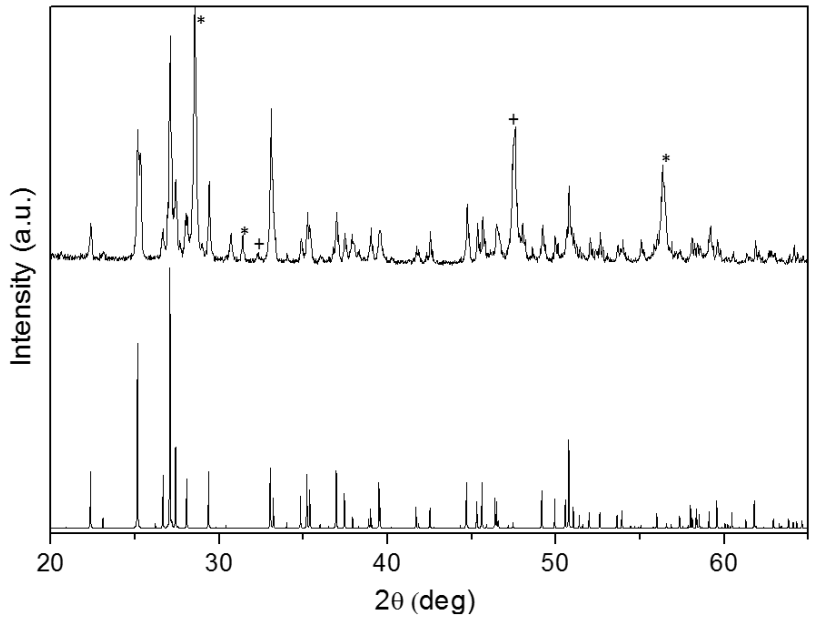

Figure 5.20: PXRD pattern of $Ce_2Ti_4O_{11}$. (Bottom) Simulated powder pattern of $Ce_2Ti_4O_{11}$; (Top) Hydrothermally grown $Ce_2Ti_4O_{11}$. Reflections from impurities $Ce(OH)_3$ (*) 00-054-1268 and Ti_2O_3 (+) 01-071-0150 indicated above.

Crystal Structure of $Dy_2Ti_2O_7$

As mentioned earlier, there is a great interest recently in the ideal cubic (*Fd-3m*) pyrochlores, $RE_2Ti_2O_7$. For completeness, a brief description of this structure type and its hydrothermal growth will be discussed. As shown in **Scheme 5.1,** a number of ideal pyrochlores $RE_2Ti_2O_7$ (RE = Gd – Lu) can be grown under hydrothermal conditions in either 30 *M* CsF or 20 *M* KOH. In both cases, a consistent battle in solution is the formation of oxy-hydroxide species, REO(OH). In most cases, the cubic pyrochlore is a minor product at high-temperatures (700-750 °C). Nevertheless, in the course of this work a number of cubic pyrochlores were identified. One recurring problem among many rare-earth pyrochlores is the tendency for the rare-earth ion to disorder over the tetravalent B-site as a result of the high-temperature crystal growth methods. Thus it is of interest to identify relatively low temperature growth methods that provide access to high quality singe crystals of the cubic pyrochlores. Single crystal data was collected on some but not all structures, but their unit cell parameters were identified using SCXRD initial scans. As a representative of this class of compounds, $Dy_2Ti_2O_7$ will be examined.

$Dy_2Ti_2O_7$ crystallizes in cubic space group Fd-3m and unit cell parameters for this system are reported in **Table 5.10**. A representative drawing for this structure is shown in **Figure 5.21**. In this structure, the rare-earth site is 8-coordinate and displays Dy(1)-O bond distances ranging from 2.1990(3)-2.4885(7)°. Each $Dy(1)O_8$ polyhedra coordinates six $Ti(2)O_6$ atoms through edge-sharing of O(1), **Figure 5.22**. While the cubic (Fd-3m) structure is considered "ideal", reported structures in the literature contain two distinct metal sites, each with mixed RE/Ti. Reported structures consistently have the *16d*

Wyckoff site with around 3-4 % Ti^{+4} by SOF.[10,12] This is consistent with our structure of $Dy_2Ti_2O_7$ in which the thermal parameters improve by substituting 2.8 % Ti into the Dy site. Therefore, in order to charge compensate the structure, a Dy substitution into the Ti *16c* Wycoff site must take place or an oxygen defect can be created by disordering one of the oxygen sites. In the literature, both types of defect pyrochlore can be observed. In this situation, it was determined that an oxygen defect was in better crystallographic agreement, than a Ti substitution into the Dy site. The $Ti(2)O_6$ site displays bond distances of 1.9722(4) Å, consistent with that of literature values. The most interesting aspect of this structure type is a spin-frustration within the magnetic lattice.[11] **Figure 5.23** is used to explain this occurence in which an examination of the triangular lattice of Dy atoms creates a situation in which at least one of the triangular corners is stuck in a frustrated spin situation. As an example of the crystal growth of the $RE_2Ti_2O_7$ pyrochlores, $Gd_2Ti_2O_7$ is shown in **Figure 5.24** as a representative example.

Table 5.10: Crystallographic data for $Dy_2Ti_2O_7$.

empirical formula	**$Dy_2Ti_2O_7$**
formula weight (g/mol)	1284.91
crystal system	cubic
space group	*Fd-3m*
temperature, K	273(2)
crystal size (mm)	0.12 x 0.08 x 0.06
a, Å	10.1566(12)
volume, $Å^3$	1047.72
calculated density ($\mu g/m^3$)	6.876
absorption coefficient (mm^{-1})	35.40
F(000)	1965
Tmax, Tmin	1.0000, 0.4169
Θ range for data	2.734-33.355
reflections collected	2352
data/restraints/parameters	72/0/12
final R [$I > 2\sigma(I)$] R1, wR2	0.0244/0.0553
final R (all data) R1, wR2	0.0254/0.0566
goodness-of-fit on F^2	1.140
largest diff. peak/hole, e/ $Å^3$	1.1469/-0.650

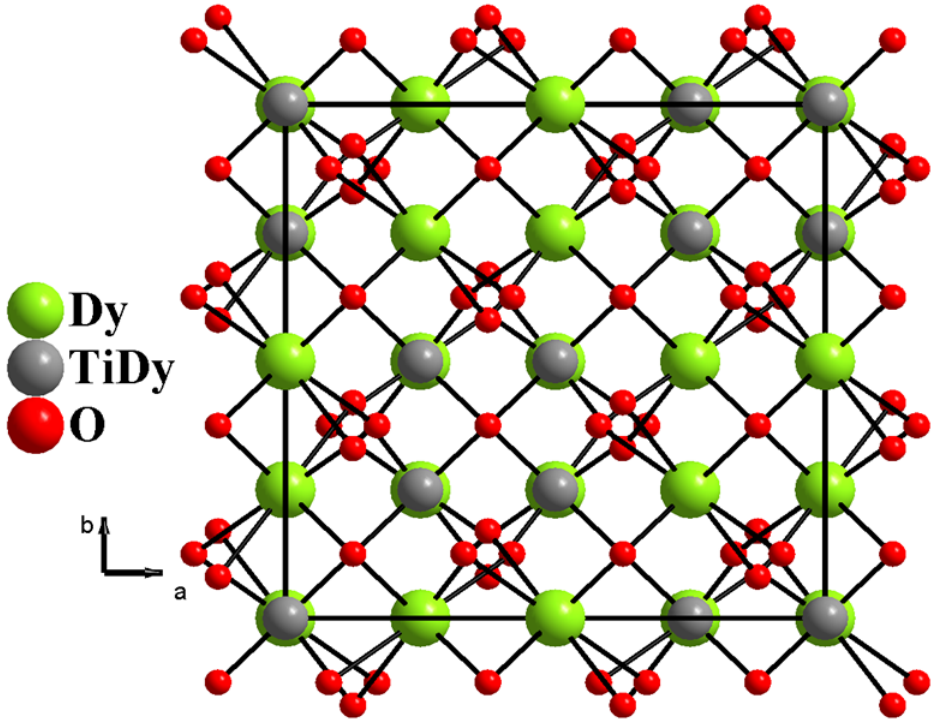

Figure 5.21: Unit cell representation of Dy2Ti2O7 along the [001] direction.

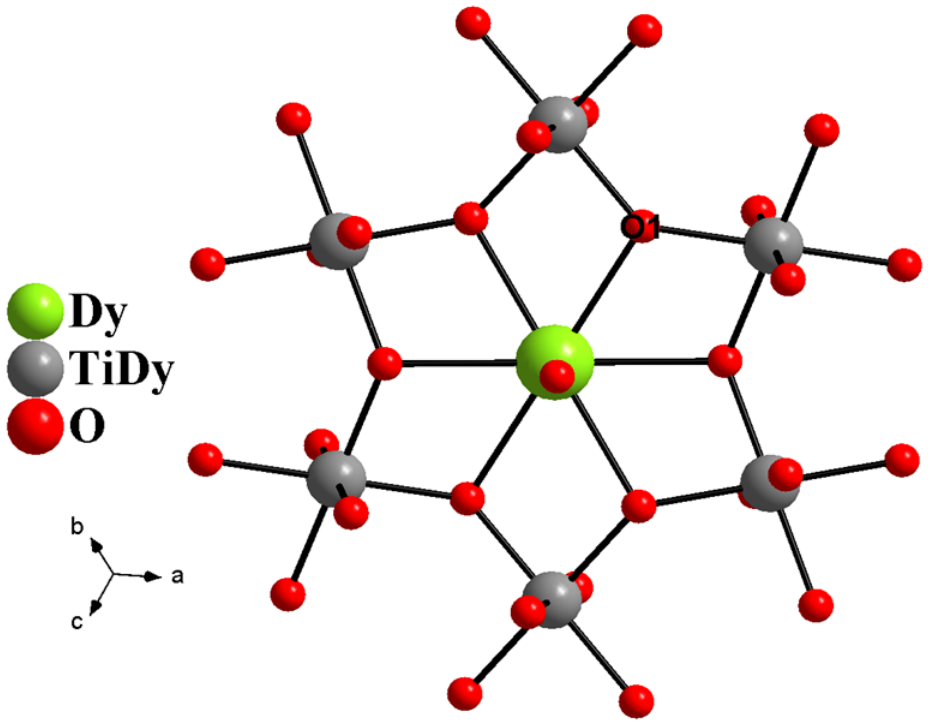

Figure 5.22: $Dy(1)O_8$ coordination of $Ti(2)O_6$ polyhedra through edge-sharing of O(1) atoms viewed along the body-diagonal of the unit cell.

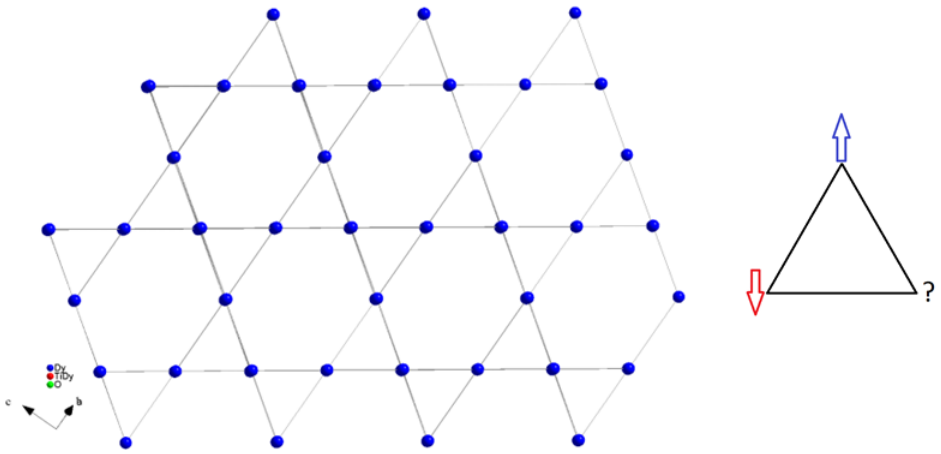

Figure 5.23: Frustrated triangular lattice representation in $Dy_2Ti_2O_7$.

Figure 5.24: Representative hydrothermal crystal growth of $Gd_2Ti_2O_7$.

Conclusions

Systematic exploration of the RE_2O_3-TiO_2 (RE=La-Lu) system by high-temperature, high-pressure hydrothermal synthesis in two different mineralizers reveals a rich chemistry and a variety of new structure types across the *f*-block. Previously, a demonstration that the rare-earth oxides could be solubilized and reacted with other tetravalent oxides such as silicates and germanates in high-temperature hydrothermal fluids was accomplished. As part of this continuing effort, investigation of the reactions of rare-earth oxides with titanium oxide to determine if rare-earth titanates can be formed and if so, what form do the final products take, was undertaken. Previously, it was determined that reactions involving very refractory oxides often provide the best results when concentrated fluoride is employed as mineralizer as opposed to concentrated hydroxide. As part of this investigation, contrasted results from both types of mineralizer were examined. In almost all cases, the formation of high quality single crystals of various rare-earth titanates was observed. The identity of various structure types across the *f*-block ions can be attributed to three essential factors: temperature, rare-earth ionic radius and mineralizer.

In general, the stability of rare-earth oxyhydroxide species, REO(OH) and $RE(OH)_3$, in lower temperature (< 600˚C) hydrothermal conditions require that hydrothermal reactions be performed at higher temperature regimes (>600˚C) to avoid formation of these solids as the dominant thermodynamic products regardless of mineralizer choice. To obtain a rational comparison, all reactions were performed using the same reaction conditions of temperature, pressure, time and relative stoichiometry.

The only difference throughout was the choice of either 20 *M* KOH or 30 *M* CsF mineralizer for each reaction.

In most cases the final product is in the form of high quality single crystals and mostly contains both the rare-earth and titanium. The Ti^{+4} ions can adopt a variety of coordination environments depending on mineralizer and associated rare-earth. The flexibility of Ti^{+4} to adopt either stable octahedral (6-coordinate) or square pyramidal (5-coordinate) titanyl coordination environments is an additional factor that leads to the variety of structural types. In all cases, observation of the color of the crystals was determined by the characteristic color of the rare-earth ion, indicating no evidence of titanium to adopt a reduced defect habit.

It was determined that there is a general tendency of concentrated hydroxide mineralizers lead to formation of a series of rare-earth titanate oxy-hydroxides with very complex structures and isolation of three such complex structures**, I, II** and **III,** was found. A primary director of dimensionality is the ionic radius of the rare-earth ion, which leads to stabilization of the larger *f*-block (La^{3+}-Nd^{+3}) ions by higher oxygen coordination numbers. This led to isolation of high quality single crystal of $RE_5Ti_4O_{15}(OH)$ (RE = La^{3+}, Er^{3+}). In the case of intermediate sized rare-earth ions the $RE_3TiO_5(OH)_3$ (RE = Sm^{3+}) For the smallest rare-earth ions the $RE_5Ti_2O_{11}(OH)$ (RE = Tm^{3+}-Lu^{3+}) formulation is observed. This $RE_5Ti_2O_{11}(OH)$ structure has similarities to the anhydrous $RE_5M_2O_{12}$ (M = Re, Mo, Ru) structure, while the $RE_3TiO_5(OH)_3$ type is like some isoelectronic $RE_3MO_5(OH)_3$(M = V^{4+}, Ge^{4+}) structures. The $RE_5Ti_4O_{15}(OH)$ family represents a completely new structural type. In the case of Nd and Pr, the known polar

$RE_2Ti_2O_7$ phase is isolated, while for Gd - Ho ions the well-known cubic pyrochlore phases are produced. It is not yet clear to us why the chemistry is so complex and rare-earth specific across the lanthanides and this is under further investigation.

In marked contrast to the MOH mineralizers, the use of highly concentrated 30 *M* cesium fluoride did not result in formation of any observable oxy-hydroxide species. When concentrated fluoride mineralizer is used, in all cases only anhydrous rare-earth titanium oxides are isolated except for Sm and Eu. These most commonly include polymorphs of the $RE_2Ti_2O_7$ pyrochlore structure, either the uniaxial monoclinic $P2_1$ phase for the larger rare-earths, or the more traditional cubic (*Fd-3m*) form for the smaller rare-earths. The traditional outlier Ce^{3+} is the only unusual species forming the unusual species $Ce_2Ti_4O_{11}$, also an anhydrous oxide.

Interestingly, in comparison to the RE-Si and RE-Ge structures reported earlier, the RE-Ti study has led to a completely new array of structure types. The main difference being that in our hands, Ti^{+4} readily adopts 5 or 6 coordinate environments in hydrothermal fluids. This is highly encouraging as this ability to incorporate various building blocks with varying geometries will surely lead to further studies of other metal oxide building blocks.

It can be concluded that the high-temperature hydrothermal technique allows for exploration of new oxides at temperatures (~700 °C) much lower than that of conventional solid-state techniques. The ability to solubilize refractory rare-earth oxides in this temperature regime allows large, high quality single crystals to be grown for detailed structural investigation as well as for possible applications such as complex

magnetic materials, nuclear waste storage, scintillator hosts and a variety of other uses. oxides such as the corresponding rare-earth tantalates, to be investigated. The conclusions reached here are highly encouraging. A natural progression of thinking has led to the investigation of rare-earth niobates as Nb^{+5} also has variable geometries (4- or 6-coordinate), while displaying a fairly stable oxidative state of +5. It is expected that the presence of Nb^{+5} will lead to new and existing compounds with increased solubility under hydrothermal conditions.

References

(1) Subramanian, M. A.; Aravamudan, G.; Subba Rao, G. V. Oxide Pyrochlores — A Review. *Prog. Solid State Chem.* **1983**, *15* (2), 55–143.

(2) Mouta, R.; Silva, R. X.; Paschoal, C. W. A. Tolerance Factor for Pyrochlores and Related Structures. *Acta Crystallogr B* **2013**, *69* (5), 439–445.

(3) Gardner, J. S.; Gingras, M. J. P.; Greedan, J. E. Magnetic Pyrochlore Oxides. *Rev. Mod. Phys.* **2010**, *82* (1), 53–107.

(4) Bramwell, S. T.; Field, M. N.; Harris, M. J.; Parkin, I. P. Bulk Magnetization of the Heavy Rare Earth Titanate Pyrochlores - a Series of Model Frustrated Magnets. *J. Phys. Condens. Matter* **2000**, *12* (4), 483.

(5) Bramwell, S. T.; Gingras, M. J. P. Spin Ice State in Frustrated Magnetic Pyrochlore Materials. *Science* **2001**, *294* (5546), 1495–1501.

(6) Fennell, T.; Deen, P. P.; Wildes, A. R.; Schmalzl, K.; Prabhakaran, D.; Boothroyd, A. T.; Aldus, R. J.; McMorrow, D. F.; Bramwell, S. T. Magnetic Coulomb Phase in the Spin Ice $Ho_2Ti_2O_7$. *Science* **2009**, *326* (5951), 415–417.

(7) Lummen, T. T. A.; Handayani, I. P.; Donker, M. C.; Fausti, D.; Dhalenne, G.; Berthet, P.; Revcolevschi, A.; van Loosdrecht, P. H. M. Phonon and Crystal Field Excitations in Geometrically Frustrated Rare Earth Titanates. *Phys. Rev. B* **2008**, *77* (21), 214310.

(8) Petrenko, O. A.; Lees, M. R.; Balakrishnan, G. Magnetization Process in the Spin-Ice Compound $Ho_2Ti_2O_7$. *Phys. Rev. B* **2003**, *68* (1), 012406.

(9) Ramirez, A. P.; Hayashi, A.; Cava, R. J.; Siddharthan, R.; Shastry, B. S. Zero-Point Entropy in "spin Ice." *Nature* **1999**, *399* (6734), 333–335.

(10) Snyder, J.; Ueland, B. G.; Slusky, J. S.; Karunadasa, H.; Cava, R. J.; Schiffer, P. Low-Temperature Spin Freezing in the $Dy_2Ti_2O_7$ Spin Ice. *Phys. Rev. B* **2004**, *69* (6), 064414.

(11) Harris, M. J.; Bramwell, S. T.; McMorrow, D. F.; Zeiske, T.; Godfrey, K. W. Geometrical Frustration in the Ferromagnetic Pyrochlore $Ho_2Ti_2O_7$. *Phys. Rev. Lett.* **1997**, *79* (13), 2554–2557.

(12) Sakakibara, T.; Tayama, T.; Hiroi, Z.; Matsuhira, K.; Takagi, S. Observation of a Liquid-Gas-Type Transition in the Pyrochlore Spin Ice Compound $Dy_2Ti_2O_7$ in a Magnetic Field. *Phys. Rev. Lett.* **2003**, *90* (20), 207205.

(13) Wuensch, B. J.; Eberman, K. W.; Heremans, C.; Ku, E. M.; Onnerud, P.; Yeo, E. M. E.; Haile, S. M.; Stalick, J. K.; Jorgensen, J. D. Connection between Oxygen-Ion Conductivity of Pyrochlore Fuel-Cell Materials and Structural Change with Composition and Temperature. *Solid State Ion.* **2000**, *129* (1), 111–133.

(14) Moon, P. K.; Tuller, H. L. Ionic Conduction in the $Gd_2Ti_2O_7$–$Gd_2Zr_2O_7$ System. *Solid State Ion.* **1988**, *28*, 470–474.

(15) Williford, R. E.; Weber, W. J.; Devanathan, R.; Gale, J. D. Effects of Cation Disorder on Oxygen Vacancy Migration in Gd2Ti2O7. *J. Electroceramics* **1999**, *3* (4), 409–424.

(16) Farmer, J. M.; Boatner, L. A.; Chakoumakos, B. C.; Du, M.-H.; Lance, M. J.; Rawn, C. J.; Bryan, J. C. Structural and Crystal Chemical Properties of Rare-Earth Titanate Pyrochlores. *J. Alloys Compd.* **2014**, *605*, 63–70.

(17) Weber, W. J.; Ewing, R. C. Plutonium Immobilization and Radiation Effects. *Science* **2000**, *289* (5487), 2051–2052.

(18) Ringwood, A. E.; Kesson, S. E.; Ware, N. G.; Hibberson, W. O.; Major, A. The SYNROC Process: A Geochemical Approach to Nuclear Waste Immobilization. *Geochem. J.* **1979**, *13* (4), 141–165.

(19) Gao, Z. P.; Yan, H. X.; Ning, H. P.; Reece, M. J. Ferroelectricity of $Pr_2Ti_2O_7$ Ceramics with Super High Curie Point. *Adv. Appl. Ceram.* **2013**, *112* (2), 69–74.

(20) Yan, H.; Ning, H.; Kan, Y.; Wang, P.; Reece, M. J. Piezoelectric Ceramics with Super-High Curie Points. *J. Am. Ceram. Soc.* **2009**, *92* (10), 2270–2275.

(21) Nanamatsu, S.; Kimura, M.; Doi, K.; Matsushita, S.; Yamada, N. A New Ferroelectric: $La_2Ti_2O_7$. *Ferroelectrics* **1974**, *8* (1), 511–513.

(22) Schmalle, H. W.; Williams, T.; Reller, A.; Linden, A.; Bednorz, J. G. The Twin Structure of $La_2Ti_2O_7$: X-ray and Transmission Electron Microscopy Studies. *Acta Crystallogr. B* **1993**, *49* (2), 235–244.

(23) Tanaka, M.; Sekii, H.; Ohi, K. Structural Study of $La_2Ti_2O_7$ by Convergent-Beam Electron Diffraction and Electron Microscopy. *Jpn. J. Appl. Phys.* **1985**, *24* (S2), 814.

(24) Zhang, F. X.; Lian, J.; Becker, U.; Ewing, R. C.; Wang, L. M.; Hu, J.; Saxena, S. K. Structural Change of Layered Perovskite $La_2Ti_2O_7$ at High Pressures. *J. Solid State Chem.* **2007**, *180* (2), 571–576.

(25) Ishizawa, N.; Marumo, F.; Iwai, S.; Kimura, M.; Kawamura, T. Compounds with Perovskite-Type Slabs. V. A High-Temperature Modification of $La_2Ti_2O_7$. *Acta Crystallogr. B* **1982**, *38* (2), 368–372.

(26) Atuchin, V. V.; Gavrilova, T. A.; Grivel, J.-C.; Kesler, V. G.; Troitskaia, I. B. Electronic Structure of Layered Ferroelectric High-K Titanate $Pr_2Ti_2O_7$. *J. Solid State Chem.* **2012**, *195*, 125–131.

(27) MacLean, D. A.; Ng, H.-N.; Greedan, J. E. Crystal Structures and Crystal Chemistry of the $RETiO_3$ Perovskites: RE = La, Nd, Sm, Gd, Y. *J. Solid State Chem.* **1979**, *30* (1), 35–44.

(28) Aughterson, R. D.; Lumpkin, G. R.; Reyes, M. de los; Sharma, N.; Ling, C. D.; Gault, B.; Smith, K. L.; Avdeev, M.; Cairney, J. M. Crystal Structures of Orthorhombic, Hexagonal, and Cubic Compounds of the $Sm_{(x)}Yb_{(2-x)}TiO_5$ Series. *J. Solid State Chem.* **2014**, *213*, 182–192.

(29) Zhang, F. X.; Wang, J. W.; Lang, M.; Zhang, J. M.; Ewing, R. C. Pressure-Induced Structural Transformations in Lanthanide Titanates: La_2TiO_5 and Nd_2TiO_5. *J. Solid State Chem.* **2010**, *183* (11), 2636–2643.

(30) Tiedemann, P.; Müller-Buschbaum, H. Zur Struktur Der Hochtemperaturform von Dy_2TiO_5. *Z. Für Anorg. Allg. Chem.* **1985**, *520* (1), 71–74.

(31) Hayun, S.; Navrotsky, A. Formation Enthalpies and Heat Capacities of Rear Earth Titanates: RE_2TiO_5 (RE=La, Nd and Gd). *J. Solid State Chem.* **2012**, *187*, 70–74.

(32) Konstantinov, P.; Krezhov, K.; Sváb, E.; Mészáros, G.; Török, G. Neutron Powder Diffraction Refinement of the Crystal Structure of La4Ti3O12. *Phys. B Condens. Matter* **2000**, *276*, 260–261.

(33) Fedorov, N. F.; Mel'nikova, O. V.; Saltykova, V. A.; Chistyakova, M. V. New perovskite-like compound of (12H) $La_4Ti_3O_{12}$. *Zhurnal Neorganicheskoj Khimii* **1979**, *24* (5), 1166–1170.

(34) Valeš, V.; Matějová, L.; Matěj, Z.; Brunátová, T.; Holý, V. Crystallization Kinetics Study of Cerium Titanate $CeTi_2O_6$. *J. Phys. Chem. Solids* **2014**, *75* (2), 265–270.

(35) Hurlen, T. On the Defect Structure of Rutile. *Acta Chem Scand* **1959**, *13* (2), 365–376.

(36) Feigelson, R. *50 Years Progress in Crystal Growth: A Reprint Collection*; Elsevier, 2004.

(37) McMillen, C. D.; Kolis, J. W. Bulk Single Crystal Growth from Hydrothermal Solutions. *Philos. Mag.* **2012**, *92* (19–21), 2686–2711.

(38) Laudise, R. A. Hydrothermal Synthesis of Single Crystals. *Prog. Inorg. Chem.* **1962**, *3*, 1–47.

(39) Byrappa, K.; Yoshimura, M. *Handbook of Hydrothermal Technology*; William Andrew, 2012.

(40) McMillen, C. W.; Kolis, J. W. Hydrothermal Synthesis as a Route to Mineralogically-Inspired Structures. *Dalton Trans.* **2016**, *45* (7), 2772–2784.

(41) McMillen, C. D.; Kolis, J. W. Hydrothermal Single Crystal Growth of Sc_2O_3 and Lanthanide-Doped Sc_2O_3. *J. Cryst. Growth* **2008**, *310* (7), 1939–1942.

(42) Mann, M.; Kolis, J. Hydrothermal Crystal Growth of Yttrium and Rare Earth Stabilized Hafnia. *J. Cryst. Growth* **2010**, *312* (3), 461–465.

(43) Mann, M.; Thompson, D.; Serivalsatit, K.; Tritt, T. M.; Ballato, J.; Kolis, J. Hydrothermal Growth and Thermal Property Characterization of ThO_2 Single Crystals. *Cryst. Growth Des.* **2010**, *10* (5), 2146–2151.

(44) Moore, C. A.; McMillen, C. D.; Kolis, J. W. Hydrothermal Growth of Single Crystals of $Lu_3Al_5O_{12}$ (LuAG) and Its Doped Analogues. *Cryst. Growth Des.* **2013**, *13* (6), 2298–2306.

(45) McMillen, C.; Thompson, D.; Tritt, T.; Kolis, J. Hydrothermal Single-Crystal Growth of Lu2O3 and Lanthanide-Doped Lu_2O_3. *Cryst. Growth Des.* **2011**, *11* (10), 4386–4391.

(46) Fulle, K.; McMillen, C. D.; Sanjeewa, L. D.; Kolis, J. W. Hydrothermal Chemistry and Growth of Fergusonite-Type $RENbO_4$ (RE = La–Lu, Y) Single Crystals and New Niobate Hydroxides. *Cryst. Growth Des.* **2016**, *16* (9), 4910–4917.

(47) Apex3; Bruker AXS Inc.: Madison, WI, 2015.

(48) Sheldrick, G. M. Crystal Structure Refinement with SHELXL. *Acta Crystallogr. Sect. C Struct. Chem.* **2015**, *71* (1), 3–8.

(49) Spek, A. L. J. Single-Crystal Structure Validation with the Program PLATON. Appl. Cryst., 2003, Vol. 36. *Надійшла До Редколегії 2905 13*, 7–13.

(50) Brese, N. E.; O'Keeffe, M. Bond-Valence Parameters for Solids. *Acta Crystallogr. B* **1991**, *47* (2), 192–197.

(51) Brown, I. D.; Altermatt, D. Bond-Valence Parameters Obtained from a Systematic Analysis of the Inorganic Crystal Structure Database. *Acta Crystallogr. B* **1985**, *41* (4), 244–247.

(52) Scheunemann, K.; Müller-Buschbaum, H. Zur Kristallstruktur von $Nd_2Ti_2O_7$. *J. Inorg. Nucl. Chem.* **1975**, *37* (11), 2261–2263.

(53) Bharathy, M.; Gemmill, W. R.; Fox, A. H.; Darriet, J.; Smith, M. D.; Hadermann, J.; Remy, M. S.; zur Loye, H.-C. Synthesis and Magnetic Properties of Rare Earth Ruthenates, $Ln_5Ru_2O_{12}$ (Ln=Pr, Nd, Sm–Tb). *J. Solid State Chem.* **2009**, *182* (5), 1164–1170.

(54) Chi, L.; Britten, J. F.; Greedan, J. E. Synthesis, Structure and Magnetic Properties of the S=1/2, One-Dimensional Antiferromagnet, $Y_5Re_2O_{12}$. *J. Solid State Chem.* **2003**, *172* (2), 451–457.

(55) Ehrenberg, H.; Hartmann, T.; Wltschek, G.; Fuess, H.; Morgenroth, W.; Krane, H.-G. The Crystal Structure of $Tm_5Re_2O_{12}$. *Acta Crystallogr. B* **1999**, *55* (6), 849–852.

(56) Jeitschko, W.; Heumannskämper, D. H.; Rodewald, Ute Ch.; Schriewer-Pöttgen, M. S. Preparation and Crystal Structure of Rare Earth Rhenates: The Series $Ln_5Re_2O_{12}$ with Ln=Y, Gd–Lu, and the Praseodymium Rhenates Pr_3ReO_8, $Pr_3Re_2O_{10}$, and $Pr_4Re_2O_{11}$. *Z. Für Anorg. Allg. Chem.* **2000**, *626* (1), 80–88.

(57) Baud, G.; Besse, J.-P.; Chevalier, R.; Gasperin, M. Synthese et Etude Structurale de L'oxyde Double $Dy_5Re_2O_{12}$. *Mater. Chem. Phys.* **1983**, *8* (2), 93–99.

(58) Hubner, N.; Gruehn, R. Preparation, Thermal Behavior and Structure Investigation of M-$Nd_2Ti_4O_{11}$. *J. Alloys Compd.* **1992**, *183* (34), 85–97.

(59) Kong, L.; Gregg, D. J.; Karatchevtseva, I.; Zhang, Z.; Blackford, M. G.; Middleburgh, S. C.; Lumpkin, G. R.; Triani, G. Novel Chemical Synthesis and Characterization of $CeTi_2O_6$ Brannerite. *Inorg. Chem.* **2014**, *53* (13), 6761–6768.

(60) Kong, L.; Gregg, D. J.; Vance, E. R.; Karatchevtseva, I.; Lumpkin, G. R.; Blackford, M. G.; Holmes, R.; Jovanovic, M.; Triani, G. Preparation of Cerium Titanate Brannerite by Solution Combustion, and Phase Transformation during Heat Treatment. *J. Eur. Ceram. Soc.* **2017**, *37* (5), 2179–2187.

(61) Matějová, L.; Valeš, V.; Fajgar, R.; Matěj, Z.; Holý, V.; Šolcová, O. Reverse Micelles Directed Synthesis of TiO_2–CeO_2 Mixed Oxides and Investigation of Their Crystal Structure and Morphology. *J. Solid State Chem.* **2013**, *198*, 485–495.

(62) McMillen, C. D.; Comer, S.; Fulle, K.; Sanjeewa, L. D.; Kolis, J. W. Crystal Chemistry of Hydrothermally Grown Ternary Alkali Rare Earth Fluorides. *Acta Crystallogr. Sect. B Struct. Sci. Cryst. Eng. Mater.* **2015**, *71* (Pt 6), 768–776.

(63) Kimani, M. M.; McMillen, C. D.; Kolis, J. W. Hydrothermal Synthesis and Comparative Coordination Chemistry of New Rare-Earth V^{4+} Compounds. *Inorg. Chem.* **2012**, *51* (6), 3588–3596.

(64) Golovastikov, N. I.; Belov, N. V. Crystal structure of yttrium germanate $Y_3GeO_5(OH)_3$. *Kristallografiya* **1982**, *27* (6), 1087–1089.

(65) Mamin, B. F.; Khalikov, R. A.; Dem'yants, L. N.; Golyshev, V. M.; Shibanova, T. A. Synthesis and atomic structure of dysprosium germanate $Dy_3GeO_5(OH)_3$. *Kristallografiya* **1987**, *32* (4), 878–881.

(66) Genkina, E. A.; Dem'yanets, L. N.; Mamin, B. F.; Maksimov, B. A. Synthesis and Structures of $Gd_3GeO_5(OH)_3$ and $Sm_3GeO_5(OH)_3$. A New Example of a Five-Fold Germanium Coordination. *Kristallografiya* **1989**, *34* (4), 1002–1005.

(67) Torardi, C. C.; Fecketter, C.; McCarroll, W. H.; DiSalvo, F. J. Structure and Properties of $Y_5Mo_2O_{12}$ and $Gd_5Mo_2O_{12}$: Mixed Valence Oxides with Structurally Equivalent Molybdenum Atoms. *J. Solid State Chem.* **1985**, *60* (3), 332–342.

(68) Cortese, A. J.; Abeysinghe, D.; Wilkins, B.; Smith, M. D.; Morrison, G.; zur Loye, H.-C. High-Temperature Salt Flux Crystal Growth of New Lanthanide Molybdenum Oxides, $Ln_5Mo_2O_{12}$ Ln = Eu, Tb, Dy, Ho, and Er: Magnetic Coupling within Mixed Valent Mo(IV/V) Rutile-Like Chains. *Inorg. Chem.* **2015**, *54* (24), 11875–11882.

CHAPTER SIX

HYDROTHERMAL CHEMISTRY AND GROWTH OF FERGUSONITE-TYPE $RENbO_4$ (RE=La-Lu, Y) SINGLE CRYSTALS AND NEW NIOBATE HYDROXIDES

Introduction

This Chapter involves a unique investigation into the refractory nature of two classes of high melting metal oxides: RE_2O_3 and Nb_2O_5 (RE = La-Lu). "The content of this Chapter is used as a reprint (adapted) from permission from Fulle, K.; McMillen, C. D.; Sanjeewa, L. D.; Kolis, J. W. Hydrothermal Chemistry and Growth of Fergusonite type $RENbO_4$ (RE=La-Lu, Y) Single Crystals and New Niobate Hydroxides. *Cryst. Growth and Des*. **2016**, *16*, 4910–4917. Copyright 2016 American Chemical Society." A duplicate of the copyright permission is located in Appendix.

Many rare-earth containing materials, such as the rare-earth orthovanadates, $REVO_4$ (RE = Y, Gd, Lu), display excellent properties as laser hosts and as birefringent materials.[1] In particular, YVO_4 is an excellent laser host for trivalent rare earth ions like Nd^{3+} in that the laser crystal $Nd:YVO_4$ has much greater absorption and emission cross sections compared to the industry standard YAG.[2] It also has a very broad absorption band for pumping.[3] These factors make it a desirable host for microlaser and miniature laser applications.[4] In addition, the YVO_4 lattice is uniaxial tetragonal (4/*mmm*) and the material has a very high birefringence (D and the material has a very high birefringence (aser and miniature laser applications.rd YAG. is located in Appendix. mal Chemistry and Growth of Fergusonite type RENbOne by Solution Comb[5] It has a low thermal

conductivity, fairly high isotropic thermal expansion coefficients, and most importantly its structure contains a weak *c*-plane, giving the crystals a large tendency to display cleavage along that plane. Also, the growth of YVO_4 single crystals is complicated by the fact that the pentavalent vanadium ions are susceptible to reduction at high-temperature.[6] Thus during typical melt growth great care must be taken to prevent the formation of V^{4+} defect centers in the crystals, as these can have a significant effect on optical quality.

In contrast to the well-examined YVO_4 crystal and its rare-earth analogs $GdVO_4$ and $LuVO_4$,[7,8] the heavier congeners $RENbO_4$ have received much less study. Nevertheless they have considerable potential as useful materials, maximizing their own positive qualities while minimizing the shortcomings of YVO_4. For example, pentavalent niobium should be more stable than V^{5+} and thus have a decreased tendency to induce oxygen defects. The rare-earth niobates also display several attractive optical and luminescent properties.[9] Furthermore, the different lattice structure of the niobates may help minimize physical detriments, such as c-plane weakness in YVO_4, making it a robust new laser host. The heavier elements may also change the absorption coefficients and thermal conductivity, and lead to a denser unit cell that could serve as useful new scintillation hosts for gamma ray detection.

In this Chapter, the use of Nb^{+5} as a structural building block is examined in a number of different mineralizers. Pentavalent niobium has a medium crystallographic radius (0.78 Å) and can adopt a variety of coordination environments from 4-coordinated to 8-coordinate. Additionally, niobium oxide has been shown to display physiochemical properties and can display Lewis and Bronsted acidities in certain basic environments.

This high level of flexibility makes niobium oxide (Nb_2O_5) an excellent candidate to react with the rare-earth ions (RE = La-Lu) to investigate new and existing materials. Herein, an examination of the $RENbO_4$ family is used as a surrogate to the $REVO_4$ family as an extension of the well-known crystal growth. The crystal growth of the family $RENbO_4$ was accomplished over several years and a breakthrough of this crystal growth occurred when implementation of a 30 *M* KOH mineralizer was used at high hydrothermal temperatures (700 °C).

Interestingly, the structural aspects of $RENbO_4$ are considerably more subtle and complex than those of YVO_4. Unlike the $REVO_4$ series, which forms in the straightforward tetragonal zircon structure type, the $RENbO_4$ phase has a more complicated structural profile. The parent material is the natural mineral fergusonite, $YNbO_4$, which is plagued by twinning issues that originally led to the assignation of the material as the tetragonal phase analogous to the scheelite structure. Subsequent work demonstrated that the room temperature phase is an *I*-centered or *C*-centered monoclinic structure.[10,11] Furthermore, the monoclinic phase was originally thought to have an acentric ferroic structure, but this was subsequently shown to be a centrosymmetric 2/*m* structure type.[12-16] Recently, Bayliss and coworkers noted that the similarity of the *a* and *c* lattice parameters in the *I*-centered monoclinic setting often leads to incorrect structural descriptions, underscoring the importance of detailed study by single crystal X-ray diffraction.[15] The tetragonal scheelite phase is stable at high-temperature but upon cooling it reverts to the monoclinic fergusonite phase near 550°C.[18-21] However the situation is even subtler than that, since the phase change induces a series of complex

micro domains that result in considerable twinning. This often precludes high quality structural refinements, or causes significant areas of electron density to remain present in the difference electron density maps. Since these micro-domains are of a ferroelastic nature they received a great deal of detailed study at the nanoscopic regime.[22-25]

Given the appeal of the $RENbO_4$ material as a potential optical host, the growth of the rare-earth niobates as high quality single crystals is of interest. The materials can be grown readily by melt techniques such as Czochralski pulling, but because they are grown at temperatures near 1800˚C and then cooled from the high-temperature melt through the phase transition, they inevitably result in twinned products as they cool to room temperature.[26] Powders of $NdNbO_4$ have been prepared through ball milling to form microwave dielectric materials,[27] and a variety of orthoniobates have been synthesized by miniature pedestal growth under conditions nearing 1300 °C.[28] While these techniques are well known, they have not yet proven effective for growth of bulk single crystals of suitable quality. Most recently, Liu and co-workers have synthesized $GdNbO_4$ on a scale up to 100 μm using a hydroflux, but the resulting $GdNbO_4$ could be considered to be more like microcystalline material than bulk single crystals.[29]

The hydrothermal technique offers a comparatively low temperature alternative for oxide crystal growth that can be used to both solubilize the refractory starting materials and enable prolonged crystal growth, provided that limitations such as the inability to observe the reactions in situ and the reactivity of the aqueous mineralizer species can be managed.[30] The ability to grow bulk single crystals of YVO_4 and its doped analogs using a high-temperature hydrothermal method suggests that the technique may

also be suitable for growth of the rare-earth niobates.[31,32] Of particular significance is the fact that the hydrothermal growth could occur near the phase transition of the monoclinic material and thus preclude the formation of the tetragonal phase to minimize or eliminate the twinning problems associated with higher temperature growth methods. This paper describes an effort to investigate the hydrothermal growth of rare-earth orthoniobates and grow high quality bulk single crystals of the fergusonite material. Single crystal X-ray diffraction of the resultant crystals demonstrates good quality structural solutions with minimal twinning or disorder across the entire rare-earth series. Preparation of lanthanide-doped $RENbO_4$ crystals was also performed to prepare for subsequent investigations of the physical and optical properties of these bulk single crystals for application as potential laser hosts. Along with a new growth protocol of this class of single crystals we also isolated several new metal niobates as part of the chemical investigations, and these are characterized as well.

In previous Chapters, thorough systematic investigations of rare-earth silicates, rare-earth germanates, and rare-earth titanates have led to very rich chemistry. The natural progression of this mentality has led to the investigation of rare-earth niobates as this Chapter entails a systematic investigation of Nb^{+5} with rare-earth ions in hydrothermal solutions.

Experimental Methods

Single crystals of $RENbO_4$ and doped Ln:$RENbO_4$ (RE= La^{+3}, Nd^{3+}, Eu^{+3}, Gd^{+3}, Lu^{+3} and Y^{+3}; Ln = Er^{3+} and Yb^{3+}) were grown under hydrothermal conditions using feedstock of the host component oxides and dopant oxides. All reagents were used directly from the commercial vendor: Y_2O_3 (HEFA Rare Earth, 99.9%), Lu_2O_3 (HEFA Rare Earth, 99.99%), Yb_2O_3 (HEFA Rare Earth, 99.99%), Er_2O_3 (Alfa Aesar, 99.99%), Gd_2O_3 (HEFA Rare Earth, 99.9%), Eu_2O_3 (HEFA Rare Earth, 99.9%), Nd_2O_3 (Alfa Aesar, 99.99%), La_2O_3 (Alfa Aesar, 99.999%), Nb_2O_5 (Alfa Aesar, 99.999%), KOH pellets (Alfa Aesar, 99.98%).

For the growth of $RENbO_4$, stoichiometric reactions of rare-earth and pentavalent oxide components, RE_2O_3 + Nb_2O_5, in a 1:1 ratio were used. In a typical reaction, component binary oxides of the desired fergusonite phase were loaded into a fine silver ampoule (3/8" x 3"), in equimolar stoichiometries to create a total of 400 mg of solid oxides with 0.8 mL of DI water and suitable solid KOH to generate a 30 molar solution at hydrothermal temperatures. Ampoules were weld-sealed and loaded into a 718 Inconel autoclave with a 75% fill of DI water to serve as the desired counter-pressure. The autoclave was affixed with ceramic band heaters and heated to a constant temperature of 700 °C for 10 days. This temperature typically results in an internal pressure of 1.5-2 kbar. For growth of lanthanide-doped $RENbO_4$, a direct component substitution was used to achieve the desired nominal doping. In these studies, the host and dopant oxide

powders were combined in a desired molar ratio, (for example, a 10% Er_2O_3/Gd_2O_3 powder combined with Nb_2O_5 generates a ratio of $Er_{0.1}Gd_{0.9}NbO_4$).

During the various synthetic studies of rare-earth orthoniobates, several new hydroxide niobate crystals were isolated as minor products during reactions performed at lower temperatures (550˚C). In reactions involving Y^{3+} and Lu^{3+}, $K_3YNb_2O_7(OH)_2$ and $K_3LuNb_2O_7(OH)_2$ crystals result as additional minor products from the reactions described above. These colorless crystals were identified and separated based on their hexagonal rod-like habit, in contrast to the plate-like crystals of the orthoniobates. Pyrochlore niobate hydroxides of $CsNb_2O_5(OH)$ and $CsNb_2O_5(OH)_{0.5}F_{0.5}$ were also isolated when CsOH was used as a mineralizer. Alternatively, crystals of $CsNb_2O_5(OH)$ can be synthesized directly using 400 mg of Nb_2O_5 and 0.8 mL of 3-6 *M* CsOH at 550 °C. Similarly the hydroxide-fluoride species, $CsNb_2O_5(OH)_{0.5}F_{0.5}$, was crystallized when substituting 5 *M* CsF as the mineralizer at 550 °C. These aforementioned cesium-containing hydroxides and hydroxide-fluorides grow as colorless polyhedral crystals on the order of 0.25-0.45 mm, occurring alongside unreacted Nb_2O_5.

Crystal Growth of Fergusonite-type $RENbO_4$ (RE=La-Lu, Y).

The direct stoichiometric reaction of various RE_2O_3 powders and Nb_2O_5 was studied under hydrothermal conditions (500-700 °C) using several different alkali hydroxide mineralizer solutions in an effort to optimize the yield and size of the target $RENbO_4$ phase. Initial reactions performed at 500-600 °C resulted in the formation of $RENbO_4$ powder along with minor amount of additional crystalline phases. Typically these minor phases consisted of more complex structures containing hydroxylated species. In the case of CsOH mineralizers at lower temperatures, $CsNb_2O_5(OH)$ was formed, while $KNbO_3$ and $K_3RENb_2O_7(OH)_2$ were formed in the case of KOH mineralizers. By increasing the KOH concentration above 15 M, and increasing the reaction temperature 700 °C, both the yield and the size of the target $RENbO_4$ crystals was improved, while the hydroxide containing phases were suppressed. The fergusonite crystals generally form in a plate-like habit for the smaller rare-earth ions (Gd-Lu), with the largest crystals obtained using 30 M KOH at 700 °C. The larger, lighter rare-earths (La-Nd) were also generally plate-like, but occasionally developed greater thicknesses to appear as more three-dimensional polyhedra. Typical crystals obtained from this high-temperature hydrothermal growth are shown in **Figure 6.1**. In general under these conditions the larger rare-earth ions appear to form somewhat larger and higher quality crystals. Single crystals up to 3 mm in diameter have been grown for $LaNbO_4$, $PrNbO_4$, $NdNbO_4$, $EuNbO_4$ and $GdNbO_4$, while crystals of $YNbO_4$ and $LuNbO_4$ have so far been limited to 0.5 mm in diameter. Appreciable thicknesses up to 1 mm have been obtained in all cases.

There are several common structure types exhibited by ABO_4 compounds, revealing a diverse chemistry, and often demonstrating complex structural transitions based on temperature and pressure.[36,37] Based on the powder diffraction patterns in **Figure 6.2** as well as our own single crystal X-ray diffraction studies (**Tables 6.1 and 6.2**), the $RENbO_4$ crystals grown in the present study all conform to the fergusonite-type structure (space group *C*2/*c* (or often reported in its non-standard setting *I*2/*a*)), regardless of size of the rare-earth. The fergusonite structure is a three-dimensional framework consisting of irregular NbO_6 and REO_8 units (**Tables 6.3 and 6.4**). Niobium occupies a *4e* Wyckoff position having two-fold symmetry, and forms shorter bonds to four oxygen atoms over a narrow range of distances (average Nb-O distances of 1.846(5) and 1.927(5) Å across the $RENbO_4$ family) and longer bonds to two other oxygen atoms (average Nb-O distance of 2.455(5) Å) to form the distorted NbO_6 unit. It is only in these two longer bonds that the NbO_6 unit shows significant variation as a function of the rare-earth ion, ranging from 2.406(5) to 2.540(3) Å between the Lu and La derivatives. The NbO_6 units form a one-dimensional zigzag chain propagating by edge-shared oxygen atoms along the c-axis. Each shared edge consists of one longer Nb1-O2 bond and one shorter Nb1-O2 bond. If only the shorter Nb1-O1 and Nb1-O2 bonds are considered, the niobate unit is an isolated distorted tetrahedron. The rare-earth atoms also occupy a *4e* site and are 8-coordinate with oxygen in a square antiprismatic geometry.

The La-O bonds range from 2.468(3) to 2.551(3) Å, while the Lu-O bonds range from 2.277(5) to 2.374(5) Å, with the other rare-earths studied intermediate to these. The interatomic distances and angles derived from the hydrothermally-grown crystals (**Tables**

6.1-6.3) compare favorably with those derived from crystals and powders prepared by other techniques in the literature.[13,15] The framework formed by edge-sharing REO_8 units can be considered to encapsulate the propagating chains of NbO_6 units to form a three-dimensional framework. The fergusonite structural arrangement is shown in **Figure 6.3**.

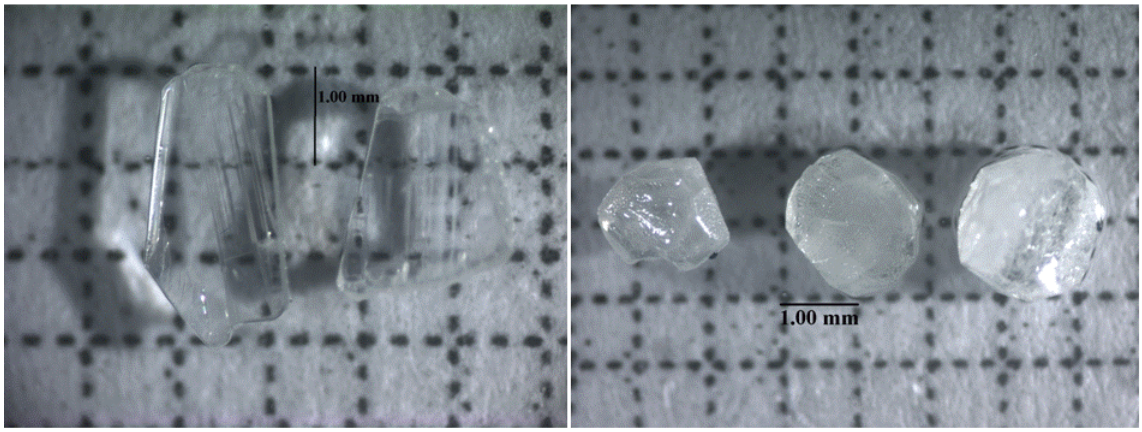

Figure 6.1: $GdNbO_4$ (left) and $LaNbO_4$ (right) single crystals grown under hydrothermal conditions.

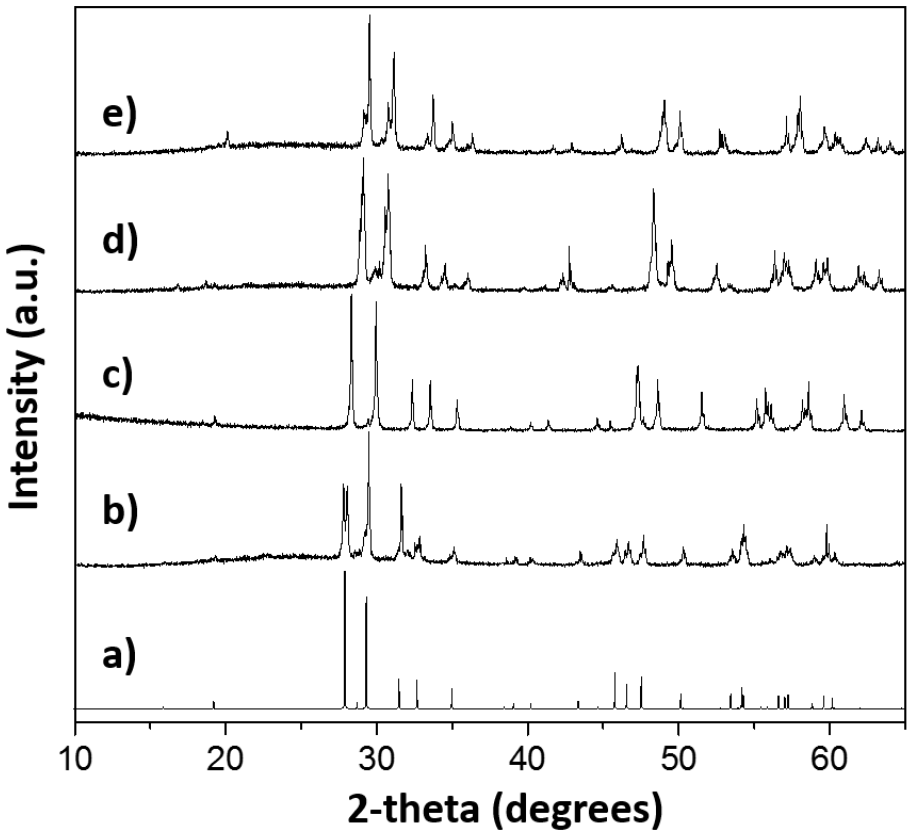

Figure 6.2: Powder diffraction patterns of selected $RENbO_4$ compounds: a) Simulated powder pattern of $LaNbO_4$ based on the crystal structure of hydrothermally grown crystals. b-e) experimental PXRD patterns of hydrothermally grown $LaNbO_4$, $GdNbO_4$, $YNbO_4$ and $LuNbO_4$, respectively.

Table 6.1: Crystallographic data of $RENbO_4$ (RE = Y, La, Nd) determined by single crystal X-ray diffraction.

empirical formula	$YNbO_4$	$LaNbO_4$	$NdNbO_4$
formula weight (g/mol)	245.82	295.82	301.15
temperature (K)	300(2)	300(2)	300(2)
crystal system	monoclinic	monoclinic	monoclinic
space group	*C2/c,* (no.15)	*C2/c,* (no.15)	*C2/c,* (no.15)
unit cell dimensions (Å,°)	*a* = 7.0516(7) *b* = 10.9560(11) *c* = 5.0760(9) β = 131.370(3)	*a* = 7.3576(15) *b* = 11.538(2) *c* = 5.2128(10) β = 130.900(3)	*a* = 7.2156(14) *b* = 11.295(2) *c* = 5.1511(10) β = 130.860(3)
volume ($Å^3$)	294.29(7)	334.49(16)	317.53(15)
Z, calcd density (Mg/m^3)	4, 5.548	4, 5.874	4, 6.299
absorption coefficient (mm^{-1})	23.324	15.857	19.601
F(000)	448	520	532
crystal size (mm)	0.08 x 0.06 x 0.03	0.11 x 0.08 x 0.06	0.16 x 0.10 x 0.08
Tmax, Tmin	1.0000, 0.6692	1.0000, 0.7145	1.0000, 0.5652
Θ range for data	3.72-26.48	3.53-25.24	3.61-25.24
reflections collected/ unique/ observed	754/306/304	1414/ 308/297	1306/290/277
data/ restraints/ parameters	306/0/30	308/0/30	290/0/30
goodness-of-fit on F^2	1.180	1.172	1.162
R1, wR2 ($I \geq 2\sigma(I)$)	0.0255, 0.0800	0.0162, 0.0405	0.0276, 0.0701
R1, wR2 (all data)	0.0255, 0.0801	0.0166, 0.0408	0.0378, 0.0849
extinction coefficient	0.051(4)	0.0114(6)	0.071(6)

Table 6.2: Crystallographic data of $RENbO_4$ (RE = Eu, Gd, Lu) determined by single crystal X-ray diffraction.

empirical formula	$EuNbO_4$	$GdNbO_4$	$LuNbO_4$
formula weight (g/mol)	308.87	314.16	331.88
temperature (K)	300(2)	300(2)	300(2)
crystal system	monoclinic	monoclinic	monoclinic
space group	*C*2/*c,* (no.15)	*C*2/*c,* (no.15)	*C*2/*c,* (no.15)
unit cell dimensions (Å,°)	*a* = 7.1328(6) *b* = 11.1385(10) *c* = 5.1180(4) β = 131.032(2)	*a* = 7.1166(8) *b* = 11.0914(11) *c* = 5.1071(10) β = 131.131(3)	*a* = 6.9805(6) *b* = 10.8271(8) *c* = 5.0406(4) β = 131.676(3)
volume ($Å^3$)	306.73(5)	303.64(8)	284.54(4)
Z, calcd density (Mg/m^3)	4, 6.689	4, 6.872	4, 7.747
absorption coefficient (mm^{-1})	23.813	25.241	38.321
F(000)	544	548	576
crystal size (mm)	0.20 x 0.10 x 0.05	0.10 x 0.08 x 0.07	0.04 x 0.02 x 0.02
Tmax, Tmin	1.0000, 0.8899	1.0000, 0.7499	1.0000, 0.7062
Θ range for data	3.66-33.18	3.67-30.52	3.76-26.47
reflections collected/ unique/ observed	2564/586/542	1135/458/451	1139/297/287
data/ restraints/ parameters	586/0/30	458/0/30	297/0/30
goodness-of-fit on F^2	1.173	1.181	1.176
R1, wR2 ($I \geq 2\sigma(I)$)	0.0198, 0.0616	0.0212, 0.0630	0.0178, 0.0489
R1, wR2 (all data)	0.0227, 0.0628	0.0214, 0.0630	0.0189, 0.0495
extinction coefficient	0.0385(17)	0.088(4)	0.0051(4)

Table 6.3: Selected interatomic distances (Å) and angles (°) in hydrothermally-grown fergusonite $RENbO_4$ (RE = Y, La, Nd, Eu, Gd, Lu)

	$YNbO_4$	**$LaNbO_4$**	**$NdNbO_4$**	**$EuNbO_4$**	**$GdNbO_4$**	**$LuNbO_4$**
Nb1–O2 (x2)	1.847(5)	1.844(3)	1.848(9)	1.845(4)	1.844(4)	1.845(5)
Nb1–O1 (x2)	1.928(5)	1.915(3)	1.931(9)	1.929(4)	1.929(4)	1.929(5)
Nb1–O1 (x2)	2.424(5)	2.541(3)	2.470(9)	2.443(4)	2.448(4)	2.406(5)
RE1–O2 (x2)	2.318(5)	2.468(3)	2.393(9)	2.365(4)	2.351(4)	2.277(5)
RE1–O1 (x2)	2.328(5)	2.492(3)	2.419(9)	2.381(4)	2.367(4)	2.285(5)
RE1–O2 (x2)	2.375(5)	2.525(3)	2.474(8)	2.424(4)	2.415(4)	2.341(5)
RE1–O1 (x2)	2.414(5)	2.551(3)	2.500(8)	2.457(4)	2.443(4)	2.374(5)
O2–Nb1–O2	103.8(3)	102.7(2)	102.7(5)	102.8(3)	103.4(3)	104.9(3)
O2–Nb1–O1 (x2)	110.03(19)	109.84(14)	109.5(4)	110.22(19)	109.84(18)	110.1(2)
O2–Nb1–O1 (x2)	100.2(2)	101.28(14)	100.9(4)	100.2(2)	100.44(18)	100.1(2)
O1–Nb1–O1	130.1(3)	129.27(19)	130.5(5)	130.5(3)	130.3(3)	129.6(3)
O2–Nb1–O1 (x2)	77.18(19)	77.48(12)	77.6(3)	77.58(17)	77.25(16)	76.7(2)
O2–Nb1–O1 (x2)	173.46(18)	174.49(12)	174.3(3)	173.57(17)	173.64(16)	173.10(19)
O1–Nb1–O1 (x2)	73.48(12)	73.62(9)	73.9(2)	73.80(11)	73.52(11)	73.14(13)
O1–Nb1–O1 (x2)	75.94(18)	75.40(14)	75.8(4)	75.87(18)	76.08(17)	75.9(2)
O1–Nb1–O1	102.6(2)	102.87(15)	102.7(4)	102.8(2)	102.8(2)	102.6(2)

Table 6.4: Bond valence analysis in hydrothermally-grown fergusonite $RENbO_4$ (RE = Y, La, Nd, Eu, Gd, Lu)

	$YNbO_4$	**$LaNbO_4$**	**$NdNbO_4$**	**$EuNbO_4$**	**$GdNbO_4$**	**$LuNbO_4$**
Nb1–O2 (x2)	1.189	1.199	1.186	1.195	1.199	1.195
Nb1–O1 (x2)	0.995	0.989	0.947	0.953	0.953	0.953
Nb1–O1 (x2)	0.250	0.182	0.221	0.237	0.234	0.262
Σ Nb	4.868	4.740	4.708	4.770	4.772	4.820
RE1–O2 (x2)	0.446	0.449	0.459	0.455	0.470	0.440
RE1–O1 (x2)	0.434	0.421	0.428	0.436	0.450	0.431
RE1–O2 (x2)	0.382	0.385	0.369	0.388	0.395	0.370
RE1–O1 (x2)	0.343	0.359	0.344	0.355	0.366	0.339
Σ RE	3.210	3.228	3.200	3.268	3.362	3.160

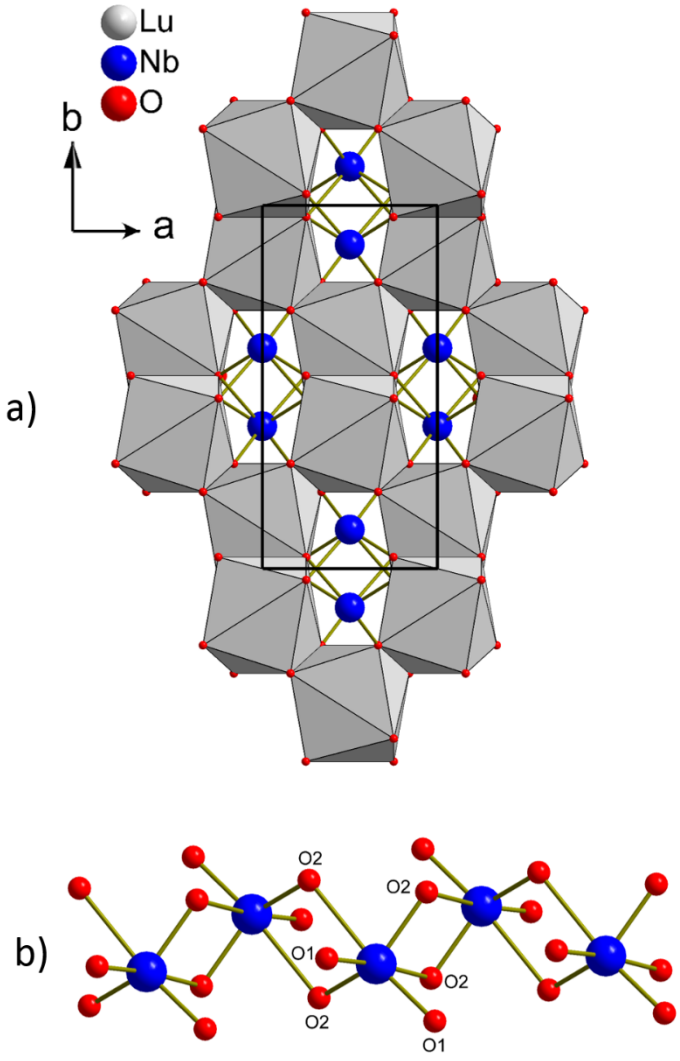

Figure 6.3: Fergusonite structure type of the rare-earth niobates: a) the framework of edge-sharing REO_8 units encapsulating chains of NbO_6 units viewed along [001]; b) propagation of the NbO_6 units along [001] through shared O2 edges.

Materials based on Eu^{3+} are particularly interesting for study due to their potential as red-emitting phosphors and the sensitivity of Eu^{3+} toward local site symmetry. As such, the emission behavior of $EuNbO_4$ was studied to complement the structure determination and demonstrate the potential of $RENbO_4$ crystals as optical materials. X-ray luminescence studies resulted in the characteristic emission for Eu^{3+} (**Figure 6.4**), and indicated no reduction of the europium ions to a divalent state. The orange-red emission of the $EuNbO_4$ crystals exhibits several bands in the range of 590-700 nm from the f-f transitions. In particular, the $^5D_0 \rightarrow {}^7F_2$ emission occurring at 615 nm is much more intense than the $^5D_0 \rightarrow {}^7F_1$ at 590 nm. This is indicative of a lack of a center of symmetry at the Eu^{3+} sites, and consistent with the assigned 4*e* crystallographic site having only 2-fold rotational symmetry.[38] This simple emission behavior is promising for targeting intense emissions in the region of 600-630 nm.

To help understand the scope and versatility of the hydrothermal crystal growth of the fergusonite structure type, the X-ray diffraction studies targeted specific $RENbO_4$ compositions that represent a wide range of sizes of rare-earth ions. In particular, this included the optically inactive rare-earths (Y, La, Gd, Lu) that are useful as hosts for those rare-earth ions that can serve as spectroscopic or scintillator dopants. The persistence of the fergusonite structure type across the entire size range of rare-earths is suggestive that nearly any combination of rare-earth host and dopant ions is plausible, offering great flexibility in the design of new optical materials. This could be particularly interesting in

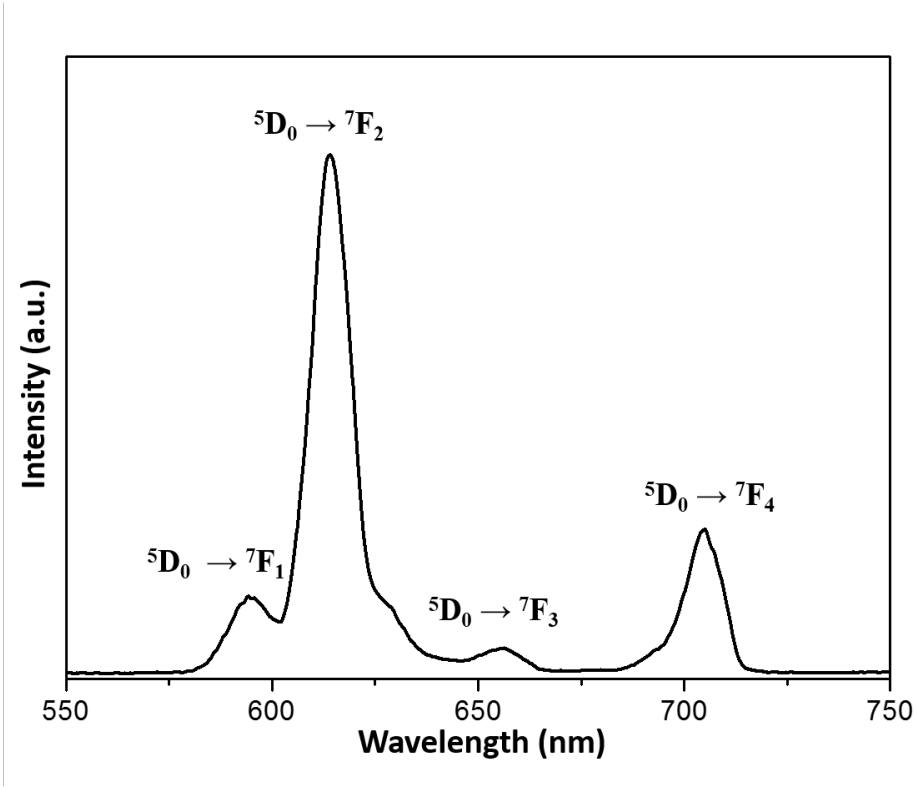

Figure 6.4: Room temperature emission spectrum of $EuNbO_4$, resulting from X-ray excitation.

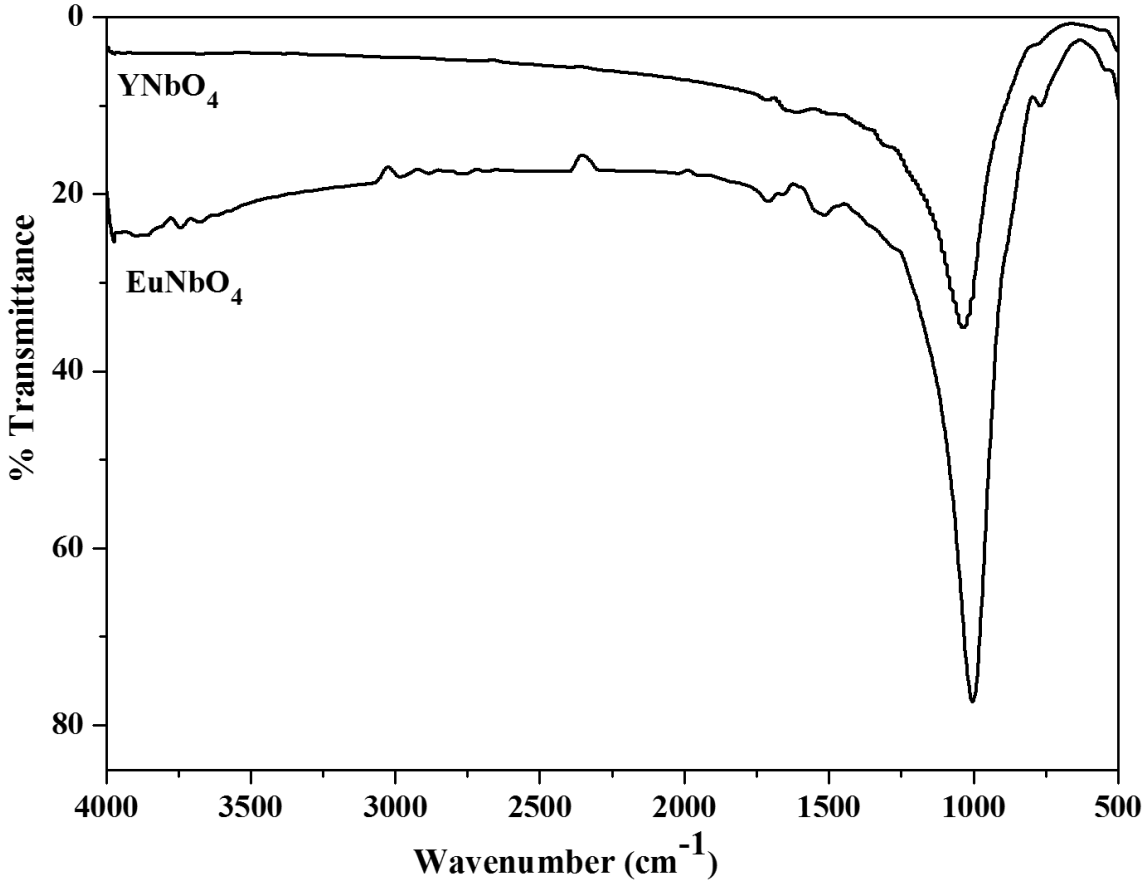

Figure 6.5: Infrared spectra of representative hydrothermally-grown fergusonite-type crystals $YNbO_4$ and $EuNbO_4$. The absence of the characteristic OH- band in the 3000-3500 cm^{-1} region supports the absence of OH- in the as-grown crystals.

the case of $LuNbO_4$. Since laser ions such as Er^{3+} and Yb^{3+} have nearly the same mass as Lu^{3+}, those crystals may be particularly efficient in their thermal management for cryogenic

or high power laser applications. In addition, the density of the materials increases significantly across the lanthanide series, and $LuNbO_4$ possesses the highest density among the fergusonite orthoniobates (~7.75 g/cm3). This is a significant density value, which could lead to excellent performance as scintillator host. The absence of OH^- groups in the crystals was verified by infrared spectroscopy, **Figure 6.5**).

Interestingly, the fergusonite structure type is considered a low temperature phase, exhibiting a phase transition to the tetragonal scheelite structure type above 500 °C, with the apparent gradual onset of the scheelite phase starting from slightly above 500 to 800°C.[18] In most previous structural studies the fergusonite material was prepared at much higher temperatures by a melt or flux technique. These preparation temperatures are well above the phase transition point, inevitably resulting in twin formation from multiple ferroelastic domains induced as the material cools through the phase transition. Since the crystals in the present study were grown near the phase transition regime, we surmise that the hydrothermal conditions facilitate the growth of the *C*2/*c* fergusonite-type phase as bulk crystals with much larger single crystalline domains.[23-25] Indeed this proved to be the case as the previously reported twinned crystals had domains on the order of tens or hundreds of nanometers, while the crystals grown in this study showed no evidence of significant twin domains over the order of tens to hundreds of microns in the single crystal diffraction studies. Reflection profiles from single crystal diffraction were

Gaussian and symmetrical (**Figure 6.6**), and exhibited narrow peak widths consistent with low mosaicity (FWHM values generally in the range of 0.25-0.45 degrees for a 0.1 degree scan width in 2-theta). Apparent domains of 0.5-1 mm are visible in the changing orientation of growth striations on the surfaces of very large crystals. Some examples are shown in **Figure 6.7**, and correspond to a domain rotation about the crystallographic b-axis. Domains well beyond the nanoscale are observed in the hydrothermally-grown fergusonite crystals.

Synthesis and Structures of New Niobate Hydroxides.

In the course of the hydrothermal synthesis of the rare-earth orthoniobates, several new alkali niobate hydroxides have also been discovered and crystallographically characterized (**Tables 6.5 and 6.6**). The work was motivated by an interest in growing the various rare-earth niobate fergusonite phases at lower reaction temperatures (ca. 500-550˚C) in an attempt to further minimize twinning domains. During these studies a number of hydrothermal conditions and mineralizers were investigated. In particular, we isolated a number of new hydroxide-containing minor phases as a function of the nature of mineralizer in the growth reactions at these lower temperatures. Sensitivity of the hydrothermal reactions toward the nature of the mineralizers resulted in the incorporation of the alkali metal ions to stabilize these new phases, which occur presumably as side products to the $RENbO_4$ phases. Two general structure types were encountered depending on whether the reaction utilized KOH or CsOH mineralizers. In the case of potassium mineralizers a new $K_3RENb_2O_7(OH)_2$ (RE = Y, Lu) phase was observed. When

cesium-based mineralizers were used $CsNb_2O_5(OH)$ was isolated regardless of rare-earth employed. In the latter instance, if a mixture of CsF/CsOH mineralizer was used, it also resulted in a mixture of OH- and F- ions in the of $CsNb_2O_5(OH)$ lattice. In all cases these materials are relatively minor impurities and can be eliminated from the final product profile by performing the growth reactions at slightly higher temperatures. In general, we find that that this type of behavior is typical of hydrothermal growth of many refractory oxides. At some lower temperatures some oxy-hydroxide phase(s) can be observed. These are often interesting and complex structures, but can often be eliminated by growth at some higher temperature.

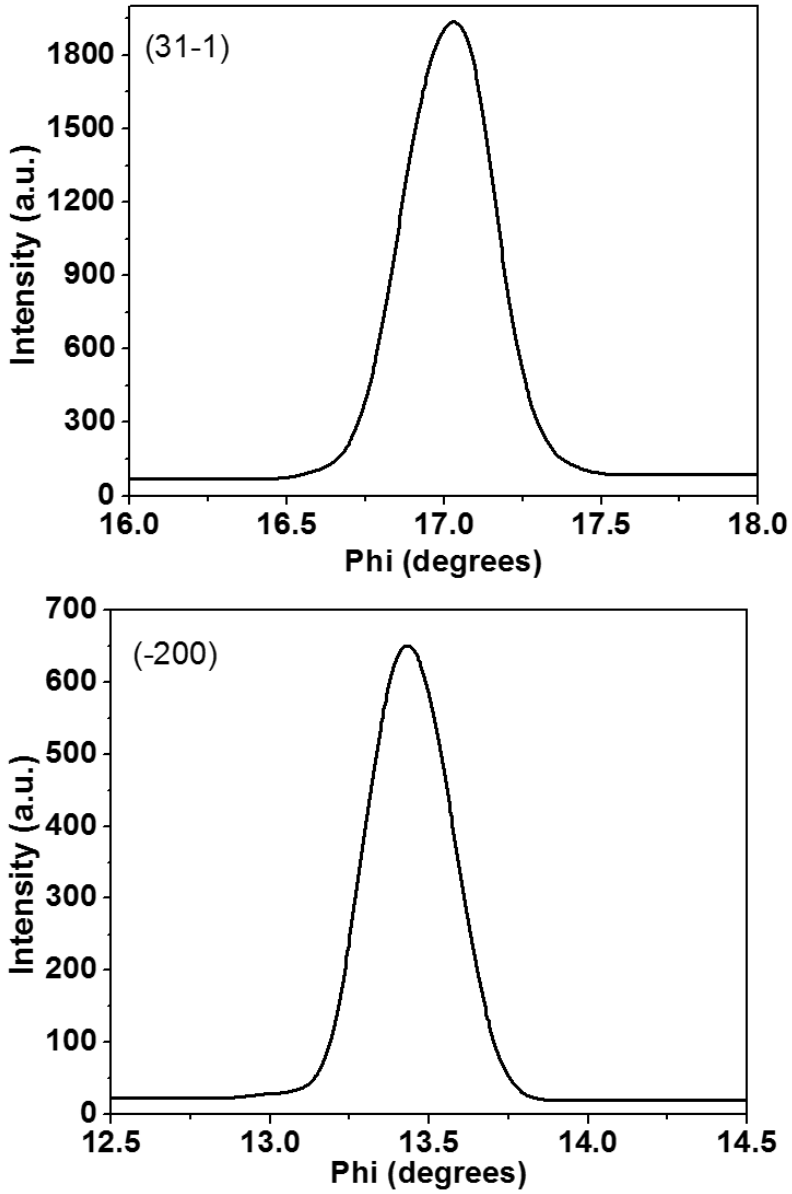

Figure 6.6: Representative rocking curve profiles from single crystal X-ray diffraction reflections of $GdNbO_4$.

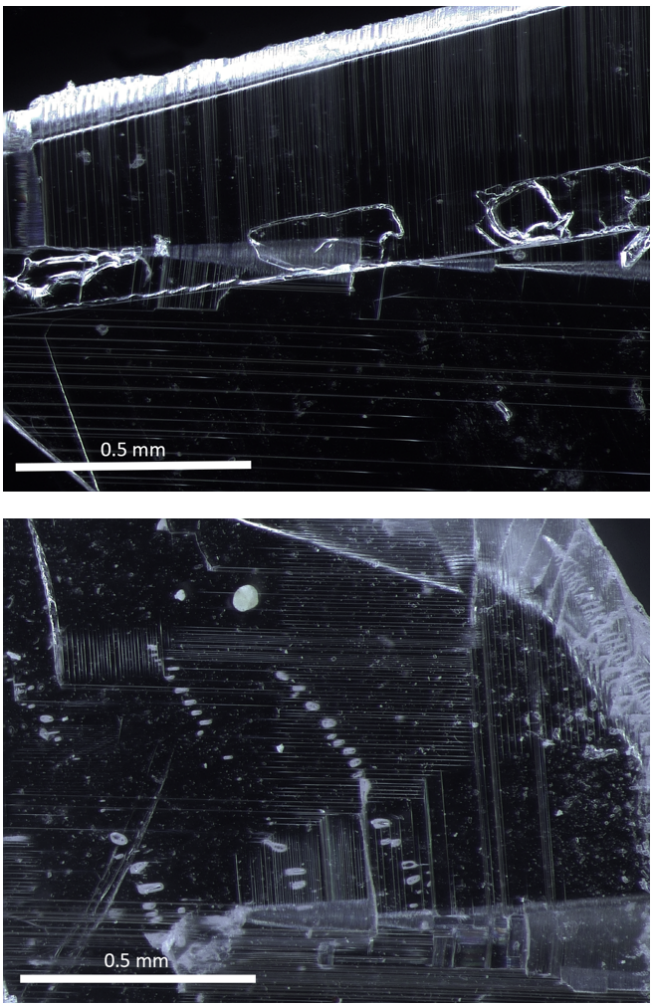

Figure 6.7: $EuNbO_4$ crystals having multiple domains as indicated by directional variations in surface striations.

The alkali rare-earth niobate hydroxides are a relatively limited class of compounds. To our knowledge, the only other reported single crystal structure in this class that exhibits a unique alkali metal site and a coordinated hydroxide group is $K_3(Sc_{0.875}Nb_{0.125})Nb_2O_7(OH)_{1.75,}$ reported previously by our group.[39] In that structure, some of the niobium ions were substitutionally disordered with scandium ions, and the blue color of the crystals was indicative of some reduction of Nb^{5+} to Nb^{3+} (compensated by a partial vacancy of the OH site). The compounds $K_3YNb_2O_7(OH)_2$ and $K_3LuNb_2O_7(OH)_2$ are isostructural with that potassium scandium niobate hydroxide, but extend our understanding of the structure type in several ways. Notably, crystals in the present study are colorless, indicating all of the niobium ions are in the pentavalent state, and thus the OH site in the structure requires no vacancy compensation. We also do not observe any apparent substitution of Nb at the rare-earth site, which was previously deduced from the anisotropic displacement parameters of the scandium site in that compound. This is likely attributed to the larger size of Lu^{3+} and Y^{3+} relative to Sc^{3+} that reduces the tendency for substitutional disorder with the smaller Nb^{3+} or Nb^{5+} ions.

The general framework of rare-earth octahedra and distorted niobium octahedra remains the same for the Sc, Lu, and Y analogs. The structure of the yttrium analog is briefly described here as the representative example (**Tables 6.7 and 6.8)** for selected interatomic distances and angles, and bond valence sums, respectively). The coordination about niobium can be described as a $NbO_4(OH)_2$ octahedron, and the niobium atom possesses *3m* site symmetry. The hydrogen atom attached to O1 was

identified from the difference electron density map, confirmed by bond valence calculations, and set to 2/3 occupancy to achieve charge balance. The $NbO_4(OH)_2$ octahedra form a $Nb_2O_7(OH)_2$ dimer through face-sharing of atom O1 (**Figure 6.8**). The Nb-O1 bonds are somewhat elongated (2.194(7) Å) compared to Nb-O2 (1.867(5) Å). A similar distortion and bridging arrangement, though without the hydrogen atom, is observed in the Nb_2O_9 dimer of $Mg_4Nb_2O_9$, which possesses trigonal symmetry (space group *P*-3*c*1) and somewhat similar unit cell parameters (a = 5.1612(7) Å, c = 14.028(1) Å).[40] Potassium atoms fill the gaps in the resulting framework of yttrium and niobium octahedra, and are 12-coordinate with oxygen at both unique potassium sites.

Table 6.5: Crystallographic Data of Niobate Hydroxide Compounds

empirical formula	**$K_3YNb_2O_7(OH)_2$**	**$K_3LuNb_2O_7(OH)_2$**
formula weight (g/mol)	538.05	624.11
crystal system	hexagonal	hexagonal
space group	*P*6$_3$/*mmc* (no.194)	*P*6$_3$/*mmc* (no.194)
unit cell dimensions (Å)	*a* = 5.9770(12) *c* = 14.901(2)	*a* = 5.9494(12) *c* = 14.8348(19)
volume (Å^3)	461.01(15)	454.74(14)
Z, calcd density (Mg/m^3)	2, 3.876	2, 4.558
absorption coefficient (mm^{-1})	10.066	14.648
F(000)	504	568
crystal size (mm)	0.17 x 0.20x 0.25	0.16 x 0.20 x 0.22
Tmax, Tmin	0.8508, 1.0000	0.5167, 1.0000
Θ range for data	2.73-25.17	2.75-25.19
reflections collected/ unique/observed	3669/191/187	3547/190/190
data/restraints/parameters	191/0/22	190/0/22
goodness-of-fit on F^2	1.146	1.181
R1, wR2 ($I \geq 2\sigma(I)$)	0.0303, 0.0761	0.0337, 0.0678
R1, wR2 (all data)	0.0309, 0.0765	0.0337, 0.0678
extinction coefficient	0.0050(15)	0.0028(11)

Table 6.6: Crystallographic Data of Niobate Hydroxide Compounds

empirical formula	**$CsNb_2O_5(OH)$**	**$CsNb_2O_5(OH)_{0.5}F_{0.5}$**
formula weight (g/mol)	415.74	416.73
crystal system	cubic	cubic
space group	*Fd*-3*m* (no.227)	*Fd*-3*m* (no.227)
unit cell dimensions (Å)	a = 10.5869(14)	a = 10.5519(12)
volume ($Å^3$)	1186.6(2)	1174.9(2)
Z, calcd density (Mg/m^3)	8, 4.654	8, 4.712
absorption coefficient (mm^{-1})	9.867	9.972
F(000)	1488	1488
crystal size (mm)	0.20 x 0.22 x 0.25	0.22 x 0.22 x 0.25
Tmax, Tmin	0.9401, 1.0000	0.6522, 1.0000
Θ range for data	3.33-25.12	3.34-25.21
reflections collected/ unique/observed	2032/70/68	2228/70/70
data/restraints/parameters	70/0/9	70/0/9
goodness-of-fit on F^2	1.139	1.192
R1, wR2 ($I \geq 2\sigma(I)$)	0.0336, 0.0741	0.0363, 0.0950
R1, wR2 (all data)	0.0343, 0.0745	0.0363, 0.0950
extinction coefficient	0.0029(5)	0.0045(8)

Table 6.7: Selected interatomic distances (Å) and angles (°) in hydrothermally-grown $.K_3RENb_2O_7(OH)_2$ (RE = Y, Lu)

	$K_3YNb_2O_7(OH)_2$	$K_3LuNb_2O_7(OH)_2$
Nb1−O2 (x3)	1.867(5)	1.868(7)
Nb1−O1 (x3)	2.194(7)	2.189(9)
RE1−O2 (x6)	2.213(5)	2.190(7)
K1−O2 (x6)	2.990(6)	2.976(9)
K1−O1 (x3)	3.050(7)	3.049(9)
K1−O2 (x3)	3.121(5)	3.091(7)
O2−Nb1−O2 (x3)	100.3(2)	100.4(3)
O2−Nb1−O1 (x6)	91.17(17)	91.2(2)
O2−Nb1−O1 (x3)	162.0(2)	161.7(3)
O1−Nb1−O1 (x3)	74.6(3)	74.3(4)
O2−RE1−O2 (x3)	180.00	180.00
O2−RE1−O2 (x6)	90.72(19)	90.6(3)
O2−RE1−O2 (x6)	89.28(19)	89.4(3)

Table 6.8: Bond valence analysis of hydrothermally-grown $K_3RENb_2O_7(OH)_2$ (RE = Y, Lu)

	$K_3YNb_2O_7(OH)_2$	$K_3LuNb_2O_7(OH)_2$
Nb1−O2 (x3)	1.126	1.123
Nb1−O1 (x3)	0.465	0.472
ΣNb	4.746	4.785
RE1−O2 (x6)	0.592	0.557
ΣRE	3.552	3.342
K1−O2 (x6)	0.098	0.102
K1−O1 (x3)	0.084	0.084
K1−O2 (x3)	0.069	0.075
ΣK	1.047	1.089

Table 6.9: Selected interatomic distances (Å) and angles (°) in hydrothermally-grown $CsNb_2O_5(OH,F)$

	$CsNb_2O_5(OH)$	**$CsNb_2O_5(OH)_{0.5}F_{0.5}$**
Nb1–O1/F1 (x6)	1.987(2)	1.9806(18)
Cs1–O1/F1 (x6)	3.302(7)	3.291(5)
Cs1–O1/F1 (x6)	3.8000(13)	3.7874(10)
O1/F1–Nb1–O1/F1 (x3)	180.00	180.00
O1/F1–Nb1–O1/F1 (x6)	90.2(3)	90.2(2)
O1/F1–Nb1–O1/F1 (x6)	89.8(3)	89.8(2)

Table 6.10: Bond valence analysis of hydrothermally-grown $CsNb_2O_5(OH,F)$

	$CsNb_2O_5(OH)$	**$CsNb_2O_5(OH)_{0.5}F_{0.5}$**
Nb1−O1/F1 (x6)	0.814	0.829
ΣNb	4.884	4.974
Cs1−O1/F1 (x6)	0.091	0.094
Cs1−O1/F1 (x6)	0.024	0.025
ΣCs	0.69	0.714

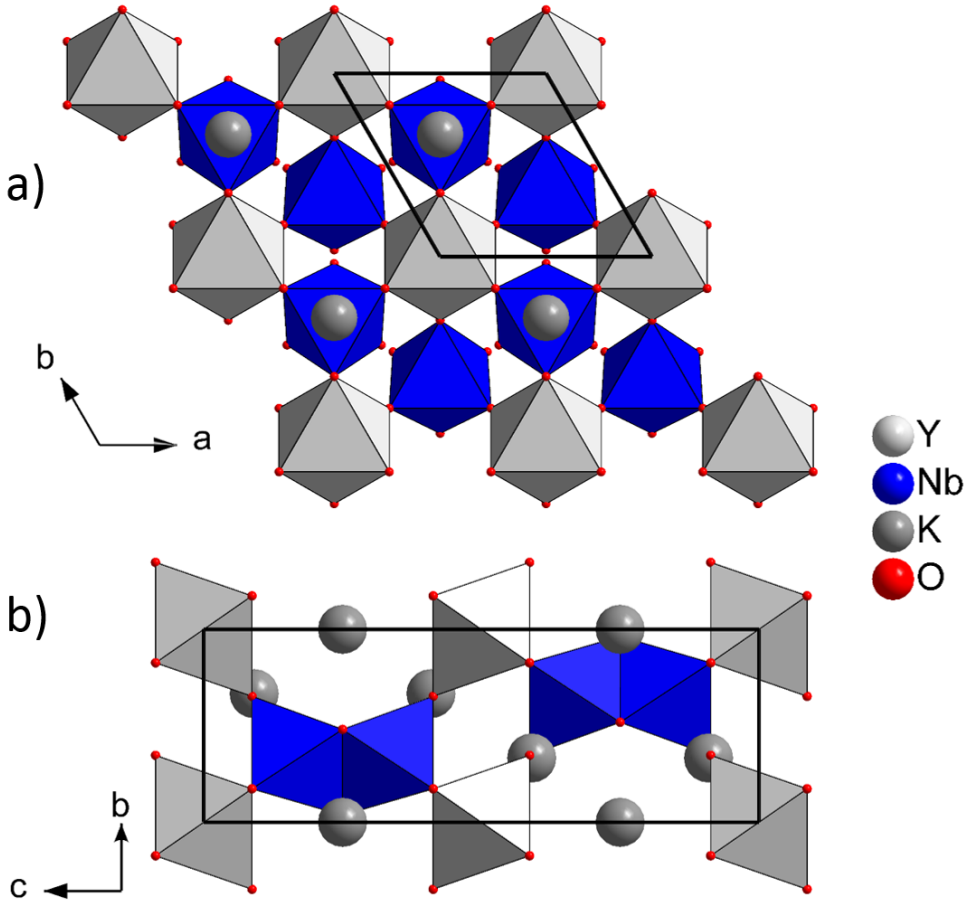

Figure 6.8: Structure of $K_3YNb_2O_7(OH)_2$: a) projection along [001] showing the corner sharing yttrium niobate framework; b) projection along [100] featuring the $Nb_2O_7(OH)_2$ dimer (hydrogen atoms omitted for clarity).

The compounds $CsNb_2O_5(OH)$ and $CsNb_2O_5(OH,F)$ are based on the pyrochlore structure type including the general formulas of $A_2B_2O_6$ and $A_2B_2O_7$ in the cubic space group *Fd*-3*m*.[41,42] The standard pyrochlore structure is based on the niobate mineral $(Na,Ca)_2Nb_2O_6(OH,F)$, where the Na/Ca atoms occupy a *16d* Wyckoff site. Alternative niobate and tantalate pyrochlores, often described as defect- or β-pyrochlores are also well known, and often obtained from low temperature hydrothermal or soft fluoride crystal growth.[43] In these cases, an alkali metal occupies the *8b* site instead of the *16d* site. This necessarily results in an anion vacancy at an *8b* site occupied in the standard pyrochlore to maintain charge balance. A number of such phases like $CsNb_2O_5F$ and $NH_4Nb_2O_5(OH,F)$ are known to adopt this arrangement,[43] and indeed this includes $CsNb_2O_5(OH)$ and $CsNb_2O_5(OH,F)$ herein. In our cases, the anion site of the defect pyrochlore is 5/6 occupied by O and 1/6 occupied by OH, or a mixture of OH/F. We note that the lattice parameter for $CsNb_2O_5(OH)$ (10.5869(14) Å) is slightly larger than that derived from powder diffraction for $CsNb_2O_5F$ (10.538(4) Å [43]), and the lattice parameter of $CsNb_2O_5(OH,F)$ is intermediate of these two values (10.5519(12) Å), consistent with the expected trend based on the anion sizes.

The presence of some fluoride substitution was supported by EDX (**Figure 6.10**) for $CsNb_2O_5(OH,F)$. The presence of hydroxide in both structures was verified by infrared spectroscopy **(Figure 6.11**). Channels are formed by a three-dimensional framework of corner sharing NbO_6 octahedra (Nb-O = 1.987(2) Å; **Tables 6.9 and 6.10**). Cesium ions are off-center in the channels (**Figure 6.9**) and staggered along their length, maintaining fairly long contacts with oxygen (Cs-O = 3.302(7) and 3.800(13) Å).

Niobate pyrochlores have been shown to be useful as solid electrolyte fuel cells with an emphasis on ionic conductivity, a characteristic enabled by cation migration through the pyrochlore channels.[44] Decomposition of $CsNb_2O_5(OH)$ occurs via water loss from the OH groups upon heating in air from 225-325 °C(**Figure 6.12**; 2.2% expected mass loss, 2.3% observed mass loss).[45]

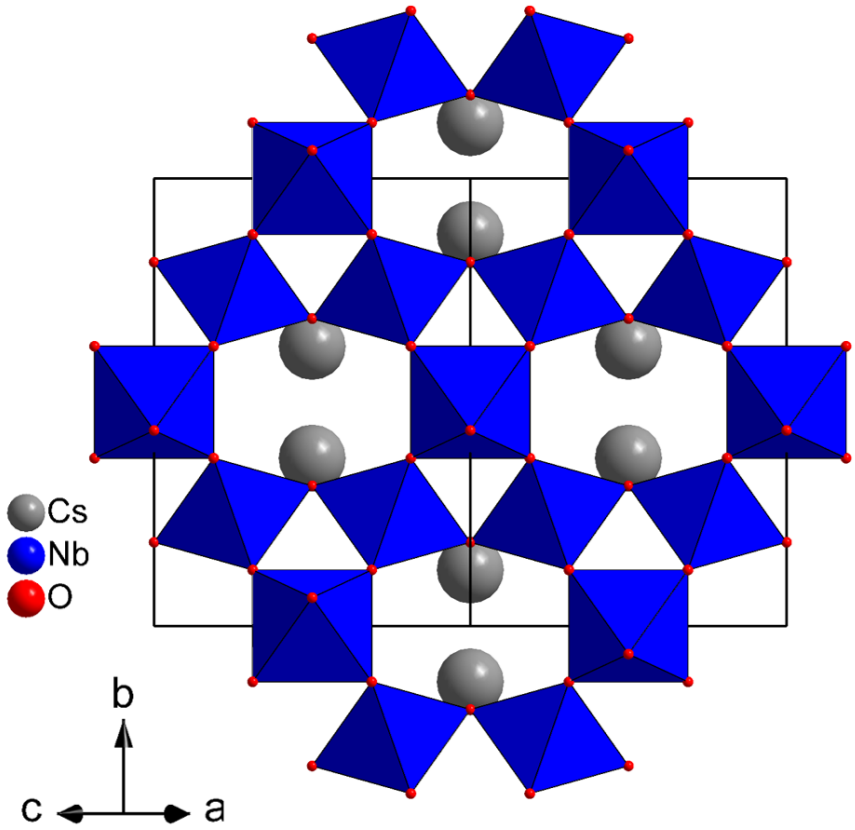

Figure 6.9: Pyrochlore structure type of $CsNb_2O_5(OH)$ and $CsNb_2O_5(OH,F)$ along the [101] projection. Channels are formed by a framework of corner-sharing niobium oxide octahedra. Disordered hydrogen atoms are omitted for clarity.

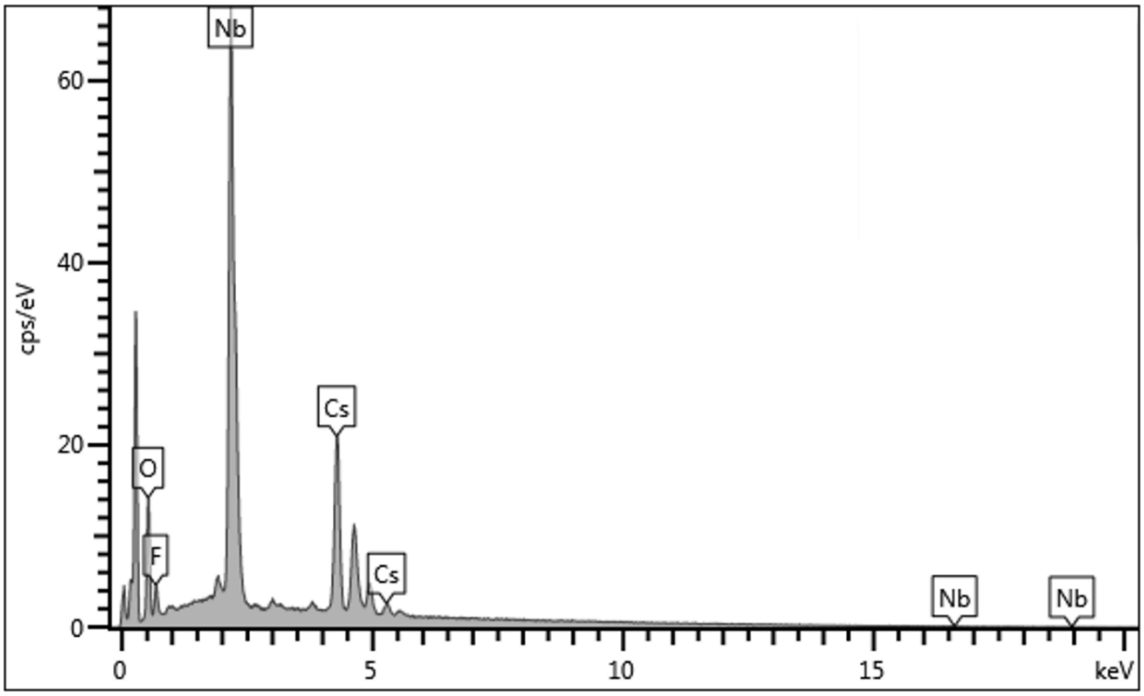

Figure 6.10: EDX spectrum of $CsNb_2O_5(OH,F)$.

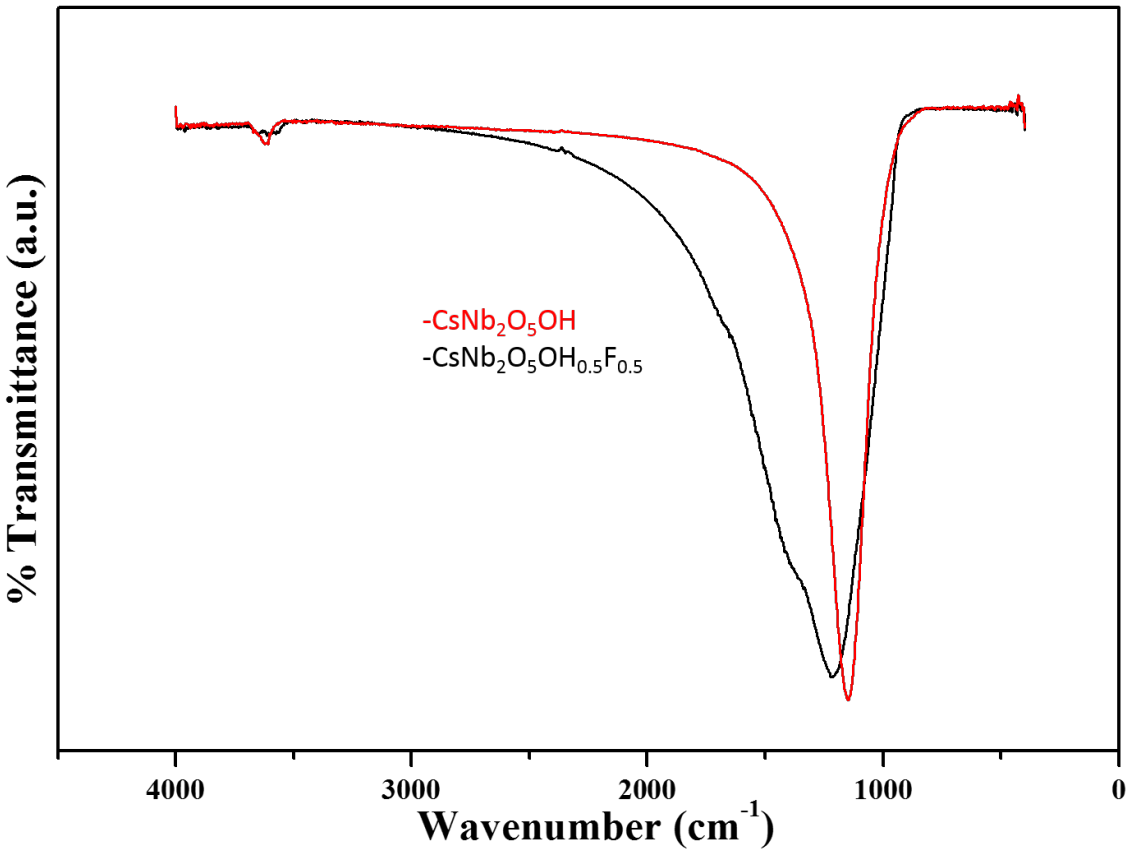

Figure 6.11: Infrared spectra of $CsNb_2O_5(OH)$ and $CsNb_2O_5(OH,F)$.

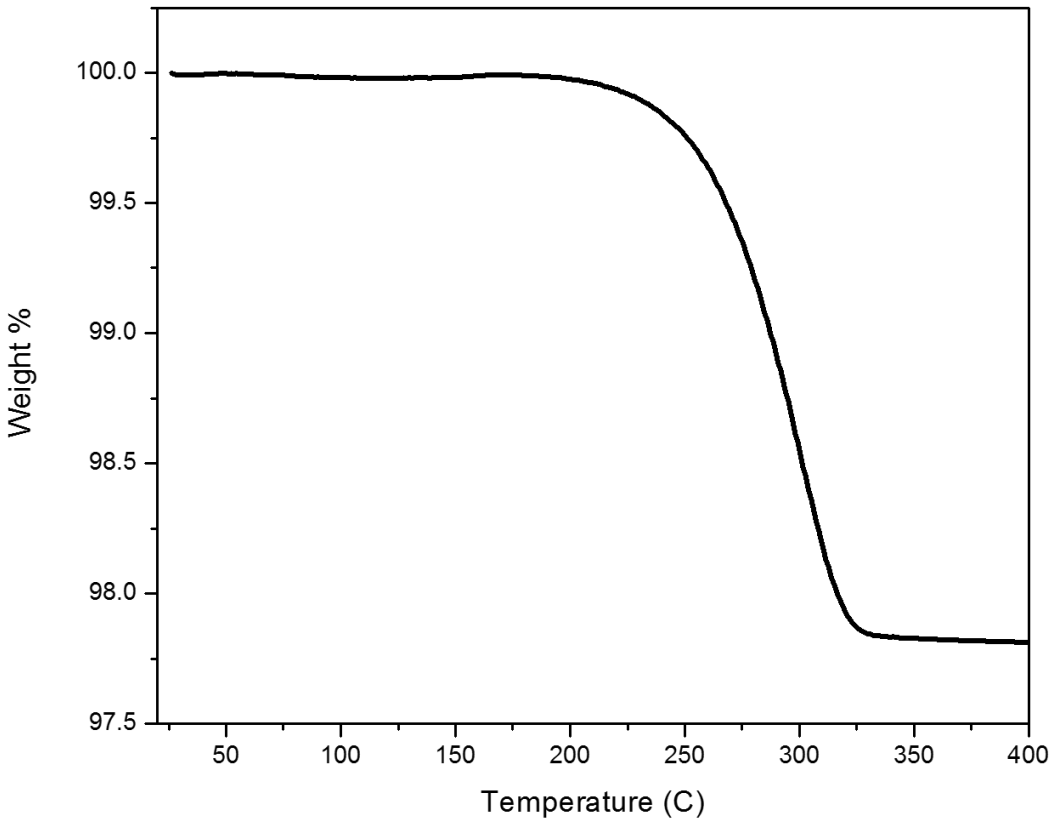

Figure 6.12: TGA of $CsNb_2O_5(OH)$.

Conclusions

In this study, a demonstration that the rare-earth niobates, $RENbO_4$ (RE = Y, La-Lu), can be grown as large high quality single crystals using a high-temperature hydrothermal technique was accomplished. The approach is a straightforward extension of our method of growing the more common YVO_4 crystals for potential optical applications. The crystals all grow in the fergusonite phase in space group *C*2/*c*, which is a low temperature phase of this composition. A tetragonal phase is known to occur when grown at high-temperatures (> 800˚C) and converts to this monoclinic phase upon cooling. This phase transformation is not a simple one and leads to the formation of ferroelastic twinning domains during the phase transition. Since the hydrothermal technique enables growth at much lower temperatures (< 700˚C) than the classical melt methods for these refractory niobates, large single crystals were grown near or below the phase transition temperature in this study. This enabled the growth of single domain crystals of all the rare-earth analogs of $RENbO_4$. At somewhat lower growth temperatures a series of hydroxy-niobates were also isolated and characterized. Similar species have been observed in the past from subcritical hydrothermal (200˚C) reactions, although not as large well-formed crystals as described herein. These species appear to be stabilized by the lower temperatures, as higher growth temperatures convert all starting material into quantitative amounts of the pure fergusonite phase. The preparation of lanthanide doped single crystals of the fergusonite phase was also achieved, and the study of their optical properties is ongoing. The $RENbO_4$ crystals based on the heaviest rare-earths also possess quite high densities, making them potential hosts for scintillation detectors.

Here, the niobium oxide serves as an excellent building block to initiate and sustain crystal growth of rare-earth niobates ($RENbO_4$) and produce new hydroxide side products. While the Nb ion is always in the Nb^{+5} state in this study, it displays a great degree of flexibility within the crystal lattice. The refractory nature of niobium oxide (Nb_2O_5) with the rare-earth ions is not surprising. The ability to encapsulate two refractory oxides and drive their crystal growth at temperatures more than 1000 °C below their melting points by the hydrothermal technique creates more evidence and continues to validate this technique in comparison to conventional solid-state techniques. Given the success of this project and the success with rare-earth titanates, exploration into refractory oxides of uranium and thorium with titanium oxide will be explored in Chapter 7. Each success gives continued confidence that the hydrothermal crystal growth with soluble building blocks will continue to lead to rich chemistry now and moving forward.

As mentioned in the introduction, previous investigations into rare-earth silicates, rare-earth germanates and rare-earth titanates has led to this current investigation of rare-earth niobates. The hydrothermal fluid in tandem with unique building blocks continues to lead to new and rich chemistry studies and the way we think about the solubility of these refractory oxides.

References

(1) Fields, R. A.; Birnbaum, M.; Fincher C. L. Highly efficient Nd:YVO_4 diode-laser end-pumped laser. *Appl. Phys. Lett.* **1987**, *51*, 1885-1886.

(2) Kalisky, Y. *The Physics and Engineering of Solid State Lasers* SPIE Press Bellingham WA, 2006.

(3) Sato, Y.; Taira, T. Comparative study on the spectroscopic properties of Nd:$GdVO_4$ and Nd:YVO_4 with hybrid process. *IEEE J. Sel. Top. Quant. Electron.* **2005**, *11*, 613-620.

(4) Zayhowski, J. J.; Dill, C. Coupled-cavity electro-optically Q-switched Nd:YVO_4 microchip lasers. *Opt. Lett.* **1995**, *20*, 716-719.

(5) Miyazawa S. Optical crystals survived in information technology systems. *Opto-Electron. Rev.* **2003**, *11*, 77-84.

(6) Erdei, S. Growth of oxygen deficiency-free YVO_4 single crystal by top-seeded solution growth technique. *J. Cryst. Growth* **1993**, *134*, 1-13.

(7) Jiang, H-D.;Zhang H-J.; Wang J-Y.; Xia H-R.; Hu X-B.; Teng B.; Zheng, C-Q. *Opt. Comm.* **2001**, *198*, 447-452.

(8) Higuchi, M.; Shimizu, T.; Takahashi, J.; Ogawa, T.; Urata, Y.; Miura, T.; Wada, S.; Machida, H. Growth of RE:$LuVO_4$ (RE=Nd, Tm, Yb) single crystals by the floating zone method and their spectroscopic properties. *J. Cryst. Growth* **2005**, *283*, 100-107.

(9) Hsiao, Y-J.; Fang, T.H.; Chang, Y.S.; Chang, Y.H.; Liu, C.H.; Ji, J.W.; Jywe, W.Y. Structure and luminescent properties of $LaNbO_4$ synthesized by sol-gel process. *J. Lumin.* **2007**, *126*, 866-870.

(10) Ferguson, R. B. The crystallography of synthetic $YTaO_4$ and fused fergusonite. *Can. Mineral.* **1957**, *6*, 72-77.

(11) As a historical note, the mineral Fergusonite is named after Scottish mineral collector Robert Ferguson (1767-1840), not Robert Ferguson, current Professor Emeritus of Geological Sciences at the University of Manitoba, who made the first serious attempts to grow single crystals and solve the structure of fergusonite (ref 10).

(12) Brixner, L. H.; Whitney, J. F.; Zumsteg, F. C.; Jones, G. A. Ferroelasticity in the $LnNbO_4$-type rare earth niobates. *Mater. Res. Bull.* **1977**, *12*, 17-24

(13) Tsunekawa, S.; Kamiyama, Sasaki, K.; Asano, H.; Fukuda, T. Precise structure analysis by neutron diffraction for $RNbO_4$ and distortion of NbO_4 tetrahedra. *Acta Crystallogr*. **1993**, *A49*, 595-600.

(14) Mariathasan, J. W. E.; Finger, L. W.; Hazen. R. W. High-pressure behavior of $LaNbO_4$. *Acta Crystallogr*. **1985**, *B41*, 179-184.

(15) Trunov,V. K.; Efremov, V. A.; Velikodnyi, Y. A.; Averina, I. M. Structure of synthetic fergusonite ($YNbO_4$) crystals at room temperature. *Kristallografiya* **1981**, *26*, 67–71.

(16) Weitzel, H.; Schröcke, H. *Z*. Kristallstrukturverfeinerungen von Euxenit, $Y(Nb_{0.5}Ti_{0.5})_2O_6$, and M-Fergusonit, $YNbG_4$. *Kristallogr*. **1980**, *152*, 69-82.

(17) Bayliss, R. D; Pramana, S. S.; .An, T.; Wei, F.; Kloc, C. L.; White, A. J. P.; Skinner, S. J.; White, T. J.; Baike, T. Fergusonite-type $CeNbO_{4+\varepsilon}$:Single crystal growth, symmetry revision and conductivity. *J*. *Solid State Chem*. **2013**, *204*, 291-297.

(18) Jurkschat, K.; Sarin, P.; Siah, L. F. Kriven, W.M. In situ high temperature phase transformations in rare earth niobates. *ICDD* **2004**, *47*, 357.

(19) David, W. I. F. The high-temperature paraelastic structure of $LaNbO_4$. *Mater*. *Res*. *Bull*. **1983**, *18*, 749-756.

(20) Tanaka, M.; Saito, R.; Watanabe, D. Symmetry determination of the room-temperature form of $LnNbO_4$ (Ln=La, Nd) by convergent-beam electron diffraction. *Acta Crystallogr*. **1980**, *A36* 350-352.

(21) Graham, J. Crystal chemistry of complex niobium and tantalum oxides. III. Relation between M, T, and M' fergusonite structures. *Am*. *Mineral*. **1974**, *59*, 1045-1046.

(22) Tsunekawa, S.; Kasuya, A.; Nishina, Y Shape and size controls of micro-domains in $LaNbO_4$ crystals. *Mater*. *Sci*. *Engin*. **1996**, *A217/218*, 215-217.

(23) Jian, L.; Huang, C.M.; Xu, G.; Wayman, C.M. The domain structure of $LaNbO_4$ in the low temperature monoclinic phase. *Mater*. *Lett*. **1994**, *21*, 105-110.

(24) Kelly, P.M. Wauchope, C.J. The origin of the domain structure in $LaNbO_4$. *Mater*. *Lett*. **1996**, *27*, 7-11.

(25) Jian, L.; Wayman, C.M. Electron back scattering study of domain structure in monoclinic phase of a rare-earth orthoniobate $LaNbO_4$. *Acta Metall. Mater.* **1995**, *43*, 3893-3901.

(26) Takei, H.; Tsunekawa, S. Growth and properties of $LaNbO_4$ and $NdNbO_4$ single crystals. *J. Cryst. Growth* **1977**, *38*, 55-60.

(27) Zhang, P.; Wang, T.; Xia, W.; Li. L. Microwave dielectric properties of a new ceramic system $NdNbO_4$ with CaF_2 addition. *J. Alloys Comp.* **2012**, *535*, 1-4.

(28) Octaviano, E. S.; Ardila, D. R.; Andrade, L. H. C.; Sui, M.; Li, L.; Andreeta. J.P. Growth and evaluation of lanthanoids orthoniobates single crystals processed by a miniature pedestal growth technique. *Cryst. Res. Technol.* **2004**, *39*, 859-863.

(29) Yang, M.; Zhao, X.; Ji, Y.; Liu, F.; Liu, W.; Sun, J.; Liu. X.; Hydrothermal approach and luminescent properties for the synthesis of orthioniobates $GdNbO_4$:Ln^{3+} (Ln= Dy, Eu) single crystals under high-temperature high-pressure conditions. *New J. Chem.* **2014**, *38*, 4249-4257.

(30) McMillen, C.D.; Kolis, J.W. Bulk single crystal growth from hydrothermal solutions. *Philos. Mag.* **2012**, *92*, 2686-2711.

(31) Forbes, A.R.; McMillen, C.D.; Giesber, H.G.; Kolis, J.W. The hydrothermal synthesis, solubility and crystal growth of YVO_4 and Nd:YVO_4. *J. Crystal Growth* **2008**, *310*, 4472- 4476.

(32) Kolis, J.W.; Syracuse, S.J. Hydrothermal growth of lanthanide vanadate crystals for use in laser and birefringent applications and devices. USPTO #7, *211*, 234.

(33) *Apex3*; Bruker AXS Inc., Madison, WI, 2015.

(34) *CrystalClear*; Rigaku and Molecular Structure Corporation: The Woodlands, TX, 2006.

(35) Sheldrick, G.M. A short history of SHELX. *Acta Crystallogr. Sect. A* **2008**, *64*, 112-122.

(36) Wang, X.; Loa, I.; Syassen, K.; Hanfland, M.; Ferrand. B. Structural properties of the zircon- and sheelite-type phases of YVO_4 at high pressure. *Phys. Rev. B* **2004**, *70*, 064109.

(37) Huse, M.; Skilbred, A.W.B.; Karlsson, M.; Eriksson, S.G.; Norby, T.; Haugsrud, R.; Knee, C.S. Neutron diffraction study of the monoclinic to tetragonal structural transition in $LaNbO_4$ and its relation to proton mobility. *J. Solid State Chem.* **2012**, *187*, 27-34.

(38) Binnemans, K. Interpretation of europium (III) spectra. *Coord. Chem. Rev.* **2015**, *295*, 1-45.

(39) Mann, M.; Kolis, J. W.; VanDerveer, D. $K_3(Sc_{0.875}Nb_{0.125})Nb_2O_9H_{1.75}$: a new scandium niobate with a unique cage structure. *Acta Crystallogr.* **2009**, *C65*, i27-i29.

(40) Kumad, N.; Taki, K.; Kinomura, N. Single crystal structure refinement of a magnesium niobium oxide: $Mg_4Nb_2O_9$. *Mater. Res. Bull.* **2000**, *35*, 1017-1021.

(41) Chakoumakos. B. C. Systematics of the pyrochlore structure type, ideal $A_2B_2X_6Y$. *J. Solid State Chem.* **1984**, *53*, 120-129.

(42) Subramanian, M. A.; Aravamudan, G.; Subba Rao, G. V. Oxide Pyrochlores-A Review. *Prog. Solid. State. Chem.* **1983**, *15*, 55-143.

(43) Britvin, S. N.; Siidra, O. I.; Lotnyk, A.; Krivovichev, S. V.; Depmeier, W. Niobate and Tantalate Pyrochlores: Soft Synthesis by the Fluoride Route. *Eur. J. Inorg. Chem.* **2010**, *2010*, 1082-1088.

(44) Goodenough, J. B.; Hong, H. Y.-P.; Kafalas. J. A. Fast Na^+-ion transport in skeleton structures. *Mater. Res. Bull.* **1976**, *11*, 203-220.

(45) Fulle, K.; McMillen, C. D.; Sanjeewa, L. D.; Kolis, J. W. Hydrothermal Chemistry and Growth of Fergusonite type $RENbO_4$ (RE=La-Lu, Y) Single Crystals and New Niobate Hydroxides. *Crystal Growth and Design*. **2016**, *16*, 4910–4917.

CHAPTER SEVEN

HYDROTHERMAL GROWTH OF $ThTi_2O_6$ AND UTi_2O_6

Introduction

The synthesis and characterization of two polymorphs of the MTi_2O_6 ($M = Th^{4+}$, U^{4+}) structure type are presented and discussed. As an extension of the titanate work presented in Chapter Six, an investigation from trivalent rare-earth ions into two refractory tetravalent actinide oxides via the high-temperature and high-pressure hydrothermal method were examined. Thorium oxide (ThO_2) and uranium (IV) oxide (UO_2) represent two refractory oxides that display minimal solubility via conventional solid-state techniques. The high melting points, > 2,800°C, of these two metal oxides make it incredibly difficult to explore their reactivity using conventional means.

Recently, our group has shown that ThO_2 can be solubilized via the hydrothermal technique to nucleate and transport crystals of ThO_2 in hydrothermal mineralizers of cesium fluoride, CsF.[1] Using this knowledge, in addition to the knowledge gained in the growth of other refractory oxides, the binary systems of ThO_2-TiO_2 and UO_2-TiO_2 were examined. For this investigation, experience from the refractory oxides of the wadeite-mineral type were combined with knowledge of rare-earth titanates. The belief being that new refractory oxides could be synthesized if the mineralizer type and temperature regime were optimized. The knowledge that ThO_2, UO_2 and TiO_2 are soluble in hydrothermal fluids paved the way for this initial investigation. A brief background on

$ThTi_2O_6$ and UTi_2O_6 will give additional merit to the difficulty in the growth of these two oxides.

Thorium titanate, $ThTi_2O_6$ has been reported in two polymorphic states. In the first case, $ThTi_2O_6$ exists as the thorutite mineral family, which is isostructural with the uranium analog known as brannerite.[1,2] Thorutite was initially described by two Russian scientists, Gotman and Khapaev, in 1958 from an unspecified location.[3] In the initial investigation, $ThTi_2O_6$ was found to contain up to 4 wt.% of rare-earth ions (RE = Ce, La or Nd). This polymorph was first reported synthetically by Ruh and Wadsley in 1966 and was synthesized via sintering of binary powder of ThO_2 and TiO_2 at 1610 °C under vacuum and further treated in air at 1000 °C to yield a single crystal which was studied.[3] The unit cell parameter of thorutite-type $ThTi_2O_6$ consists of a = 9.822(5) Å, b = 3.824(2) Å, and c = 7.036(5) Å with β = 118.84(5) °, consistent with that of other brannerite-type minerals, UTi_2O_6 and $CeTi_2O_6$ in space group *C2/m*.[5] A second examination of this composition was performed by Mitchell and Chakhmouradian in which sintered powder of $ThTi_2O_6$ (*C2/m*) was synthesized and a solid solution series was explored with perovskite-type laporite, $NaLREETi_2O_6$ (RE = La-Nd), in which Th^{4+} uptake was examined as a route to actinide immobilization.[4] The monoclinic *C2/c* setting of $ThTi_2O_6$ has been reported by Zunic' and Loye and have been synthesized via melt techniques.[6,7] The unit cell parameters reported by Loye and co-workers consists of a = 10.808(2) Å, b = 8.580(2) Å, and c = 5.196(2) Å with β = 115.25(8)°.[6] Both titanate structures are built on layers of edge-sharing TiO_6 coordinated by either six- or eight-coordinated thorium

atoms. In the thorutite form (*C2/m*) thorium polyhedra adopt a 6-coordinate environment and in the second form (*C2/c*), thorium titanate adopts an 8-coordinate environment.[4]

Uranium titanate, UTi_2O_6, appears to only adopt the brannerite form *C2/m* form as no reports of the *C2/c* setting can be found. The first crystal structure of this compound reported by single crystal diffraction was by Szymanksi and Scott in 1982.[8] Interestingly, the authors point out that $ThTi_2O_6$ in *C2/c* was incorrectly referred to as a brannerite mineral by Ruh and Wadsley in 1966. In that study, a cryolite-fusion technique was employed in their powder and single crystal synthesis of UTi_2O_6. A second report of UTi_2O_6 is described by Vance and co-workers in which the limits of Ca^{2+} and Gd^{3+} substitution into the U^{4+} site was investigated.

In all cases, no large bulk crystal growth of $ThTi_2O_6$ or UTi_2O_6 were described. For uses in actinide remediation and immobilization, crystal growth of sufficient size is necessary to examine incorporation of ions and stability of the natural product. In the case of $ThTi_2O_6$, it is difficult to pinpoint a phase director as the hydrothermal crystal growth of $ThTi_2O_6$ at high-pressure and high-temperature clearly indicates that Mitchell and Chakhmouradian's statement that, "$ThTi_2O_6$ does not crystallize at high-pressure…" was incorrect.[4] Herein, a report of the crystal growth of thorium titanate $ThTi_2O_6$ (*C2/c*) and uranium titanate (*C2/m*) are described for the first time via high-pressure and high-temperature hydrothermal synthesis.

Interestingly, according to Ruh and Wadsley, brannerite UTi_2O_6 is not related to the columbite structure type, ($Fe^{2+}Nb_2O_6$), which adopts an orthorhombic symmetry in *Pbcn*.[5] However, it does appear that brannerite UTi_2O_6 is a defect form of rutile, TiO_2,

with sheets sliced along the (101) direction correlating to the sheets of octahedra found in the unit cell of UTi_2O_6 along the *b-axis*.[5] For thorutite, $ThTi_2O_6$, besides forming anatase-like chains of the titanium oxide polyhedra in the structure, there appears to be no direct correlation to other AB_2O_6 structures like orthorhombic columbite.[7]

Experimental Methods

Single crystals of $ThTi_2O_6$ and UTi_2O_6 were grown from stoichiometric reactions of binary oxides under high-temperature and high-pressure hydrothermal reactions. In the case of $ThTi_2O_6$, ThO_2 (93 mg, 0.354 mmol) was reacted with TiO_2 (57 mg, 0.708 mmol) at 750 °C for 7 days with 0.4 mL of 6 *M* CsF mineralizer. No presence of impurities was detected in the as-grown material by PXRD, **Figure 7.6**. In the case of UTi_2O_6, UO_2 (94 mg, 0.349 mmol) was reacted with TiO_2 (56 mg, 0.698 mmol) at 750 °C for 7 days with 0.4 mL of 6 *M* CsF mineralizer. No presence of impurities was detected in the as-grown material by PXRD, **Figure 7.7**. For preparation of UO_2 powder, uranium acetate ($UO_2(C_2H_3O_2)_2 + 2H_2O$) was decomposed at 500 °C for 6 hours. The resultant black chunky powder was ground and pressed into a pellet using a hydraulic pellet press. The pellet was subsequently heated at 500 °C for 6 hours. This powder was subsequently treated with TiO_2 as described above.

Crystal Structure of $ThTi_2O_6$

The crystal structure of hydrothermally grown thorium titanate, $ThTi_2O_6$, is described. The unit cell parameters are given below in **Table 7.1**. $ThTi_2O_6$ (*C2/c*) is based on two unique metal sites, $Th(1)O_8$ and $Ti(1)O_6$, and three unique oxygen sites. Bond distances for $ThTi_2O_6$ are reported in **Table 7.2**. Bond valence sum calculations were performed and are in good agreement with the oxidation states reported in the titanate structures, **Table 7.3**. Sample crystal growth for $ThTi_2O_6$ is shown below in **Figure 7.1b**.

The hydrothermally grown crystals grow as nice 3-D polyhedra habits and can be grown up to several millimeters in size with the aid of concentrated CsF mineralizers.

The full unit cell representation is shown in **Figure 7.2**. Th(1) is 8-coordinate and displays Th(1)-O bond distances ranging from 2.368(4)-2.658(4) Å. Thorium oxide polyhedra form a one-dimensional zigzag chain extending in the [001] direction through edge-sharing of O(1) atoms, **Figure 7.3a**. These chains form solid-state pillars within the framework and aid in stabilizing the crystal lattice. Within the lattice, $Ti(1)O_6$ can be seen forming layers in the (100) plane. Each $Ti(1)O_6$ polyhedra is edge-sharing of O(1) and O(3) atoms to form a continues titanate sheet, **Figure 7.3b**. Each $Th(1)O_8$ polyhedra coordinates twelve $Ti(1)O_6$ polyhedra through edge-sharing of O(1), corner-sharing of O(1), corner-sharing of O(2), edge-sharing of O(1)/O(2), or corner-sharing of O(3) atoms. Ti(1)-O bond lengths range from 1.864(4)-2.014(4) Å and are in good agreement with expected $Ti(1)O_6$ environments. $ThTi_2O_6$ can be grown as a phase pure product under hydrothermal conditions indicated by the PXRD of the as-grown and simulated material, **Figure 7.6**.

Crystal Structure of UTi_2O_6

The crystal structure of hydrothermally grown uranium titanate, UTi_2O_6, is described. The unit cell parameters are given below in **Table 7.1**. UTi_2O_6 (*C2/m*) is based on two unique metal sites, $U(1)O_8$ and $Ti(1)O_6$, and three unique oxygen sites. Bond distances for UTi_2O_6 are reported in **Table 7.2**. Bond valence sum calculations were performed and are in good agreement with the oxidation states reported in the titanate

structures, **Table 7.3**. Sample crystal growth for UTi_2O_6 is shown below in **Figure 7.1a**. The hydrothermally grown crystals grow as well-formed rods and can be grown up to 3-5 millimeters in size with the aid of concentrated CsF mineralizers. The crystals show a characteristic green color (U^{4+}) which appears black in the bulk material.

The full unit cell representation is shown in **Figure 7.4**. U(1) can be described as 6 + 2-coordinate and displays U(1)-O bond distances ranging from 2.264(5)-2.264(5) Å with two long bonds to O(1) at 2.836(5) Å. Uranium oxide polyhedra form a one-dimensional chain extending in the [010] direction through edge-sharing of O(2) atoms, **Figure 7.5a**. These chains form solid-state pillars within the framework and aid in stabilizing the crystal lattice. Within the lattice, $Ti(1)O_6$ can be seen forming layers in the (001) plane. Each $Ti(1)O_6$ polyhedra is edge-sharing of O(1) and O(3) atoms to form a continues titanate ladder arrangement, **Figure 7.5b**. Each $U(1)O_8$ polyhedra coordinates four $Ti(1)O_6$ polyhedra through edge-sharing of O(2)and corner-sharing of O(3) atoms. Ti(1)-O bond lengths range from 1.850(6)-2.105(5) Å and are in good agreement with expected $Ti(1)O_6$ environments. UTi_2O_6 can be grown as a phase pure product under hydrothermal conditions indicated by the PXRD of the as-grown and simulated material, **Figure 7.7**.

Table 7.1: Crystallographic data for $ThTi_2O_6$ and UTi_2O_6.

empirical formula	**$ThTi_2O_6$**	UTi_2O_6
formula weight (g/mol)	423.84	429.83
crystal system	Monoclinic	Monoclinic
space group, *Z*	*C2/c*, 4	*C2/m*, 2
temperature, K	298(2)	298(2)
crystal size (mm)	0.06 x 0.06 x 0.07	0.05 x 0.05 x0.06
***a*, Å**	10.8202(6)	9.8245(7)
***b*, Å**	8.5891(4)	3.7726(2)
***c*, Å**	5.2020(3)	6.9388(5)
***β*, °**	115.2951(17	118.970(3)
volume, Å^3	437.10(4)	225.00(3)
calculated density (µg/m^3)	6.441	6.344
absorption coefficient (mm^{-1})	37.442	39.302
F(000)	728	368
Tmax, Tmin	1.0000, 0.3552	1.0000, 0.7542
Θ range for data	3.156-30.594	3.356-25.998
reflections collected	10471	1188
data/restraints/parameters	675/0/42	259/0/30
final R [*I*> 2σ(*I*)] R1, wR2	0.0177, 0.0420	0.0143, 0.0368,
final R (all data) R1, wR2	0.0182, 0.0421	0.0143, 0.0368
goodness-of-fit on F^2	1.179	1.048
largest diff. peak/hole, e/ Å^3	1.313, -2.521	1.252, -1.154

Table 7.2: Bond distances (Å) for $ThTi_2O_6$ and UTi_2O_6.

$ThTi_2O_6$		**UTi_2O_6**	
$Th(1)O_8$		**$U(1)O_8$**	
Th(1)-O(1) x2	2.368(4)	U(1)-O(1) x2	2.836(5)
Th(1)-O(1) x2	2.658(4)	U(1)-O(2) x4	2.298(3)
Th(1)-O(2) x2	2.326(4)	U(1)-O(3) x2	2.264(5)
Th(1)-O(3) x2	2.467(4)	**$Ti(1)O_6$**	
$Ti(1)O_6$		Ti(1)-O(1) x2	1.9455(13)
Ti(1)-O(1)	2.001(4)	Ti(1)-O(1)	2.105(5)
Ti(1)-O(1)	2.007(4)	Ti(1)-O(2)	1.874(5)
Ti(1)-O(2)	1.864(4)	Ti(1)-O(3)	1.850(6)
Ti(1)-O(2)	2.014(4)	Ti(1)-O(3)	2.055(5)
Ti(1)-O(3)	1.928(4)		
Ti(1)-O(3)	1.946(4)		

Table 7.3: Bond Valence Sum Calculations for $ThTi_2O_6$ and UTi_2O_6.

$ThTi_2O_6$		**UTi_2O_6**	
$Th(1)O_8$		**$U(1)O_8$**	
Th(1)-O(1) x2	1.162	U(1)-O(1) x2	0.283
Th(1)-O(1) x2	0.531	U(1)-O(2) x4	2.420
Th(1)-O(2) x2	1.301	U(1)-O(3) x2	1.326
Th(1)-O(3) x2	0.889	**ΣU(1)**	4.03
ΣTh(1)	3.88	**$Ti(1)O_6$**	
$Ti(1)O_6$		Ti(1)-O(1) x2	1.401
Ti(1)-O(1)	0.605	Ti(1)-O(1)	0.457
Ti(1)-O(1)	0.595	Ti(1)-O(2)	0.853
Ti(1)-O(2)	0.876	Ti(1)-O(3)	0.910
Ti(1)-O(2)	0.584	Ti(1)-O(3)	0.523
Ti(1)-O(3)	0.737	**ΣTi(1)**	4.15
Ti(1)-O(3)	0.702		
ΣTi(1)	4.09		

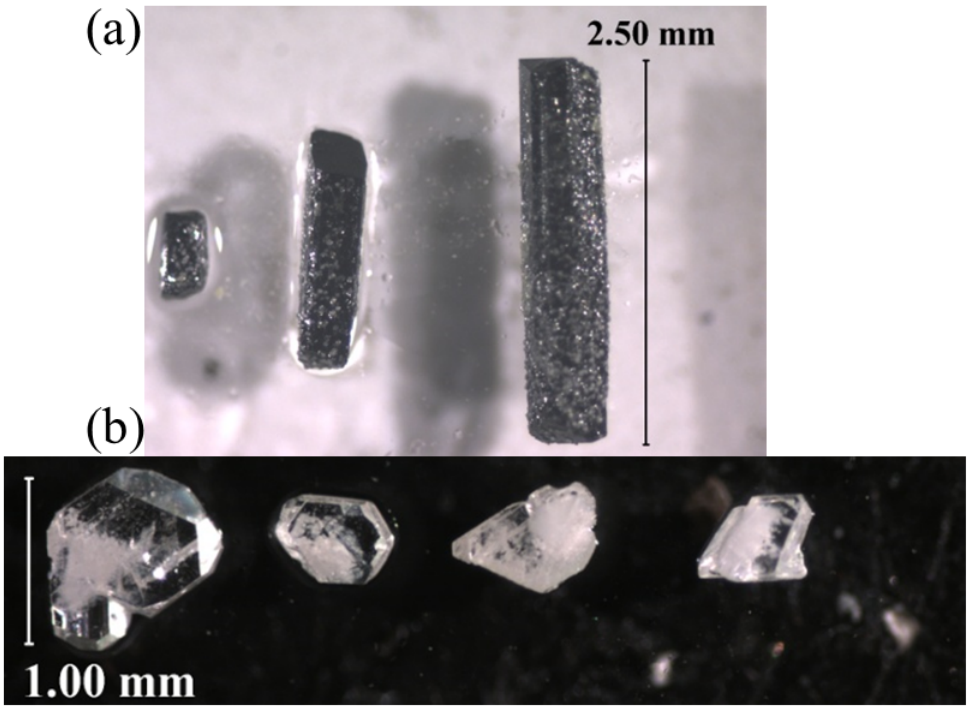

Figure 7.1: Sample crystal growth and habit for (a) UTi_2O_6 and (b) $ThTi_2O_6$ crystals.

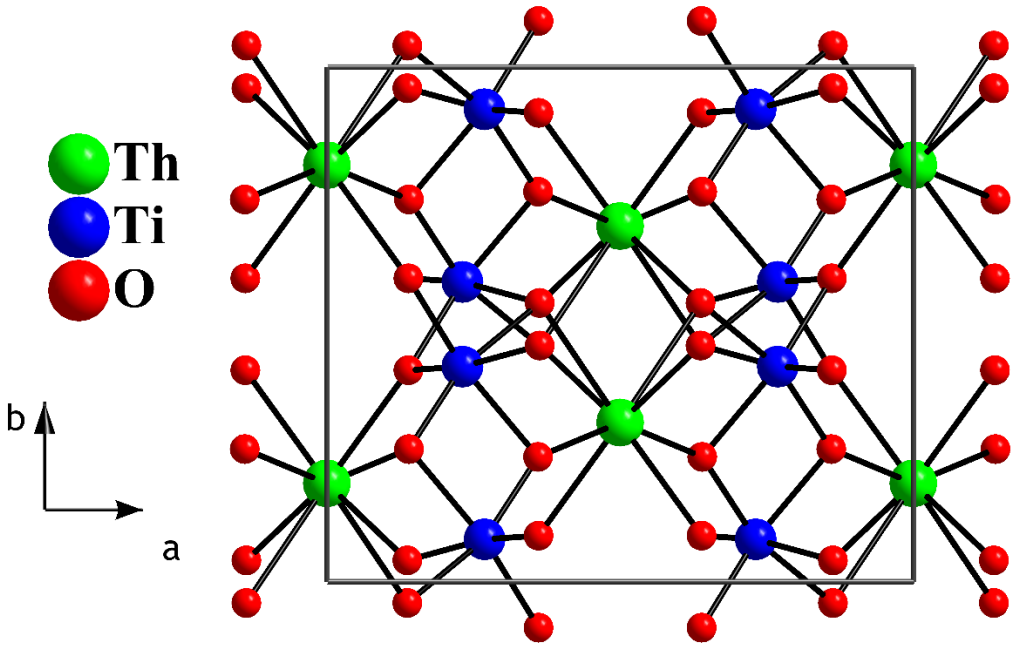

Figure 7.2: Full unit cell representation of $ThTi_2O_6$ highlighting chains of thorium oxide and layers titanium oxide extending in the *bc*-plane.

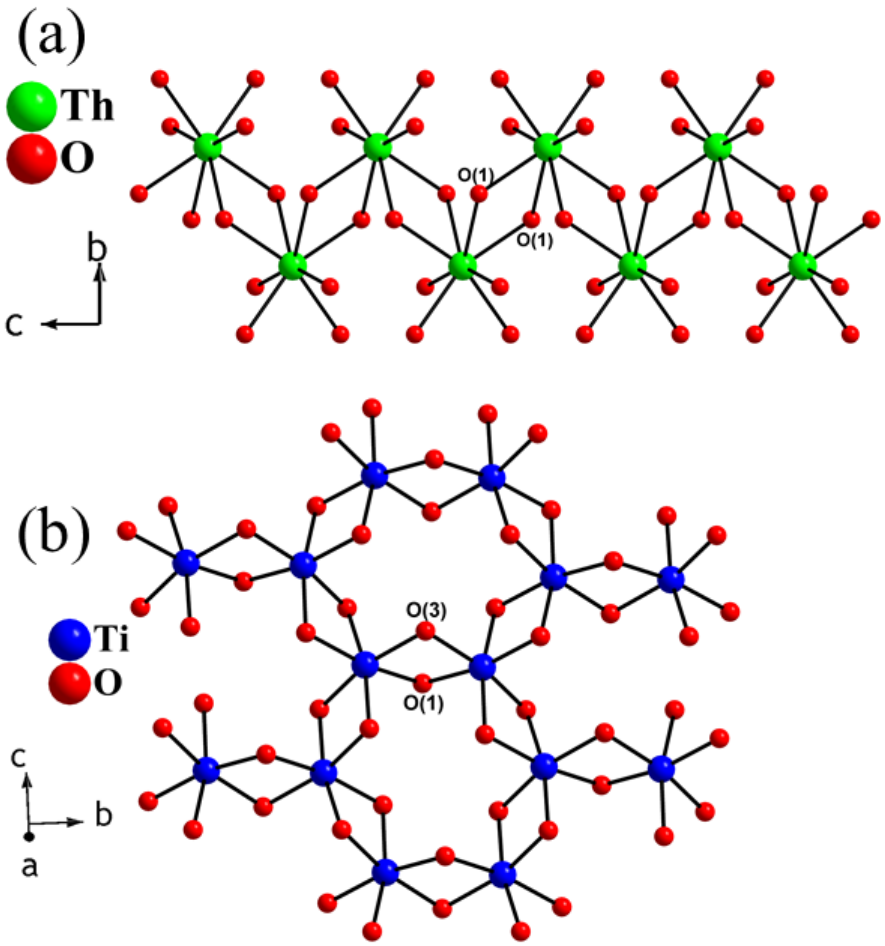

Figure 7.3: (a) Th(1) chain extending along the [001] direction through edge-sharing of O(1) atoms. **(b)** Titanium oxide sheet highlighting edge-sharing of O(1) and O(3) atoms in the (100) plane.

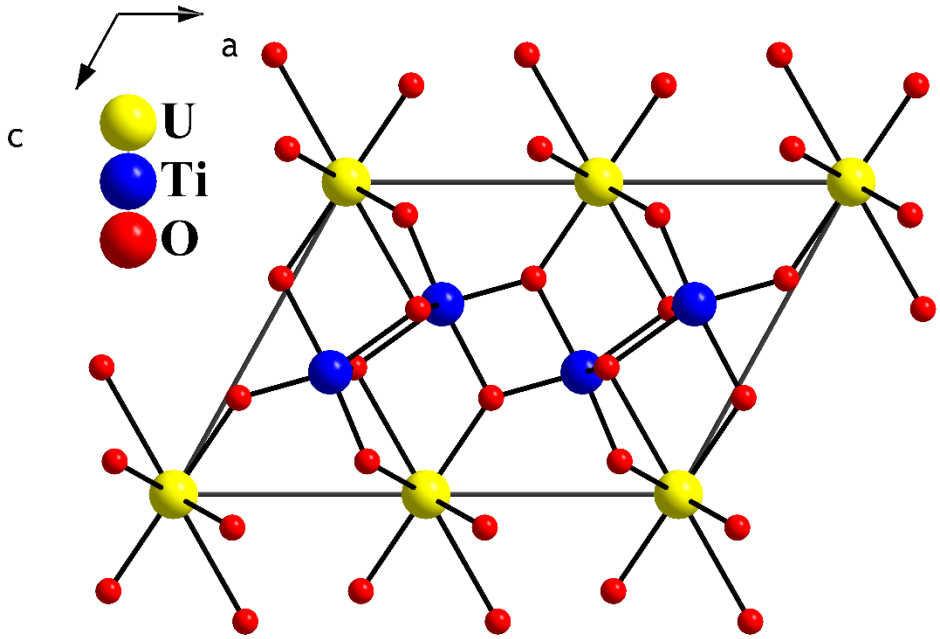

Figure 7.4: Full unit cell representation of UTi_2O_6 highlighting chains of uranium oxide and layers titanium oxide extending in [010] direction.

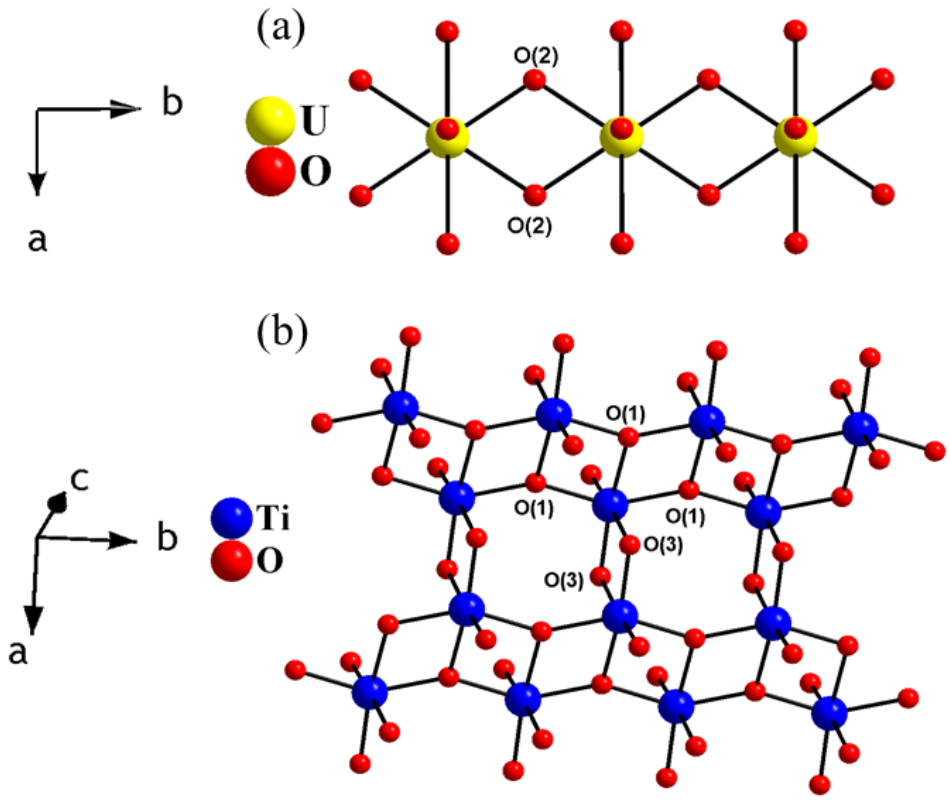

Figure 7.5: (a) U(1) chain extending along the [010] direction through edge-sharing of O(2) atoms. **(b)** Titanium oxide sheet highlighting edge-sharing of O(1) and O(3) atoms in the (001) plane.

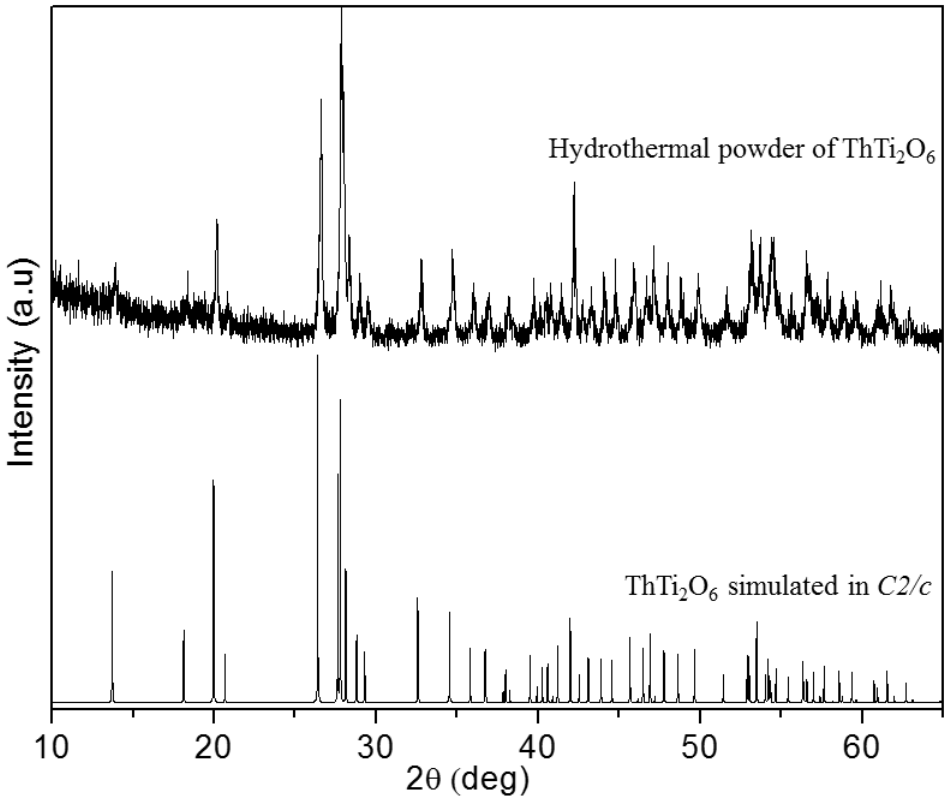

Figure 7.6: Simulated and experimental powder patter of $ThTi_2O_6$ showing no indication of impurities in the hydrothermally-grown powder.

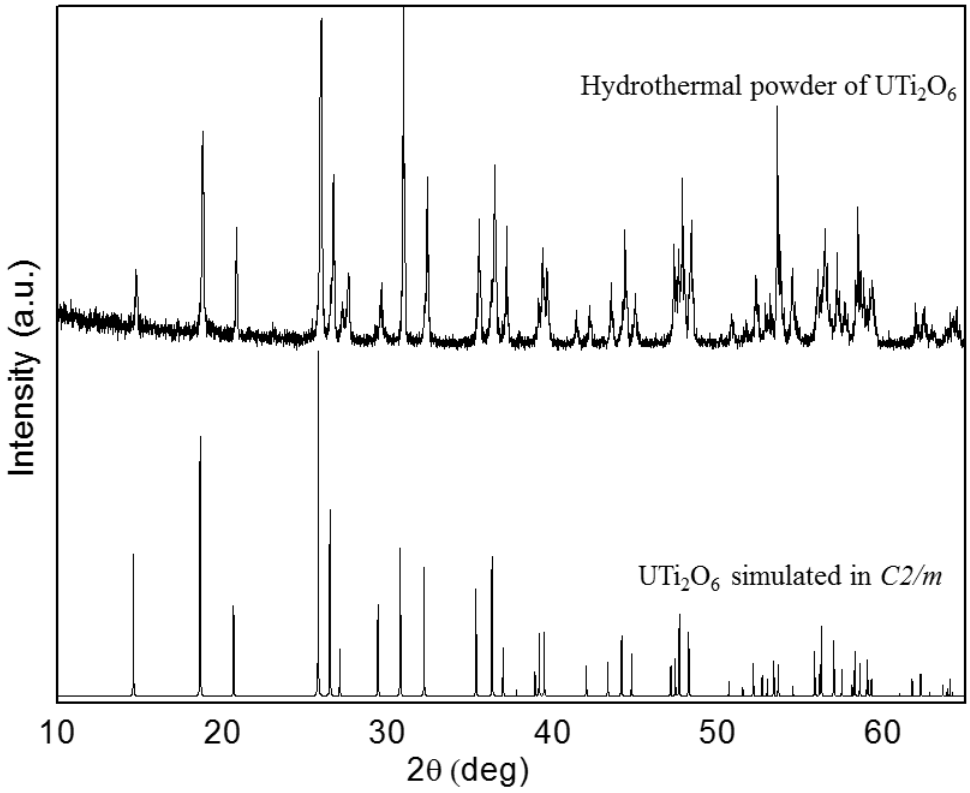

Figure 7.7: Simulated and experimental powder patter of UTi_2O_6 showing no indication of impurities in the hydrothermally-grown powder.

Conclusions

In this Chapter, it has been demonstrated that two highly refractory oxides can be grown from the high-temperature and high-pressure hydrothermal technique. The first examples of bulk crystal growth of $ThTi_2O_6$ and UTi_2O_6 have been shown. To grow single crystals of these two compounds, component oxides of ThO_2 and UO_2 were combined in a stoichiometric fashion in the presence of TiO_2 to examine the phase space of products under hydrothermal conditions. It was found that cesium fluoride, CsF, gives the best conditions for crystal growth of the reported compounds. The use of potassium containing mineralizers, KF, KOH and K_2CO_3, resulted in potassium titanate formation.

It appears from the results reported here, in tandem with previous Chapters, that concentrated fluoride mineralizers provide an excellent avenue into the solubility and growth of highly refractory oxides. While the melting points of ThO_2 and UO_2 exceed 2500 °C, we have shown that exploratory chemistry can be accomplished under hydrothermal thermal regimes nearly 2000 °C lower.

It should be noted that the two compounds reported in this Chapter represent the two most refractory compounds reported in this dissertation. Additionally, the ability to stabilize U^{4+} under highly basic mineralizer is encouraging for future research in which the spin state, $S = 1$, can be examined in other systems like hafnates and zirconates. While U^{6+} products such as $Cs_2U_2O_7$ were also synthesized in this project, the ability to maintain a certain level of chemical control over heavy metals that are susceptible to multiple oxidation states is encouraging moving forward.

References

(1) Kong, L.; Gregg, D. J.; Karatchevtseva, I.; Zhang, Z.; Blackford, M. G.; Middleburgh, S. C.; Lumpkin, G. R.; Triani, G. Novel Chemical Synthesis and Characterization of $CeTi_2O_6$ Brannerite. *Inorg. Chem.* **2014**, *53* (13), 6761–6768.

(2) Kong, L.; Gregg, D. J.; Vance, E. R.; Karatchevtseva, I.; Lumpkin, G. R.; Blackford, M. G.; Holmes, R.; Jovanovic, M.; Triani, G. Preparation of Cerium Titanate Brannerite by Solution Combustion, and Phase Transformation during Heat Treatment. *J. Eur. Ceram. Soc.* **2017**, *37* (5), 2179–2187.

(3) Mann, M.; Thompson, D.; Serivalsatit, K.; Tritt, T. M.; Ballato, J.; Kolis, J. Hydrothermal Growth and Thermal Property Characterization of ThO_2 Single Crystals. *Cryst. Growth Des.* **2010**, *10* (5), 2146–2151.

(4) Mitchell, R. H.; Chakhmouradian, A. R. Solid Solubility in the System $NaLREETi_2O_6$– $ThTi_2O_6$ (LREE, Light Rare-Earth Elements): Experimental and Analytical Data. *Phys. Chem. Miner.* **1999**, *26* (5), 396–405.

(5) Ruh, R.; Wadsley, A. D. The Crystal Structure of $ThTi_2O_6$ (Brannerite). *Acta Crystallogr.* **1966**, *21* (6), 974–978.

(6) Loye, O.; Laruelle, P.; Harari, A. Structure Cristalline de La Forme de Basse Température de L'oxyde Double $ThTi_2O_6$. *CR Séances Acad SciSer C* **1968**, *266*.

(7) Zunic, T. B.; Scavnicar, S.; Grobenski, Z. The Structure of Thorium (IV) Dititanium (IV) Oxide, $ThTi_2O_6$. *Croat. Chem. ACTA.* **1984**, *57* (4), 645–651.

(8) Szymanski, J. T.; Scott, J. D. A Crystal-Structure Refinement of Synthetic Brannerite, UTi_2O_6, and Its Bearing on Rate of Alkaline-Carbonate Leaching of Brannerite in Ore. *Can. Mineral.* **1982**, *20* (2), 271–280.

CHAPTER EIGHT

CONCLUSIONS

A demonstration of the high-temperature and high-pressure hydrothermal technique as a route to crystal growth of new and existing refractory oxides has been achieved. Crystal growth is an interesting field to explore due to the ability of the crystal grower to gain experience over many disciples including: solid-state synthesis, analytical and physical chemistry, characterization, optical and magnetic spectroscopy, just to list a few. The exposure and interaction with many disciplines and experts in these fields facilitates a crystal grower that has a wide understanding of materials.

In this dissertation, focus on the solubility and crystal-growth of highly refractory oxides have been achieved. Refractory oxides are a general class of materials that display melting points generally in the range of 2000 °C or higher. There are very few solid-state techniques that can achieve solubility or crystal growth of oxides in this range due to the inherit oxygen-defects, poor crystal quality, and inclusion of metal contaminants of these techniques. Therefore, very little crystal growth and basic material synthesis has been accomplished and explored with refractory oxides. Generally, these materials have high densities, high thermal electric and laser damage thresholds that make them ideal candidates for applications in scintillators, lasers, and actinide remediation, just to list a few.

Throughout this dissertation, several points of discussion have continued to be highlighted. As a general course of action, the hypothesis that the hydrothermal technique could be used in tandem with soluble tetravalent and pentavalent metal oxides in highly basic fluoride and hydroxide mineralizers to drive solubility of refractory oxides into solution has been discussed. It was found that oxides of SiO_2, GeO_2, TiO_2, and Nb_2O_5 can display Lewis acid-type of properties in the presence of highly basic mineralizers of hydroxide and fluoride alkali metals. These soluble oxides were used as small-to-medium sized building blocks which would go into solution first at much lower temperatures and aid in the solubility of more refractory oxides as higher thermal regimes were reached and maintained over serval days or weeks.

In Chapter Three, an examination of rare-earth and select tetravalent metal refractory oxides in the presence of soluble building blocks of silicates and select germanates was discussed. Several structural classes were discussed including: $Ba_2RE_2Si_4O_{13}$, $Ba_2RE_2Si_4O_{12}F_2$, $KSrRESi_3O_9$, and wadeite-mineral type $A_2MB_3O_9$. In each of these studies, it was determined that the silicate or germanate building block (SiO_2 or GeO_2) in junction with highly basic hydrothermal alkali mineralizers (AF or AOH), provide an excellent environment in which refractory oxides of rare-earth (RE = La-Lu) or tetravalent (Sn, U, Hf, Zr) ions can be stabilized in solution and subsequently nucleated to yield high-quality, low defect single crystals that can be used to explore physical and optical measurements. For $Ba_2RE_2Si_4O_{13}$ and $Ba_2RE_2Si_4O_{12}F_2$ it was determined that the role of BaO in solution plays a crucial role in stabilizing the crystalline structure and providing additional hydroxide (OH^-) when BaO reacts with

water to yield $Ba(OH)_2$ within the hydrothermal silver ampoule. Using the knowledge and experience in the silicate Chapter, an exploration of rare-earth oxides with germanium oxide (GeO_2) was undertaken.

In Chapter Four, an extensive examination of the role of the germanium ion (Ge^{4+}) as a hydrothermal building block in the presence of rare-earth oxides (La-Lu) was investigated. Initially, it was assumed this slightly larger tetravalent tetrahedral building block would display many of the same structural types that were realized in the silicate system. To our surprise and enjoyment, the germanates and silicates display very different solution chemistry that led to the high-quality single crystal growth of several new rare-earth germanates. These structures types include: $RE_{13}(GeO_4)_6O_7(OH)$, $K_2Tb(IV)Ge_2O_7$, $BaRE_{10}(GeO_4)_4O_8$, $BaREGeO_4(OH)$, and $Cs_{0.5}RE_{13}(GeO_4)_6O_{3.5}F_{8.5}(OH)$. Interestingly, the slight increase in ionic size for Ge^{4+} over Si^{4+} led to the discovery and investigation of completely different structure types. Additionally, the discovery of a stable Tb(IV) polygermanate, $K_2TbGe_2O_7$ is currently opening many avenues of discovery for rare-earth ions that can mimic oxidation states of actinide ions like Bk^{4+} and U^{4+}. In each of these studies, the key to new materials being realized in control of the thermal regime, hydrothermal mineralizer, and solubility of the refractory oxide of choice using a preconceived building block to aid in solubility at high-temperatures. The results of this study led to an investigation involving Ti^{4+} as a stable building block and natural extension of tetravalent ions of Si^{4+} and Ge^{4+}.

As the role of hydrothermal building blocks in hydrothermal fluids continues to be understood, an interesting investigation into the RE-Ti system was investigated using

either concentrated hydroxide (20 *M* KOH/ 20 *M* CsOH) or concentrated fluoride (30 *M* CsF). In this study, many new structure types were realized, these include: $Lu_5Ti_4O_{15}(OH)$, $Lu_5Ti_2O_{11}(OH)$, $Sm_3TiO_5(OH)_3$ and $Ce_2Ti_4O_{11}$ species. These compounds were synthesized under high-temperature thermal protocols from 700-750 °C. In general, it was noted that highly basic hydroxide mineralizers give rise to hydroxide rare-earth titanates. For the fluoride mineralizer CsF, a general note that pure rare-earth oxide can be synthesized. It is incredible to think that two metal oxides that have melting points over 1800 °C can become solubilized at 700 °C in highly basic mineralizers. Each new structure and data point continues to point to the fact that the hydrothermal technique provides unrivaled performance in bulk crystal growth. The results of the rare-earth titanate study led to the conclusion that higher oxidation building blocks could possibly be used, if they adopt octahedral symmetry. Thus, an investigation into the rare-earth niobates was a natural extension of this research given success with rare-earth vanadates by Dr. Kimani in previous years.

In Chapter 6, the exploratory of rare-earth niobates and new niobate hydroxides was realized. This was an especially difficult project early on due mainly to the recumbent metal oxides utilized throughout the study. Eventually, a breakthrough in crystal growth occurred when the thermal regime and hydroxide mineralizer concentration was taken up to 700 °C and 30 *M* KOH. These extremely basic conditions provided an adequate environment in which Nb_2O_5 could be solubilized in tandem with the rare-earth oxides (La-Lu). In this system the fergusonite structure type, $RENbO_4$, was found to crystallize across the entire f-block and displays a flexible framework that can

accommodate a variety of f-block ion sizes. Additionally, in the identification of an appropriate hydrothermal mineralizer, several niobate hydroxide structures were synthesized as minor products. These products include: $CsNb_2O_5(OH)$, $CsNb_2O_5(OH/F)$, $K_3LuNb_2O_7(OH)_2$. Again, the role of the building block, Nb^{+5}, plays a crucial role in being a soluble participant in establishing the solid-state framework which can nucleate under highly-basic conditions. With the knowledge gained during his systematic study, a binary study of U^{4+}-Ti^{4+} and Th^{4+}-Ti^{4+} was undertaken. It has been shown that both UO_2 and ThO_2 can be solubilized under hydrothermal conditions in this thesis. Additionally, the rich chemistry from the rare-earth titanate study concluded that Ti^{4+} can adapt 5 or 6-coordinate geometry under hydrothermal conditions. Thus, to synthesize truly refractory oxide crystals that are unattainable by conventional solid-state techniques, $ThTi_2O_6$ and UTi_2O_6 were explored.

In Chapter 7, the bulk crystal growth of $ThTi_2O_6$ and UTi_2O_6 was explored for the first time. These two compounds represent the two most refractory oxides that have been discussed in this dissertation. These materials were synthesized under 6 *M* CsF at 750 °C under several weeks. The ability to solubilize and perform solution chemistry is amazing when one considers that ThO_2 and UO_2 display melting points exceeding 2800 °C. Additionally, the ability to chemically control U^{4+} and prevent oxidation to U^{6+} is leading to new chemistry in the lab. Uranium, especially U^{4+}, will be a very interesting system to investigate in terms of its $S = 1$ magnetic properties.

To further these projects, it is worthwhile to speculate on additional reaction and projects that should be carried out be future grad students in the hydrothermal context.

With each project presented in this thesis, a continuous pursuit of highly refractory oxides has been undertaken. Thus, a natural progression would be to look systematically at systems such as Hf^{4+}-Ta, Zr^{+4}-Ta, Sn^{+4}-Ta, and U^{+4}-Ta. It has been shown in this thesis that each of these tetravalent refractory oxides is at least somewhat soluble under hydrothermal conditions. Additionally, Ta^{+5}, in the form of Ta_2O_5 would be an excellent extension of known rare-earth niobate knowledge. To this end, Ta^{+5} should adopt octahedral symmetry, but the larger size in comparison to Nb^{+5} could lead to investigations of new materials that are highly refractory. For this study, the formation of $CsTaO_5OH$ and $CsTaO_5F$ will need to be avoided as these side products will surely present themselves as was the case for the rare-earth niobate study. However, the use of KF and RbOH should not form the defect-pyrochlore structure as the structure type is heavily dependent on the size of the alkali metal present.

In addition to this project, it has been suggested that materials $Th_2Ta_2O_9$ and $U_2Ta_2O_9$ could be synthesized under hydrothermal conditions. $Th_2Ta_2O_9$ has been reported once by Schmidt and Gruehn under chemical transport with the aid of Cl_2 or NH_4Cl as transporting agents.[1] This compound has been reported to crystallize in space group $C222_1$ to an R_1=9.1%. It is this researcher's belief that this is a twinned primitive or monoclinic unit cell giving the appearance of c-centering. Additionally, the high density of this reported material, 9.68 g/cm^3, makes it a very attractive candidate for bulk crystallization using the high-temperature and high-pressure hydrothermal technique. Most likely this compound will need to be synthesized using a mixture of 6 M CsF/ 1 M CsOH, to drive crystal formation. If $CsTaO_5OH$ and $CsTaO_5F$ single crystal are found,

synthesis using 6 M KF/ 1 M KOH or 6 M RbOH/ 1M RbOH should prove to be a useful mineralizer. This system should be explored in temperature regimes from 650-750 °C due to the limited solubility of ThO_2 and UO_2 in even the best mineralizer choices. If U^{+4} is unstable in this project, it would be wise to use platinum tubing to protect the autoclave from damage and allow the researcher to add reducing agents, like hydrazine, to maintain a tetravalent uranium state. This has proven helpful in recent years when exploring metal oxides with various stable oxidation states in hydrothermal conditions.

In conclusion, many systems have been explored by hydrothermal synthesis. In all cases, the role of the hydrothermal mineralizer, building block oxide, thermal profile, and nature of refractory oxides drive the results reported. Surely in the coming months and years, new high-density refractory oxides will be synthesized using these results as a platform for new materials science. With the continued emergence of new high-temperature alloys and materials, the high-temperature hydrothermal technique will continue to push the limits of what is possible in solution chemistry thus leading the way for new materials to be investigated.

References

(1) Schmidt, G.; Gruehn, R. Darstellung Und Struktur von $Th_2Ta_2O_9$. *J. Common Met.* **1989**, *156* (1), 75–86.

APPENDIX

COPYRIGHT INFORMATION

Title:	Hydrothermal Chemistry and Growth of Fergusonite-type $RENbO_4$ (RE = La–Lu, Y) Single Crystals and New Niobate Hydroxides
Author:	Kyle Fulle, Colin D. McMillen, Liurukara D. Sanjeewa, et al
Publication:	Crystal Growth and Design
Publisher:	American Chemical Society
Date:	Sep 1, 2016

PERMISSION/LICENSE IS GRANTED FOR YOUR ORDER AT NO CHARGE

This type of permission/license, instead of the standard Terms & Conditions, is sent to you because no fee is being charged for your order. Please note the following:

- Permission is granted for your request in both print and electronic formats, and translations.
- If figures and/or tables were requested, they may be adapted or used in part.
- Please print this page for your records and send a copy of it to your publisher/graduate school.
- Appropriate credit for the requested material should be given as follows: "Reprinted (adapted) with permission from (COMPLETE REFERENCE CITATION). Copyright (YEAR) American Chemical Society." Insert appropriate information in place of the capitalized words.
- One-time permission is granted only for the use specified in your request. No additional uses are granted (such as derivative works or other editions). For any other uses, please submit a new request.

Title:	One-Pot Hydrothermal Synthesis of $Tb^{III}_{13}(GeO_4)_6O_7(OH)$ and $K_2Tb^{IV}Ge_2O_7$: Preparation of a Stable Terbium(4+) Complex
Author:	Kyle Fulle, Liurukara D. Sanjeewa, Colin D. McMillen, et al
Publication:	Inorganic Chemistry
Publisher:	American Chemical Society
Date:	June 1, 2017

Dear Kyle Fulle,

Thank you for your message. Permission is hereby granted, on behalf of the IUCr, for you to reproduce the material specified below, subject to the following conditions:

1. Reproduction is intended in a primary journal, secondary journal, CD-ROM, book or thesis.

2. The original article in which the material appeared is cited.

3. IUCr's copyright permission is indicated next to the Figure in print. In electronic form, this acknowledgement must be visible at the same time as the Figure, and must be hyperlinked to Crystallography Journals Online (http://journals.iucr.org/10.1107/S2052520617009544).

Best wishes

Peter

Peter Strickland, Executive Managing Editor, IUCr Journals
IUCr Editorial Office, 5 Abbey Square, Chester CH1 2HU, England
Phone: 44 1244 342878 Email: ps@iucr.org WWW: http://journals.iucr.org